MODELLING OF ELECTRON TRANSPORT AND OF SAWTOOTH ACTIVITY IN TOKAMAKS

THÈSE N^{O} 2469 (2001)

PRÉSENTÉE AU DÉPARTEMENT DE PHYSIQUE

ÉCOLE POLYTECHNIQUE FÉDERALE DE LAUSANNE

POUR L'OBTENTION DU GRADE DE DOCTEUR ÈS SCIENCES

PAR

Clemente ANGIONI

dottore in ingegneria nucleare, Politecnico di Torino, Italie
et de nationalité italienne

acceptée sur proposition du jury:

Dr O. Sauter, directeur de thèse
Prof. R. Chawla, rapporteur
Dr G. T. Hoang, rapporteur
Dr J.-M. Moret, rapporteur
Dr A. G. Peeters , rapporteur
Prof. M. Q. Tran, rapporteur
Dr L. Villard, rapporteur

Lausanne, EPFL
2001

For our knowledge is imperfect and our prophecy is imperfect

Car partielle est notre science, partielle aussi notre prophétie

Perché imperfetta è la nostra conoscenza ed imperfetta la nostra profezia

Saint Paul, Apostle, First Letter to Corinthians, 13, 9.

Version abrégée

Les phénomènes de transport dans les plasmas de tokamak réduisent fortement le confinement de particules et d'énergie et constituent un obstacle majeur à la fusion thermonucléaire contrôlée. Parmi les nombreux thèmes relatifs à l'études du transport, trois points ont été abordés dans le cadre de cette thèse: premièrement, le calcul numérique des coefficients de transport néoclassique pour les équilibres axisymétriques généraux et un régime collisionel arbitraire, deuxièmement, l'analyse du comportement de la température électronique et la modélisation du transport dans les décharges de plasma du Tokamak à Configuration Variable (TCV), troisièmement, la modélisation et la simulation de l'activité de dents de scie sous différentes conditions de chauffage.

Le travail consacrée à la théorie néoclassique a été entrepris avant tout afin d'identifier analytiquement un ensemble d'équations adaptées à être implémentées dans les codes Fokker-Planck existants. La modification de ces codes nous a permis de calculer les coefficients de transport néoclassique tout en considérant différentes configurations réalistes d'équilibre magnétique et en faisent varier sur un large spectre les trois paramètres clés suivants: le rapport d'aspect, la collisionalité et la charge effective. La comparaison des résultats numériques avec une limite analytique a conduit à l'identification de deux expressions donnant la fraction des particules piégées; ces expressions, incluant les effets géométriques, permirent de faire correspondre chaque coefficient avec une seule fonction analytique. En conséquence, de simples formules analytiques pour les coefficients de transport néoclassique purent être établies, formules valables pour un rapport d'aspect et une collisionalité quelconques et dans une géométrie réaliste et générale. Cette étude est particulièrement utile pour évaluer correctement la contribution néoclassique dans un scénario pour le tokamak caractérisé par une grande composante de courant bootstrap, ou dans un régime de confinement amélioré avec faible transport anormal, et pour déterminer le profil de densité de courant, la conductivité du plasma étant généralement supposée néoclassique.

Ces résultats furent inclus dans le code de transport PRETOR. Son champ d'application fut développé afin de pouvoir simuler le transport électronique dans TCV. Dans les simulations de profil de température électronique de plasmas Ohmiques avec dents de scie, la description correcte du profil de densité de courant et de l'activité des dents de scie joue le rôle principal, et non pas le modèle spécifique de transport, pourvu qu'un seul paramètre du modèle soit ajusté de manière à reproduire la performance globale du plasma. Dans les décharges TCV avec chauffage cyclotronique électronique (CCE), le comportement de la température électronique fait preuve de caractéristiques récemment observées comme étant communes à plusieurs tokamaks. En particulier, en présence de chauffage central, le profil de température électronique est rigide à l'extérieur de la région de déposition de puissance et essentiellement constant le long du rayon mineur. En présence de chauffage hors-axe, le transport est fortement réduit dans la région centrale du plasma, tandis qu'une forte augmentation de la conductivité de chaleur est observée au lieu de déposition de la puissance. Bien que le modèle de transport semi-empirique de Rebut–Lallia–Watkins (RLW) n'implique pas une échelle de gradient critique, comme l'observation expérimentale le suggère, mais plutôt un gradient critique de température électronique, nous avons montré que ce modèle permet de faire des simulations en très bon accord avec les caractéristiques expérimentales décrites plus haut. Grâce au relativement bas champ magnétique torique de TCV, le gradient expérimental de température avec CCE excède de loin le seuil inclus dans le modèle. Il peut par conséquent être affirmé que la dépendance paramétrique de la conductivité électronique de chaleur de ce modèle de transport reproduit adéquatement le transport électronique pour des paramètres de plasma dans le domaine d'opération de TCV. PRETOR, interfacé avec les données expérimentales et le code TORAY–GA pour le calcul de la source CCE, a ainsi pu être utilisé comme un instrument fiable pour l'analyse de transport et la planification de nouvelles expériences. Ceci a contribué à l'identification d'un régime de confinement central électronique amélioré (CCEA) dans TCV, caractérisé par un schéma précis de chauffage (forte génération de courant cyclotronique électronique, au centre du plasma et dans la direction contre-courant, avec chauffage hors-axe localisé) avec une séquence de temps spécifique. Des simulations et analyses de transport de ce régime, en particulier consacrées à la reconstruction du profil de densité de courant pendant la phase de haute performance, ont motivé des expériences additionnelles, confirmant les prédictions numériques et permettant d' identifier l'inversion du cisaillement magnétique comme étant l'ingrédient crucial du CCEA.

Le puissant système CCE dans TCV ne permet pas de modifier fortement le profil de courant que de manière globale, mais aussi localement, ce qui influence significativement l'activité de dents de scie. Un modèle pour la prédiction de la période des dents de scie dans le "International Thermonuclear Experimental Reactor" (ITER) a été étendu et rendu applicable aux décharges Ohmiques et CCE de TCV. Le modèle est en accord avec les observations expérimentales, nous permettant par conséquent d'identifier les mécanismes physiques à l'origine du contrôle de la periode de dent de scie par le CCE. La dépendance paramétrique du seuil relevant de stabilité est consistant avec les expériences consacrées à la démonstration des effets du chauffage localisé et de la génération de courant sur la période de dent de scie. Les effets du cisaillement magnétique et du gradient de pression à la surface $q = 1$ ont été mis en évidence. De plus, il a été constaté que le lieu de chauffage le plus efficace pour stabiliser la période des dents de scie est situé à l'extérieur de la surface $q = 1$ avant l'écroulement des dents de scie. Le même modèle a été utilisé pour simuler la période des dents de scie de récentes décharges avec chauffage par injection de neutres (CIN) dans le "Joint European Torus" (JET), effectuées dans le but d'établir le rôle des ions rapides du faisceau sur la stabilisation des dents de scie. Grâce à l'inclusion de l'expression analytique de la contribution des ions rapi-

des à l'énergie potentielle de l'instabilité de torsion interne, validée par le code hybride cinétique/magnétohydrodynamique NOVA-K, les résultats de simulations se sont révélés être remarquablement proches des observations expérimentales. Ce travail a démontré le rôle des ions rapides du CIN dans la stabilisation des dents de scie et validé le seuil de stabilité pour l'instabilité résistive de torsion interne, prédite comme étant, pour le régime d'opération d'ITER, le déclencheur de l'écroulement de la dent de scie.

Summary

Transport phenomena in tokamak plasmas strongly limit the particle and energy confinement and represent a crucial obstacle to controlled thermonuclear fusion. Within the vast framework of transport studies, three topics have been tackled in the present thesis: first, the computation of neoclassical transport coefficients for general axisymmetric equilibria and arbitrary collisionality regime; second, the analysis of the electron temperature behaviour and transport modelling of plasma discharges in the Tokamak à Configuration Variable (TCV); third, the modelling and simulation of the sawtooth activity with different plasma heating conditions.

The work dedicated to neoclassical theory has been undertaken in order to first analytically identify a set of equations suited for implementation in existing Fokker–Planck codes. Modifications of these codes enabled us to compute the neoclassical transport coefficients considering different realistic magnetic equilibrium configurations and covering a large range of variation of three key parameters: aspect ratio, collisionality, and effective charge number. A comparison of the numerical results with an analytical limit has permitted the identification of two expressions for the trapped particle fraction, capable of encapsulating the geometrical effects and thus enabling each transport coefficient to be fitted with a single analytical function. This has allowed us to provide simple analytical formulae for all the neoclassical transport coefficients valid for arbitrary aspect ratio and collisionality in general realistic geometry. This work is particularly useful for a correct evaluation of the neoclassical contribution in tokamak scenarios with large bootstrap current fraction, or improved confinement regimes with low anomalous transport and for the determination of the plasma current density profile, since the plasma conductivity is usually assumed neoclassical.

These results have been included in the plasma transport code PRETOR. This code has been further extended and applied to the simulation of electron transport in TCV. In simulating the electron temperature profile of Ohmic sawtoothing plasmas, the proper description of the current density profile and the sawtooth activity play the dominant role and not the specific transport model, provided that a single parameter in the model is adjusted to match the global plasma performance. In TCV discharges with electron cyclotron heating (ECH), the behaviour of the electron temperature exhibits some characteristics which have been recently observed to be common to several tokamaks. In particular, with central heating the electron temperature profile is stiff outside the power deposition region, that is the gradient scale length is independent of the heating power and essentially constant along the minor radius. With off–axis heating, transport is strongly reduced in the central region of the plasma, whereas a steep increase of the heat conductivity is observed at the power deposition location. Although the semi–empirical Rebut–Lallia–Watkins (RLW) transport model does not involve a critical gradient scale

length, as the experimental observations would suggest, rather a critical electron temperature gradient, we have shown that it allows simulations which reproduce the described experimental features with very good agreement. Due to the relatively low toroidal magnetic field of TCV, the experimental temperature gradient with ECH exceeds by far the threshold included in the model. It can thus be stated that the parametric dependence of the electron heat conductivity of this transport model is adequate to reproduce the electron transport for plasma parameters in the operation domain of TCV. PRETOR, interfaced with the experimental data and the code TORAY–GA for the computation of the ECH source, has hence been used as a reliable tool for transport analysis and planning of new experiments. This has contributed to the identification of an improved central electron confinement (ICEC) regime in TCV, characterized by a precise heating scheme (strong electron cyclotron current drive in the counter–direction in the plasma center, and localized off–axis heating), with a specific time sequence. Transport simulations and investigations of this regime, in particular dedicated to the reconstruction of the current density profile during the high performance phase, have motivated further experiments which have confirmed numerical predictions. As a consequence, the magnetic shear reversal has been identified as the crucial ingredient for ICEC.

The powerful ECH system in TCV does not allow only strong global current profile modifications but also local tailoring which has significant effects on sawtooth activity. A model introduced for the prediction of the sawtooth period in the proposed International Thermonuclear Experimental Reactor (ITER) has been extended to be applicable to Ohmic and ECH discharges in TCV. The model has been found in agreement with the experimental observations and thereby we were able to identify the physical mechanisms which make ECH capable of controlling the sawtooth period. The parameter dependence of the relevant stability threshold has been found consistent with dedicated experiments demonstrating the effects of localized heating and current drive on the sawtooth period. The simulations have pointed out the effects of the magnetic shear and of the pressure gradient at the $q = 1$ surface. Moreover, the most efficient heating location to stabilize the sawtooth period has been identified as located outside the $q = 1$ surface before the sawtooth crash. The same period model has been used for the simulation of the sawtooth period in recent discharges with neutral beam injection (NBI) in the Joint European Torus (JET), performed to assess the role of beam ions on sawtooth stabilization. With the inclusion of an analytical expression for the fast ion contribution to the internal kink potential energy, validated by the hybrid kinetic/MHD code NOVA–K, the simulations have been found in remarkable good agreement with the experimental observations. This work has demontrated the role of beam ions in sawtooth stabilization and validated the stability threshold for the resistive internal kink which was predicted to be the sawtooth crash trigger relevant for ITER operation.

Contents

1 **Introduction** **1**

2 **Neoclassical transport** **7**

2.1 Introduction 7
2.2 Kinetic theory 10
2.2.1 Transport coefficients 10
2.2.2 Onsager symmetry of the transport coefficients 14
2.2.3 Banana regime: bounce-averaged equations 15
2.2.4 Lorentz model 16
2.3 Numerical results 17
2.3.1 Benchmarks 17
2.3.2 Comparison with previous results, behaviour at small aspect ratio . 20
2.3.3 Neoclassical conductivity and bootstrap current coefficients at arbitrary collisionality 24
2.4 Transport coefficients formulae 26
2.4.1 Analytical fits to the numerical results for the banana regime 26
2.4.2 Analytical fits to the numerical results for parallel transport at all collisionality 31
2.4.3 Combined formulae for radial transport at all collisionality 33
2.4.4 Coefficients for the combined formulae of subsection 2.4.3 36
2.5 Conclusion 37
2.6 Appendix 39

3 **1-1/2 D simulation of a tokamak plasma** **49**

3.1 Introduction to 1-1/2 D simulations 51
3.2 Transport equations in toroidal geometry 53
3.3 Self–consistent magnetic equilibrium evolution 61
3.4 Energy sources and losses in PRETOR 65
3.5 Numerical details about PRETOR 68
3.6 Transport models 69

3.6.1 The Rebut–Lallia–Watkins local transport model 70
3.6.2 Transport coefficients in PRETOR 71

4 Modelling transport in TCV 79
4.1 Introduction 79
4.2 Brief description of TCV 79
4.3 The TCV Electron Cyclotron heating system 81
4.4 Electron temperature behaviour with ECH in TCV 84
4.4.1 Central heating 84
4.4.2 Off–axis heating 88
4.5 The RLW transport model applied to TCV discharges 92
4.5.1 The RLW critical gradient in TCV plasmas 93
4.5.2 Ohmic plasmas 98
4.5.3 Adapting the RLW model to plasmas with large q_{edge} 105
4.5.4 Electron cyclotron heated plasmas 107
4.6 Improved Central Electron Confinement 115
4.6.1 Simulation methodology for the time evolution of an ECH discharge 116
4.6.2 Central electron temperature enhancement with counter–ECCD . . 117
4.6.3 Experimental observations of ICEC 119
4.6.4 Central heating, simulation of shot ♯18604 123
4.6.5 ICEC discharges 125
4.7 Summary and Conclusions 134

5 Sawtooth period modelling 141
5.1 Introduction 141
5.2 Sawtooth period model 144
5.2.1 Sawtooth crash triggering conditions 144
5.2.2 Prescriptions for the relaxed profiles 152
5.3 Sawtooth period modelling of TCV discharges 158
5.3.1 Ohmic discharges 158
5.3.2 Adding electron cyclotron heating 162
5.3.3 Sawtooth period and ECH power density 164
5.3.4 Sawtooth period and current drive 166
5.3.5 Simulation of a full poloidal sweep 167
5.4 Sawtooth stabilisation by NBI in JET 168
5.4.1 Experimental observations 170
5.4.2 Numerical computation of $\delta\hat{W}_{fast}$ and validation of an analytical expression 172

5.4.3 Comparison between theory and experiment 176
5.5 Summary and Conclusions 183

6 Conclusions and outlook **193**

Chapter 1

Introduction

Nuclear fusion is a reaction in which two light nuclei fuse to form a heavier nucleus. The nuclear rearrangement results in a reduction of the total mass and consequently in a release of energy. These reactions are of extreme importance in nature, since they supply stars with energy. On earth, controlled thermonuclear fusion is one of the principal long–term, safe, and rather clean potential sources of energy. Coulomb repulsion of the positively charged nuclei needs to be overcome by providing high kinetic energies to the nuclei. Even at high energy the probability of a fusion reaction occurring is much lower than that for Coulomb scattering. The solution offered by thermonuclear fusion is to heat a reagent mixture until thermal velocities are sufficiently high for fusion reactions to occur with a significant frequency. The most favourable reagents found in nature are two hydrogen isotopes, deuterium (D) and tritium (T), which fuse yielding a fast α–particle of 3.5 MeV and a neutron of 14.1 MeV. With this reaction the required thermal energy for the reagent mixture is of the order of 10 keV, which corresponds to a temperature of 116 million degrees Kelvin. At this temperature atoms are fully ionised. The positive electrostatic charge of ions is neutralized by the presence of an equal negative charge of electrons, resulting in a neutral gas called plasma. To maintain this high temperature, the plasma needs to be confined to minimize the contact with material walls. A possible method is to use a magnetic field. One of the devices which have been developed over the years to produce a magnetic confinement configuration for thermonuclear plasmas is the tokamak. In this device a set of external toroidal field coils and an electric current induced in the plasma, usually by transformer action, generate a closed toroidal structure consisting of an infinite set of nested toroidal magnetic surfaces.

The tokamak is regarded today as the most promising device and the most likely to become the future reactor in a nuclear fusion power plant. The ignition condition, at which the thermonuclear power produced by fusion reactions inside the plasma provides sufficient plasma heating to balance the power losses, reads, for a D–T mixture around

10 keV,

$$nT\tau_E > 5\ 10^{21}\mathrm{m}^{-3}\,\mathrm{keV\,s},$$

where n is the plasma density, T the ion temperature and τ_E the thermal energy confinement time. The heating power required to reach the desired values of energy confinement time and central plasma temperature is determined by the magnitude of energy transport. Therefore, research on energy transport in tokamaks is of crucial importance for nuclear fusion.

An unavoidable physical mechanism involving energy and particle transport is collisions. In a magnetized plasma, "classical" collisional transport arises from collisions affecting the charged particles gyromotion around the field lines. In toroidal magnetic confinement systems a supplementary contribution to collisional transport, the so-called "neoclassical" transport, is present. Neoclassical transport is generated by collisions affecting the guiding centre orbits caused by the closed field lines of the magnetic confinement configuration. Since the radial excursion of these orbits can be macroscopically significant ("banana" orbits), the neoclassical term provides the dominant contribution to collisional transport. Nevertheless, even taking into account neoclassical enhancements, collisions are far from being able to account for the energy and particle losses which are observed experimentally in tokamaks. Other mechanisms, much more effective than collisions, are unfortunately at play. They produce the so-called "anomalous" transport.

Research on anomalous transport is aimed at developing physical models capable of providing reliable predictions of the confinement properties of future devices. This research might allow also the identification of configurations and plasma conditions where anomalous transport is reduced or even absent. Improvements need both experimental and theoretical approaches. Dedicated experiments can highlight specific parametric dependences and identify plasma conditions in which confinement is improved. Theoretical models must be developed in order to explain experimental observations, and predict new plasma behaviours under experimentally unexplored conditions. Since the tokamak is a rather complex system, the comparison itself between theoretical predictions and experimental measurements is not a trivial task. The link between theory and experiments requires numerical tools capable of transforming theoretical models into measurable quantities. It is in this activity that we can locate the main body of the present research work.

The first goal of this work has been to extend an existing transport code, PRETOR, in order to supply the TCV device with numerical tools for analysis and simulation of plasma transport. The Tokamak à Configuration Variable (TCV) is a medium size tokamak located at the Centre de Recherches en Physique des Plasmas (CRPP) in the École

Polytechnique Fédérale de Lausanne (EPFL). It has been designed to investigate the effects of plasma shape on confinement and stability. The strong shape flexibility of TCV and its powerful electron cyclotron heating (ECH) system allow transport studies which can address specific issues of great relevance to fusion research. In addition, the peculiarities of TCV imply precise requirements for a transport simulation code. In particular, the shape flexibility demands a realistic description of the magnetic surface configuration. The auxiliary heating sources, enabling also strong current drive, require a correct description of the plasma current density evolution.

In constrast with perpendicular transport, the plasma conductivity is believed to be mainly determined by collisions, and therefore by neoclassical theory. Another important effect of collisions, predicted by neoclassical theory, is to self–generate a plasma current, known as "bootstrap current", in the presence of inhomogeneities of the pressure and density profiles. For applications to TCV, as in general for shaped plasmas in tokamaks which are not in the large aspect ratio limit, it is particularly important to have expressions for the neoclassical parallel transport coefficients which take into account the real geometry and plasma collisionality. This has motivated us to reformulate the standard neoclassical theory in order to obtain analytically a set of equations simple enough to be easily implemented in existing Fokker–Planck codes which take into account the axisymmetric magnetic surface configuration. This work has enabled us to obtain a set of formulae for all the neoclassical coefficients describing parallel and perpendicular electron and ion transport, taking into account both collisionality and finite aspect ratio effects in realistic geometries. In this way we have been able to perform transport simulations of shaped plasmas including the most correct neoclassical description of both plasma conductivity and bootstrap current.

Transport modelling has been dedicated to the simulation of both ohmic and ECH discharges in TCV. We have analyzed the experimental behaviour of the electron temperature in TCV in order to identify the main experimental characteristics which must be expected to be reproduced by a transport model. We have applied the Rebut–Lallia–Watkins (RLW) transport model to both Ohmic and ECH plasmas. This model provides a global scaling law for the energy confinement time which was found to be in very good agreement with TCV data in Ohmic and ECH discharges in low confinement (L–) mode. The local RLW transport model had already been applied in the literature to the simulation of transport in other tokamaks. In those studies it provided many successful results, in particular in the simulation of the electron heat transport, but it was not found consistent with the experimental observations in all cases. We shall show that, when applied to TCV plasmas, the model is well inside the validity domain identified by previous analysis.

It turns out to be successful in the simulation of a very large variety of TCV heating and plasma conditions. This model must be regarded as almost completely empirical, in the sense that it is not derived from a consistent theoretical model based on first principle physics. Because of this, it should be stressed that the application of such a model has limited relevance in transport studies dedicated to identifying the real physical mechanisms producing anomalous transport. We believe that reliable predictions of the confinement properties of future devices cannot simply be based on empirical models or scaling laws, but require that the real physics responsible for anomalous transport is identified and understood. Nevertheless, TCV plasmas with extreme auxiliary heating conditions and record values of the electron temperature gradients have been simulated with surprising accuracy by the RLW model. In this sense we are confident that its parameter dependence can provide useful indications on the nature of electron transport, hopefully motivating new dedicated theoretical investigations and experiments.

The application of this model has allowed us to provide a transport code which has been used on a regular basis not only in simulations, but also in the preparation and design of new experiments, and regarded as a useful and reliable tool by TCV experimentalists. In particular it has provided valuable help in the discovery of an improved central electron confinement regime in TCV. The correct description of the current density profile evolution in PRETOR has also allowed us to identify the modification of the central magnetic shear, namely the shear reversal produced by strong counter current drive, as the key for the improved confinement.

Most standard tokamak scenarios are characterized by the presence of an internal instability which generates periodic oscillations of central temperature, density and other plasma parameters. These oscillations are called sawteeth because of their characteristic sawtooth shape, as observed on soft X–ray signals. Transport simulations of sawtoothing discharges can not be performed purely on the basis of a transport model, but must also incorporate a specific model for the sawtooth period and amplitude. Since sawteeth cause an outward transfer of energy and particles, the sawtooth model must be actually regarded as an integral part of the transport model. For this reason, in parallel with transport analysis and simulation, we have been involved in modelling the sawtooth activity, with specific emphasis on sawtooth period simulations. We have generalized a sawtooth period model previously introduced for the prediction of the sawtooth period in the proposed International Thermonuclear Experimental Reactor (ITER), a project that involves almost all the industrialized countries in the world and will provide the next step device towards a fusion reactor. We have applied the sawtooth period model in the simulation of Ohmic and ECH TCV discharges, as well as of discharges with neutral beam injection (NBI) in the Joint European Torus (JET, located in the Culham Science Centre in Great Britain, is the largest tokamak in the world and it is the result of a collaboration amongst several European countries). The application of the model in two different tokamaks has allowed us to investigate the physics of different sawtooth crash trigger conditions, and to identify the plasma parameters most likely to be at play in sawtooth stabilization. In particular the analysis and simulation of TCV experiments have highlighted the role of local current profile modifications produced both by localized electron heating and current drive. ECH turns out to be a powerful tool for modifying and controlling the sawtooth period. This is of specific relevance to future applications in nuclear fusion research. Long sawteeth can have undesirable consequences, such as the creation of seed magnetic islands capable of triggering pressure–limiting instabilities, highly reducing the plasma performance. Therefore, understanding the physical mechanisms which govern sawtooth activity must be considered a crucial issue for the scientific development towards a fusion reactor.

Moreover, in a burning plasma the dominant role in the determination of the sawtooth period is likely to be played by α–particles. The investigation of the effects of fast particles on sawtooth stabilization is therefore of particular interest. For this reason, we have performed a detailed analysis and simulation of dedicated JET discharges with NBI, assessing the role of beam ions in sawtooth stabilization. In this way we have obtained the first detailed understanding of the role of NBI on sawteeth. The sawtooth period model, including a stabilizing contribution by beam ions, has been found to provide simulations of the sawtooth period in good quantitative agreement with the experimental observations, by means of a sawtooth crash trigger condition which was predicted by a previous work as the most likely to be relevant for ITER operation.
The present work is the first detailed test of a sawtooth model fully integrated in transport simulations. The application to TCV and JET discharges made it possible to validate almost all the aspects of the model.

I firmly believe in nuclear fusion as the main road towards satisfying the growing energy demand of mankind. In view of the large number of physical and technological problems which still remain to be solved towards a complete mastery of this almost unlimited natural source of energy, I hope I have been able to provide, with the present work, a small but non completely negligible contribution.

Outline

In **Chapter 2** we present the computation of the neoclassical transport coefficients for general axisymmetric magnetic configurations and arbitrary collisionality regime. First we describe the analytical derivation of a set of kinetic equations suited for implementation in numerical Fokker–Planck codes. Then we discuss the numerical results, with particular emphasis on the behaviour at small aspect ratio, and we compare with previous formulae available in the literature. We identify the parameters able to correctly describe the geometrical and collisional effects on the coefficients and then we present a set of formulae of general validity, obtained by fitting the numerical results.

In **Chapter 3** we introduce the concept of 1-1/2 D transport simulations for tokamak plasmas. We present the equations describing transport and magnetic field evolution, following more closely what is implemented in the code PRETOR. Finally, we present and briefly discuss the Rebut–Lallia–Watkins local transport model, for both energy and particle transport, in the form in which it has been implemented in the code.

Chapter 4 contains the results related to transport modelling of TCV discharges. After a brief description of the TCV device and of the ECH system, we present an analysis of the experimental behaviour of the electron temperature in discharges with auxiliary heating. Afterwards we discuss the application of the RLW transport model to TCV plasmas, in particular pointing out that the critical temperature gradient involved in the model plays an almost negligible role. We present simulations of both Ohmic and ECH plasmas, highlighting the characteristics of the model which are responsible for the good agreement with the experimental observations. Finally a long section dedicated to the improved electron confinement obtained in TCV provides a description of the experiments and of the experimental observations, shows the results of some PRETOR simulations, and discusses the effects of current profile tailoring on plasma confinement.

Chapter 5 is devoted to sawtooth period modelling. We first give a detailed description and discussion of the sawtooth period model and of the prescriptions for computing the relaxed post–crash plasma profiles. Then we present the application of the model to Ohmic TCV plasmas, identifying the relevant instability regime and stability threshold for TCV operation. The model is then applied to ECH discharges in which dedicated experiments have been performed in order to test the effects of power localization and current drive on sawtooth activity. In the last section we present the work performed at JET, with the goal of experimentally and theoretically assessing the effect of fast ions arising from NBI on sawtooth stabilization.

In **Chapter 6** conclusions are drawn on the work presented, and proposals for future work are outlined.

Chapter 2

Neoclassical transport

2.1 Introduction

The expression neoclassical transport has been introduced to identify a supplementary contribution to the classical collisional transport in magnetically confined plasmas, arising from the toroidal effects due to the confinement system [1]. Classical transport is due to Coulomb collisions affecting the Larmor orbits [2], whereas neoclassical transport is caused by collisions affecting the guiding centre orbits created by the magnetic field of the toroidal magnetic confinement system. Depending on the value of the collision frequency compared to the transit frequencies of the various possible guiding center orbits, several different additional collisional transport processes can be involved and different collisional transport regimes can be identified. Neoclassical transport is largely dominant as compared with classical transport. Nevertheless the experimentally observed radial transport occurring in a tokamak turns out to be in general significantly larger than the one which can be ascribed only to collisional effects: the amount of transport which can not be explained by collisional theory is usually called anomalous. On the contrary, transport parallel to the magnetic field lines is believed to be well described by neoclassical theory. For this reason recent improvements in neoclassical transport theory are almost completely dedicated to parallel transport.

The neoclassical resistivity and the self–generated bootstrap current are widely used to analyze experimental data and design new experiments (e.g. see Ref. [3]). Nevertheless, perpendicular neoclassical transport needs also a precise computation in order to allow a correct evaluation of the anomalous contribution by means of the comparison with the experimentally measured heat and particle fluxes. This is becoming even more important with the recent improved confinement modes of operation, with internal transport barriers and relatively small anomalous transport in the plasma core. The formulae used for the neoclassical transport coefficients are in most cases based on works done 15–20 years ago, where the results have been obtained for large aspect ratio, in the limits of small or of very large collisionality, or with a reduced expression for the Coulomb collision operator. In particular, relatively simple formulae for all the neoclassical transport coefficients exist, valid for low inverse aspect ratio, $\epsilon \ll 1$, and arbitrary collisionality ν_{e*} [4] (ν_{e*} being the ratio of the trapped particle bounce time to the collision time). For the neoclassical resistivity and the bootstrap current, Hirshman has computed formulae which are valid for arbitrary plasma equilibrium and low collisionality [5]. In Ref. [6] Harris has derived simple formulae connecting these two limits using [4] and [5]. This enabled one to study any configuration [7]: as near the center one has typically $\epsilon \ll 1$ and $\nu_{e*} \sim 1$, at mid-radius $\nu_{e*} \ll 1$ and at the plasma edge $\epsilon \leq 1$ and $\nu_{e*} \sim 1$, even in reactor-like plasmas. A recent important improvement has been to solve a set of multi–species fluid equations using the three odd velocity moments of the Fokker-Planck equation [8], following the work of Hirshman, using interpolation formulae for viscosity moments from low and large collisionality regimes. This enables one to compute not only the neoclassical conductivity and the bootstrap current, but also the particle and heat neoclassical fluxes, for arbitrary collisionality and aspect ratio, in addition to multi–species effects. However, as a set of equations has to be solved in a specific code NCLASS, it is not of convenient use for rapid experimental diagnostics or tokamak design over a wide range of parameters. Simple formulae for the perpendicular neoclassical transport, valid for arbitrary aspect ratio, have been computed only for the ion thermal conductivity in the banana regime [9, 10, 11], and for various collision frequencies [12]. All these latter results [8]–[12] use an approximate collision operator, usually following the expansion method of Hirshman and Sigmar [13]. This method was also used to compute the like–particle collisions contribution on the viscosity matrix [9], and these results were applied in Ref. [5] to compute the bootstrap current coefficients at low aspect ratio. It has been shown in Ref. [14], and mentioned in Ref. [8], that such an approximation for the Coulomb collision operator can lead to errors up to 20% for the bootstrap current coefficients in which the contribution given by the like–particle collision operator is particularly important. In Ref. [15] the work published in Ref. [16] and [17] has been extended, and a complete accurate and analytical set of formulae for the neoclassical resistivity and all the bootstrap current coefficients has been provided, taking into account the full collision operator and including the advection parallel to the magnetic field, considering the realistic axisymmetric magnetic configuration of the flux surface. This set of formulae are therefore valid for general axisymmetric equilibria and arbitrary collisionality regimes. In the collisionless limit, namely the banana regime, formulae turn out to be in very good agreement with the ones obtained in the same collisionless limit for arbitrary aspect ratio in Ref. [5], using the reduced like–particle collision operator, but the non negligible discrepancy of two bootstrap current coefficients, caused by this approximation, has been confirmed. This has provided strong motivation to extend the work of Ref. [15] in order to compute all the neoclassical transport coefficients, in particular the ion and electron thermal conductivities. Indeed, as already mentioned, all the previous and more recent evaluation of the neoclassical ion thermal conductivity valid for arbitrary aspect ratio, are obtained using the reduced like–particle collision operator, in particular [10] and [11]. Moreover, for all the electron perpendicular transport coefficients, the only formulae available at small aspect ratio are those in Ref. [18], valid in the banana regime, which use the analytical values of the transport coefficients at $\epsilon = 1$ and the values at large aspect ratio of Ref. [19] to obtain a set of formulae with a linear interpolation between these two limits, which should be valid also at small aspect ratio. In the more recent investigations on the ion thermal conductivity, [10] and [11], the intermediate aspect ratio corrections show a difference with the results of [18] of almost a factor of two. For this reason, the work done in Ref. [20], provides a necessary investigation of the small aspect ratio corrections for all the neoclassical transport coefficients, taking into account the full collision operator.

In Section 2.2 we describe the approach to obtain the linear drift-kinetic equations suitable for implementation in a Fokker-Planck code and the expressions to compute the transport coefficients as simple integrals of the distribution functions. The related bounce-averaged equations in the banana regime are then obtained, and the Lorentz model is investigated analytically. In Section 2.3 we show the numerical results for the banana regime, computed with the Fokker-Planck code CQL3D [21], which solves the linearized drift–kinetic bounce-averaged equation with the full collision operator and considering the realistic axisymmetric configuration of the magnetic surfaces. Some benchmarks are considered to validate the results, and the comparison with some previous numerical and analytical results is shown. Then we present and discuss the numerical results obtained for the neoclassical conductivity and the bootstrap current coefficients, obtained solving the non–bounce–averaged drift–kinetic equations, with the code CQLP [16], and hence valid for collisional regimes. In Section 2.4 we give a set of formulae which fit our numerical results and allow to easily evaluate all the neoclassical transport coefficients in general axisymmetric equilibria for arbitrary aspect ratio and ion charge. In subsection 2.4.1 formulae for all the transport coefficients are presented, valid in the banana regime. In subsection 2.4.2, formulae fitting the code results for the parallel transport coefficients, valid for arbitrary collisionality and ion charge, are then presented. For the perpendicular transport coefficients, combined formulae for arbitrary collisionality regime are proposed in the last subsection.

2.2 Kinetic theory

2.2.1 Transport coefficients

Our approach follows the standard neoclassical theory, in particular the one of Ref. [4]. Definitions of thermodynamic forces and fluxes are only slightly different. We begin considering the Linearized Drift–Kinetic (LDK) Fokker–Planck equations [4] [Eqs. (5.21–24)]

$$\begin{aligned} v_{\|}\,\hat{\mathbf{b}}\cdot\nabla f_{e1} - C_e^l(f_{e1}) &= -(v_D\cdot\nabla\psi)_e\,\frac{\partial f_{e0}}{\partial\psi} - \frac{q_e E_{\|}}{m_e}\frac{\partial f_{e0}}{\partial v_{\|}}, && (2.1)\\ v_{\|}\,\hat{\mathbf{b}}\cdot\nabla f_{i1} - C_{ii}^l(f_{i1}) &= -(v_D\cdot\nabla\psi)_i\,\frac{\partial f_{i0}}{\partial\psi}, && (2.2) \end{aligned}$$

with

$$C_e^l = C_{ee}^l + C_{ei}^l \quad \text{linearized collision operator,}$$

$$(v_D\cdot\nabla\psi)_\sigma = I(\psi)v_{\|}\,\hat{\mathbf{b}}\cdot\nabla\left(\frac{v_{\|}}{\Omega_\sigma}\right),$$

$$\frac{\partial f_{\sigma0}}{\partial\psi} = f_{\sigma0}\left[\frac{\partial\ln n_{\sigma0}}{\partial\psi} + \frac{q_\sigma}{T_\sigma}\frac{\partial\langle\Phi\rangle}{\partial\psi} + \left(\frac{v^2}{v_{T_\sigma}^2} - \frac{3}{2}\right)\frac{\partial\ln T_{\sigma0}}{\partial\psi}\right],$$

and where $f_{\sigma0}$ is the unperturbed Maxwellian distribution function with related density $n_{\sigma0}$ and temperature $T_{\sigma0}$ of particle species σ, whose mass is m_σ and electric charge q_σ. $v_{T\sigma}^2 = 2T_{\sigma0}^2/m_\sigma$ and $\Omega_\sigma = q_\sigma B/m_\sigma$ are the thermal velocity and the cyclotron frequency, $I(\psi) = RB_\phi$, $\hat{\mathbf{b}} = \mathbf{B}/B$, and $\langle\Phi\rangle$ is the flux surface averaged electrostatic potential. Similar to the derivation presented in Ref. [4], we perform the following transformation of the distribution functions

$$f_{e1} = \frac{2v_{\|}\,u_{i\|}}{v_{Te}^2}f_{e0} + \frac{B\langle E_{\|}B\rangle}{\langle B^2\rangle}v_{\|}\,f_{se} + \frac{q_e}{T_e}f_{e0}\int_0^{l_p}\frac{dl_p}{B_p}\left(BE_{\|} - \frac{B^2\langle E_{\|}B\rangle}{\langle B^2\rangle}\right) + H_e,$$

$$f_{i1} = -\frac{I(\psi)v_{\|}}{\Omega_i}\left(\frac{\partial\ln p_i}{\partial\psi} + \frac{q_i}{T_i}\frac{\partial\langle\Phi\rangle}{\partial\psi}\right)f_{i0} + \frac{q_i}{T_i}f_{i0}\int_0^{l_p}\frac{dl_p}{B_p}\left(BE_* - \frac{B^2\langle E_*B\rangle}{\langle B^2\rangle}\right) + H_i,$$

where

$$u_{i\|} = \frac{K_i(\psi)B}{n_i} - \frac{I(\psi)}{B}\left(\frac{Ti}{q_i}\frac{\partial\ln p_i}{\partial\psi}\right) + \frac{\partial\langle\Phi\rangle}{\partial\psi},$$

$\langle\ \rangle$ denotes the flux surface average, f_{se} is the Spitzer function [22] and $K_i(\psi)$ is a function of the magnetic poloidal flux ψ which will be determined later; $E_* \doteq E_{\|}+F_{i\|}(q_i n_i)^{-1}$ is the so-called "effective electric field" and $F_{i\|}$ is the friction force between ions and electrons. For the new distribution functions H_e and H_i, the LDK equations can be written in the following "canonical" form:

$$\begin{aligned} v_{\|}\,\hat{\mathbf{b}}\cdot\nabla H_e - C_{e0}^l(H_e) &= -\sum_n v_{\|}\,\hat{\mathbf{b}}\cdot\nabla(\gamma_{en})\;A_{en}f_{e0},\\ v_{\|}\,\hat{\mathbf{b}}\cdot\nabla H_i - C_{ii}^l(H_i) &= -\sum_n \beta_{in}\;A_{in}f_{i0}, \end{aligned}$$

where we have introduced the flux surface averaged thermodynamic forces, as follows:

$$
\begin{aligned}
A_{e1} &= \frac{1}{p_e}\frac{\partial p_e}{\partial \psi} + \frac{1}{p_e}\frac{\partial p_i}{\partial \psi}, & & \\
A_{e2} &= \frac{1}{T_e}\frac{\partial T_e}{\partial \psi}, & A_{i1} &= -\frac{\langle E_* B\rangle}{\langle B^2\rangle}, \\
A_{e3} &= \frac{\langle E_\| B\rangle}{\langle B^2\rangle}, & A_{i2} &= \frac{1}{T_i}\frac{\partial T_i}{\partial \psi}, \\
A_{e4} &= \frac{q_e\, K_i(\psi)\,\langle B^2\rangle}{n_i I(\psi)\, T_e}. & &
\end{aligned}
$$

$$
\begin{aligned}
\gamma_{e1} &= \frac{I(\psi) v_\|}{\Omega_e}, & \gamma_{e2} &= \gamma_{e1}\left(\frac{v^2}{v_{Te}^2} - \frac{5}{2}\right), \\
\gamma_{e3} &= \frac{v_\|\, f_{se}}{f_{e0}} B, & \gamma_{e4} &= \gamma_{e1}\frac{B^2}{\langle B^2\rangle}, \\
\beta_{i1} &= \frac{q_i v_\|}{T_i} B, & \beta_{i2} &= v_\|\, \hat{\mathbf{b}}\cdot\nabla(\gamma_{i2}),
\end{aligned}
$$

$$
\gamma_{i2} = \frac{I(\psi) v_\|}{\Omega_i}\left(\frac{v^2}{v_{Ti}^2} - \frac{5}{2}\right).
$$

The conjugated neoclassical thermodynamic fluxes are identified in the expression of the linearized entropy production [4], and can be defined as follows

$$
B_{en} = \langle \int d\mathbf{v} \left(v_\|\, \hat{\mathbf{b}}\cdot\nabla\gamma_{en}\right) H_e\rangle, \qquad n = 1,2,3,4, \tag{2.3}
$$

$$
B_{in} = \langle \int d\mathbf{v}\, \beta_{in}\, H_i\rangle, \qquad n = 1,2, \tag{2.4}
$$

which gives, with ρ the generic radial coordinate

$$
\begin{aligned}
B_{e1} &= \Gamma_e \frac{d\psi}{d\rho}, & B_{e2} &= \frac{Q_e}{T_e}\frac{d\psi}{d\rho}, \\
B_{e3} &= \frac{\langle j_\| B\rangle}{T_e} - \frac{\langle j_{\|S} B\rangle}{T_e}, & B_{e4} &= -\frac{\langle E_* B\rangle}{\langle B^2\rangle} I(\psi) n_e. \\
B_{i1} &= \frac{\langle j_{\|Ri} B\rangle}{T_i}, & B_{i2} &= \frac{Q_i}{T_i}\frac{d\psi}{d\rho},
\end{aligned}
$$

where Γ_σ and Q_σ are the particle and heat fluxes of species σ, $j_\|$ is the total parallel electric current, $j_{\|S}$ is the so-called Spitzer current and $j_{\|Ri}$ is the ion contribution to the so-called "return current". The flux surface average $\langle j_{\|Ri} B\rangle$ is related to the function $K_i(\psi)$ by the following equation

$$
\langle j_{\|Ri} B\rangle = q_i\, K_i(\psi)\langle B^2\rangle.
$$

Note that ion and electron forces and fluxes are mutually dependent

$$
B_{i1} = -I(\psi) n_e \frac{T_e}{T_i} A_{e4}, \qquad B_{e4} = I(\psi) n_e\, A_{i1}. \tag{2.5}
$$

The transport coefficients linearly relate forces with fluxes, $B_{\sigma m} = \sum_n \mathcal{L}^{\sigma}_{mn} \, A_{\sigma n}$. To easily identify the role of each transport coefficient, we show the complete relation between electron and ion forces and fluxes in the following form

$$\left(\begin{array}{c} \Gamma_e \frac{d\psi}{d\rho} \\ \frac{Q_e}{T_e} \frac{d\psi}{d\rho} \\ \langle \frac{j_\| B}{T_e} \rangle - \langle \frac{j_{\| S} B}{T_e} \rangle \\ -\frac{I(\psi)\langle E_* B\rangle n_e}{\langle B^2 \rangle} \end{array} \right) = \left[\begin{array}{cccc} \mathcal{L}^e_{11} & \mathcal{L}^e_{12} & \mathcal{L}^e_{13} & \mathcal{L}^e_{14} \\ \mathcal{L}^e_{21} & \mathcal{L}^e_{22} & \mathcal{L}^e_{23} & \mathcal{L}^e_{24} \\ \mathcal{L}^e_{31} & \mathcal{L}^e_{32} & \mathcal{L}^e_{33} & \mathcal{L}^e_{34} \\ \mathcal{L}^e_{41} & \mathcal{L}^e_{42} & \mathcal{L}^e_{43} & \mathcal{L}^e_{44} \end{array} \right] \left(\begin{array}{c} \frac{1}{p_e} \frac{\partial p_e}{\partial \psi} + \frac{1}{p_e} \frac{\partial p_i}{\partial \psi} \\ \frac{1}{T_e} \frac{\partial T_e}{\partial \psi} \\ \frac{\langle E_\| B \rangle}{\langle B^2 \rangle} \\ \frac{q_e}{n_i T_e} \frac{K_i(\psi)}{I(\psi)} \langle B^2 \rangle \end{array} \right),$$

$$\left(\begin{array}{c} \frac{\langle j_{\| Ri} B \rangle}{T_i} \\ \frac{Q_i}{T_i} \frac{d\psi}{d\rho} \end{array} \right) = \left[\begin{array}{cc} \mathcal{L}^i_{11} & \mathcal{L}^i_{12} \\ \mathcal{L}^i_{21} & \mathcal{L}^i_{22} \end{array} \right] \left(\begin{array}{c} -\frac{\langle E_* B \rangle}{\langle B^2 \rangle} \\ \frac{1}{T_i} \frac{\partial T_i}{\partial \psi} \end{array} \right).$$

The transport matrices in neoclassical theory are full, namely not only diagonal terms are present, but also off–diagonal terms are non–negligible. The formers are easily related to standard particle and heat diffusivities, whereas the latters involve supplementary effects, connecting for instance particle fluxes with temperature gradients and heat fluxes with density gradients. Furthermore, off–diagonal terms connect particle and heat fluxes with the parallel electric field. This is the case of the Ware pinch [23], given by coefficients $\mathcal{L}^e_{n3}$, with $n = 1, 2, 4$, while the symmetric coefficients imply the bootstrap current [24, 25], yielding a contribution to the electric current due to density and temperature gradients. We now perform the second transformation

$$\begin{aligned} G_e &= H_e + \sum_n \gamma_{en} A_{en} f_{e0}, \\ G_i &= H_i + \gamma_{i2} A_{i2} f_{i0}. \end{aligned}$$

The LDK equations for the new distribution functions are

$$v_\| \, \hat{\mathbf{b}} \cdot \nabla G_e - C^l_{e0}(G_e) = -\sum_n C^l_{e0}(\gamma_{en} f_{e0}) A_{en}, \tag{2.6}$$

$$v_\| \, \hat{\mathbf{b}} \cdot \nabla G_i - C^l_{e0}(G_i) = -\beta_{i1} f_{i0} A_{i1} - C^l_{ii}(\gamma_{i2} f_{i0}) A_{i2}. \tag{2.7}$$

Note that now all the coefficients of the thermodynamic forces in the source terms can be evaluated analytically [14],

$$-C^l_{e0}(\gamma_{e1} f_{e0}) = Z_i \nu_{e0}(v) \gamma_{e1} f_{e0}, \tag{2.8a}$$

$$-C^l_{e0}(\gamma_{e2} f_{e0}) = Z_i \nu_{e0}(v) \gamma_{e2} f_{e0} - \nu_{e0}(v) h \left(\frac{v}{v_{Te}} \right) \gamma_{e1} f_{e0}, \tag{2.8b}$$

$$-C^l_{e0}(\gamma_{e3} f_{e0}) = \frac{q_e v_\| B}{T_e} f_{e0}, \tag{2.8c}$$

$$-C^l_{e0}(\gamma_{e4} f_{e0}) = Z_i \nu_{e0}(v) \gamma_{e4} f_{e0}, \tag{2.8d}$$

$$-C^l_{ii}(\gamma_{i2} f_{e0}) = -\nu_{i0}(v) h \left(\frac{v}{v_{Ti}} \right) \frac{I(\psi) v_\|}{\Omega_i} f_{i0}, \tag{2.8e}$$

with

$$\begin{aligned}
\nu_{e0}(v) &\doteq \frac{3\sqrt{\pi}\, v_{Te}^3}{4 Z_i \tau_e\, v^3}, \qquad \nu_{i0}(v) \doteq \frac{3\sqrt{\pi}\, v_{Ti}^3}{2\sqrt{2}\tau_i\, v^3},\\
h(x) &= (10-4\,x^2)\,\mathrm{erf}(x) - 10\,x\,\mathrm{erf}'(x),\\
\frac{1}{\tau_e} &= \frac{4\sqrt{2\pi}}{3}\,\frac{n_{i0}\,Z_i^2\,e^4\,\mathrm{ln}\Lambda}{m_e^{1/2}\,T_{e0}^{3/2}}, \qquad \frac{1}{\tau_i} = \frac{4\sqrt{\pi}}{3}\,\frac{n_{i0}\,Z_i^4\,e^4\,\mathrm{ln}\Lambda}{m_i^{1/2}\,T_{i0}^{3/2}}.
\end{aligned} \tag{2.9}$$

In Appendix at the end of the Chapter, Section 2.6, we present the derivation of Eqs. (2.8b) and (2.8e). As the equations are linear and the thermodynamic forces can be treated as independent, we can write the unknown function G_e for the electrons as a linear combination in the following form: $G_e = \sum_n g_{en} A_{en}$. For the set of functions g_{en}, Eq. (2.6) can be decoupled, leading to the following set of equations

$$v_{\|}\,\hat{\mathbf{b}}\cdot\nabla g_{en} - C_{e0}^l(g_{en}) = -C_{e0}^l(\gamma_{en} f_{e0}), \qquad n = 1,2,3,4. \tag{2.10}$$

In the same way, introducing $G_i = \sum_n g_{in} A_{in}$ in Eq. (2.7) for the ions, we obtain

$$v_{\|}\,\hat{\mathbf{b}}\cdot\nabla g_{i1} - C_{ii}^l(g_{i1}) = -\beta_{i1} f_{i0}, \tag{2.11a}$$

$$v_{\|}\,\hat{\mathbf{b}}\cdot\nabla g_{i2} - C_{ii}^l(g_{i2}) = -C_{ii}^l(\gamma_{i2} f_{i0}). \tag{2.11b}$$

We look now at the definitions of the thermodynamic fluxes, Eqs.(2.3) and (2.4); a simple calculation shows that for the electrons we can write

$$B_{en} = \sum_m \left[\langle \int d\mathbf{v} \gamma_{em} C_{e0}^l(\gamma_{en}\, f_{e0}) \rangle - \langle \int d\mathbf{v} \frac{g_{em}}{f_{e0}}\, C_{e0}^l(\gamma_{en}\, f_{e0}) \rangle \right] A_{em}.$$

Analogously the ion fluxes read

$$\begin{aligned}
B_{i1} &= \sum_n \langle \int d\mathbf{v} \beta_{i1}\, g_{in} \rangle\, A_{in},\\
B_{i2} &= \langle \int d\mathbf{v} \gamma_{i2} C_{e0}^l(\gamma_{i2}\, f_{i0}) \rangle\, A_{i2} - \sum_m \langle \int d\mathbf{v} \frac{g_{im}}{f_{i0}} C_{ii}^l(\gamma_{i2} f_{i0}) \rangle\, A_{im}.
\end{aligned}$$

At this point we can identify the transport coefficients

$$\mathcal{L}_{mn}^e = \langle \int d\mathbf{v} \gamma_{em} C_{e0}^l(\gamma_{en}\, f_{e0}) \rangle - \langle \int d\mathbf{v} \frac{g_{em}}{f_{e0}}\, C_{e0}^l(\gamma_{en}\, f_{e0}) \rangle, \quad n,m = 1,2,3,4, \tag{2.12}$$

$$\begin{aligned}
\mathcal{L}_{1n}^i &= \langle \int d\mathbf{v} g_{in}\, \beta_{i1} \rangle, \qquad n = 1,2,\\
\mathcal{L}_{21}^i &= -\langle \int d\mathbf{v} \frac{g_{i1}}{f_{i0}} C_{ii}^l(\gamma_{i2}\, f_{i0}) \rangle,\\
\mathcal{L}_{22}^i &= \langle \int d\mathbf{v} \gamma_{i2} C_{ii}^l(\gamma_{i2}\, f_{i0}) \rangle - \langle \int d\mathbf{v} \frac{g_{i2}}{f_{i0}} C_{ii}^l(\gamma_{i2}\, f_{i0}) \rangle.
\end{aligned} \tag{2.13}$$

In this way we have obtained a simple set of expressions to compute all the neoclassical transport coefficients, once we have solved the drift–kinetic equations, Eqs. (2.10) and

(2.11), to obtain the distribution functions g_{en} and g_{in}. We see that every expression is composed of the sum of two terms: the first one is an integral that can be computed analytically and that, for some coefficients, is identically zero; the second one has an integrand in which the only term to be computed numerically is the distribution function g_{en} or g_{in}. Note that in the banana regime the first term, computed analytically, gives directly the value of the transport coefficient at $\epsilon = 1$, when all the particles are trapped; the second term gives the reduction of transport due to the presence of passing particles. In subsection 2.2.2 we show that Eqs. (2.12) and (2.13) satisfy the Onsager relations [26] of symmetry as expected. In Ref. [15] the expressions for the neoclassical conductivity and the bootstrap current coefficients, Eqs. (7)-(11) in the Reference, where obtained in terms of the adjoint functions χ_e and χ_i, solving the adjoint equations, Eqs. (3) and (4) in the Reference, which were obtained following the work of Ref. [27] adapted to this problem in [14] and also described in Ref. [16]. In the present formulation, which follows the one of Ref. [20], the adjoint formalism is shown to be not necessary, as the effect of introducing the adjoint functions is equivalent to the linear decoupling of the direct equations, which allows to pass from Eqs. (2.6) and (2.7) to Eqs. (2.10) and (2.11). With a simple calculation, analogous to the one presented in subsection 2.2.2 for the Onsager symmetry, it can be shown that the expressions given for the neoclassical conductivity and the bootstrap current coefficients in Ref. [15] are completely equivalent to the ones of Eqs. (2.12), with $m = 3$, and Eq. (2.13), $m = 2$, $n = 1$. For this reason in the following sections the numerical results of Ref. [15] will be presented together with the ones of [20], without making any distinction. Also it should be noted that the resulting equations to be solved are similar to standard Fokker–Planck equations, with just source terms modified. As the source terms can be easily evaluated by Eq. (2.8), the use of the codes CQL3D and CQLP was straightforward. In addition, due to the different transformations, the source terms do not need any information on plasma profiles ($A_{\sigma n}$), which enables generic transport coefficients to be calculated.

2.2.2 Onsager symmetry of the transport coefficients

The expressions for the transport coefficients given by Eqs. (2.12) for the electrons and by Eqs. (2.13) for the ions satisfy the Onsager relations of symmetry, as expected [4]. We begin with the electron case. In Eq. (2.12), the first term, ${\mathcal{L}^e_{mn}}^{(1)} \doteq \langle \int d\mathbf{v} \gamma_{em} C^l_{e0}(\gamma_{en} f_{e0}) \rangle$, is symmetric directly from the self-adjointness of the collision operator. Hence

$${\mathcal{L}^e_{mn}}^{(1)} \doteq \langle \int d\mathbf{v} \gamma_{em} C^l_{e0}(\gamma_{en} f_{e0}) \rangle = \langle \int d\mathbf{v} \gamma_{en} C^l_{e0}(\gamma_{em} f_{e0}) \rangle \doteq {\mathcal{L}^e_{nm}}^{(1)}. \qquad (2.14)$$

For the second term, ${\mathcal{L}^e_{mn}}^{(2)} \doteq \langle \int d\mathbf{v} g_{em}/f_{e0}\, C^l_{e0}(\gamma_{en} f_{e0}) \rangle$, we shall rewrite it in a symmetric form. Introducing the following notation [4], for a generic function $f(\mathbf{v})$, $f^+ \doteq$

$\frac{1}{2}\left[f(\sigma=+1)+f(\sigma=-1)\right]$ is its even part in $\sigma = v_\parallel/|v_\parallel|$ and $f^- \doteq \frac{1}{2}\left[f(\sigma=+1)-f(\sigma=-1)\right]$ is the odd part, so that

$$\begin{aligned}
|v_\parallel|\, \hat{\mathbf{b}}\cdot\nabla g_{en}^{+} - C_{e0}^{l}(g_{en}^{-}) &= -C_{e0}^{l}(\gamma_{en} f_{e0}),\\
|v_\parallel|\, \hat{\mathbf{b}}\cdot\nabla g_{en}^{-} - C_{e0}^{l}(g_{en}^{+}) &= 0,
\end{aligned}$$

(as $C_{e0}^{l}(\gamma_{en} f_{e0})^{-} = C_{e0}^{l}(\gamma_{en} f_{e0})$ and $C_{e0}^{l}(\gamma_{en} f_{e0})^{+} = 0$, $n = 1,2,3,4$),
we can perform the following derivation:

$$\begin{aligned}
&{\mathcal{L}^{e}_{mn}}^{(2)} \doteq \langle \int d\mathbf{v} \frac{g_{em}}{f_{e0}} C_{e0}^{l}(\gamma_{en} f_{e0})\rangle = \langle \int d\mathbf{v} \frac{g_{em}^{-}}{f_{e0}} C_{e0}^{l}(\gamma_{en} f_{e0})^{-}\rangle = \\
&-\langle \int d\mathbf{v} \frac{g_{em}^{-}}{f_{e0}} \left[v_\parallel\, \hat{\mathbf{b}}\cdot\nabla g_{en}^{+} - C_{e0}^{l}(g_{en}^{-})\right]\rangle = \\
&-\langle \int d\mathbf{v} \frac{1}{f_{e0}} \left[-g_{em}^{+}|v_\parallel|\, \hat{\mathbf{b}}\cdot\nabla g_{en}^{-} - g_{em}^{-}\, C_{e0}^{l}(g_{en}^{-})\right]\rangle = \\
&-\langle \int d\mathbf{v} \frac{1}{f_{e0}} \left[-g_{em}^{+}\, C_{e0}^{l}(g_{en}^{+}) - g_{em}^{-}\, C_{e0}^{l}(g_{en}^{-})\right]\rangle = \\
&\langle \int d\mathbf{v} \frac{1}{f_{e0}}\, g_{em}\, C_{e0}^{l}(g_{en})\rangle = \langle \int d\mathbf{v} \frac{1}{f_{e0}}\, g_{en}\, C_{e0}^{l}(g_{em})\rangle \;=\; {\mathcal{L}^{e}_{nm}}^{(2)}, \qquad (2.15)
\end{aligned}$$

which is a symmetric expression, using the self-adjointness of the collision operator. (Note that we have used in this derivation the fact that the operator $-v_\parallel\, \hat{\mathbf{b}}\cdot\nabla$ is the adjoint of the operator $v_\parallel\, \hat{\mathbf{b}}\cdot\nabla$). A somewhat analogous calculation can be performed for the ion coefficients $\mathcal{L}^{i}_{12}$ and $\mathcal{L}^{i}_{21}$, which shows that the two given expressions, Eqs. (2.13), satisfy the following relation

$$\mathcal{L}^{i}_{12} \;=\; -\mathcal{L}^{i}_{21}, \qquad (2.16)$$

consistently with the result in Ref. [4], Eq. (5.99).

2.2.3 Banana regime: bounce-averaged equations

When the collision frequency $\nu_{ei}(v) = Z_i\, \nu_{e0} \doteq (3\pi^{1/2}/4\tau_e)(v_{Te}/v)^3$ is much smaller than the bounce frequency $\nu_b \sim \epsilon^{1/2}\, v_{Te}/qR$, the distribution functions g_{en} can be expanded as follows

$$g_{en} = g_{en}^{0} + \left(\frac{\nu_{ei}}{\nu_b}\right) g_{en}^{1} + O\left[\left(\frac{\nu_{ei}}{\nu_b}\right)^2\right],$$

and analogously for the ion distribution functions. A somewhat standard derivation, [4, 19], shows that the functions $g_{\sigma n}^{0}$ are independent of the poloidal angle θ_p, and that they are zero in the trapped particle region of velocity space. In the passing particle region, the functions $g_{\sigma n}^{0}$ satisfy the following bounce-averaged equations

$$\int_{-\pi}^{\pi} d\theta_p \frac{B}{|v_\parallel|} C_{e0}^{l}(g_{en}^{0}) = S_{en}, \qquad n = 1,2,3,4, \qquad (2.17a)$$

$$\int_{-\pi}^{\pi} d\theta_p \frac{B}{|v_\parallel|} C_{ii}^{l}(g_{in}^{0}) = S_{in}, \qquad n = 1,2, \qquad (2.17b)$$

with

$$S_{en} \doteq 2\pi\sigma\,\langle B\,C^{\gamma}_{en}(v,B)\rangle\, f_{e0}, \qquad n = 1,2,3,4, \tag{2.17c}$$

$$S_{i1} \doteq 2\pi\sigma\,\frac{q_i\,\langle B^2\rangle}{T_i}\, f_{i0}, \qquad S_{i2} \doteq 2\pi\sigma\,\langle B\,C^{\gamma}_{i2}(v,B)\rangle\, f_{i0}, \tag{2.17d}$$

where $\sigma = v_{\parallel}/|v_{\parallel}|$ and where we have introduced the set of functions $C^{\gamma}_{\sigma n}(v,B)$, defined as follows

$$C^{\gamma}_{\sigma n}(v,B) \;\doteq\; C^{l}_{\sigma}(\gamma_{\sigma n} f_{\sigma 0})/(v_{\parallel}\, f_{\sigma 0}).$$

The analytical expressions of these functions can easily be obtained from Eqs. (2.8). Note that $\langle B\,C^{\gamma}_{e4}(v,B)\rangle = \langle B\,C^{\gamma}_{e1}(v,B)\rangle$, so that the functions g^{0}_{e1} and g^{0}_{e4} solve the same equation in the banana regime; in particular it follows that $\mathcal{L}_{44} = \mathcal{L}_{14}$: this is a consequence of our choice of thermodynamic forces and fluxes. We see that at $\epsilon = 1$, when all the particles are trapped, the distribution functions g^{0}_{en} are zero everywhere, and the first terms in the expressions for the transport coefficients, Eqs. (2.12) and (2.13), give directly the entire coefficient. The code CQL3D has been modified to solve Eqs. (2.17) in general axisymmetric equilibria and with the full collision operator.

2.2.4 Lorentz model

For the Lorentz gas model, $Z_i \gg 1$, the set of Eqs. (2.17a) is solved analytically, [4][28]. In fact, as collisions between electrons can be neglected, the collision operator can be approximated by the pitch-angle scattering operator:

$$C^{l}_{e0} = \nu_{ei}(v)\,L \doteq \nu_{ei}(v)\,\frac{1}{2}\frac{\partial}{\partial\xi}(1-\xi^2)\frac{\partial}{\partial\xi} \qquad \text{and} \qquad \xi \doteq \frac{v_{\parallel}}{v}.$$

The solutions of Eqs. (2.17a) in this approximation can be written in the following form

$$g^{0}_{en} = -\sigma\frac{v}{2\,\nu_{ei}(v)}\langle B\,C^{\gamma}_{en}(v,B)\rangle\, f_{e0}\int_{\lambda}^{\lambda_c}\frac{d\lambda'}{\langle(1-\lambda' B)^{1/2}\rangle}\,H(\lambda_c-\lambda), \tag{2.18}$$

where $\lambda \doteq (1-\xi^2)/B$, $\lambda_c \doteq 1/B_{max}$ and $H(x)$ is the Heaviside function. Introducing Eq. (2.18) in the expressions for the coefficients Eqs. (2.12), all the electron transport coefficients can be written as integrals in the absolute value of velocity v:

$$\mathcal{L}^{e}_{mn} = \frac{4\pi}{3}\int_0^{\infty} v^4\,dv\langle\frac{\gamma_{em}}{v_{\parallel}}C^{\gamma}_{en}\rangle\, f_{e0} + \pi\int_0^{\infty}\frac{v^4\,dv}{\nu_{ei}(v)}\langle B\,C^{\gamma}_{em}\rangle\langle B\,C^{\gamma}_{en}\rangle\, f_{e0}, \quad n,m = 1,2,3,4.$$

The integrals of v can easily be computed analytically, and the results have been compared with Ref. [4], Eqs. (5.121), (5.124 - 5.130), finding a complete agreement. As the Lorentz model coefficients will be used not only as a benchmark for the results of CQL3D, but also to analyze the results of the code with the full collision operator and in different axisymmetric configurations, we report all the electron transport coefficients, which can be written in the following simple form

$$\mathcal{L}^e_{11} = -0.5\,\mathcal{L}_d[B_0^2\langle B^{-2}\rangle]f_t^d, \tag{2.19a}$$

$$\mathcal{L}^e_{21} = 0.75\,\mathcal{L}_d[B_0^2\langle B^{-2}\rangle]f_t^d, \qquad \mathcal{L}^e_{22} = -\frac{13}{8}\mathcal{L}_d[B_0^2\langle B^{-2}\rangle]f_t^d, \tag{2.19b}$$

$$\mathcal{L}^e_{31} = \mathcal{L}^e_{34} = -\mathcal{L}_b f_t, \qquad \mathcal{L}^e_{32} = 0, \qquad \mathcal{L}^e_{33} = -\frac{32}{3\pi}\mathcal{L}_\sigma[B_0^{-2}\langle B^2\rangle]f_t, \tag{2.19c}$$

$$\mathcal{L}^e_{41} = \mathcal{L}^e_{44} = -0.5\,\mathcal{L}_d[B_0^2\langle B^2\rangle^{-1}]f_t, \qquad \mathcal{L}^e_{42} = 0.75\,\mathcal{L}_d[B_0^2\langle B^2\rangle^{-1}]f_t, \tag{2.19d}$$

with

$$\mathcal{L}_d = \frac{n_e\rho_{ep}^2}{\tau_e}\left(\frac{d\psi}{d\rho}\right)^2, \qquad \mathcal{L}_b = I(\psi)n_e, \qquad \mathcal{L}_\sigma = \frac{n_e q_e^2\tau_e}{m_e T_e}B_0^2, \tag{2.20}$$

and where we have introduced two definitions for the trapped fraction

$$f_t^d = 1 - \frac{3}{4}\langle B^{-2}\rangle^{-1}\mathcal{I}_\lambda, \qquad f_t = 1 - \frac{3}{4}\langle B^2\rangle\,\mathcal{I}_\lambda, \tag{2.21}$$

$$\mathcal{I}_\lambda = \int_0^{\lambda_c}\frac{\lambda' d\lambda'}{\langle(1-\lambda' B)^{1/2}\rangle}.$$

The second one, f_t, is the usual definition for the trapped particle fraction [9]. Note that the integral $\mathcal{I}_\lambda$ can easily be evaluated using the formulae in Ref. [29]. The poloidal gyroradius $\rho_{\sigma p}$ of species σ is given by

$$\rho_{\sigma p}(\rho) = \frac{v_{T\sigma}}{|\Omega_{\sigma p}|} = \frac{\sqrt{2\,m_\sigma T_\sigma}}{|q_\sigma|\,B_{po}(\rho)}, \tag{2.22}$$

like in Ref. [4], Eq. (5.122), where the poloidal magnetic field $B_{po}(\rho)$ is defined by $B_{po} \doteq (d\psi/d\rho)B_0(\psi)/I(\psi)$, and $B_0(\psi)$ is an arbitrarily chosen function introduced to normalize the magnetic field on a given flux surface. Note that the flux surface averaged integrals I_{11}, I_{13} and I_{33} which appear in the results of Ref. [4] can be reduced to only the two trapped fractions, Eqs. (2.21), with the following relations

$$I_{11} = \frac{4}{3}[B_0^2\langle B^{-2}\rangle]\,f_t^d, \qquad I_{13} = \frac{4}{3}\,f_t, \qquad I_{33} = \frac{4}{3}[B_0^{-2}\langle B^2\rangle]\,f_t. \tag{2.23}$$

We see therefore that all the coefficients in the Lorentz model depend essentially on f_t^d and f_t. We shall show in the next Sections that in the general case this property remains true, namely that all the equilibrium effects on the neoclassical transport coefficients are functions of only these two trapped fractions.

2.3 Numerical results

2.3.1 Benchmarks

As the Lorentz model gives an analytical solution, it can be used as a first benchmark for the numerical results. In Figure 2.1 we show the transport coefficients $\mathcal{L}^e_{1n}$ and $\mathcal{L}^e_{2n}$ relative

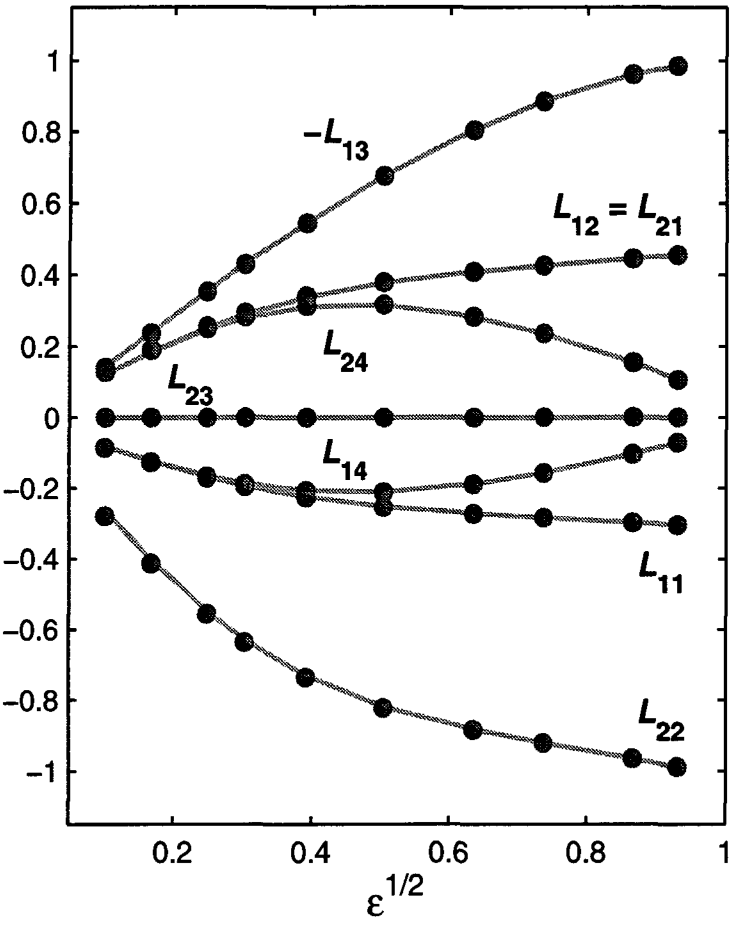

Figure 2.1: *Transport coefficients* $\mathcal{L}^e_{1n}$ *and* $\mathcal{L}^e_{2n}$ *for an almost cylindrical equilibrium, computed by CQL3D in the approximation of the Lorentz model (circles), and compared with the analytical results, Eq. (2.19) (solid lines).*

to the sources S_{e1} and S_{e2}, Eqs. (2.17), computed by CQL3D in the approximation of the Lorentz model: very good agreement is obtained for all ϵ. The coefficients in the Figure, indicated by L^e_{mn}, are plotted normalized by the relative factors $\mathcal{L}_d$ or $\mathcal{L}_b$ given in Eqs. (2.20). This normalization for the electron transport coefficients is also kept in Figure 2.2 and Figure 2.7, and analogously in Figure 2.6 for the ion transport coefficients. The complete definition of a set of dimensionless coefficients will be given in the next section.

When the full collision operator is used, the symmetry of the transport matrix gives a second benchmark of the numerical results: indeed, each off-diagonal coefficient can be computed in two different ways, $\mathcal{L}_{nm}$ and $\mathcal{L}_{mn}$. In Figure 2.2(a) we plot the results for the coefficient $\mathcal{L}^e_{13}$, computed solving the kinetic equation with the source S_{e1}, Eqs. (2.17a,c), $n = 1$: they are perfectly aligned with the solid line representing the code results for the

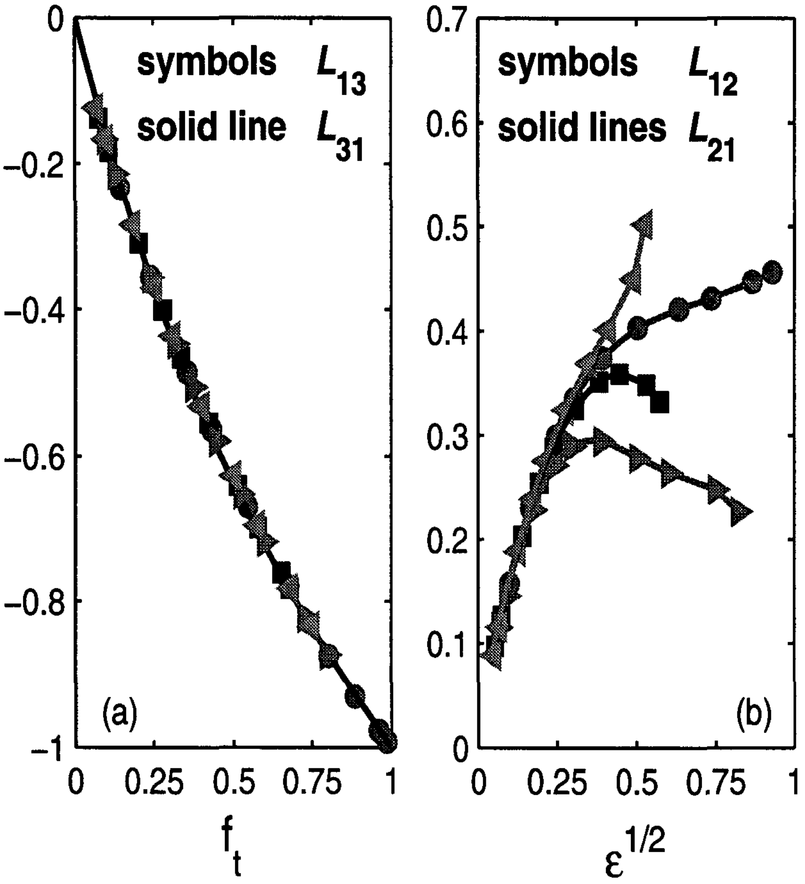

Figure 2.2: *Onsager symmetry is correctly respected by the numerical results. (a) The transport coefficient* $\mathcal{L}_{13}^e$ *(symbols), plotted vs* f_t, *is well aligned with the numerical results for the bootstrap current coefficient* $\mathcal{L}_{31}^e$ *(solid line). The different symbols refer to different equilibria in all the Figures. Note that the results given by the different equilibria are perfectly overlapped, as they are plotted vs* f_t. *(b) Transport coefficient* $\mathcal{L}_{12}^e$ *(symbols) and* $\mathcal{L}_{21}^e$ *(solid lines) computed with four different equilibria, plotted vs* $\epsilon^{1/2}$. *Note that when the complete coefficients are plotted vs the inverse aspect ratio, a strong dependence on equilibria appears at small aspect ratio, large* ϵ.

bootstrap current coefficient $\mathcal{L}_{31}^e$, hence computed with the source S_{e3}, Eqs. (2.17a,c), $n = 3$. In Figure 2.2(b) we plot the two coefficients $\mathcal{L}_{12}^e$ and $\mathcal{L}_{21}^e$, computed considering four different equilibria, as shown in Figure 2.3, and whose main specifications and related symbols, full or open, used in all the Figures are given in Table 2.1. The coefficient $\mathcal{L}_{12}^e$, obtained solving Eq. (2.17a,c), $n = 1$, is plotted with symbols, the coefficient $\mathcal{L}_{21}^e$, obtained solving Eq. (2.17a,c), $n = 2$, is plotted with solid lines: we find a very good agreement between the two coefficients, within 1% for $\epsilon \geq 0.1$. We see also that the behaviour of the transport coefficient strongly depends on the equilibrium at small aspect ratio. Previous formulae, which give the transport coefficients with an expansion in powers of $\epsilon^{1/2}$, are correct only for almost cylindrical equilibria and are of practical interest in

Symbol	R_{mag} [m]	R_{geo} [m]	a [m]	k	δ
○	2.13	2.13	1.925	1.0	0
□	8.44	8.00	2.750	1.8	0.32
▷	1.67	1.22	0.875	3.0	0.56
◁	0.92	0.88	0.252	2.5	-0.65

Table 2.1: *Equilibria specifications and related symbols used in the Figures.*

general equilibria only for $\epsilon < 0.1$: this must be taken into account when comparing with our results. It indicates that for each transport coefficient an appropriate geometrical parameter, like f_t for $\mathcal{L}_{31}^e$ and $\mathcal{L}_{13}^e$ in Fig. 2(a), needs to be used instead of ϵ, as it will be shown in the next subsection.

2.3.2 Comparison with previous results, behaviour at small aspect ratio

As mentioned in Section 2.1, formulae for arbitrary aspect ratio for the transport coefficients are available only for the neoclassical conductivity, the bootstrap current coefficients and the ion thermal conductivity. When comparing the numerical results of the code CQL3D with Hirshman's formulae for the neoclassical conductivity [9] and the bootstrap current coefficients [5], general very good agreement is found, exception made for coefficients in which the contribution given by the like–particle collision operator is

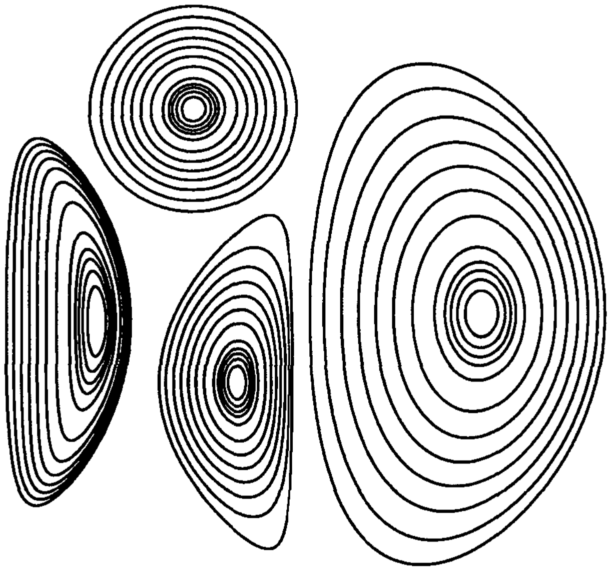

Figure 2.3: *Different equilibria used for the numerical computation of the transport coefficients, whose main specifications are given in Table 2.1.*

particularly important, hence coefficients $\mathcal{L}^e_{32}$ and $\mathcal{L}^i_{21}$. The bootstrap current coefficient $L_{32} = -\mathcal{L}^e_{32}/I\, n_e$ computed with CQL3D is compared with the Hirshman's formulae in Figure 2.4. The disagreement is more significant at small values of the charge number Z, pointing out that it must be ascribed to the like–particle collision contribution. Indeed, as it can be seen from Eq. (2.12) and Eq. (2.8), the term $-C^l_{e0}(\gamma_{e2} f_{e0})$ is given by two contribution of opposite signs, one involving electron-ion collisions, the other involving electron-electron collisions. Consequently, the integrand in Eq. (2.12), $m = 3$, $n = 2$, has different contributions from the small and large v spectra; in particular, the term deriving from the like–particle collision operator, involving the function $h(v/v_{Te})$, has its main contribution from the high energy tail, in the region $v/v_{Te} \sim 2$, which therefore explains the discrepancies with the results obtained adopting an approximate collision operator. The velocity dependence of the two contributions involved in the integrand of the bootstrap current coefficient L_{32}, and called for simplicity $\mathcal{L}_{32\_ee}$ and $\mathcal{L}_{32\_ei}$ are shown in Figure 2.5, with solid circles in the case of low collisionality.

The most recent investigations on perpendicular neoclassical transport were dedicated only to the ion thermal conductivity [10, 11]. In Figure 2.6 we compare our results for the coefficient $\mathcal{L}^i_{22}$, obtained with an almost cylindrical equilibrium, with the results of Refs. [10, 11, 18]. The simple geometry is necessary for the comparison, since some of the previous results are valid only in this limit. As mentioned at the end of the previous paragraph, a correct geometrical parameter must be chosen to plot a given transport coefficient. As it can be inferred from the Lorentz model results for the electron coefficient $\mathcal{L}^e_{22}$, Eq. (2.19b), and as it will be presented later, the ion heat conductivity is a function of the trapped fraction f^d_t, Eq. (2.21). We find good agreement with the most recent formulae of Refs. [10] and [11]. These results enable to finally resolve the discrepancy between the formulae given in Refs. [10] and [11], obtained with approximated collision operators. It turns out that the results with the full collision operator, CQL3D, are in between the previous results. Note that the plotted formula of Ref. [18] has been modified, keeping in the expression for the transport coefficient the flux surface average of the magnetic field, which were correctly computed in the Reference to obtain the limit at $\epsilon = 1$, but then not taken into account in the final formulae.

When different axisymmetric equilibria are considered in the numerical calculations, the transport coefficients exhibit particular geometrical effects at small aspect ratio, as already highlighted in Figure 2.2(b). In Figure 2.7 we also show the electron coefficient $\mathcal{L}^e_{22}$ ($\sim \chi_e$, electron heat conductivity), computed with the four different equilibria of Table 2.1. In Figure 2.7(a), $\mathcal{L}^e_{22}$ is plotted versus $\epsilon^{1/2}$: we see differences up to 30% already at $\epsilon = 0.15$. In Figure 2.7(b) we show the same coefficient $\mathcal{L}^e_{22}$ divided by the appropriate flux surface average ($B_0^2 < B^{-2} >$) and still plotted versus $\epsilon^{1/2}$. Although the correct normalization, the geometrical parameter is not adequate to allow the overlapping of the curves obtained with the different equilibria. Therefore such a paramter would not enable one to produce a unique fitting formula for the transport coefficient with a global geometrical validity. In Figure 2.7(c) we plot $\mathcal{L}_{22}^e/(B_0^2 < B^{-2} >)$ versus the trapped particle fraction f_t^d, defined in Eq. (2.21), as suggested by the results of the Lorentz model: the points are well–aligned at all f_t^d, i.e. at all ϵ. The same behaviour is obtained for all the

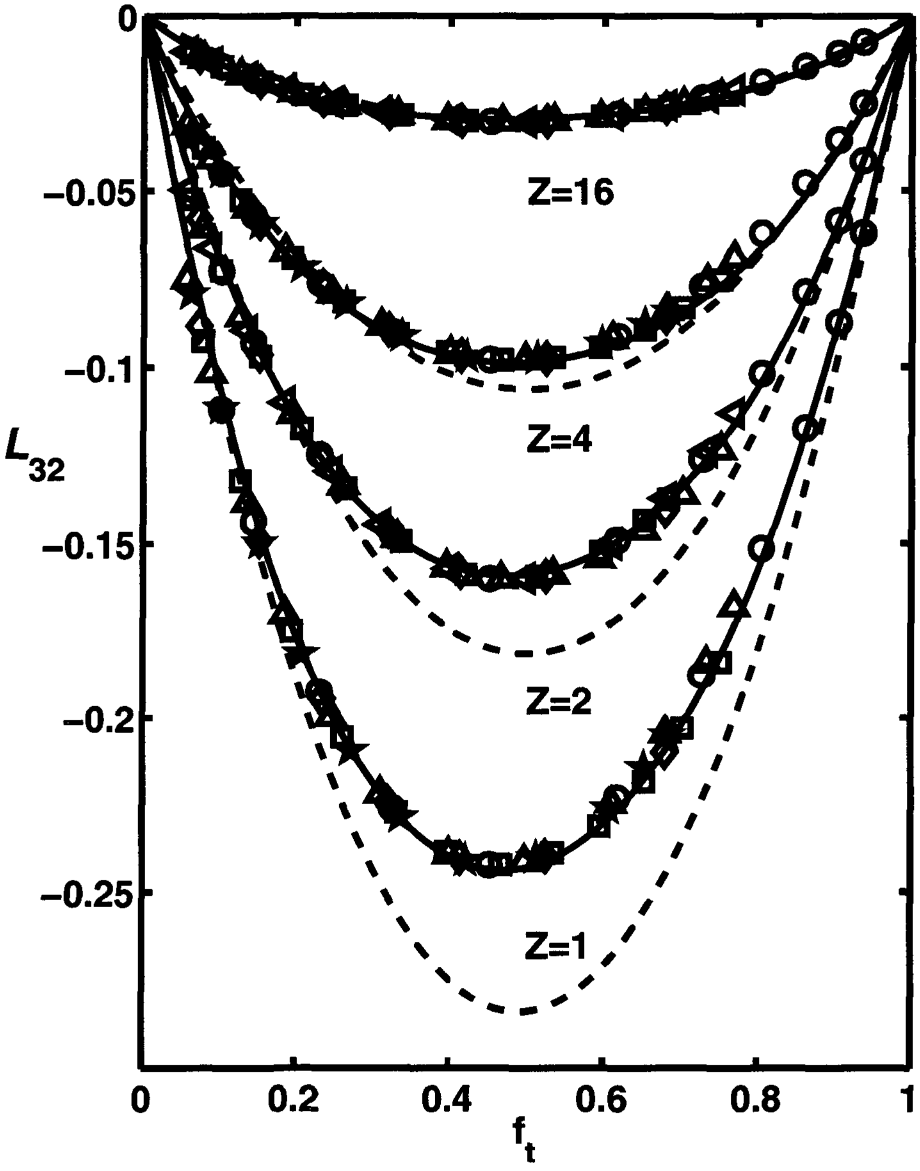

Figure 2.4: *Bootstrap current coefficient* $L_{32} = -\mathcal{L}_{32}^e/I\,n_e$ *versus* f_t*, for different charge number* Z *in the collisionless limit (CQL3D). Solid lines are obtained from Eqs. (2.26f), (2.27e) and (2.27f). The dashed lines are obtained from Hirshman's formula.*

other transport coefficients: the coefficients must be normalized by a suitable flux surface average and a correct geometrical parameter must be used to encapsulate the effects of the different equilibria. Note that the definition of a new trapped particle fraction, f_t^d, Eq. (2.21), is effectively necessary, as suggested by the Lorentz model, to correctly describe the geometrical behaviour of certain coefficients, in particular all the particle and heat conductivities, for which the usual one, f_t, turns out to be inadequate. From Figure 2.2 or Figure 2.7 it is also evident that, when plotted versus the correct parameter, the transport coefficients turn out to be very simple functions, almost proportional to the appropriate trapped fraction. This allows to express the transport coefficients with particularly simple formulae in terms of the appropriate geometrical parameter, as it will be presented in Section 2.4 and shown in Figure 2.9, for all the perpendicular transport coefficients. Hence the study of the effects of plasma shape on the neoclassical transport can be simply obtained considering the dependence of the trapped fraction on plasma elongation and triangularity at a given aspect ratio. Both the two given expressions for the trapped fraction, f_t and f_t^d, Eq. (2.21), turn out to be almost independent of elongation, and increasing when decreasing triangularity. In this sense, in the neoclassical transport, at a given value of the aspect ratio, a highly triangular plasma shape is favorable for confinement, as shown in Figure 2.2(b) and Figure 2.7(a) (symbol $\triangleright$), but not favorable for driving bootstrap current.

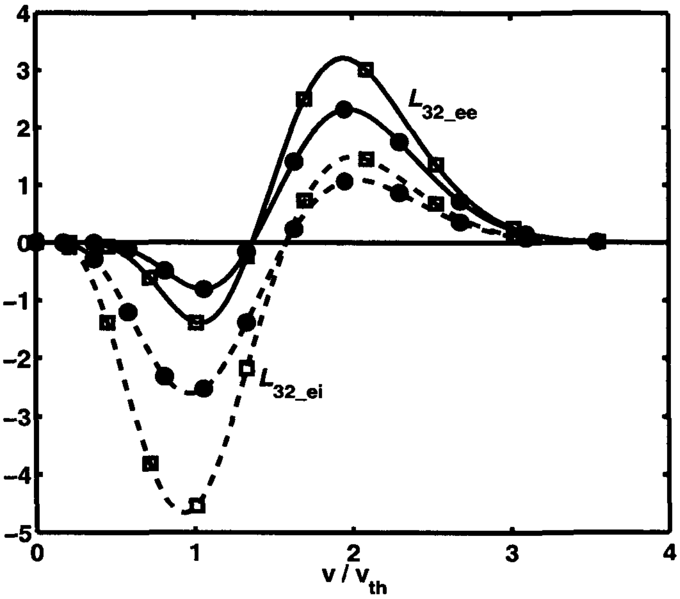

Figure 2.5: *Velocity dependence, normalized to* $v_{th} = \sqrt{2T_e/m_e}$, *of the integrands of* $L_{32\_ee} = \mathcal{L}_{32\_ee}/I\,n_e$, *solid lines, and* $L_{32\_ei} = \mathcal{L}_{32\_ei}/I\,n_e$, *dashed lines, of the bootstrap current coefficient* $L_{32} = -\mathcal{L}_{32}^e/I\,n_e$. *Solid circles for a low collisionality case (CQL3D), open squares for an high collisionality cases (CQLP)*

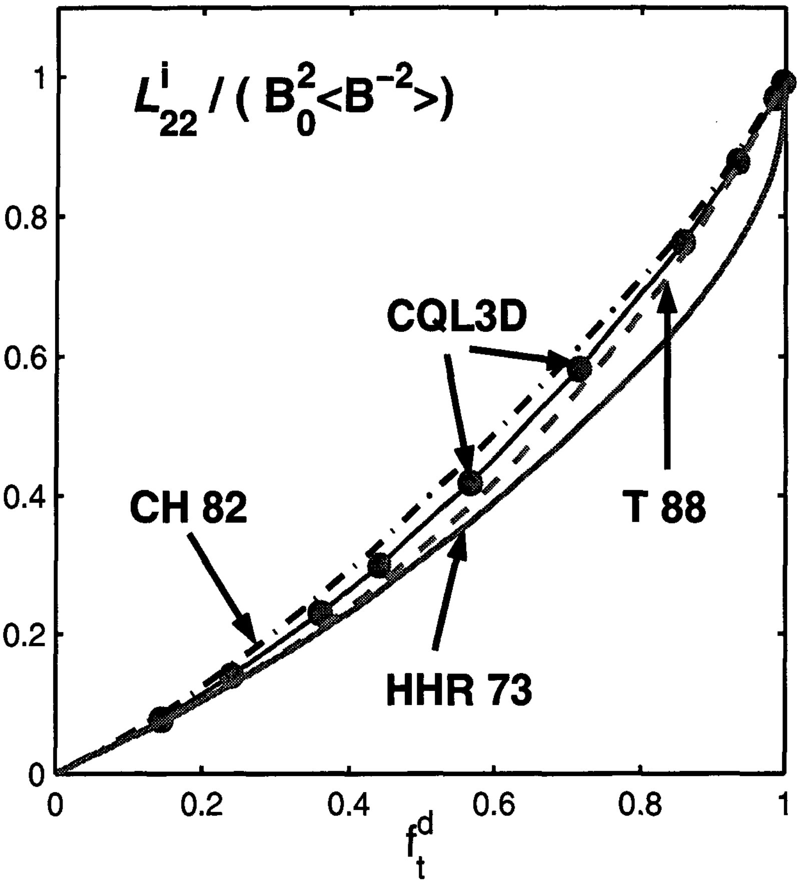

Figure 2.6: *The ion heat conductivity, transport coefficient* $\mathcal{L}^i_{22}$*, computed by CQL3D with an almost cylindrical equilibrium (solid circles), divided by the flux surface average* $B_0^2 \langle B^{-2} \rangle$*, plotted vs the trapped particle fraction* f_t^d *and compared with formulae of Ref. 5, CH 82 (dashed-dotted line), Ref. 6, T 88 (dashed line), and Ref. 10 (modified), HHR 73 (solid line).*

2.3.3 Neoclassical conductivity and bootstrap current coefficients at arbitrary collisionality

The code CQLP [16] solves the Fokker-Planck equation using the linearized operator on a magnetic flux surface, including the advection parallel to the magnetic field. It does not make any assumption on the ratio of the collision frequency to the bounce frequency. Moreover, like CQL3D, the code uses the magnetic geometry as calculated by a toroidal equilibrium code and therefore uses the realistic axisymmetric magnetic configuration of the flux surface. With this code we have solved Eqs. (2.12), with $m = 4$, and Eq. (2.13), $m = 2$, $n = 1$, in order to compute the neoclassical conductivity and bootstrap current coefficients for arbitrary collisionality. Particular care in this context have been taken in order to compute the bootstrap coefficient $L_{32} = -\mathcal{L}^e_{32}/I\, n_e$. As we have already mentioned, this coefficient is given by two different contributions, arising from electron-

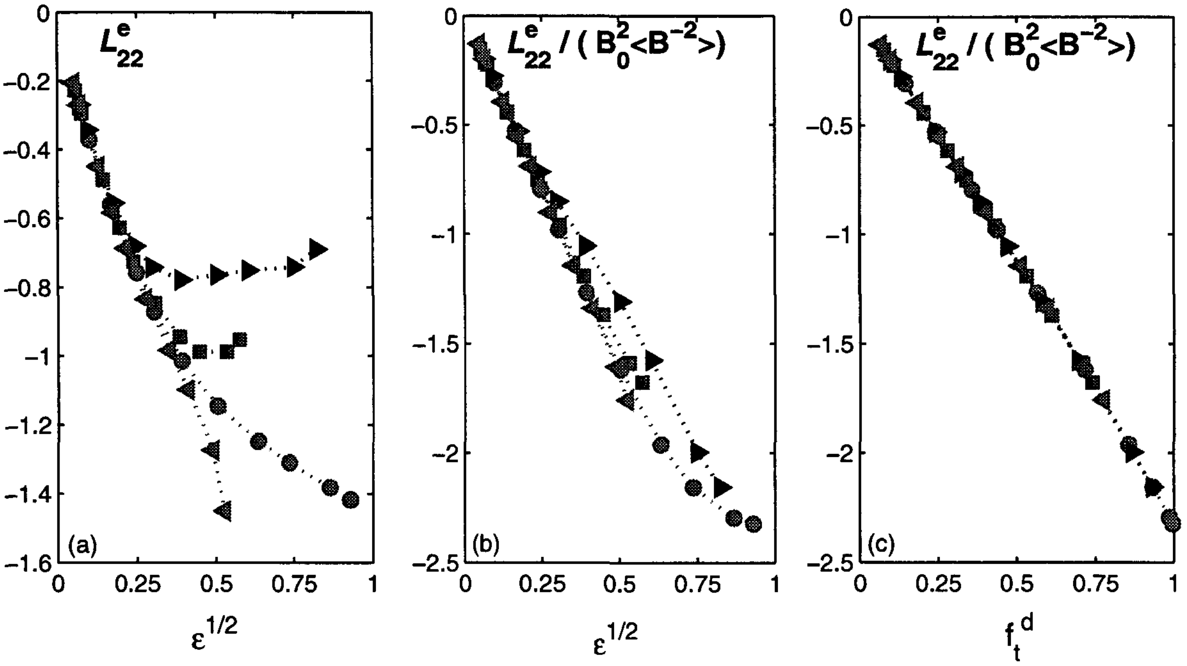

Figure 2.7: *The transport coefficient $\mathcal{L}^e_{22}$, main contribution to the electron heat conductivity, computed by CQL3D with four different equilibria: (a) the complete coefficient is plotted vs $\epsilon^{1/2}$, a strong dependence on the different equilibria appears at small aspect ratio; (b) the coefficient is divided by an appropriate flux surface average $B_0^2 \langle B^{-2} \rangle$, and still plotted vs $\epsilon^{1/2}$: although the correct renormalization, the geometrical parameter is not yet adequate to encapsulate all the geometrical effetcs; (c) same as (b) but plotted vs the correct geometrical parameter, f_t^d, which allows to perfectly align all the points of the different equilibria.*

ion and electron-electron collisions respectively, which are of opposite signs and which, for like–particle collisions, involve dominant terms from the fast spectrum of the distribution function. In Figure 2.5, with open squares, the integrands $L_{32_{ee}}$ and $L_{32_{ei}}$ are shown for a CQLP run at high collisionality. Moreover it can be inferred from this plot that both terms will have a different collisionality dependence, as their main contributions come from different v region. Increasing collisionality modifies first the small v region, and therefore modifies first $\mathcal{L}_{32\_ei}$. This is shown in Figure 2.8, where both terms, $\mathcal{L}_{32\_ee}$ and $\mathcal{L}_{32\_ei}$, are plotted versus ν_{e*}. Note first that, at very low collisionality, the results of CQL3D for the banana regime are correctly recovered by the collisionality dependent code CQLP. On the other hand, at very high collisionality, the limit of $\mathcal{L}_{32}$ is zero and therefore $\mathcal{L}_{32\_ee}$ = - $\mathcal{L}_{32\_ei}$ for $\nu_{e*} \gg 10$. Solid lines in Figure 2.8 show the fitting expressions of the numeric results for the transport coefficients computed in terms of f_t, ν_{e*}, and Z, and which will be presented in the next Section.

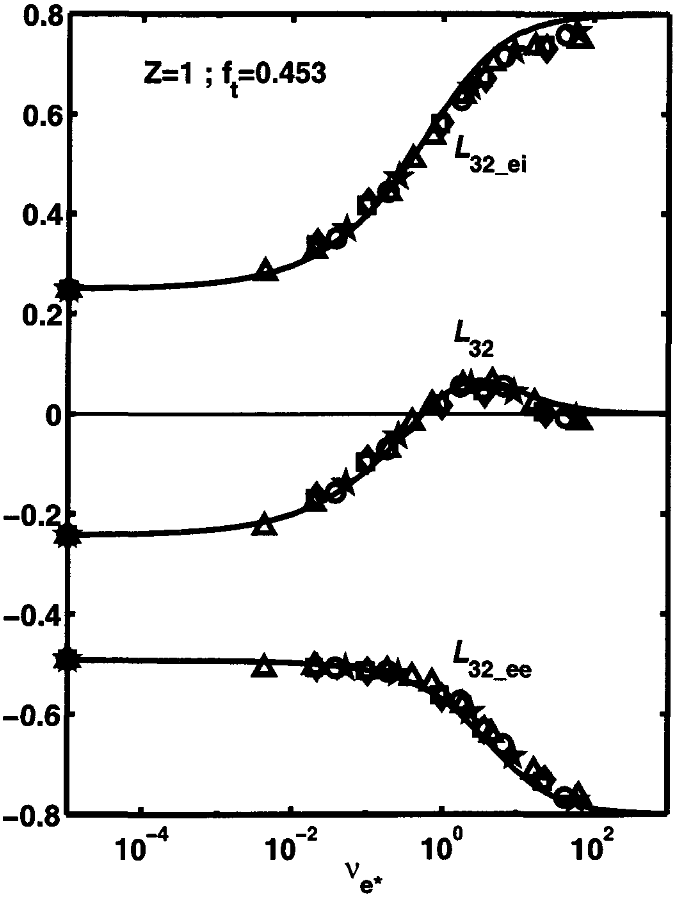

Figure 2.8: *Bootstrap current coefficient* $L_{32} = -\mathcal{L}_{32}/\mathcal{L}_b = L_{32\_ee} + L_{32\_ei}$ *versus collisionality* ν_{e*}.

2.4 Transport coefficients formulae

2.4.1 Analytical fits to the numerical results for the banana regime

Considering the results of the previous section, we can introduce a set of dimensionless electron and ion transport coefficients $\mathcal{K}^{\sigma}_{mn}$

$$\begin{aligned}
\mathcal{L}^e_{nm} &= \mathcal{L}_d[B_0^2\langle B^{-2}\rangle]\,\mathcal{K}^e_{nm}(f_t^d), && n,m=1,2. && \text{(2.24a)}\\
\mathcal{L}^e_{n3} &= \mathcal{L}_b\,\mathcal{K}^e_{n3}(f_t), && n=1,2,4, && \text{(2.24b)}\\
\mathcal{L}^e_{n4} &= \mathcal{L}_d[B_0^2\langle B^2\rangle^{-1}]\,\mathcal{K}^e_{n4}(f_t), && n=1,2, && \text{(2.24c)}\\
\mathcal{L}^e_{33} &= \mathcal{L}_\sigma[B_0^{-2}\langle B^2\rangle]\,\mathcal{K}^e_{33}(f_t), && && \text{(2.24d)}\\
\mathcal{L}^i_{11} &= \mathcal{L}^i_\sigma[B_0^{-2}\langle B^2\rangle]\,\mathcal{K}^i_{11}(f_t), && && \text{(2.24e)}\\
\mathcal{L}^i_{12} &= \mathcal{L}^i_b\,\mathcal{K}^i_{12}(f_t), && && \text{(2.24f)}\\
\mathcal{L}^i_{22} &= \mathcal{L}^i_d[B_0^2\langle B^{-2}\rangle]\,\mathcal{K}^i_{22}(f_t^d), && && \text{(2.24g)}
\end{aligned}$$

and analogously all their symmetrics, where $\mathcal{L}_d$, $\mathcal{L}_b$ and $\mathcal{L}_\sigma$ are defined by Eqs. (2.20); the ion normalization factors, $\mathcal{L}_d^i$, $\mathcal{L}_b^i$ and $\mathcal{L}_\sigma^i$, are defined as follows:

$$\mathcal{L}_d^i = \frac{n_i \rho_{ip}^2}{\tau_i}\left(\frac{d\psi}{d\rho}\right)^2, \qquad \mathcal{L}_b^i = I(\psi) n_i, \qquad \mathcal{L}_\sigma^i = \frac{n_i q_i^2 \tau_i}{m_i T_i} B_0^2, \tag{2.25}$$

The dimensionless coefficients are functions of only one suitable geometrical parameter, i.e. a trapped fraction, which completely encapsulates the effects of the various equilibria: in this way the code results for the coefficients $\mathcal{K}_{mn}^\sigma$ can be fitted in terms of the appropriate trapped fraction, f_t or f_t^d, as they perfectly overlap, regardless the equilibrium considered in the calculation, even highly non-circular and at small aspect ratio. Note that only in this way relatively simple formulae valid in general axisymmetric equilibria and at all aspect ratios can be given. We have run the code CQL3D with different equilibria and for the electron coefficients we have also varied the ion charge, to obtain the dependence on the effective charge Z. Our idea is that, at least for the electron transport coefficients, an effective charge approximation for multispecies cases should still be valid: collisions between electrons and main ions, or between electrons and impurity ions are almost of the same kind, involving basically the pitch-angle scattering. In any case, the comparison with the results of multispecies codes [8] should enable one to determine the correct form of Z, instead of the usual definition of Z_{eff}, to be used in our formulae. For the ions, the presence of one heavy impurity species leads to collisions between main ions and impurity ions which involve basically the pitch-angle scattering, and which are completely different from like–particle collisions. In this case, as shown in Ref. [30], the thermal conductivity computed as Z_{eff} times the pure ion conductivity is underestimated. Using the results of Ref. [30], which uses the large aspect ratio limit of Ref. [31], we have generalized our formula for the transport coefficient $\mathcal{L}_{22}^i$, to include the effect of a single heavy impurity species in the Pfirsch-Schlüter regime. We have also adapted the formula for the bootstrap current coefficient α in the banana regime, obtained fitting the CQL3D results, in order to include the same effect, using the large aspect ratio limit of Ref. [31], and noting that at $\epsilon = 1$ not only the pure plasma coefficient, but also the impurity contribution must be equal to zero. The analytical fits to the results of CQL3D for all the transport coefficients valid in the banana regime, for arbitrary trapped fraction and Z, read as follows:

$$\begin{aligned}
\mathcal{K}^e_{11}(f^d_t) &= -0.5\,F_{11}(f^d_t), &(2.26a)\\
\mathcal{K}^e_{12}(f^d_t) &= 0.75\,F_{12}(f^d_t), &(2.26b)\\
\mathcal{K}^e_{13}(f_t) &= \mathcal{K}^e_{34} = -\,F_{13}(f_t), &(2.26c)\\
\mathcal{K}^e_{14}(f_t) &= \mathcal{K}^e_{44} = -0.5\,F_{11}(f_t), &(2.26d)\\
\mathcal{K}^e_{22}(f^d_t) &= -\left(\frac{13}{8}+\frac{\sqrt{2}}{2Z}\right)F_{22}(f^d_t), &(2.26e)\\
\mathcal{K}^e_{23}(f_t) &= -\left(F_{23\_ee}(f_t) + F_{23\_ei}(f_t)\right), &(2.26f)\\
\mathcal{K}^e_{24}(f_t) &= 0.75\,F_{12}(f_t), &(2.26g)\\
\mathcal{K}^e_{33}(f_t) &= (F_{33}(f_t)-1)/Z/N(Z), &(2.26h)\\
\mathcal{K}^i_{22}(f^d_t) &= -\,F^i_{22}(f^d_t), &(2.26i)
\end{aligned}$$

$$\begin{aligned}
F_{11}(X) &\doteq (1+\frac{0.9}{Z+0.5})X-\frac{1.9}{Z+0.5}X^2+\frac{1.6}{Z+0.5}X^3-\frac{0.6}{Z+0.5}X^4, &(2.27a)\\
F_{12}(X) &\doteq (1+\frac{0.6}{Z+0.5})X-\frac{0.95}{Z+0.5}X^2+\frac{0.3}{Z+0.5}X^3+\frac{0.05}{Z+0.5}X^4, &(2.27b)\\
F_{13}(X) &\doteq (1+\frac{1.4}{Z+1})X-\frac{1.9}{Z+1}X^2+\frac{0.3}{Z+1}X^3+\frac{0.2}{Z+1}X^4, &(2.27c)\\
F_{22}(X) &\doteq (1-\frac{0.11}{Z+0.5})X+\frac{0.08}{Z+0.5}X^2+\frac{0.03}{Z+0.5}X^3, &(2.27d)\\
F_{23\_ee}(X) &\doteq \frac{0.05+0.62Z}{Z(1+0.44Z)}(X-X^4)+\\
&+\frac{1}{1+0.22Z}\left[X^2-X^4-1.2(X^3-X^4)\right]+\frac{1.2}{1+0.5Z}X^4, &(2.27e)\\
F_{23\_ei}(Y) &\doteq -\frac{0.56+1.93Z}{Z(1+0.44Z)}(Y-Y^4)+\\
&\frac{4.95}{1+2.48Z}\left[Y^2-Y^4-0.55(Y^3-Y^4)\right]-\frac{1.2}{1+0.5Z}Y^4, &(2.27f)\\
F_{33}(X) &\doteq 1-(1+\frac{0.36}{Z})X+\frac{0.59}{Z}X^2-\frac{0.23}{Z}X^3, &(2.27g)\\
F^i_{22}(X) &\doteq (1-\,0.55)\,(1+\,1.54\,\alpha_I)\,X\,+\\
&\left(0.75\,X^2\,-\,0.7\,X^3\,+\,0.5\,X^4\right)(1+\,2.92\,\alpha_I), &(2.27h)
\end{aligned}$$

$$\alpha(f_t) = \mathcal{K}^i_{21} = -\frac{0.62+1.5\,\alpha_I}{0.53+\alpha_I}\,\frac{1-f_t}{1-0.22f_t-0.19f_t^2}, \qquad (2.28)$$

where $\alpha_I = n_I Z_I^2/n_i Z_i^2$ is the usual impurity strength parameter, and index I refers to the ion impurity species. The factorizations used in Eqs. (2.26) and (2.27) are such that the Lorentz limit ($Z \rightarrow \infty$), the low ($f_t \rightarrow 0$) and the large aspect ratio ($f_t \rightarrow 1$) are easily recovered. Moreover the functions F_{ij} have values within $[0, 1]$. Note that $\mathcal{K}^e_{11}$ and $\mathcal{K}^e_{14}$, as well as $\mathcal{K}^e_{12}$ and $\mathcal{K}^e_{24}$ have the same functional dependence on their respective trapped fraction. The coefficient $\mathcal{K}_{33}$ is obviously directly related to the neoclassical conductivity: indeed it reads

$$\frac{\sigma_{neo}(f_t)}{\sigma_{Sptz}} = Z\,N(Z)\,K_{33} + 1 = F_{33}(f_t), \tag{2.29}$$

where

$$\sigma_{Sptz} = 1.9012 \cdot 10^4\,\frac{T_e[eV]^{3/2}}{ZN(Z)ln\Lambda_e}[\mathrm{m}^{-1}\Omega^{-1}] \;\; ; \;\; N(Z) = 0.58 + \frac{0.74}{0.76+Z}.$$

This set of relations can be considered as the extension to a general axisymmetric equilibrium at all aspect ratios of Eqs. (6.28) - (6.30) and Eq. (6.47) in Ref. [4]. We have also computed the coefficient $\mathcal{L}^i_{11}$, which is usually not considered, using the weak-coupling approximation which neglects the force A_{i1}. For completeness, we give also the fit to the code results for the transport coefficient $\mathcal{K}^i_{11}$:

$$\mathcal{K}^i_{11}(f_t) = (0.11 + 1.7\,f_t - 1.25\,f_t^2 + 0.44\,f_t^3)^{-1} \; - \; 1.$$

Note that Eqs. (2.5) allow one to reduce the number of independent thermodynamic forces from 6 to 4, hence with only 4 conjugated thermodynamic fluxes. Taking the first 3 electron forces and the second ion force, whose conjugated fluxes have more direct physical meaning and more direct application in the fluid transport equations, the relations which connect fluxes with forces read as follows:

$$\begin{aligned} B_{en} &= \sum_{m=1}^{3} \left\{ \mathcal{L}^e_{nm} - \frac{1}{\mathcal{F}}\,\frac{T_i}{Z_i^2 T_e}\,\frac{\mathcal{L}^i_{11}\mathcal{L}^e_{n4}}{[I(\psi)n_i]^2} \right\} A_{em} \\ &\qquad - \frac{1}{\mathcal{F}}\,\frac{T_i}{Z_i T_e}\,\mathcal{L}^e_{n4}\,\frac{\mathcal{L}^i_{12}}{I(\psi)n_i}\,A_{i2}, \qquad n = 1,2,3, \end{aligned} \tag{2.30a}$$

$$B_{i2} = \frac{1}{\mathcal{F}}\,\frac{\mathcal{L}^i_{21}}{I(\psi)n_i} \sum_{m=1}^{3} \mathcal{L}^e_{4m} A_{em} + \left\{ \mathcal{L}^i_{22} - \frac{1}{\mathcal{F}}\,\frac{T_i}{Z_i^2 T_e}\,\frac{\mathcal{L}^i_{12}\mathcal{L}^i_{21}}{[I(\psi)n_i]^2}\mathcal{L}^e_{44} \right\} A_{i2}, \tag{2.30b}$$

where

$$\mathcal{F} \doteq 1 + \frac{T_i}{Z_i^2 T_e}\,\frac{\mathcal{L}^i_{11}\mathcal{L}^e_{44}}{[I(\psi)n_i]^2},$$

and Z_i is the main ion charge number. The condition for the validity of the weak-coupling approximation is given by Eq. (5.86) in Ref. [4], and is simply $\mathcal{F} - 1 \ll 1$. Introducing the dimensionless coefficients $\mathcal{K}^\sigma_{mn}$, this relation reads, consistently with the estimate given in Ref. [4], Table IV:

$$\frac{2\sqrt{2}}{Z_i}\left(\frac{m_e}{m_i}\right)^{\frac{1}{2}}\left(\frac{T_i}{T_e}\right)^{\frac{3}{2}}\mathcal{K}^e_{14}\,\mathcal{K}^i_{11} \ll 1. \tag{2.31}$$

The absolute value of the term $\mathcal{K}^e_{14}\,\mathcal{K}^i_{11}$ turns out to be smaller then 0.25, which confirms the validity of the weak coupling approximation in the banana regime. In this way Eqs. (2.30) are reduced to:

$$B_{en} = \sum_{m=1}^{3} \mathcal{L}^e_{nm} A_{em} - \frac{T_i}{Z_i T_e} \mathcal{L}^e_{n4} \frac{\mathcal{L}^i_{12}}{I(\psi) n_i} A_{i2}, \qquad n = 1, 2, 3, \tag{2.32a}$$

$$B_{i2} = \frac{\mathcal{L}^i_{21}}{I(\psi) n_i} \sum_{m=1}^{3} \mathcal{L}^e_{4m} A_{em} + \left\{ \mathcal{L}^i_{22} - \frac{T_i}{Z_i^2 T_e} \frac{\mathcal{L}^i_{12} \mathcal{L}^i_{21}}{[I(\psi) n_i]^2} \mathcal{L}^e_{44} \right\} A_{i2}. \tag{2.32b}$$

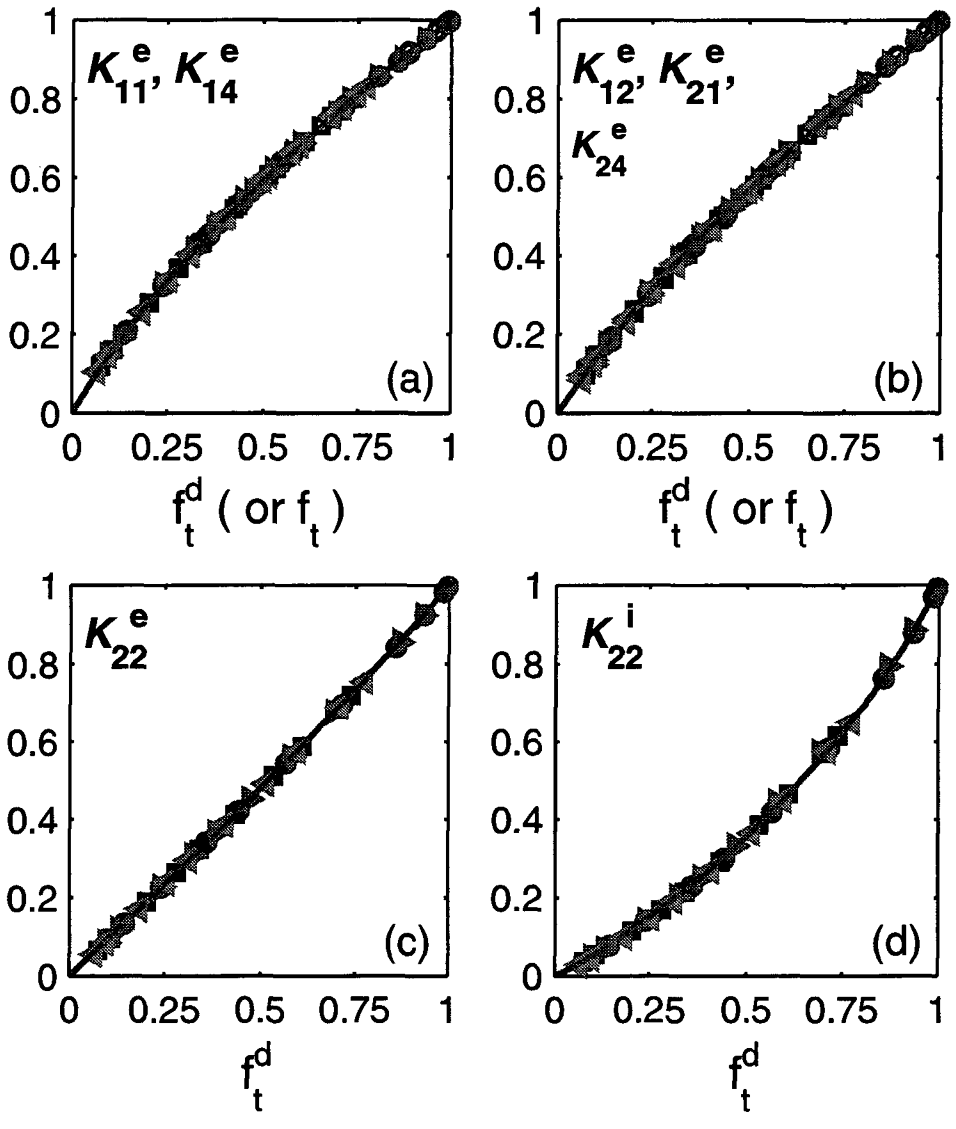

Figure 2.9: *Computed values of the dimensionless transport coefficients* $\mathcal{K}^\sigma_{mn}$ *(symbols), compared with the fitting formulae, Eqs. (2.26) and (2.27), (solid lines). (a) Coefficients* $\mathcal{K}^e_{11}$ *plotted vs* f^d_t, *(solid symbols), and* $\mathcal{K}^e_{14}$ *plotted vs* f_t, *(open symbols). (b) Coefficients* $\mathcal{K}^e_{12}$ *and* $\mathcal{K}^e_{21}$, *plotted vs* f^d_t, *(solid symbols), and* $\mathcal{K}^e_{24}$ *plotted vs* f_t, *(open symbols). (c) Coefficient* $\mathcal{K}^e_{22}$ *plotted vs* f^d_t, *(solid symbols). (d) Coefficient* $\mathcal{K}^i_{22}$ *plotted vs* f^d_t, *(solid symbols).*

In Figure 2.9 we compare the code results for the dimensionless transport coefficients $\mathcal{K}^{\sigma}_{nm}$ (symbols) with the algebraic formulae, Eqs. (2.26) and Eqs. (2.27), which fit the data, (solid lines).

2.4.2 Analytical fits to the numerical results for parallel transport at all collisionality

As already presented in subsection 2.3.3, the code CQLP has been used to compute the neoclassical conductivity and the bootstrap current coefficients for arbitrary collisionality, solving the non–bounce–averaged kinetic equations, Eq. (2.10), $n = 3$, and Eq. (2.11b). As we have shown at the end of subsection 2.3.2, as well as in the previous subsection, the trapped particle fractions, f_t and f_t^d, turn out to be the best parameters in order to encapsulate the geometrical effects on the transport coefficients in the collisionless limit. For this reason it seems better, when fitting the numerical results for collisional regimes, to change only f_t as a function of ν_{e*} if possible. In this way one can first find the polynomial dependence of $\mathcal{K}_{3n}$ on f_t in the collisionless limit using CQL3D, which is faster and more accurate, as presented in the previous subsection, and then determine the effective trapped fraction $f_t(\nu_{e*})$ for finite collisionality, while keeping the coefficient of the polynomials independent of ν_{e*}. This procedure is also easier to find an analytic formula valid for arbitrary f_t and ν_{e*}, as one does essentially two 1D fits, instead of one 2D fit. Finally it is interesting as one naturally obtains an estimate of the effect of collisionality on the fraction of trapped particles. This procedure was shown to be possible for σ_{neo} and the bootstrap coefficient $\mathcal{L}_{31}$ in Ref. [17]. In this way, the dependence on collisionality for the coefficients $\mathcal{K}_{3n}$ can be simply obtained replacing, in the corresponding functions F_{3n}, the effective trapped particle fractions, depending on collisionality,

$$f^{31}_{\text{teff}}(\nu_{e*}) = \frac{f_t}{1+(1-0.1f_t)\sqrt{\nu_{e*}}+0.5(1-f_t)\nu_{e*}/Z}, \tag{2.33a}$$

$$f^{32\_ee}_{\text{teff}}(\nu_{e*}) = \frac{f_t}{1+0.26(1-f_t)\sqrt{\nu_{e*}}+0.18(1-0.37f_t)\nu_{e*}/\sqrt{Z}}, \tag{2.33b}$$

$$f^{32\_ei}_{\text{teff}}(\nu_{e*}) = \frac{f_t}{1+(1+0.6f_t)\sqrt{\nu_{e*}}+0.85(1-0.37f_t)\nu_{e*}(1+Z)}, \tag{2.33c}$$

$$f^{33}_{\text{teff}}(\nu_{e*}) = \frac{f_t}{1+(0.55-0.1f_t)\sqrt{\nu_{e*}}+0.45(1-f_t)\nu_{e*}/Z^{3/2}}, \tag{2.33d}$$

$$f^{34}_{\text{teff}}(\nu_{e*}) = \frac{f_t}{1+(1-0.1f_t)\sqrt{\nu_{e*}}+0.5(1-0.5f_t)\nu_{e*}/Z}. \tag{2.33e}$$

We have tested different definitions of ν_{e*} and ν_{i*}, using some averaged poloidal magnetic field instead of rB/qR and/or some function of f_t instead of $\epsilon^{3/2}$ for example. However the simple following definitions

$$\nu_{e*} = 6.921 \cdot 10^{-18}\,\frac{qRn_eZ ln\Lambda_e}{T_e^2\epsilon^{3/2}}, \quad ; \quad \nu_{i*} = 4.90 \cdot 10^{-18}\,\frac{qRn_iZ^4 ln\Lambda_{ii}}{T_i^2\epsilon^{3/2}}, \tag{2.34}$$

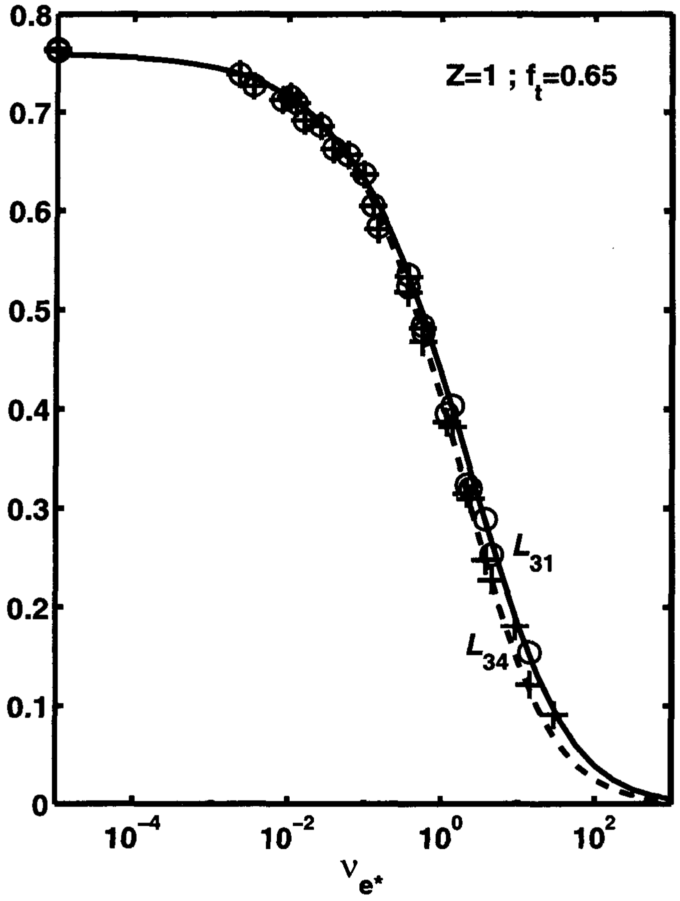

Figure 2.10: *The bootstrap current coefficient* $\mathcal{L}_{31} = -\mathcal{K}^e_{31}$*, open circles, and* $\mathcal{L}_{34} = -\mathcal{K}^e_{34}$*, crosses, vs. collisionality* ν_{e*}*, as obtained with CQLP. The solid lines are obtained applying the formulae given in Eq. (2.26c), Eqs. (2.33a) and (2.33e) respectively.*

where

$$\ln\Lambda_e = 31.3 - \ln\left(\frac{\sqrt{n_e}}{T_e}\right), \qquad \ln\Lambda_{ii} = 30 - \ln\left(\frac{Z^3\sqrt{n_i}}{T_i^{3/2}}\right),$$

with the combination of Rq and $\epsilon^{-3/2}$, gives the best overlap of the results of the different equilibria at same values of f_t and ν_{e*}, as shown in Figure 2.8 and Figure 2.10. We see also from Eqs. (2.33a, 2.33e) that $\mathcal{K}^e_{31}$ is indeed almost equal to $\mathcal{K}^e_{34}$, except at very large ν_{e*}, as seen in Figure 2.10 and in agreement with Ref. [4]. This is why we only had to change slightly the collisionality dependence of f^{31}_{teff}, as it can be easily shown, using the bounce-averaged equations, that $\mathcal{L}_{34}$=$\mathcal{L}_{31}$ in the collisionless limit. For the bootstrap current coefficient $\alpha = -\mathcal{K}^i_{12}$, we have not used the same structure. First it should be emphasized that the actual coefficient for the ion temperature gradient is $\mathcal{K}_{34}\,\alpha$. Second, Figure 2.11(a), the coefficient has a very sharp ν_{i*} dependence, which is very sensitive also to f_t as shown in Figure 2.11(b). It is therefore not possible to decouple the f_t and ν_{i*} dependences as it is done for the other coefficients. This is why we have modified

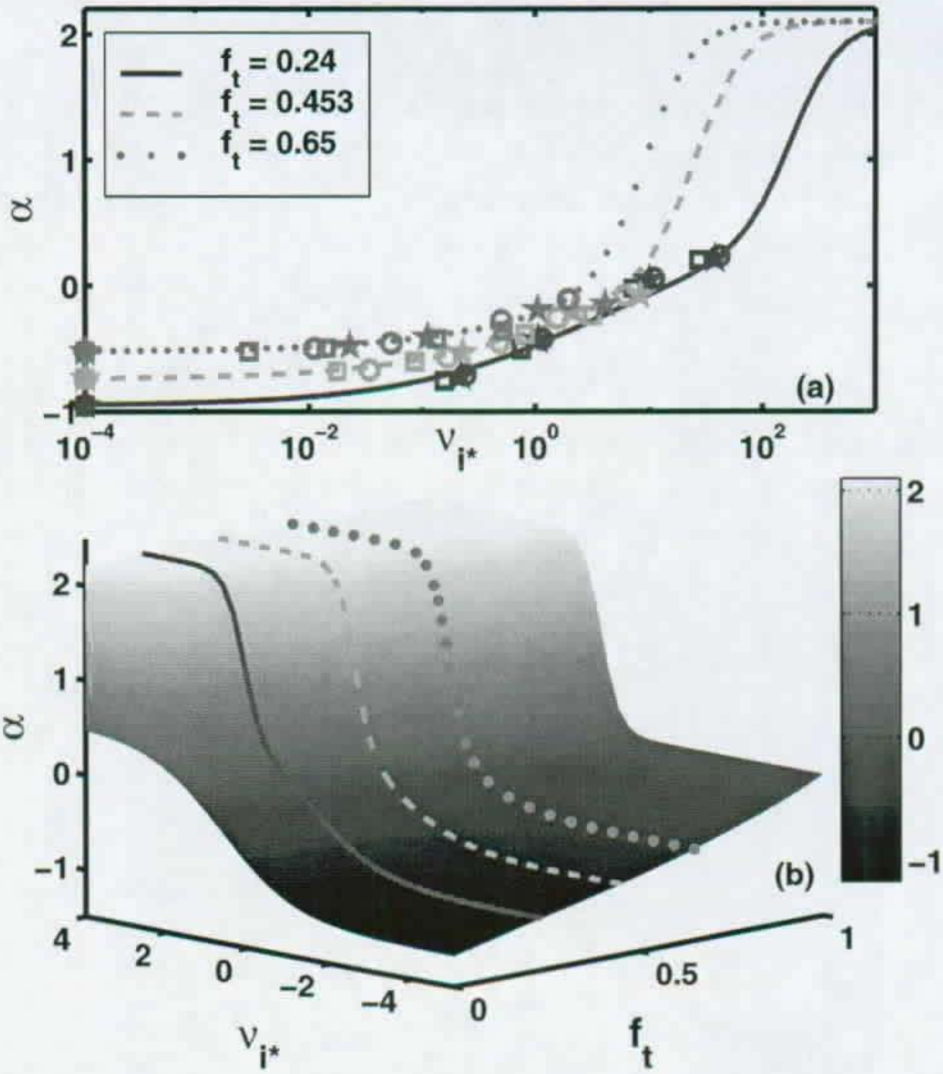

Figure 2.11: *(a) Coefficient* α *for three different values of* f_t *vs* ν_{i*}*. The lines correspond to Eq. (2.35), and they are reproduced on the 3D plot. (b) 3D view of the coefficient* α *in terms of* f_t *and* ν_{i*} *for* $Z = 1$*. Note that the sharp rise depends strongly on both* f_t *and* ν_{i*}*.*

the formula proposed by Harris [6] such as to reproduce the correct results in the banana regime, Eq. (2.28), as well as in the plateau region, and such as to have a function of f_t rather than ϵ in order to be valid for any axisymmetric geometry

$$\alpha(\nu_{i*}) = \left[\frac{\alpha_0 + 0.25(1-f_t^2)\sqrt{\nu_{i*}}}{1+0.5\sqrt{\nu_{i*}}} + 0.315\nu_{i*}^2 f_t^6\right]\frac{1}{1+0.15\nu_{i*}^2 f_t^6}. \qquad (2.35)$$

2.4.3 Combined formulae for radial transport at all collisionality

In order to compute the neoclassical radial transport coefficients at arbitrary collisionality regime, the non–bounce–averaged kinetic equations, Eqs. (2.10) and (2.11), must be solved, as it has been done for the parallel transport coefficients and presented in the previous subsection. This long task has not been performed yet, mainly because we can use the knowledge gained in calculating the parallel transport coefficients to derive directly formulae for the perpendicular transport coefficients. In order to strictly compare only the dependence on collisionality, in Figure 2.12 we have plotted formulae of subsection 2.4.2 (solid lines) and those of Ref. [4], Sec. VI F (dashed lines), in which we have replaced the banana limit with the correct results of the code CQL3D. The neoclassical resistivity is shown in Figure 2.12(a) and the bootstrap current coefficient $\mathcal{L}_{31}^{e}$ in Figure 2.12(b), for three values of the trapped fraction. At low aspect ratio there is a very good agreement, which falls down at larger values of the trapped fraction. This comes from the main approximation adopted to compute the banana–plateau regime, in Ref. [32], which neglects the energy scattering in the like–particle collision operator and which underestimates the neoclassical transport at low aspect ratio [12]. However for

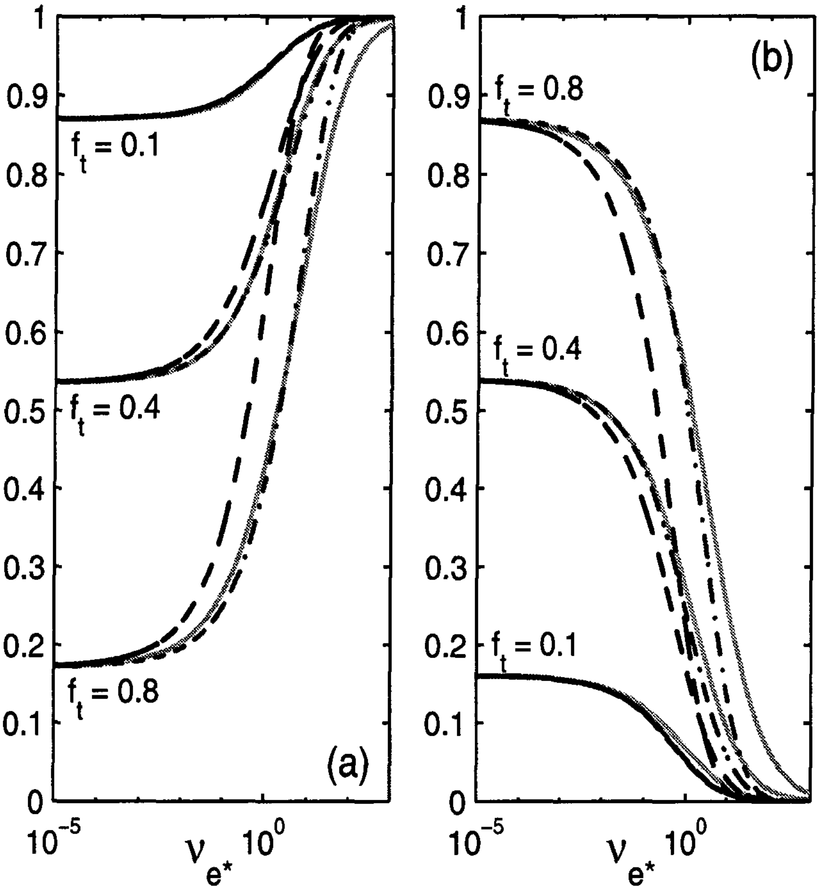

Figure 2.12: *Dependence on collisionality for the transport coefficients* σ_{neo}, *(a), and* $\mathcal{L}_{31}^{e}$, *(b), for different values of the trapped fraction* f_t, *as given by Ref. 2, (solid lines), by Ref. 3, with the value at* $\nu_{e*} = 0$, *banana limit, corrected with the results of Ref. 2, (dashed lines), and still by Ref. 3, with also the collisional parameter rescaled by Eq. (2.36), (dashed–dotted lines).*

both the neoclassical resistivity and the bootstrap current coefficient $\mathcal{L}^e_{31}$, and also for the coefficient $\mathcal{L}^e_{32}$ not shown here, formulae of Ref. [4] go down to zero at smaller values of ν_{e*} with respect to the rigorous results of subsection 2.4.2, with approximatively the same behaviour. When the collisional parameter $\nu_{\sigma*}$, defined in Eq. (2.34), is rescaled in terms of the trapped fraction with the simple transformation

$$\nu_{\sigma f*} = \frac{\nu_{\sigma*}}{1+7\, f_t^2}, \tag{2.36}$$

formulae of Ref. [4] allow an agreement within 20% for all the bootstrap current coefficients and the neoclassical resistivity (dashed–dotted lines), comparing with subsection 2.4.2. Hence, following the idea of Ref. [10], in which a formula valid for all collisionality regimes for the ion heat conductivity is obtained connecting a new banana limit, valid also at small aspect ratio, with the collisional dependence of Ref. [4], we propose to combine formulae of Ref. [4], Sec. VI F, adapted to small aspect ratio, with the results of subsection 2.4.1, in the limit at $\nu_{\sigma*} = 0$. The electron transport coefficients $\mathcal{K}^e_{mn}$, $m, n = 1, 2$ can be computed at arbitrary collisionality regimes as follows:

$$\begin{aligned} \mathcal{K}^e_{11}(f_t^d, \nu_{e*}) &= \mathcal{H}^e_{11}, \qquad \mathcal{K}^e_{12}(f_t^d, \nu_{e*}) = \mathcal{H}^e_{12} - \frac{5}{2}\,\mathcal{H}^e_{11}, \\ \mathcal{K}^e_{22}(f_t^d, \nu_{e*}) &= \mathcal{H}^e_{22} - 5\,\mathcal{H}^e_{12} + \tfrac{25}{4}\,\mathcal{H}^e_{11}, \end{aligned} \tag{2.37a}$$

$$\begin{aligned} \mathcal{H}^e_{mn}(f_t^d, \nu_{e*}) = {} & \frac{\mathcal{H}^{e\,(0)}_{mn}(f_t^d, \nu_{e*}=0)}{1 + a_{mn}(Z)\,\nu_{ef*}^{1/2} + b_{mn}(Z)\,\nu_{ef*}} - \\ & \frac{d_{mn}(Z)\,\nu_{ef*}\, f_t^{d^3}\,(1 + f_t^{d^6})}{1 + c_{mn}(Z)\,\nu_{ef*}\, f_t^{d^3}\,(1 + f_t^{d^6})} F_{PS}, \end{aligned} \tag{2.37b}$$

where the banana limit coefficients $\mathcal{H}^{e\,(0)}_{mn}(f_t^d, \nu_{e*} = 0)$ can be readily evaluated using Eqs. (2.26) and (2.27), with:

$$\begin{aligned} \mathcal{H}^{e\,(0)}_{11} &= \mathcal{K}^e_{11}(f_t^d), \qquad \mathcal{H}^{e\,(0)}_{12} = \mathcal{K}^e_{12}(f_t^d) + \frac{5}{2}\,\mathcal{K}^e_{11}(f_t^d), \\ \mathcal{H}^{e\,(0)}_{22} &= \mathcal{K}^e_{22}(f_t^d) + 5\,\mathcal{K}^e_{12}(f_t^d) - \tfrac{25}{4}\,\mathcal{K}^e_{11}(f_t^d). \end{aligned} \tag{2.37c}$$

The coefficients $\mathcal{K}^e_{4n}$ are given by:

$$\mathcal{K}^e_{41}(f_t, \nu_{e*}) = \mathcal{H}^e_{41}, \qquad \mathcal{K}^e_{42}(f_t, \nu_{e*}) = \mathcal{H}^e_{42} - \frac{5}{2}\,\mathcal{H}^e_{41}. \tag{2.37d}$$

$$\begin{aligned} & \mathcal{H}^e_{4n}(f_t, \nu_{e*}) = \\ & \left[\frac{\mathcal{H}^{e\,(0)}_{4n}(f_t, \nu_{e*}=0)}{1 + a_{1n}(Z)\nu_{ef*}^{1/2} + b_{1n}(Z)\nu_{ef*}} - \frac{d_{1n}(Z)\,\nu_{ef*}\, {f_t}^3\,(1 + 0.8\, {f_t}^3)}{1 + c_{1n}(Z)\nu_{ef*} {f_t}^3\,(1 + 0.8\, {f_t}^3)} F^{(4)}_{PS} \right] \\ & \frac{1}{1 + \nu_{ef*}^2\, f_t^{12}} \end{aligned} \tag{2.37e}$$

where analogously:

$$\mathcal{H}_{41}^{e(0)} = \mathcal{K}_{41}^{e}(f_t), \qquad \mathcal{H}_{42}^{e(0)} = \mathcal{K}_{42}^{e}(f_t) + \frac{5}{2}\,\mathcal{K}_{41}^{e}(f_t), \tag{2.37f}$$

and with

$$F_{PS} = 1 - \frac{1}{\langle B^2\rangle \langle B^{-2}\rangle}, \qquad F_{PS}^{(4)} = \langle B^{-2}\rangle \langle B^2\rangle - 1. \tag{2.37g}$$

The ion thermal conductivity $\mathcal{K}_{22}^{i}$ is given by:

$$\mathcal{K}_{22}^{i}(f_t^d, \nu_{i*}) = \frac{\mathcal{K}_{22}^{i}(f_t^d)}{1 + a_2\,\mu_{if*}^{1/2} + b_2\,\mu_{if*}} - \frac{d_2\,\mu_{if*}\,f_t^{d3}\,(1 + f_t^{d6})}{1 + c_2\,\mu_{if*}\,f_t^{d3}\,(1 + f_t^{d6})} H_P\,F_{PS}, \tag{2.37h}$$

with $\mu_{if*} = \nu_{if*}\,(1 + 1.54\,\alpha_I)$ and $H_P = 1 + 1.33\,\alpha_I\,(1 + 0.60\alpha_I)\,/\,(1 + 1.79\,\alpha_I)$, [30]. The coefficients $a_{mn}(Z)$, $b_{mn}(Z)$, $c_{mn}(Z)$ and $d_{mn}(Z)$ are given in subsection 2.4.4 and are obtained by interpolation of the data given in Ref. [4], Table III, for the electron coefficients and below Eq. (6.133) for the ion coefficient. The dependence on ϵ of the plateau–collisional terms of the formulae of Ref. [4], first computed in Ref. [33], has been rescaled on f_t or f_t^d. Finite aspect ratio effects in these terms have been taken into account, like in Ref. [10], introducing the complete expression of the Pfirsch-Schlüter geometrical factor, by means of F_{PS} and $F_{PS}^{(4)}$, Eqs. (2.37g). Note that Eq. (2.37h) for the ion thermal conductivity $\mathcal{K}_{22}^{i}$ includes the effects of a single heavy impurity species in the Pfirsch-Schlüter regime, according to [30], using the modified ion collisionality parameter μ_{if*} and the factor H_P, which take into account the enhancement of main ion thermal transport due to the presence of the impurity species [30].

2.4.4 Coefficients for the combined formulae of subsection 2.4.3

The coefficients $a_{mn}(Z)$, $b_{mn}(Z)$, $c_{mn}(Z)$ and $d_{mn}(Z)$ for the electron transport coefficients are defined as follows:

$$a_{11}(Z) = \frac{1 + 3\,Z}{0.77 + 1.22\,Z}, \quad a_{12}(Z) = \frac{0.72 + 0.42\,Z}{1 + 0.5\,Z}, \quad a_{22}(Z) = 0.46, \tag{2.38a}$$

$$b_{11}(Z) = \frac{1 + 1.1\,Z}{1.37\,Z}, \quad b_{12}(Z) = \frac{1 + Z}{2.99\,Z}, \quad b_{22}(Z) = \frac{Z}{-3 + 5.32\,Z}, \tag{2.38b}$$

$$c_{11}(Z) = \frac{0.1 + 0.34\,Z}{1.65\,Z}, \quad c_{12}(Z) = \frac{0.27 + 0.4\,Z}{1 + 3\,Z}, \quad c_{22}(Z) = \frac{0.22 + 0.55\,Z}{-1 + 7\,Z}, \tag{2.38c}$$

$$d_{11}(Z) = \frac{0.23\,Z}{-1 + 3.85\,Z}, \quad d_{12}(Z) = \frac{0.22 + 0.38\,Z}{1 + 6.1\,Z}, \quad d_{22}(Z) = \frac{0.25 + 0.05\,Z}{1 + 0.82\,Z}. \tag{2.38d}$$

For the ion thermal conductivity, the coefficients are:

$$a_2 = 1.03, \qquad b_2 = 0.31, \qquad c_2 = 0.22, \qquad d_2 = 0.175. \tag{2.39}$$

2.5 Conclusion

We have presented an approach for the neoclassical transport theory which allows to obtain simple equations suited for implementation in numerical codes in order to compute all the neoclassical transport coefficients. The code CQL3D, solving the bounce-averaged linearized drift–kinetic Fokker-Planck equation with the full collision operator, has been modified to calculate all these coefficients at all aspect ratios of various axisymmetric equilibria in the banana regime. We have shown that the limits at large and unit aspect ratio are correctly respected by the numerical results, as also the Onsager symmetry of the non-diagonal transport coefficients. Investigating the dependence of the coefficients on geometry parameters, we have shown that appropriate normalizations and definitions of trapped fractions are required in order to encapsulate all the geometry effects in a single variable. In this way, a set of simple formulae can be obtained from the numerical results and allow the evaluation of any transport coefficient for every axisymmetric equilibrium and at all aspect ratios. Our formula for the ion thermal conductivity is in good agreement with the most recent evaluations of this coefficient [10, 11] which however do not use the full collision operator, with errors at finite aspect ratio of about 10% by excess and by defect respectively. For all the other perpendicular transport coefficients, in particular the electron thermal conductivity, our formulae are the only existing to date and to our knowledge, computed for general axisymmetric equilibria taking into account finite aspect ratio effects. For parallel transport, neoclassical conductivity and bootstrap current coefficients are in good agreement in general with the previous formulae of Ref. [5], which do not use the full collision operator. Because of this, however, errors up to 20 % have been found in transport coefficients in which the contribution given by the like–particle collision operator is particularly important. The transport coefficients formulae, which fit the numerical results in the banana regime, are given by Eqs. (2.24), Eqs. (2.27) and Eq. (2.28) of subsection 2.4.1. With the code CQLP we have solved the non-bounce–averaged drift–kinetic equation, Eq. (2.10) for $m = 3$ and Eq. (2.11) for $m = 2$, taking into account the advection parallel to the magnetic field and without making any assumption on the ratio of the collision frequency to the bounce frequency. The code results have been fitted by simple analytical expressions, providing simple formulae for the neoclassical conductivity and the bootstrap current coefficients valid for all collisionality and aspect ratio. An effective trapped particle fraction has been introduced for each transport coefficient, in order to easily describe the collisional effect keeping the correct parameter, the trapped fraction, encapsulating the geometrical effects. These results for the parallel transport coefficients, compared with the ones of Refs. [4] and [10], have motivated us to propose combined formulae for all the other transport coefficients, valid for arbitrary collisionality regime, albeit without solving for Eqs. (2.10) and Eq. (2.11).

These combined formulae are necessary to correctly evaluate the coefficients over the whole plasma minor radius. The thermodynamic fluxes

$$B_{e1} = \Gamma_e \frac{d\psi}{d\rho}, \quad B_{e2} = \frac{Q_e}{T_e}\frac{d\psi}{d\rho}, \quad B_{e3} = \frac{\langle j_{\|} B\rangle}{T_e} - \frac{\langle j_{\|S} B\rangle}{T_e}, \quad B_{i2} = \frac{Q_i}{T_i}\frac{d\psi}{d\rho}, \tag{2.40a}$$

where Γ_e is the perpendicular electron particle flux, Q_e is the electron perpendicular heat flux, $j_{\|}$ and $j_{\|S}$ are the parallel electric current and the Spitzer current, and Q_i is the ion perpendicular heat flux, are given by Eqs. (2.32), in the weak coupling approximation, whose validity is confirmed by Eq. (2.31). Eqs. (2.32) can be reordered, and the thermodynamic fluxes can be expressed directly in terms of the electron and ion temperature and density perpendicular gradients and the parallel electric field

$$\begin{aligned}
B_{en} &= \mathcal{L}^e_{n1}\frac{\partial \ln n_e}{\partial\psi} + (\mathcal{L}^e_{n1} + \mathcal{L}^e_{n2})\frac{\partial \ln T_e}{\partial\psi} + \frac{1-R_{pe}}{R_{pe}}\mathcal{L}^e_{n1}\frac{\partial \ln n_i}{\partial\psi} + \\
&+ \frac{1-R_{pe}}{R_{pe}}(\mathcal{L}^e_{n1} + \alpha\mathcal{L}^e_{n4})\frac{\partial \ln T_i}{\partial\psi} + \mathcal{L}^e_{n3}\frac{\langle E_{\|}B\rangle}{\langle B^2\rangle}, \qquad n = 1,2,3, && \text{(2.40b)}\\
B_{i2} &= \frac{Q_i}{T_i}\frac{d\psi}{d\rho} = \\
&= \alpha\left[\mathcal{L}^e_{41}\frac{\partial \ln n_e}{\partial\psi} + (\mathcal{L}^e_{41} + \mathcal{L}^e_{42})\frac{\partial \ln T_e}{\partial\psi} + \mathcal{L}^e_{41}\frac{1-R_{pe}}{R_{pe}}\frac{\partial \ln n_i}{\partial\psi} + \mathcal{L}^e_{43}\frac{\langle E_{\|}B\rangle}{\langle B^2\rangle}\right] + \\
&+ \left(\mathcal{L}^i_{22} + \frac{1-R_{pe}}{R_{pe}}\frac{\alpha^2}{Z_i}\mathcal{L}^e_{44}\right)\frac{\partial \ln T_i}{\partial\psi}, && \text{(2.40c)}
\end{aligned}$$

where $R_{pe} \doteq p_e/p$ and Z_i is the main ion charge number. The perpendicular transport coefficients $\mathcal{L}^\sigma_{mn}$, for general axisymmetric equilibria and arbitrary collisionality regime, are given by Eqs. (2.37a) of subsection 2.4.3 in terms of the trapped fractions f_t or f_t^d, Eq. (2.21), the collisionality parameter ν_* and the effective charge number Z. The neoclassical conductivity and the bootstrap current coefficients, $\mathcal{L}^e_{3n}$ and α, are given by Eqs. (2.26cfh), (2.27cefg), (2.28) and by Eqs. (2.33), (2.35).

2.6 Appendix

Linearized Coulomb collision operator of $\gamma_{\sigma 2} f_M$

In Eqs. (2.8) we have shown that the linearized Coulomb collision operator applied to the functions $\gamma_{\sigma n}$ can always be computed analytically. This is a well-known and almost straightforward result for functions $\gamma_{\sigma n}$, $n \neq 2$. On the contrary, for $n = 2$, Eqs. (2.8b) and (2.8e), this is a somewhat unknown result, presented for the first time in Ref. [14], but whose derivation, which is far from being trivial, has never been presented before. The complexity of the derivation comes from the calculation of the like–particle collision operator of the function $\gamma_{\sigma 2}$, namely $C^l_{\sigma\sigma}(\gamma_{\sigma 2} f_M)$. Note that this is also a useful result, since it is crucial for developments in neoclassical theory similar to the one presented in this Chapter. For this reason we have performed independently this analytical calculation and we present the details in this Appendix. This also provides a pedagogical example of a calculation of the Coulomb collision operator, which is in general not frequent in the literature.

We start reminding the definition of the linearized collision operator for like–particle collisions of species σ

$$C^l_{\sigma\sigma}(f_1) = C_{\sigma\sigma}(f_{\sigma 0}, f_{\sigma 1}) + C_{\sigma\sigma}(f_{\sigma 1}, f_{\sigma 0}), \tag{2.41}$$

where $f_{\sigma 0} = f_M$ is the Maxwellian distribution function and $f_{\sigma 1}$ is the first order perturbation in the Larmor radius expansion. In our specific application, the expression of $f_{\sigma 1}$ reads

$$f_{\sigma 1} = v_\| \left(\frac{v^2}{v^2_{T\sigma}} - \frac{5}{2} \right) \frac{I}{\Omega} f_{\sigma 0}$$

Let us introduce the dimensionless function $\beta = u_\| \, (u^2 - 5/2)$, with $\mathbf{u} = \mathbf{v}/v_{T\sigma}$. Therefore, the goal is to compute

$$C^l_{\sigma\sigma}(\beta f_M) = C_{\sigma\sigma}(f_M, \beta f_M) + C_{\sigma\sigma}(\beta f_M, f_M) \tag{2.42}$$

A very useful expression for the Coulomb collision operator is the one derived by Rosenbluth, MacDonald and Judd [34], which can be written, for like–particle collisions, in the following form

$$C_{\sigma\sigma}(f, g) = \frac{\gamma_{\sigma\sigma}}{2m_\sigma} \left[\frac{\partial^2}{\partial v_\alpha v_\beta} \left(f \frac{\partial^2 \mathcal{G}(g)}{\partial v_\alpha v_\beta} \right) - 4 \frac{\partial}{\partial v_\alpha} \left(f \frac{\partial \mathcal{H}(g)}{\partial v_\alpha} \right) \right], \tag{2.43}$$

where $\gamma_{\sigma\sigma} = 4\pi e^4_\sigma \ln\Lambda \,/\, m_\sigma$. The functionals $\mathcal{G}(g)$ and $\mathcal{H}(g)$ are usually known as Rosenbluth potentials and defined as follows

$$\mathcal{G}(g) = G(\mathbf{v}) \doteq \int_{\Re_3} \mathrm{d}\mathbf{v}' \; g(\mathbf{v}) \, |\mathbf{v} - \mathbf{v}'|,$$

$$\mathcal{H}(g) = H(\mathrm{v}) \doteq \int_{\Re_3} \mathrm{d}\mathrm{v}' \, \frac{g(\mathrm{v})}{|\mathrm{v} - \mathrm{v}'|},$$

where the integrals are extended to the full velocity space $\Re_3$. In Eq. (2.43) the standard notation assuming summation over any repeated index has been adopted. Note that in cartesian coordinates no distinction between covariant and controvariant components needs to be made. The Rosenbluth potentials for a maxwellian function

$$f_M = \frac{n_\sigma}{\pi\sqrt{\pi}\, v_{T\sigma}^3} \, e^{-u^2}$$

and for the function βf_M will be derived at the end of this Appendix

$$\begin{aligned}
\mathcal{G}(f_M) = G_M(\mathrm{v}) &= \frac{n_\sigma \, v_{T\sigma}}{2} \left[\mathrm{erf}'(u) + \left(\frac{1}{u} + 2u \right) \mathrm{erf}(u) \right], \\
\mathcal{H}(f_M) = H_M(\mathrm{v}) &= \frac{n_\sigma}{v_{T\sigma}} \left(\frac{\mathrm{erf}(u)}{u} \right), \\
\mathcal{G}(\beta f_M) = G_1(\mathrm{v}) &= n_\sigma \, v_{T\sigma} \, u_\| \left[\frac{1}{4u^2} \left(\frac{\mathrm{erf}(u)}{u} - \mathrm{erf}'(u) \right) \right], && \text{(2.44a)} \\
\mathcal{H}(\beta f_M) = H_1(\mathrm{v}) &= \frac{n_\sigma}{v_{T\sigma}} u_\| \left(-\frac{\mathrm{erf}'(u)}{2} \right), && \text{(2.44b)}
\end{aligned}$$

where erf(u) is the error function.

$C_{\sigma\sigma}(\beta f_M, f_M)$

We start from the term involving the maxwellian Rosenbluth potentials, namely the term $C_{\sigma\sigma}(\beta f_M, f_M)$ in Eq. (2.42),

$$C_{\sigma\sigma}(\beta f_M, f_M) = \frac{\gamma_{\sigma\sigma}}{2m_\sigma} \left[\frac{\partial^2}{\partial v_\alpha v_\beta} \left(\beta f_M \frac{\partial^2 G_M}{\partial v_\alpha v_\beta} \right) - 4 \frac{\partial}{\partial v_\alpha} \left(\beta f_M \frac{\partial H_M}{\partial v_\alpha} \right) \right].$$

We begin considering the part involving G_M,

$$\frac{\partial G_M}{\partial v_\beta} = n_\sigma \left(\frac{u_\beta}{u} \frac{\mathrm{d} g_M}{\mathrm{d}u} \right)$$

where we have introduced the function g_M as follows

$$G_M = n_\sigma \, v_{T\sigma} g_M, \quad g_M(u) = \frac{\mathrm{erf}'(u)}{2} + \left(\frac{1}{2u} + u \right) \mathrm{erf}(u).$$

$$\frac{\partial^2 G_M}{\partial v_\alpha \partial v_\beta} = \frac{n_\sigma}{v_{T\sigma}} \left\{ \delta_{\alpha\beta} \frac{1}{u} \frac{\mathrm{d} g_M}{\mathrm{d}u} + u_\alpha u_\beta \left[\frac{1}{u} \frac{\mathrm{d}}{\mathrm{d}u} \left(\frac{1}{u} \frac{\mathrm{d} g_M}{\mathrm{d}u} \right) \right] \right\},$$

where $\delta_{\alpha\beta}$ is the Kroenecker delta. Developing the calculation one obtains

$$\beta f_M \frac{\partial^2 G_M}{\partial v_\alpha \partial v_\beta} = \frac{n_\sigma^2}{\pi\sqrt{\pi}\, v_{T\sigma}^4} \left(\delta_{\alpha\beta} \, u_3 K_a(u) + u_\alpha u_\beta u_3 K_b(u) \right)$$

where we have aligned the third cartesian coordinate along the magnetic field, $u_{\|} \equiv u_3$, and we have introduced the two functions

$$K_a(u) = \left(u^2 - \frac{5}{2}\right) \frac{1}{u} \frac{\mathrm{d}g_M}{\mathrm{d}u} e^{-u^2}, \qquad K_b(u) = \left(u^2 - \frac{5}{2}\right) \frac{1}{u} \frac{\mathrm{d}}{\mathrm{d}u} \left(\frac{1}{u} \frac{\mathrm{d}g_M}{\mathrm{d}u}\right) e^{-u^2}.$$

Then we compute

$$\frac{\partial}{\partial v_\beta} \left(\beta f_M \frac{\partial^2 G_M}{\partial v_\alpha \partial v_\beta}\right) = \frac{n_\sigma^2}{\pi \sqrt{\pi}\, v_{T\sigma}^5} \left(\delta_{\alpha 3} K_a(u) + u_\alpha u_3 K_c(u)\right)$$

where we have introduced the function

$$K_c(u) = \frac{1}{u} \frac{\mathrm{d}K_a}{\mathrm{d}u} + 5K_b + u\frac{\mathrm{d}K_b}{\mathrm{d}u}.$$

At this point we can take the divergence on the last index α

$$\begin{aligned} &\frac{\partial^2}{\partial v_\alpha \partial v_\beta} \left(\beta f_M \frac{\partial^2 G_M}{\partial v_\alpha \partial v_\beta}\right) = \\ &= \frac{n_\sigma^2}{\pi \sqrt{\pi}\, v_{T\sigma}^6} \left(\delta_{\alpha 3} \frac{u_\alpha}{u} \frac{\mathrm{d}K_a}{\mathrm{d}u} + 3u_3 K_c + u_\alpha \delta_{\alpha 3} K_c + u_\alpha u_3 \frac{u_\alpha}{u} \frac{\mathrm{d}K_c}{\mathrm{d}u}\right) = \\ &= \frac{n_\sigma^2}{\pi \sqrt{\pi}\, v_{T\sigma}^6} u_{\|} \left(\frac{1}{u} \frac{\mathrm{d}K_a}{\mathrm{d}u} + 4K_c + u\frac{\mathrm{d}K_c}{\mathrm{d}u}\right). \end{aligned} \tag{2.45}$$

We pass now to the term in $C_{\sigma\sigma}(\beta f_M, f_M)$ involving H_M.

$$\frac{\partial H_M}{\partial v_\alpha} = \frac{n_\sigma}{v_{T\sigma}^2} \frac{u_\alpha}{u} \frac{\mathrm{d}h_M}{\mathrm{d}u}$$

where analogously we have introduced the function h_M as follows

$$H_M = \frac{n_\sigma}{v_{T\sigma}} h_M, \qquad h_M(u) = \frac{\mathrm{erf}(u)}{u}.$$

Then we have

$$\frac{\partial}{\partial v_\alpha} \beta f_M \frac{\partial H_M}{\partial v_\alpha} = \frac{n_\sigma^2}{\pi \sqrt{\pi}\, v_{T\sigma}^6} u_{\|} \left(4L_a + u\frac{\mathrm{d}L_a}{\mathrm{d}u}\right), \tag{2.46}$$

where the function $L_a(u)$ is given by

$$L_a(u) = \left(u^2 - \frac{5}{2}\right) \frac{1}{u} \frac{\mathrm{d}h_M}{\mathrm{d}u} e^{-u^2}.$$

Combining the G_M and H_M contributions, Eqs. (2.45) and (2.46) respectively, we find

$$C_{\sigma\sigma}(\beta f_M, f_M) = \frac{\gamma_{\sigma\sigma}}{2m_\sigma} \left\{ \frac{n_\sigma^2}{\pi \sqrt{\pi}\, v_{T\sigma}^6} u_{\|} \left[\left(\frac{1}{u} \frac{\mathrm{d}K_a}{\mathrm{d}u} + 4K_c + u\frac{\mathrm{d}K_c}{\mathrm{d}u}\right) - 4\left(4L_a + u\frac{\mathrm{d}L_a}{\mathrm{d}u}\right)\right]\right\}$$

Performing all the long but not complex derivations on u, one finally finds

$$C_{\sigma\sigma}(\beta f_M, f_M) = \nu_{\sigma 0}(v)\, f_M\, u_{\|} \, \left[(7 - 4u^2)\,\mathrm{erf}(u) - 2(7 - 6u^2)\, u\, \mathrm{erf}'(u)\right], \tag{2.47}$$

where we remind that $\nu_{\sigma 0}(v) = n_\sigma \gamma_{\sigma\sigma} \, / \, (m_\sigma v^3)$.

$C_{\sigma\sigma}(f_M, \beta f_M)$

Now we compute the term involving the Rosenbluth potentials G_1 and H_1 of the first order perturbation βf_M, namely $C_{\sigma\sigma}(f_M, \beta f_M)$ in Eq. (2.42).

$$C_{\sigma\sigma}(f_M, \beta f_M) = \frac{\gamma_{\sigma\sigma}}{2m_\sigma}\left[\frac{\partial^2}{\partial v_\alpha v_\beta}\left(F_M \frac{\partial^2 G_1}{\partial v_\alpha v_\beta}\right) - 4\frac{\partial}{\partial v_\alpha}\left(f_M \frac{\partial H_1}{\partial v_\alpha}\right)\right].$$

From Eqs. (2.44b) and (2.44b), we introduce the functions $g_1(u)$ and $h_1(u)$ as follows

$$\begin{aligned} G_1(u) &= n_\sigma \, v_{T\sigma} \, u_\parallel \, g_1(u), & g_1(u) &= \frac{1}{4\,u^2}\left(\frac{\mathrm{erf}(u)}{u} - \mathrm{erf}'(u)\right), \\ H_1(u) &= \frac{n_\sigma}{v_{T\sigma}} u_\parallel \, h_1(u), & h_1(u) &= -\frac{\mathrm{erf}'(u)}{2}, \end{aligned} \tag{2.48}$$

As usual, we compute first

$$\begin{aligned} \frac{\partial^2 G_1}{\partial v_\alpha \partial v_\beta} &= \frac{n_\sigma}{v_{T\sigma}} \frac{\partial}{\partial u_\alpha}\left[\frac{\partial}{\partial u_\beta}\left(u_3 \, g_1(u)\right)\right] = \\ &= \frac{n_\sigma}{v_{T\sigma}} \frac{\partial}{\partial u_\alpha}\left(\delta_{\beta 3} g_1(u) + \frac{u_3 u_\beta}{u}\frac{\mathrm{d}g_1}{\mathrm{d}u}\right) = \\ &= \frac{n_\sigma}{v_{T\sigma}}\left[\left(u_\alpha \delta_{\beta 3} + u_\beta \delta_{\alpha 3} + u_3 \delta_{\alpha\beta}\right)\frac{1}{u}\frac{\mathrm{d}g_1}{\mathrm{d}u} + u_\alpha \, u_\beta \, u_3 \frac{1}{u}\frac{\mathrm{d}}{\mathrm{d}u}\left(\frac{1}{u}\frac{\mathrm{d}g_1}{\mathrm{d}u}\right)\right]. \end{aligned}$$

Therefore we obtain

$$f_M \frac{\partial^2 G_1}{\partial v_\alpha \partial v_\beta} = \frac{n_\sigma^2}{\pi\sqrt{\pi} v_{T\sigma}^4}\left[\left(u_\alpha \delta_{\beta 3} + u_\beta \delta_{\alpha 3} + u_3 \delta_{\alpha\beta}\right) M_a + u_\alpha \, u_\beta \, u_3 M_b\right]$$

where we have introduced the functions $M_a(u)$ and $M_b(u)$ as follows

$$M_a(u) = \frac{1}{u}\frac{\mathrm{d}g_1}{\mathrm{d}u}\, e^{-u^2}, \qquad M_b(u) = \frac{\mathrm{d}}{\mathrm{d}u}\left(\frac{1}{u}\frac{\mathrm{d}g_1}{\mathrm{d}u}\right)\, e^{-u^2}$$

We now take the divergence on the index β,

$$\begin{aligned} &\frac{\partial}{\partial v_\beta}\left(f_M \frac{\partial^2 G_1}{\partial v_\alpha \partial v_\beta}\right) = \\ &= \frac{n_\sigma^2}{\pi\sqrt{\pi} v_{T\sigma}^5}\left[5\,\delta_{\alpha 3}\, M_a + \left(2\, u_\alpha u_3 + u^2\, \delta_{\alpha 3}\right)\frac{1}{u}\frac{\mathrm{d}M_a}{\mathrm{d}u} + 5\, u_\alpha u_3 M_b + u_\alpha u_3 u \frac{\mathrm{d}M_b}{\mathrm{d}u}\right] = \\ &= \frac{n_\sigma^2}{\pi\sqrt{\pi} v_{T\sigma}^5}\left(\delta_{\alpha 3}\, M_c + u_\alpha u_3\, M_d\right), \end{aligned}$$

where the functions $M_c(u)$ and $M_d(u)$ are given by

$$M_c(u) = 5\, M_a(u) + u\frac{\mathrm{d}M_a}{\mathrm{d}u}, \qquad M_d(u) = \frac{2}{u}\frac{\mathrm{d}M_a}{\mathrm{d}u} + 5\, M_b + u\,\frac{\mathrm{d}M_b}{\mathrm{d}u}.$$

The derivative on index α then yields

$$
\begin{aligned}
&\frac{\partial^2}{\partial v_\alpha \partial v_\beta}\left(f_M \frac{\partial^2 G_1}{\partial v_\alpha \partial v_\beta}\right) = \\
&= \frac{n_\sigma^2}{\pi\sqrt{\pi} v_{T\sigma}^6}\left(\delta_{\alpha 3}\frac{u_\alpha}{u}\frac{\mathrm{d}M_c}{\mathrm{d}u} + 3\,u_3\,M_d + u_\alpha \delta_{\alpha 3}\,M_d + u_\alpha u_3 \frac{u_\alpha}{u}\frac{\mathrm{d}M_d}{\mathrm{d}u}\right) = \\
&= \frac{n_\sigma^2}{\pi\sqrt{\pi} v_{T\sigma}^6}\left(\frac{1}{u}\frac{\mathrm{d}M_c}{\mathrm{d}u} + 4\,M_d + u\,\frac{\mathrm{d}M_d}{\mathrm{d}u}\right). \qquad (2.49)
\end{aligned}
$$

We now consider the term involving H_1,

$$
\frac{\partial H_1}{\partial v_\alpha} = \frac{n_\sigma}{v_{T\sigma}^2}\left(\delta_{\alpha 3} h_1 + \frac{u_\alpha u_3}{u}\frac{\mathrm{d}h_1}{\mathrm{d}u}\right).
$$

Therefore

$$
\frac{\partial}{\partial v_\alpha}\left(f_M \frac{\partial H_1}{\partial v_\alpha}\right) = \frac{n_\sigma^2}{\pi\sqrt{\pi} v_{T\sigma}^6}\frac{\partial}{\partial u_\alpha}\left(\delta_{\alpha 3}\,N_a + u_\alpha u_3\,N_b\right),
$$

where we have introduced the functions $N_a(u)$ and $N_b(u)$ as follows

$$
N_a(u) = h_1\,e^{-u^2}, \qquad N_b(u) = \frac{1}{u}\frac{\mathrm{d}h_1}{\mathrm{d}u}\,e^{-u^2},
$$

Derivating on index α, we obtain

$$
\frac{\partial}{\partial v_\alpha}\left(f_M \frac{\partial H_1}{\partial v_\alpha}\right) = \frac{n_\sigma^2}{\pi\sqrt{\pi} v_{T\sigma}^6}\,u_\parallel\left(\frac{1}{u}\frac{\mathrm{d}N_a}{\mathrm{d}u} + 4\,N_b + u\,\frac{\mathrm{d}N_b}{\mathrm{d}u}\right). \qquad (2.50)
$$

Combining the G_1 and H_1 contributions, Eqs. (2.49) and (2.50) respectively, we find

$$
\begin{aligned}
&C_{\sigma\sigma}(f_M, \beta f_M) = \qquad (2.51) \\
&= \frac{\gamma_{\sigma\sigma}}{2m_\sigma}\left\{\frac{n_\sigma^2}{\pi\sqrt{\pi} v_{T\sigma}^6} u_\parallel\left[\left(\frac{1}{u}\frac{\mathrm{d}M_c}{\mathrm{d}u} + 4\,M_d + u\,\frac{\mathrm{d}M_d}{\mathrm{d}u}\right) + -4\left(\frac{1}{u}\frac{\mathrm{d}N_a}{\mathrm{d}u} + 4\,N_b + u\,\frac{\mathrm{d}N_b}{\mathrm{d}u}\right)\right]\right\}.
\end{aligned}
$$

Performing all the long but not complex derivations on u, one finally finds

$$
C_{\sigma\sigma}(f_M, \beta f_M) = \nu_{\sigma 0}(v)\,f_M\,u_\parallel\,3\,\left[\mathrm{erf}(u) - u\,\left(1 + 2\,u^2\right)\,\mathrm{erf}'(u)\right]. \qquad (2.52)
$$

Combining Eqs. (2.47) and (2.52), one obtains

$$
C_{\sigma\sigma}^l(f_1) = \nu_{\sigma 0}(v)\,f_M\,u_\parallel\,\frac{1}{u}\,\left[\left(10 - 4\,u^2\right)\,\mathrm{erf}(u) - 10\,u\,\mathrm{erf}'(u)\right]
$$

which is the result we are looking for, as reported in Eqs. (2.8b) and (2.8e).

Rosenbluth Potentials

$\mathbf{G_M}$

$$\begin{aligned} G_M &= \int_{\Re 3} \mathrm{d}\mathbf{v}' \, |\mathbf{v}-\mathbf{v}'| \, f_M(\mathbf{v}') = \\ &= \frac{n_\sigma \, v_{T\sigma}}{\pi\sqrt{\pi}} \int_0^\infty u'^2 \mathrm{d}u' \int_{-1}^{1} \mathrm{d}(cos\theta') \int_0^{2\pi} \mathrm{d}\phi' \, |\mathbf{u}-\mathbf{u}'| \, e^{-u^2} \end{aligned} \tag{2.53}$$

We call χ the angle between $\mathbf{u}$ and $\mathbf{u}'$. Expanding in Legendre polynomials, the distance $|\mathbf{u}-\mathbf{u}'|$ can be written as follows

$$|\mathbf{u}-\mathbf{u}'| = -\sum_{l=0}^{\infty} \frac{u_<^l}{u_>^{l-1}} \left(1 - \frac{l-1/2}{l+3/2}\frac{u_<^2}{u_>^2}\right) \frac{P_l(cos\chi)}{2l-1},$$

where $u_< = \min(u, u')$ and $u_> = \max(u, u')$. We now use the standard expansion of the Legendre polynomials $P_l(\cos\chi)$ in spherical harmonics Y_{lm}, which yields

$$|\mathbf{u}-\mathbf{u}'| = -\sum_{l=0}^{\infty} \sum_{m=-l}^{l} \frac{u_<^l}{u_>^{l-1}} \left(1 - \frac{l-1/2}{l+3/2}\frac{u_<^2}{u_>^2}\right) \frac{4\pi}{2l-1} Y_{lm}^*(\theta,\phi) Y_{lm}(\theta',\phi').$$

Therefore

$$\begin{aligned} G_M &= \frac{n_\sigma \, v_{T\sigma}}{\pi\sqrt{\pi}} \int_0^\infty u'^2 \mathrm{d}u' \Bigg[-u'^2 e^{-u'^2} \sum_{l=0}^{\infty} \sum_{m=-l}^{l} \frac{u_<^l}{u_>^{l-1}} \left(1 - \frac{l-1/2}{l+3/2}\frac{u_<^2}{u_>^2}\right) \\ & \frac{4\pi}{2l-1} Y_{lm}^*(\theta,\phi) \int_{-1}^{1} \mathrm{d}(\cos\theta') \int_0^{2\pi} \mathrm{d}\phi' Y_{lm}(\theta',\phi') \Bigg]. \end{aligned}$$

We can now use the orthogonality of the spherical harmonic functions, which gives

$$\int_{-1}^{1} \mathrm{d}(\cos\theta') \int_0^{2\pi} \mathrm{d}\phi' Y_{lm}(\theta',\phi') = \delta_{l0}\, \delta_{m0}\, 2\sqrt{\pi},$$

and we remind that

$$2\sqrt{\pi}\, Y_{00} = 1$$

Hence we find

$$\begin{aligned} G_M &= \frac{n_\sigma \, v_{T\sigma}}{\pi\sqrt{\pi}} 4\pi \int_0^\infty \mathrm{d}u' \, u'^2 e^{-u'^2} \left[u_> \left(1 + \frac{1}{3}\frac{u_<^2}{u_>^2}\right)\right] = \\ &= \frac{4n\, v_{T\sigma}}{\sqrt{\pi}} \left[\int_0^u \mathrm{d}u' u'^2 e^{-u'^2} u \left(1 + \frac{1}{3}\frac{u'^2}{u^2}\right) + \int_u^\infty \mathrm{d}u' u'^3 e^{-u'^2} \left(1 + \frac{1}{3}\frac{u^2}{u'^2}\right)\right] = \\ &= \frac{n_\sigma \, v_{T\sigma}}{2u} \left[\left(2u^2+1\right) \mathrm{erf}(u) + u\, \mathrm{erf}'(u) \right] \end{aligned}$$

$\mathbf{H_M}$

$$\begin{aligned} H_M &= \int_{\Re 3} \mathrm{d}\mathbf{v}' \, \frac{f_M(\mathbf{v}')}{|\mathbf{v}-\mathbf{v}'|} = \\ &= \frac{n_\sigma}{\pi\sqrt{\pi}\, v_{T\sigma}} \int_0^\infty u'^2 \, \mathrm{d}u' \int_{-1}^{1} \mathrm{d}(\cos\theta') \int_0^{2\pi} \mathrm{d}\phi' \frac{e^{-u^2}}{|\mathbf{u}-\mathbf{u}'|} \end{aligned} \tag{2.54}$$

We use the well–known expansion usually adopted in order to compute the electrostatic potential of a space distribution of electric charges

$$\frac{1}{|\mathbf{u}-\mathbf{u}'|} = \sum_{l=0}^{\infty} \frac{u_<^l}{u_>^{l+1}} P_l(\cos\chi) = \sum_{l=0}^{\infty} \sum_{m=-l}^{l} \frac{u_<^l}{u_>^{l+1}} \frac{4\pi}{2l+1} Y^*_{lm}(\theta,\phi)\, Y_{lm}(\theta',\phi').$$

Therefore

$$\begin{aligned} H_M &= \frac{n_\sigma}{\pi\sqrt{\pi}\, v_{T\sigma}} \int_0^\infty \mathrm{d}u' \left[u'^2 e^{-u'^2} \sum_{l=0}^{\infty} \sum_{m=-l}^{l} \frac{u_<^l}{u_>^{l+1}} \right. \\ &\qquad \left. \frac{4\pi}{2l+1} Y^*_{lm}(\theta,\phi) \left(\int_{-1}^{1} \mathrm{d}(\cos\theta') \int_0^{2\pi} \mathrm{d}\phi' \, Y_{lm}(\theta',\phi') \right) \right] = \\ &= \frac{n_\sigma}{\pi\sqrt{\pi}\, v_{T\sigma}} 4\pi \int_0^\infty \mathrm{d}u' u'^2 \, e^{-u'^2} \, \frac{u_<}{u_>} = \\ &= \frac{n_\sigma}{\pi\sqrt{\pi}\, v_{T\sigma}} 4\pi \left(\int_0^u \mathrm{d}u' \, \frac{u'^3}{u} e^{-u'^2} + u \int_u^\infty \mathrm{d}u' \, u' \, e^{-u'^2} \right) = \\ &= \frac{n_\sigma}{v_{T\sigma}} \frac{\mathrm{erf}(u)}{u} \end{aligned}$$

We now consider the Rosenbluth potentials of the function $\beta\, f_M$.

$\mathbf{G_1}$

$$\begin{aligned} G_1 &= \int_{\Re 3} \mathrm{d}\mathbf{v}' \, u'_{\|} \left(u'^2 - \frac{5}{2} \right) |\mathbf{v}-\mathbf{v}'| \, f_M(\mathbf{v}') = \\ &= \frac{n_\sigma \, v_{T\sigma}}{\pi\sqrt{\pi}} \int_0^\infty u'^2 \, \mathrm{d}u' \, u' \left(u'^2 - \frac{5}{2} \right) e^{-u^2} \int_{-1}^{1} \mathrm{d}(\cos\theta') \cos\theta' \int_0^{2\pi} \mathrm{d}\phi' |\mathbf{u}-\mathbf{u}'| \end{aligned}$$

Adopting the development in spherical harmonics for $|\mathbf{u}-\mathbf{u}'|$,

$$\begin{aligned} G_1 &= \frac{n_\sigma \, v_{T\sigma}}{\pi\sqrt{\pi}} \int_0^\infty \mathrm{d}u' \, u'^3 \left(u'^2 - \frac{5}{2} \right) e^{-u^2} \left[-\sum_{l=0}^{\infty} \sum_{m=-l}^{l} \frac{u_<^l}{u_>^{l-1}} \left(1 - \frac{l-1/2}{l+3/2} \frac{u_<^2}{u_>^2} \right) \right. \\ &\qquad \left. \frac{4\pi}{2l-1} \int_{-1}^{1} \mathrm{d}(\cos\theta') \cos\theta' \int_0^{2\pi} \mathrm{d}\phi' Y^*_{lm}(\theta,\phi)\, Y_{lm}(\theta',\phi') \right]. \end{aligned}$$

We remind that

$$\sqrt{\frac{4\pi}{3}}Y_{10}(\theta,\phi) = \cos\theta$$

and therefore

$$\int_{-1}^{1} \mathrm{d}(\cos\theta') \int_0^{2\pi} \mathrm{d}\phi' \, \cos\theta' \, Y_{lm}(\theta',\phi') = \delta_{l1}\,\delta_{m0}\sqrt{\frac{4\pi}{3}}.$$

This gives

$$\begin{aligned}
G_1 &= -\frac{n_\sigma\, v_{T\sigma}}{\pi\sqrt{\pi}}\,\frac{4\pi}{3}\cos\theta\int_0^\infty \mathrm{d}u'\left[u'^3\left(u'^2-\frac{5}{2}\right)e^{-u^2}\,u_<\left(1-\frac{1}{5}\frac{u_<^2}{u_>^2}\right)\right] = \\
&= -\frac{n_\sigma\, v_{T\sigma}}{\pi\sqrt{\pi}}\,\frac{4\pi}{3}\,\frac{u_\|}{u}\int_0^u \mathrm{d}u'\left[u'^4\left(u'^2-\frac{5}{2}\right)\left(1-\frac{1}{5}\frac{u'^2}{u^2}\right)e^{-u^2}+\right. \\
&\quad \left. +\, u\int_u^\infty \mathrm{d}u'\mathrm{d}u'u'^3\left(u'^2-\frac{5}{2}\right)\left(1-\frac{1}{5}\frac{u^2}{u'^2}\right)e^{-u^2}\right] = \\
&= n_\sigma\, v_{T\sigma}\, u_\|\,\frac{1}{4\,u^2}\left(\frac{\mathrm{erf}(u)}{u}-\mathrm{erf}'(u)\right).
\end{aligned}$$

$\mathbf{H}_1$

$$\begin{aligned}
H_1 &= \int_{\Re3}\mathrm{d}\mathbf{v}'\,u'_\|\left(u'^2-\frac{5}{2}\right)\frac{f_M(\mathbf{v}')}{|\mathbf{v}-\mathbf{v}'|} = \\
&= \frac{n_\sigma\, v_{T\sigma}}{\pi\sqrt{\pi}}\int_0^\infty u'^2\,\mathrm{d}u'\,u'\left(u'^2-\frac{5}{2}\right)e^{-u^2}\int_{-1}^{1}\mathrm{d}(\cos\theta')\cos\theta'\int_0^{2\pi}\mathrm{d}\phi'\frac{1}{|\mathbf{u}-\mathbf{u}'|}
\end{aligned}$$

Adopting the development for $1/|\mathbf{u}-\mathbf{u}'|$, we find

$$\begin{aligned}
H_1 = \frac{n_\sigma}{\pi\sqrt{\pi}\,v_{T\sigma}}\int_0^\infty \mathrm{d}u'&\left[u'^3\left(u'^2-\frac{5}{2}\right)e^{-u'^2}\sum_{l=0}^{\infty}\sum_{m=-l} l\,\frac{u_<^l}{u_>^{l+1}}\right. \\
&\left.\frac{4\pi}{2l+1}Y_{lm}^*(\theta,\phi)\left(\int_{-1}^{1}\mathrm{d}(\cos\theta')\cos\theta'\int_0^{2\pi}\mathrm{d}\phi'\,Y_{lm}(\theta',\phi')\right)\right],
\end{aligned}$$

and the orthogonality of the spherical harmonics gives

$$\begin{aligned}
H_1 &= \frac{n_\sigma}{\pi\sqrt{\pi}\,v_{T\sigma}}\,\frac{4\pi}{3}\cos\theta\int_0^\infty \mathrm{d}u'u'^3\left(u'^2-\frac{5}{2}\right)\frac{u_<}{u_>^2}e^{-u'^2} = \\
&= \frac{n_\sigma}{\sqrt{\pi}\,v_{T\sigma}}\,\frac{4}{3}\,\frac{u_\|}{u}\left(\frac{1}{u^2}\int_0^u \mathrm{d}u'\frac{u'^4}{u}\left(u'^2-\frac{5}{2}\right)e^{-u'^2}+u\int_u^\infty \mathrm{d}u'\,u'\left(u'^2-\frac{5}{2}\right)e^{-u'^2}\right) = \\
&= \frac{n_\sigma}{v_{T\sigma}}\,u_\|\left(-\frac{\mathrm{erf}'(u)}{2}\right).
\end{aligned}$$

Bibliography

[1] A. A. Galeev and R. Z. Sagdeev, Soviet Physics JETP **26**, 233 (1968).

[2] S. I. Braginskii, *Reviews of Plasma Physics*, ed. by M.A. Leontovich (Consultants Bureau, New York), Vol. 1, p. 205 (1965).

[3] A.G. Peeters, Plasma Phys. Control. Fusion **42**, B231 (2000).

[4] F. L. Hinton and R. D. Hazeltine, Rev. Mod. Phys. **48**, 239 (1976).

[5] S. P. Hirshman, Phys. Fluids **31**, 3150 (1988).

[6] G. R. Harris, Rep. EUR-CEA-FC-1436, Dèpart. Rech. Fusion Contr., Centre d'ètudes de Cadarache, Saint-Paul-lez-Durance (1991).

[7] C. E. Kessel, Nucl. Fusion **34**, 1221 (1994).

[8] W. A. Houlberg, K. C. Shaing, S. P. Hirshman, and M. C. Zarnstorff, Phys. Plasmas **4**, 3230 (1997).

[9] S. P. Hirshman and D. J. Sigmar, Nucl. Fusion **21**, 1079 (1981).

[10] C. S. Chang and F. L. Hinton, Phys. Fluids **25**, 1493 (1982).

[11] M. Taguchi, Phys. Contr. Fus. **30**, 1897 (1988).

[12] C. Bolton and A. A. Ware, Phys. Fluids **26**, 459 (1983).

[13] S. P. Hirshman and D. J. Sigmar, Phys. Fluids **19**, 1532 (1976).

[14] Y. R. Lin-Liu, F. L. Hinton, C. F.F. Karney and S. P. Hirshman, International Sherwood Theory Conference, Dallas, Texas (1994), paper 3C37.

[15] O. Sauter, C. Angioni and Y. R. Lin-Liu, Phys. Plasmas **6**, 2834 (1999).

[16] O. Sauter *et al*, Contrib. Plasma Physics **34**, 169 (1994).

[17] O. Sauter *et al*, in Proc. of the Theory of Fusion Plasmas workshop, Varenna 1994, Editrice Compositori E. Sindoni, Bologna (1994), p. 337.

[18] R. D. Hazeltine, F. L. Hinton and M. N. Rosenbluth, Phys. Fluids **16**, 1645 (1973).

[19] M. N. Rosenbluth, R. D. Hazeltine and F. L. Hinton, Phys. Fluids **15**, 116 (1972).

[20] C. Angioni and O. Sauter, Phys. Plasmas **7**, 1224 (2000).

[21] R. W. Harvey and M. G. McCoy, in Proceedings of International Atomic Energy Agency Technical Committee Meeting on Advances in Simulation and Modeling of Thermonuclear Plasmas, Montreal, 1992 (International Atomic Energy Agency, Vienna, 1993), pp.489-526;
J. Killeen, G. D. Kerbel, M.G. McCoy, A. A. Mirin, *Computational Methods for Kinetic Models of Magnetically Confined Plasmas*, Springer-Verlag, New York 1986.

[22] L. Spitzer, R. Härm, Phys. Rev. **89**, 977 (1953).

[23] A.A. Ware, Phys. Rev. Lett. **25**, 916 (1970).

[24] A.A. Galeev, Soviet Physics JETP **32**, 752 (1971).

[25] R.J. Bickerton, J.W. Connor, and J.B. Taylor, Nat. Phys. Sci. **229**, 110 (1971).

[26] L. Onsager, Phys. Rev **38**, 2265 (1931).

[27] C. F. F. Karney *et al*, in Proc. 8th Top. Conf. on RF Power in Plasma, Irvine (1989) (AIP), p. 430.

[28] P. H. Rutherford, Phys. Fluids **13**, 482 (1970).

[29] Y. R. Lin-Liu and R. L. Miller, Phys. Plasmas **2**, 1666 (1995).

[30] C. S. Chang and F. L. Hinton, Phys. Fluids **29**, 1493 (1986).

[31] S. P. Hirshman, Phys. Fluids **19**, 155 (1976).

[32] F. L. Hinton and M. N. Rosenbluth, Phys. Fluids **16**, 836 (1973).

[33] J. M. Rawls, M. S. Chu and F. L. Hinton, Phys. Fluids **18**, 1160 (1975).

[34] M. N. Rosenbluth, W. MacDonald, D.J. Judd, Phys. Review **107**, 1 (1957).

Chapter 3

1-1/2 D simulation of a tokamak plasma

Transport in tokamak plasmas is commonly described adopting the standard paradigm of local diffusion. Macroscopic quantities like temperatures and densities solve continuity equations directly derived as velocity moments of the Boltzmann–Vlasov kinetic equation. Particle and heat fluxes occuring in the fluid equations are assumed proportional to the gradients of macroscopic quantities like densities and temperatures, by means of diffusion (transport) coefficients. The previous chapter has shown a specific application in this framework. Kinetic calculations undertaken assuming the so–called drift–ordering for a magnetized plasma allowed us to compute transport coefficients resulting from collisional processes affecting guiding centre orbits caused by the axisymmetric magnetic confinement system. Due to the orderings assumed in the model, other transport phenomena, which are nevertheless present in the plasma, have not been taken into account. For instance the basic classical collisional transport, due to collisions affecting the Larmor gyromotion, is not included in the solution of the drift–kinetic equations, since the effects of collisions on gyromotion have been averaged out.

In a magnetized plasma, microinstabilities provide an alternative transport channel which in general is largely dominant compared to collisional effects. These physical phenomena, usually called drift–waves, need appropriate orderings and theoretical models to be described. Analogously to what has been done in the previous Chapter for the neoclassical transport coefficients, the common approach is to use kinetic and/or fluid models in order to obtain expressions of the transport coefficients providing the anomalous transport enhancement in terms of local macroscopic plasma parameters. The most complete and first principle approach is that of tackling directly the Boltzmann–Vlasov equation, in particular in the gyrokinetic ordering, which allows short range radial plasma variations of the same order of the Larmor radius [1, 2]. The evaluation of the transport coefficients from the growth rates of the most unstable modes is usually done adopting more or less sophisticated mixing length arguments [3, 4].

Nevertheless, experimental observations have pointed out the occurence of several unexpected features in plasma transport. The appropriate physical framework for their description is still under discussion. Although the kinetic equation in principle encompasses all the observed physics, the approximations made to allow a solution and the usual assumption of diffusive transport made in order to compute macroscopic quantities like temperatures and densities could be inadequate. For instance, non–local phenomena have been observed [5]: long–range responses take place in time scales which are two orders of magnitude smaller than the time scale of diffusive transport. Moreover these phenomena present an inverse polarity compared to standard diffusive transport phenomena, namely cooling at the plasma edge provokes a sudden enhancement of the temperature in the plasma centre. Recently, electron temperature fluctuations measured in the DIII–D tokamak have shown some of the characteristics of avalanche like events [6]. Theoretical models have revealed that avalanches, namely very fast radial propagations of a heat pulse, are likely to occur [7, 8]. These events have suggested alternative descriptions of plasma turbulent transport, adopting in particular the self–organized criticality (SOC) paradigm [7, 9]. The standard approach of local diffusive transport is indeed non adequate to describe some of the most exotic phenomena observed, and a controversial debate on this issue is being developed in the literature [10, 11, 12].

Furthermore, in a magnetized plasma, magnetic topology can play a non–negligible role on transport. The presence of magnetic islands arising close to resonant surfaces can involve strong modifications of the transport properties due to rapid convection along the field lines [13]. It has been proposed that their effect can explain some observed structures ("filaments") of the electron temperature profile. In this framework, the description of the magnetic topology would be of primary importance compared to that of kinetic, diffusive or non–diffusive radial transport effects.

For all the limits and the open issues briefly discussed above, our approach is indeed the most conventional. We shall assume that plasma transport can be described by standard local diffusion equations, with transport coefficients obtained from gyrokinetic or gyrofluid solutions, or semi–empirical expressions. Moreover, we shall assume that for time and space scales relevant for transport phenomena the magnetic topology can always be considered in equilibrium, and therefore the flux surface configuration is determined by the solution of the magnetohydrodynamic (MHD) equilibrium equation.

3.1 Introduction to 1-1/2 D simulations

The simulation of a tokamak plasma needs physical models able to describe every plasma and magnetic equilibrium quantity as a function of both time and space, from the plasma center up to the edge, including edge effects and even out to the scrape–off layer and the wall. In this global approach, equations for the time evolution of a large set of physical quantities describing the plasma must be identified and solved consistently. A generical macroscopic physical quantity G belonging to this set, like density and temperature of each particle species, is assumed to solve a continuity equation, whose general form in three dimensional (3D) geometry reads

$$\frac{\partial G}{\partial t} + \nabla \cdot \mathbf{\Gamma}_G = S_G. \tag{3.1}$$

The physical quantity $G = G(R, Z, \phi, t)$, solution of the continuity equation [Eq. (3.1)], assuming toroidal axisymmetry, hence neglecting the toroidal coordinate ϕ, depends on two spatial coordinates spanning the poloidal plane, which are usually called in cartesian coordinates R, the major radius, and Z, the vertical position. A physical description limited to transport perpendicular to the magnetic surfaces, called radial transport, allows to assume that all the plasma quantities, like densities and temperatures, are constant over a flux surface. This assumption is justified directly by the small gyroradius ordering for a magnetized plasma. This implies that transport parallel to the magnetic field lines is much faster than the one occuring in the direction perpendicular to the flux surfaces. Spatial variations of physical variables like temperature and density on a given flux surface can be neglected when phenomena of interest occur in time scales and length scales which are relevant for radial transport. Therefore we can introduce a flux surface label ρ, which plays the role of a radial coordinate, in such a way that flux surfaces are defined by the simple equation $\rho(R, Z) =$ constant. The physical quantity G can be written in the form $G = G(\rho(R, Z), t)$. Taking the flux surface average of Eq. (3.1), the 3D continuity equation [Eq. (3.1)] can be reduced to a 1D equation of the form

$$\frac{1}{V'}\frac{\partial}{\partial t}(V'G) + \frac{1}{V'}\frac{\partial}{\partial \rho}\left(V' \langle \mathbf{\Gamma}_G \cdot \nabla\rho \rangle_\rho\right) = \langle S_G \rangle. \tag{3.2}$$

Here the index $'$ for flux surface labels means derivation on ρ, namely $V' = \partial V \,/\, \partial \rho$, and V is the volume enclosed by the surface of label ρ. The symbol $\langle\ \rangle$ indicates the operation of flux surface average on a magnetic surface. From the point of view of the numerical implementation, this allows to compute plasma transport with a 1D code. Nevertheless the continuity equations in toroidal geometry involve quantities which describe the magnetic surface configuration. In realistic configurations, these quantities can be computed only by a 2D magnetic equilibrium solver. The equilibrium solver has to be coupled with the transport code, in order to compute the magnetic surface configuration consistent with the updated pressure and magnetic field profiles. In this sense, the package consisting of the 1D transport code and the 2D equilibrium solver provides a 1-1/2D description of the plasma in a tokamak device.

Each continuity equation, Eq. (3.2), involves the knowledge of two separate terms, the flux $\mathbf{\Gamma}_G$ and the source S_G corresponding to the quantity G. The continuity equations are coupled to one another by several different physical mechanisms. In particular, the fluxes $\mathbf{\Gamma}_G$ and sources S_G directly depend on local plasma conditions, defined by the set of physical quantities like G, which are the unknown variables of the set of equations. For instance this is the case for off–diagonal transport effects in the fluxes, like the ones pointed out in neoclassical transport (subsection 2.2.1), or the equipartition term in the sources of the temperature equations, coupling the electron and ion temperatures. Moreover, other indirect mechanisms can couple the equations. The evaluation of the fluxes is usually made through the computation of the transport coefficients, relating fluxes with the thermodynamic forces, namely the gradients of temperatures and densities. Since the transport coefficients depend on the local plasma parameters, this makes another indirect coupling mechanism. Also in the sources indirect coupling terms can be involved. In particular, the auxiliary heating effects depend on the local plasma conditions, and thus imply another coupling mechanism among the equations. Heating effects are usually difficult to compute, and specific codes describing the different heating sources must be considered and consistently coupled to the transport code. The same can happen for the computation of the transport coefficients: some transport models provide analytical expressions directly relating heat and particle diffusivities with the plasma and equilibrium parameters, which can be easily implemented in the transport code. Other models involve the coupling of the transport code with separate specific codes. All this implies that, finally, a complete and consistent numerical tool describing a tokamak plasma is provided by the connection of several different codes. The main body of the package, the transport code, solves a set of several coupled continuity equations.

The final results of the code critically depend on the specific transport model adopted. For this reason, the availability of several different models within the same transport code is particularly useful in order to perform comparisons on the predictions of the different models and comparisons with the experimental measurements. In the present work the Rebut–Lallia–Watkins (RLW) model [15] has been the one regularly applied in the simulation of TCV discharges, both in Ohmic and with ECH. During the present thesis work, other models have been implemented in PRETOR, the Multi Mode Model 95 (MMM95) [16], and the IFS/PPPL model [17]. At this stage, the numerical implementation of these models have been checked, and preliminary physical applications have been performed.

The comparison with the experimental data in TCV is not sufficiently stringent for a complete and reliable validation, since measurements of the ion temperature profile are not yet available on TCV. Therefore, the application of these models will be the subject of further work and is out of the scope of the present thesis.

In the following section we present the transport equations for the time evolution of plasma temperatures and densities. In order to provide a sufficiently precise description of the numerical tool used in this work and since in PRETOR the equations are solved in sequence, the presentation will follow the same order in which the equations are solved in the code. Similar transport equations have been implemented in several other plasma transport codes, which have been developed by the fusion community over the years. We mention here for example the codes ASTRA [18], BALDUR [19], and JETTO [20]. Different extensive treatments of specific effects have been introduced in some of these codes, in such a way that the codes can be considered quite complementary. Section 3.3 describes the equations which compute the self–consistent evolution of the magnetic equilibrium. We present in detail how the 2D magnetic surface configuration is taken into account in the 1D field diffusion equation. PRETOR is coupled with a fixed boundary 2D equilibrium solver. In Section 3.4 explicit expressions for the source and loss terms involved in the heat transport equations are given. Formulae and algorithms are those which have been specifically used in the simulations presented in this thesis. In this context we must emphasize that, even if some of these formulae are standard and of general validity, like in the case of energy losses due to bremmsstrahlung, other formulae, like in the case of losses due to cyclotron emission or to line radiation, provide only rough approximations, and can be quite different from formulae implemented in other transport codes. In Section 3.5 we provide a few numerical details about the code implementation. Finally, in subsection 3.6 we present the local RLW transport model, giving details about its implementation in PRETOR.

3.2 Transport equations in toroidal geometry

As already mentioned, in Eq. (3.2) G represents each physical quantity describing the plasma, namely the temperature and density of each particle species. In particular the transport code PRETOR computes the time dependent evolution of the following quantities:

- Electron density n_e and temperature T_e
- Main ion density n_i
- First impurity ion density n_p and ionization stage Z
- Ions temperature T_i

- Densities of neutral atoms
- Current and magnetic fields

The equations describing the time evolution of the electric currents and magnetic fields will be presented in the next section. In this paragraph we concentrate on the continuity equations for densities and temperatures. Two ion species are considered: the main ion species, usually deuterium or a mixture of deuterium and tritium which is in any case considered as a single plasma species, and the impurity ion, carbon in the specific case of TCV, or α-particles in the case of a burning plasma. The densities of the two ion species are evolved in time indipendently, but the same temperature is assumed for both. Note that while this latter assumption is usually made in all the transport codes, other codes allow one to compute independently the density evolution of a large number of ion species. In particular BALDUR can take into account up to 4 different impurity species. In PRETOR a third impurity species can be included as a fixed percentage of the electron density, in particular in order to be able to take into account a second plasma impurity in a burning plasma, like beryllium for ITER simulations [21]. Neutral atoms, even if they can be considered as ions with a zero ionization stage, are treated separately: indeed they obey completely different equations. As already mentioned, in the following description of all the transport equations, we follow the detailed sequence adopted in PRETOR during the computation of a single time step.

The starting point is given by all the updated plasma profiles, densities and temperatures, and the consistently computed magnetic equilibrium. The first step is to compute all the new particle and heat sources, as it will be described in Section 3.4. Afterwards the particle and heat transport coefficients are updated, according to a specific transport model (Section 3.6).

Neutrals

The first transport equations considered are the ones which update the density profiles of the neutral populations. These are involved in the particle source terms for the ion densities. In PRETOR three independent neutral species are considered. The main neutral density n_{Ni}, which appears in the source term of the density continuity equation of the main ions, Eq. (3.7), is splitted in a cold and a hot part, $n_{Ni} = n_{Nic} + n_{Nih}$. This allows one to more adequately take into account the effects of charge exchange, which involve a source term in the whole plasma volume, and edge effects due to recycling and gas puffing. In this context, it must be mentioned that BALDUR treats the problem of neutrals transport with particular accuracy compared to other codes. This code computes the neutral gas sources by means of a specific Monte Carlo algorithm and an extensive atomic physics package. In PRETOR the neutrals densities are updated by simple diffusion equations.

The equation for the cold neutrals n_{Nic} reads

$$\frac{1}{V'}\frac{\partial}{\partial\rho}V'\Gamma_{Nic} = -(\alpha_I + \alpha_{CX})n_{Nic}, \quad \text{where} \quad \Gamma_{Nic} = -\frac{\langle|\nabla\rho|^2\rangle}{\alpha_I + \alpha_{CX}}\frac{\partial}{\partial\rho}(v_{Nic}^2 n_{Nic}), \tag{3.3}$$

with α_{CX} the charge exchange rate and α_I the ionization rate. The speed v_{Nic} is related to the cold neutrals energy, which is given as input. The charge exchange rate is computed from the ion density and temperature profiles

$$\alpha_{CX} = 10^5 \left(\ln T_i + 6.6\right)\frac{n_i}{M_G},$$

with density in $10^{19}\,\mathrm{m}^{-3}$, temperature in keV and the main ion mass M_G in proton mass units. The ionization rate is related to the electron density and temperature by

$$\alpha_I = 10^8 \left[\sqrt{T_e/E_i}\,\exp(\sqrt{T_e/E_i})\right]\frac{n_e}{E_i^{1.5}\left(\sqrt{T_e/E_i}+6\right)},$$

with the same units of the previous formula, and where E_i is the main ion ionization energy, in keV. The boundary condition sets a defined flux Γ_{Nic} at the last close flux surface (LCFS), due to gas puffing: in the simulation this term can be either kept equal to zero, or it can be determined by the code in order to match a given value of the volume average density, also taking into account, if requested, the main ion density reduction rate due to fusion reactions in a burning plasma. The hot neutrals are produced by cold neutrals in case of charge exchange reactions. Their density n_{Nih} is computed as follows

$$\begin{aligned}\frac{1}{V'}\frac{\partial}{\partial\rho}V'\Gamma_{Nih} &= -\alpha_I n_{Nih} + \alpha_{CX} n_{Nic},\\ &\text{where} \quad \Gamma_{Nih} = -\frac{\langle|\nabla\rho|^2\rangle}{\alpha_I + \alpha_{CX}}\frac{\partial}{\partial\rho}\left[\left(\frac{T_i}{m_i}\right)n_{Nih}\right],\end{aligned} \tag{3.4}$$

in which the source term, due to charge exchange, involves the population of cold neutrals. The boundary condition for hot neutrals sets the flux which crosses the LCFS equal to zero. The third neutral species is the one which describes the neutral atoms of the first impurity. Assuming a low density of the impurity ions compared to the electron density, charge exchange reactions are sufficiently rare to justify to consider a single impurity neutral population, not splitted in hot and cold particles. Therefore the density n_{Np} is updated solving the single equation

$$\begin{aligned}\frac{1}{V'}\frac{\partial}{\partial\rho}V'\Gamma_{Np} &= -\alpha_I n_{Np}\\ &\text{where} \quad \Gamma_{Np} = -\frac{\langle|\nabla\rho|^2\rangle}{\alpha_I}\frac{\partial}{\partial\rho}(v_{Np}^2 n_{Np}).\end{aligned} \tag{3.5}$$

The boundary condition defines the value of the flux Γ_{Np} at the LCFS. This value, depending on whether the simulation includes fusion reactions or not, and hence depending on whether the first impurity is given by α–particles or not, can be determined in different ways. This boundary condition turns out to be essential in order to compute the value of the effective charge number. The inward edge flux of the impurity neutrals is in some way related to the outward edge fluxes of both the impurity ions and the main ions. Several different options can be chosen in the code, in order to adapt the simulation to specific applications. The most general and simple choice is to impose to the inward impurity neutrals flux to match a given fraction of the outward impurity ions flux, due mainly to recombination. In the simulation such a fraction can be determined for instance in order to fit the value of the experimentally measured effective charge number. The largest is this fraction, the largest is the resulting effective charge number, computed with Eq. (3.11). For non–burning plasmas, the first impurity is usually determined by the material of the first wall, like carbon for TCV. In this case additional effects of both deuterium and self sputtering can be taken into account, involving both the main ion and the impurity ion edge fluxes. This is the option which was chosen in all the simulations performed in this thesis work, when also the density evolution was computed. An additional term can be also included in order to take into account the impurity release ascribed to the radiofrequency antennas, taken proportional to the additional power. In case the first impurity is given by α–particles, the fraction of the impurity ion flux can be modified by a supplementary factor related to the ratio between the energy confinement time and the α–particles confinement time, given as input.

Once the density profiles of the neutral populations have been updated, the determination of the charge profile Z_p of the first impurity is considered. Two options are possible: either we assume simply that ions are completely ionized everywhere in the plasma or a diffusion equation for the impurity charge is considered. In this second case we solve the equation

$$\frac{1}{V'}\frac{\partial}{\partial\rho}V'\Gamma_Z = c_Z\,(Z_c - Z), \quad \text{where} \quad \Gamma_Z = -D_Z\langle|\nabla\rho|^2\rangle\frac{\partial Z}{\partial\rho} + Z\,v_{PZ}\langle|\nabla\rho|\rangle. \qquad (3.6)$$

Here Z_c is the coronal equilibrium ionization state, which is function of the updated electron temperature profile. In particular for the principal TCV impurity, carbon, we take $Z_c = 6$, where the electron temperature is larger than 300 eV, while partially ionized states are considered for lower temperatures. The coefficient c_Z is proportional to the electron collision frequency, and given by $156\,n_e Z/T_e^{1.5}$, with densities in $10^{19}\,\mathrm{m}^{-3}$ and temperatures in keV. The diffusion coefficient D_Z and the pinch term v_{PZ} are taken equal to the ones for the first impurity diffusion equation, D_p and V_{Pp}, Eq. (3.10).

Ion and electron densities

At this point the continuity equations for the ion densities are considered. The density of the main ions n_i is determined by the following equation

$$\begin{aligned} \frac{\partial n_i}{\partial t} + \frac{1}{V'}\frac{\partial}{\partial \rho} V'\Gamma_i &= S_{NBI\,i} - 2\mathcal{R} + n_{Ni}\alpha_I, \\ \text{where} \quad \Gamma_i &= -D_i\langle|\nabla\rho|^2\rangle\frac{\partial n_i}{\partial \rho} + n_i v_{Pi}\langle|\nabla\rho|\rangle, \end{aligned} \tag{3.7}$$

with D_i and v_{Pi} the diffusion coefficient and the pinch velocity respectively, provided by the transport model. In the source term, $S_{NBI\,i}$ represents the main ion source arising from neutral beam injection, $\mathcal{R} = r_T(1 - r_T)n_i^2\langle\sigma v\rangle$ is the total fusion reaction rate per unit volume, with r_T the tritium concentration and $\langle\sigma v\rangle$ the fusion cross–section; α_I is the ionization rate. Note that time variations of the volume included in a flux surface are ignored in PRETOR, on the basis that they are negligible compared to the other terms of the equation with fixed plasma boundary conditions. Codes which allow free plasma boundary conditions need to include terms such as $n_i/V'\ (\partial V'/\partial t)$ in the transport equations. This is for instance the case of the code JETTO, as in the application described in Ref. [22]. We must also stress that off–diagonal terms in the fluxes are not explicitely taken into account in PRETOR. Off–diagonal terms can be included only introducing effective diffusivities defined by

$$D_{\text{eff}} = \frac{\Gamma_{\text{tot}}}{\partial n/\partial \rho},$$

where Γ_{tot} is a diffusive flux in which off–diagonal terms are taken into account. Note however that these procedure must be adopted with caution as it can produce artificial singularities when the density gradient is equal to zero. This is the case of hollow density profiles, in which off–diagonal terms could be expected to play a non–negligible role. The boundary condition for Eq. (3.7) is obtained modelling a toroidal belt limiter. The flux which goes out of the plasma, crossing radially the last closed flux surface (LCFS), matches the flux reaching the limiter, assuming that no significative change of density occurs in the SOL, in particular in the absence of ionization. Transport across the LCFS is assumed to be equal to the radial transport immediately inside the plasma. Calling Γ_S the global ion flux crossing the LCFS, and Γ_L the ion flux reaching the limiter, and making the previous assumptions, the equation for the density evolution in the SOL reads

$$\frac{d}{dt}\int_{V_{SOL}} n_i\, dV = \Gamma_S - \Gamma_L = 0, \tag{3.8}$$

where $\Gamma_L \simeq n_i v_{\parallel} S_L$, $v_{\parallel}$ being the particle speed along the magnetic field lines and S_L the limiter surface perpendicular to the field lines. Treating these parallel losses as a uniform sink term in the SOL [23], neglecting a radial pinch velocity and estimating the ion velocity parallel to the field lines as equal to the ion sound speed c_{si}, in slab geometry, the previous equation can be written in the simple differential form

$$-D_{\perp}\frac{d^2 n_i}{dr^2} = \frac{n_i c_{si}}{L_c},$$

where $L_c = 2\pi R_0 q_{edge}$ is the connection length for the toroidal limiter. This equation yields a simple exponential radial decay for the density in the SOL, for $r > a$, of the form $n_i(r) = n_i(a) \exp[(a-r)/\lambda_S]$, with a SOL characteristic length $\lambda_S = (D_\perp L_c/c_{si})^{1/2}$, which provides an evaluation of the effective radial thickness of the SOL. Applying again Eq. (3.8), we find the following boundary condition for the main ion density

$$\Gamma_i\big|_{\rho=a} = -D_i \langle|\nabla\rho|^2\rangle \frac{\partial n_i}{\partial\rho}\bigg|_{\rho=a} + n_i v_{Pi} \langle|\nabla\rho|\rangle\big|_{\rho=a} = R_S^2 \frac{\lambda_S\, n_i c_{si}}{2\pi R_0}, \tag{3.9}$$

where R_S is a parameter which provides the "effective" limiter surface fraction, and represents the ratio between the limiter and the edge plasma surface. This parameter can be given as input. Large values allow steeper density edge gradients and lower densities. On the contrary, low values of this parameter allow to increase the edge density, producing a pedestal and therefore simulating the presence of a divertor region in which a fraction of the neutrals are ionized increasing the edge density. This parameter can be adjusted in order to reproduce the density pedestal in H–modes.

The first impurity ion density n_p solves the following continuity equation

$$\begin{aligned} \frac{\partial n_p}{\partial t} + \frac{1}{V'}\frac{\partial}{\partial\rho} V'\Gamma_p &= S_{NBIp} + \mathcal{R} + n_{Np}\alpha_I \\ \text{where} \quad \Gamma_p &= -D_p\langle|\nabla\rho|^2\rangle \frac{\partial n_p}{\partial\rho} + n_p v_{Pp}\langle|\nabla\rho|\rangle \end{aligned} \tag{3.10}$$

and n_{Np} is the impurity neutrals density. S_{NBIp} describes a NBI source, in the case of injection of impurity particles, and $\mathcal{R}$ is again the fusion reaction rate, in the case of simulations of a burning plasma, since in this case the first impurity is given by α–particles. The boundary condition is imposed in the same way as described for Eq. (3.7).

The electron density is then obtained by quasi-neutrality and the effective charge is computed as usual:

$$n_e = \frac{Z_i n_i + Z_p n_p}{1 - Z_3 C_3} \quad ; \quad Z_{\text{eff}} = \frac{Z_i^2 n_i + Z_p^2 n_p + Z_3^2 C_3 n_e}{n_e}, \tag{3.11}$$

where C_3 and Z_3 are the charge and the concentration, given as a fraction of the electron density, of the third ion species.

Temperatures

When all the density profiles have been updated, the heat transport is tackled in order to update also the temperature profiles. Note that an option in the input is available in order to set the density profiles equal to the experimental measurements and by–pass in the code all the calculations related to particle transport. This allows one to focus the simulations on heat transport, particularly in the presence of external heat and particle sources, in which the correct simulation of the experimental density behaviour becomes a very complex task. In PRETOR only two heat continuity equations are solved, one for the electron temperature T_e, and one for the ion temperature T_i, since T_i is assumed the same for all the ion species. Therefore, in the ion heat transport equation, a total ion density $n_{Ti} = n_i + n_p$ and a total ion particle flux $\Gamma_{Ti} = \Gamma_i + \Gamma_p$ must be introduced,

$$\begin{aligned} \frac{3}{2}\frac{\partial(n_{Ti}T_i)}{\partial t} + \frac{1}{V'}\frac{\partial}{\partial\rho}V'Q_{Ti} &= S_i \\ \text{where} \quad Q_{Ti} &= -n_{Ti}\,\chi_i\langle|\nabla\rho|^2\rangle\frac{\partial T_i}{\partial\rho} + \frac{5}{2}\Gamma_{Ti}T_i + v_{PTi}\,n_{Ti}T_i. \end{aligned} \quad (3.12)$$

In the expression for the heat flux we have included thermal diffusion, thermal convection and heat pinch. Like for particles, off–diagonal terms are not included. The description of off-diagonal terms is in general rather limited in plasma transport codes. For this purpose, transport models which in principle can involve full transport matrices, like for instance the MMM95 [16], introduce a set of diagonal effective conductivities which allow to obtain the total heat fluxes only proportional to the conjugated temperature gradients. In the source term S_i we take into account equipartition and auxiliary heating as radio frequency (RF), neutral beam injection (NBI), and eventually a fraction of the α heating

$$S_i = p_{RF\,i} + p_{NBI\,i} + p_{\alpha i} + n_e\nu_E(T_e - T_i). \quad (3.13)$$

The neoclassical equipartition frequency, for a single ion species, is given by

$$\nu_E = 3\frac{m_e}{m_i\,\tau_e}, \quad \text{where} \quad \tau_e = \frac{3}{16\pi^{1/2}}\frac{m_e^2\,v_{the}^3}{Z^2e^4n_i\ln\Lambda}$$

is the electron–ion momentum exchange time, also called electron collision time. In the case of three ion species considered together in the same heat transport equation, like in the case of PRETOR, the equipartition power provided by electrons to each ion species must be added, and the following formula can be used

$$\nu_E = \frac{0.041}{T_e^{3/2}}\left(\sum_j \frac{Z_j^2}{M_j}n_j\right),$$

where the summation is extended to all the ion species considered, densities are expressed in $10^{19}\,\mathrm{m}^{-3}$, temperatures are expressed in keV, and the masses M_j in units of the proton mass.

The equation for the electron temperature is

$$\begin{aligned} \frac{3}{2}\frac{\partial(n_eT_e)}{\partial t} + \frac{1}{V'}\frac{\partial}{\partial\rho}V'Q_e &= S_e \\ \text{where} \quad Q_e &= -n_e\,\chi_e\langle|\nabla\rho|^2\rangle\frac{\partial T_e}{\partial\rho} + \frac{5}{2}\Gamma_eT_e + v_{PTe}\,n_eT_e \end{aligned} \quad (3.14)$$

where again the term $v_{PTe} n_e T_e$ includes a heat pinch contribution. Γ_e is the electron particle flow and it is computed assuming ambipolarity

$$\Gamma_e = Z_i \Gamma_i + Z_p \Gamma_p, \tag{3.15}$$

and neglecting the particle flow of the second impurity. The source of electron energy is given by:

$$S_e = p_{ohm} + p_{RFe} + p_{NBIe} + p_{\alpha e} - n_e \nu_E (T_e - T_i) - p_{cyc} - p_{brems} - p_{Imp} - p_{Ion} \tag{3.16}$$

where the terms with positive sign are due to ohmic heating, RF, NBI and α heating respectively. Energy losses for the electrons are the neoclassical equipartition, the radiation losses due to cyclotron radiation p_{cyc}, Eq. (3.34), bremsstrahlung p_{brems}, Eq. (3.33), and atomic processes, like recombination and line radiation, due to the presence of impurities p_{Imp}, Eq. (3.35), as well as losses involved by ionization processes p_{Ion}, Eq. (3.37). The boundary conditions for the heat transport equations can be of different type. One possibility is to give the value of the edge electron and ion temperature as input. This is the option which has been used on a regular basis during the present thesis work. A different possibility is analogous to the one described for the ion density, Eq. (3.9). Physically, a power balance condition is imposed stating that the total conductive and convective heat flux crossing the LCFS must equate the total heat flux reaching the limiter, therefore assuming that no heat source is located in the SOL. This condition, always with the assumption that transport across the LCFS is equal to the radial transport immediately inside the plasma, can be translated in the following equations

$$Q_e|_{\rho=a} = -\chi_e n_e \langle|\nabla\rho|^2\rangle \frac{\partial T_e}{\partial \rho}|_{\rho=a} + \frac{5}{2}\Gamma_e T_e \langle|\nabla\rho|\rangle|_{\rho=a} = R_S^2 \frac{\lambda_S}{2\pi R_0} q_{Le}, \tag{3.17}$$

$$Q_{Ti}|_{\rho=a} = -\chi_i n_{Ti} \langle|\nabla\rho|^2\rangle \frac{\partial T_i}{\partial \rho}|_{\rho=a} + \frac{5}{2}\Gamma_{Ti} T_i \langle|\nabla\rho|\rangle|_{\rho=a} = R_S^2 \frac{\lambda_S}{2\pi R_0} q_{Li}, \tag{3.18}$$

which provide the boundary conditions for the electron and the ion temperature respectively. The elelctron and ion heat fluxes reaching the limiter, q_{Le} and q_{Li}, are evaluated as follows

$$\begin{aligned} q_{Le} &= \left[2 + 3.7 + 0.5\ln\left(\frac{T_e}{T_i}\right)\right] T_e \left[(n_i Z_G + Z_3 C_3 n_e)\, c_{si} + Z_p n_p c_{sp}\right], \\ q_{Li} &= \frac{5}{2} T_i \left[(n_i Z_G + Z_3 C_3 n_e)\, c_{si} + Z_p n_p c_{sp}\right], \end{aligned}$$

where, like precedently, c_{si} and c_{sp} are the sound speeds of main ions and impurity ions respectively. As already discussed for the ion density boundary condition, the input parameter R_S allows to modify the edge temperature gradient and to produce a pedestal in both the density and the temperature profiles. It becomes particularly important in order to fit the value of the pedestal density and temperature in simulations of H–mode profiles. Low values of this parameter, yielding low net outgoing flux across the LCFS, allow high values of both the pedestal temperature and density.

In the expressions for the particle fluxes, Eqs. (3.7) and (3.10), and for the heat fluxes, Eqs. (3.12) and (3.14), we have respectively the following transport coefficients: the diffusion coefficients D_i and D_p, the pinch velocity terms v_{Pi} and v_{Pp}, the two heat conductivities χ_e and χ_i as well as the two heat pinch velocities v_{PTi} and v_{PTe}. The expressions used for these coefficients depend on the transport model which is assumed: the standard neoclassical theory being insufficient, different models for anomalous transport have been developed and are available in the literature. The code PRETOR uses a version of the RLW model [15] which has been extended also to particle transport [14] and which will be described in Section 3.6. For predictions of burning plasmas in ITER, a factor can be introduced "normalizing" the transport coefficients in order to obtain in the simulation a plasma performance which follows a given ITER global scaling law.

3.3 Self–consistent magnetic equilibrium evolution

A correct description of the time evolution of the equilibrium magnetic fields and current densities in transport simulations is of great importance in tokamak physics. In these devices transport phenomena and geometrical effects deriving from the magnetic configuration are to a certain extent linked together. Therefore transport and geometry must be described consistently. This is particularly important for TCV, because of the large shape flexibility (Section 4.2), and of the powerful auxiliary heating system (Section 4.3). Indeed, with intense ECH power and strong ECCD, the effects of the external sources on the magnetic equilibrium configuration can be significant. For this reason, we shall describe in detail the equations which allow to compute the evolution of the equilibrium magnetic fields and current density profiles, following the definitions adopted in PRETOR.

Note that in general currents and fields are not constant on a given flux surface, differently from densities and temperatures. Moreover currents and fields are vectorial quantities. Therefore appropriate definitions must be introduced in order to reduce the 3D vectorial equations, namely Faraday and Ampere laws, to 1D scalar equations, adequate to be implemented in a 1D transport code. First of all we introduce, for a generic physical quantity A, the flux surface average in the standard form

$$\langle A \rangle = \frac{\oint A \, \mathrm{d}l/B_p}{\oint \mathrm{d}l/B_p},$$

where $B_p = |\nabla\Psi|/R$, Ψ being the poloidal magnetic flux and R the major radius. For a vectorial field $\mathbf{a}$, we introduce the following flux surface averaged parallel component to the magnetic field

$$\tilde{a} = \frac{2\pi \langle \mathbf{a} \cdot \mathbf{B} \rangle}{\mu_0 F R_0 \langle R^{-2} \rangle}, \tag{3.19}$$

where μ_0 is the free space permeability and F is proportional to the toroidal covariant component of the magnetic field $R B_\Phi$ by means of the relation $F = 2\pi R B_\Phi / \mu_0$, R_0 being the major radius of the geometric axis. We consider an effective minor radius ρ which is a proper flux label. Several definitions have been introduced for ρ in the literature. One of the most common possibilities, introduced in [24], and adopted for instance in JETTO, is to define ρ in terms of the toroidal flux Φ by the relation $B_{\mathrm{To}} \pi \rho^2 = \Phi$, where B_{To} is a constant, representative value of the toroidal field, and usually chosen as the vacuum magnetic field at the geometric axis B_0. In PRETOR the defintion of ρ follows the choice which has been made for the variable "RMINOR" in the ITER Profile Database [25] (variable number 68). In PRETOR ρ is defined for each flux surface to be the average horizontal minor radius at the vertical position of the magnetic axis. A more detailed definition, together with a description of the radial mesh used in PRETOR is provided in Section 3.5.

A somewhat standard derivation (see, for instance, Eq. (7.14) in [24]) allows one to write the toroidal component of Faraday law in the form

$$\frac{\partial B_{po}}{\partial t} = \frac{\partial \tilde{E}}{\partial \rho}, \tag{3.20}$$

where, following [24], we have introduced the effective poloidal magnetic field in terms of the radial coordinate ρ

$$B_{po} = \frac{1}{R_0} \frac{\mathrm{d}\Psi}{\mathrm{d}\rho}.$$

The averaged parallel electric field $\tilde{E}$ is related to the ohmic current by means of the plasma resistivity, which is assumed neoclassical. Therefore we can write

$$\tilde{E} = \eta_{neo} \tilde{\jmath}_{ohm} = \eta_{neo} \left(\tilde{\jmath} - \tilde{\jmath}_{BS} - \tilde{\jmath}_{CD} \right). \tag{3.21}$$

The neoclassical resistivity η_{neo} and the bootstrap current $\tilde{\jmath}_{BS}$ are computed using formulae presented in Section 2.4, which are the only available in the literature taking into account both geometrical and collisional effects. Note that the neoclassical resistivity is a surface label and the bootstrap current is computed already in the flux surface averaged form suitable for application in Eq. (3.21), as defined in Eq. (2.3). In Eq. (3.21) we have also included a current drive density profile $\tilde{\jmath}_{CD}$. Note that also $\tilde{\jmath}_{CD}$ is introduced using the defintion of Eq. (3.19), hence it must be eventually adequately transformed when it is taken from the output of a separate code, like for instance the ray–tracing code TORAY–GA [26] [see Eq. (3.29)]. In Eq. (3.21) the total current density profile $\tilde{\jmath}$ can be written in terms of the effective poloidal magnetic field taking the projection of Ampere law parallel to the magnetic field. One can write (see for instance Eq. (7.20) in [24]),

$$\tilde{\jmath} = \frac{F}{\mu_0 G_\Phi} \frac{\partial}{\partial \rho} \left(\frac{G_\theta B_{po}}{F} \right), \tag{3.22}$$

where

$$G_\Phi = \frac{V'}{(2\pi)^2} \langle \frac{1}{R^2} \rangle, \quad \text{and} \quad G_\theta = \frac{\langle B_p^2 \rangle}{V'}. \tag{3.23}$$

Introducing Eq. (3.22) in Eq. (3.20), we obtain a diffusion equation for the effective poloidal field B_{po}, in which the radial derivatives of the bootstrap and driven current densities take the place of source terms, and the neoclassical resisitivity appears in a term which takes the place of the diffusion coefficient

$$\frac{\partial B_{po}}{\partial t} = -\frac{\partial}{\partial \rho} \left[\eta_{neo} \frac{F}{\mu_0 G_\Phi} \frac{\partial}{\partial \rho} \left(\frac{G_\theta B_{po}}{F} \right) \right] + \frac{\partial\, \eta_{neo} \left(\tilde{\jmath}_{BS} + \tilde{\jmath}_{CD} \right)}{\partial \rho}. \tag{3.24}$$

Therefore, during a time step of the transport code, once all the equations presented in subsection 3.2 have been solved, then the neoclassical resisistivity and bootstrap current can be computed with the updated density and temperature profiles, by means of neoclassical formulae Eqs. (2.30) and (2.33), as well as eventually the new source term $\tilde{\jmath}_{CD}$. Afterwards, the poloidal magnetic field diffusion equation is solved. With the updated poloidal magnetic field profile, several different current and magnetic field profiles can be obtained. The integrated current density profile $I_t(\rho)$ can be easily related to the poloidal magnetic field B_{po} considering the flux of Ampere law through the poloidal cross section of the magnetic surface of radial coordinate ρ. This provides

$$I_t = \frac{2\pi R_0}{\mu_0} G_\theta B_{po}. \tag{3.25}$$

The flux surface label F is then updated through the relation

$$F^2 = F_0^2 + \int_\rho^a \frac{2V'}{\mu_0 G_\Phi} \frac{\partial P}{\partial \rho} \mathrm{d}\rho + \int_\rho^a \frac{1}{G_\theta G_\Phi} \frac{\partial I_t^2}{\partial \rho} \mathrm{d}\rho. \tag{3.26}$$

where $F_0 = 2\pi R_0 B_0 / \mu_0$. The knowledge of the intergrated current I_t allows to easily compute the flux surface average toroidal current density $\tilde{\jmath}_{OH} = R_0 \langle j_\Phi / R \rangle$, given by

$$\tilde{\jmath}_{OH} = \frac{2\pi R_0}{V'} I_t' \tag{3.27}$$

This current density is involved in the expression for the ohmic power density $p_{ohm} = \tilde{E}\, \tilde{\jmath}_{OH}$. The safety factor and current density profiles are then given by

$$q = G_\theta G_\Phi \frac{F}{I_t}, \qquad \tilde{\jmath} = \frac{1}{2\pi R_0} \frac{F}{G_\Phi} \frac{\partial}{\partial \rho} \left(\frac{I_t}{F} \right). \tag{3.28}$$

Note that this last equation relates $\tilde{\jmath}$ to the integrated current, and can be used to compute $\tilde{\jmath}_{CD}$ from the current drive profile given as output by a separate code

$$\tilde{\jmath}_{CD} = \frac{2\pi}{R_0 \langle R^{-2} \rangle} \left(\frac{\mathrm{d}I_{CD}}{\mathrm{d}V} - \frac{I_{CD}}{F} \frac{\mathrm{d}F}{\mathrm{d}V} \right) \tag{3.29}$$

where $I_{CD}(\rho)$ is the integrated driven current inside the surface of radius ρ. In particular both I_{CD} and $\mathrm{d}I_{CD}/\mathrm{d}V$ are provided by the TORAY–GA output. The radial derivatives of the total pressure profile and of the toroidal covariant component of the magnetic field, $p'(\rho)$ and $FF'(\rho)$ respectively, are used as source terms in the Grad-Shafranov equation solved in PRETOR by a 2D coupled equilibrium solver

$$\frac{\partial^2 \Psi}{\partial R^2} + \frac{\partial^2 \Psi}{\partial Z^2} - \frac{1}{R} \frac{\partial \Psi}{\partial Z} = -\frac{\mu_0}{R_0 B_{po}} \left[Rp' + \frac{\mu_0}{(2\pi)^2 R} FF' \right]. \tag{3.30}$$

The 2D fixed boundary equilibrium solver uses a defined plasma boundary as boundary condition. The solver uses a mesh in R and Z on the poloidal cross section on which the poloidal magnetic flux Ψ is defined. Such a mesh allows very fast solutions of the Grad-Shafranov equation, but is not particularly adequate to treat short length scale variations of the input profiles in the plasma centre. For specific applications a large number of mesh points on R and Z and an appropriate smoothing of the input profiles is needed. The updated magnetic equilibrium allows the calculation of all the metric functions needed in the transport equations. In particular, $V' = \mathrm{d}V/\mathrm{d}\rho$ is obtained computing the volume enclosed in each flux surface of the R, Z mesh corresponding to a point of the grid on the ρ coordinate. The flux surface average $< |\nabla\rho|^2 >$, which occurs in the heat and particle diffusion equations, is given by

$$< |\nabla\rho|^2 >= \frac{\langle R^2 B_p^2 \rangle}{(R_0 B_{po})^2}. \tag{3.31}$$

The functions G_Φ and G_θ are computed using Eq. (3.23).

Radial electric field

We must also mention that PRETOR does not compute the radial electric field E_r. This can be easily justified by the fact that the RLW transport model does not involve E_r. Therefore for simulations with this model the radial electric field is not necessary. Nevertheless, accurate calculations of the radial electric field are today of great relevance for the fusion community. The application of theory based transport models, in particular in the simulation of regimes with improved confinement or internal transport barriers (ITB), especially in the ion transport channel, calls for the inclusion of the effects due to the $\omega_{E\times B}$ shearing rate. This term plays an important role in the stabilization of drift–wave turbulence and is commonly regarded as a very crucial factor in the ITB formation, both in theories and experiment analysis [27]. The $\omega_{E\times B}$ shearing rate can be computed following Ref. [28]

$$\omega_{E\times B} = \left| \frac{RB_p^2}{B_t} \frac{\partial}{\partial \Psi} \frac{E_r}{RB_p} \right| .$$

The radial electric field profile is therefore the only term which is not yet computed in PRETOR in order to evaluate $\omega_{E\times B}$. It can be computed by the radial component of the momentum balance equation for the main plasma ions

$$E_r = \frac{1}{Zen_i} \frac{\partial p_i}{\partial \rho} - v_p B_t + v_t B_p .$$

Here v_p and v_t are the poloidal and toroidal velocities. The calculation of the radial electric field profile involves the knowledge of the poloidal and toroidal plasma rotations. Usually, the poloidal rotation is assumed neoclassical, and the toroidal rotation is obtained by experimental measurements. The assumption of neoclassical poloidal rotation implies that the pressure term and the poloidal rotation term in the expression of E_r are usually similar and of opposite signs [27]. Therefore the dominant contribution is the one given by the toroidal rotation which calls for careful measurements. These are usually provided by charge exchange spectroscopy using an intrinsic impurity, like carbon for TCV. This diagnostics has been very recently installed on TCV. It should allow further transport investigations beyond the results of the present thesis.

3.4 Energy sources and losses in PRETOR

Energy sources

The intrinsic energy source in tokamaks is that provided by ohmic heating. As already mentioned, the ohmic power involved in the source term of the electron heat transport equation [Eq. (3.14] is computed as follows

$$p_{ohm} = \tilde{E}\, \tilde{\jmath}_{OH} . \tag{3.32}$$

The flux surface averaged parallel electric field $\tilde{E}$ is given by Eq. (3.21), while the flux surface average toroidal current density $\tilde{\jmath}_{OH}$ is given by Eq. (3.27).

Auxiliary heating sources are governed by complex physics. The plasma absorbed power densities must be generally computed by separate codes, interfaced or coupled with the transport code. For instance, PRETOR has been coupled with the code PION [29], computing the ion cyclotron resonance heating (ICRH) source, and used for predictions of ITER performances with various ICRH schemes [30]. As already mentioned, during the present thesis work, interfaces with a few codes computing RF or NBI heating sources have been implemented in PRETOR for applications on two tokamaks, TCV and JET. Details are provided in Section 3.5. Nevertheless, for fast predicting simulations it is useful in a transport code to have the option of modelling the effect of a heat source by means of a set of simple gaussian power density profiles absorbed by the plasma, whose total powers, locations along the minor radius and widths can be provided as input. In PRETOR we have implemented the possibility of taking into account up to six different independent gaussian power density profiles, simulating for instance the power depositions due to the six X2 gyrotrons available on TCV, Section 4.3. The corresponding power density profile is given by

$$p_{RF} = \sum_{l=1}^{N} P_l \exp\left[-\frac{(\rho-\rho_l)^2}{\Delta_l^2}\right] \left\{\int_0^1 \exp\left[-\frac{(\rho-\rho_l)^2}{\Delta_l^2}\right] V'\mathrm{d}\rho\right\}^{-1},$$

where P_l is the total power in MW produced by the l–th gaussian profile, whose center is ρ_l and standard deviation Δ_l. These three quantities, for each gaussian, are all time dependent, allowing the simulation of power ramps or modulations, and deposition sweeps. Each power P_l is divided into two fractions, one to be included in the ion heat sources, and the other in the electron heat sources.

Energy Losses

Radiation losses arise from several different physical mechanisms. In a pure hydrogen plasma, they can be ascribed basically to the radiation emitted by charged particles when accelerated. Because of their lighter mass, only electrons need to be considered, while ions can be neglected. Two different accelerations affect the electron motion, the first ascribed to collisions with ions, the second to the cyclotron gyro–motion. The consequent radiations are usually called bremsstrahlung and cyclotron radiation respectively. The bremsstrahlung radiation losses p_{brems} can be easily evaluated considering the Hertz formula, giving the radiated power in the dipole approximation, and taking into account quantum mechanical effects which determine the effective cross section of Coulomb collisions. An easy and somewhat standard formula [23] is obtained

$$p_{brems} = 5.35\,10^{-5} \sum_j Z_j^2 n_j\, n_e T_e^{1/2}, \tag{3.33}$$

where p_{brems} is given in MW/m^3, temperatures in keV, densities in $10^{19}\,\mathrm{m}^{-3}$. The summation is extended over all the ion species of the plasma. Note that impurities contribute significantly because of the higher values of the charge number. The plasma cyclotron radiation losses p_{cyc} are, on the contrary, quite difficult to evaluate. Indeed they involve emission and absorption at harmonics of the cyclotron frequency in spatially varying plasma and magnetic field. Moreover the plasma behaves as optically thick to radiation at the fundamental cyclotron frequency. The principal energy loss occurs at harmonics of the cyclotron frequency, generated through relativistic effects, for which the transition from optically thick to optically thin behaviour occurs. Several formulae are available in the literature in order to take into account all these effects [31]. In PRETOR the following formula has been implemented, derived from [32]

$$\begin{aligned}\Phi_{Th} &= 2.15\,10^{-4}\left[\left(1+\frac{18\,a}{R_0\sqrt{T_e}}\right)(1-R_{wall})\,\frac{T_e^3\,B_t}{a\,n_e}\right]^{1/2}, \\ p_{cyc} &= 6.20\,10^{-4}\,\frac{\Phi_{Th}}{1+\Phi_{Th}}\,B_t^2\,T_e\,n_e, \end{aligned} \tag{3.34}$$

where p_{cyc} is in MW/m^3, lengths are in m temperatures in keV, densities in $10^{19}\,\mathrm{m}^{-3}$, and B_t in T. R_{wall} is a wall reflection coefficient to be given in input, and the term involving Φ_{Th} takes into account the plasma optical thickness. Note however that cyclotron radiated losses are generally negligible. In particular for TCV they are usually below 10 W/m^3, which is small compared to other loss mechanisms. When cyclotron radiation losses are important, more precise separate computations can be performed using coupled codes. In particular PRETOR has been coupled with the routine described in Ref. [33]. Due to the very low values for TCV, in the present thesis work this routine was never used, and cyclotron radiation losses were always computed by Eq. (3.34) The presence of impurities not only implies an increase in the radiation losses due to bremsstrahlung, but involves atomic processes causing additional and usually dominant radiation losses, namely line radiation and recombination. Simple formulae evaluating radiation losses due to atomic processes are usually strongly approximated, and has the general form

$$p_{Imp} = n_e\,n_p\,R_p(T_e) \tag{3.35}$$

where the radiation parameter R_P is a function of the electron temperature. The option which has been adopted in PRETOR in all the simulations performed in the present thesis work has been to use the following very simple formula

$$R_p(T_e) = \sqrt{Z_p}\,\frac{T_e\,10^4}{Z_p^2 + (T_e\,10^4)^2/Z_p^2}. \tag{3.36}$$

More complicated formulae can be used, obtained by interpolating atomic data tables [34], but they will not be discussed here. Note that atomic processes become important usually in the edge region, $r/a > 0.8$. Since the usual boundary condition used in the simulations imposes the temperature at the edge, the temperature profile is less sensitive to the power balance in the edge region, where atomic radiation losses become dominant. An additional energy sink must be ascribed to ionisation losses. These are evaluated in PRETOR as follows

$$p_{Ion} = 1.6\,10^{-6}\,E_i\,20\,\alpha_I\,(n_{Ni} + n_{Np}), \tag{3.37}$$

where $E_i = 10\,\mathrm{eV}$ is the ionisation energy, to be expressed in eV in the formula.

3.5 Numerical details about PRETOR

The radial coordinate

As already mentioned, the radial coordinate ρ in PRETOR is defined to be the average horizontal minor radius at the vertical position of the magnetic axis. Let us consider a given flux surface and denote by d the horizontal diameter of this flux surface, measured at the vertical position of the magnetic axis. In other words, d is the midplane width of the flux surface. We denote with D the horizontal diameter of the LCFS, still measured at the vertical position of the magnetic axis. Then, for each flux surface, we define $\rho \doteq d/2$, so that $0 \leq \rho \leq D/2$. On this radial coordinate the radial mesh is chosen in order to allow a more dense distribution of points close to the edge. The points of the radial mesh are equidistant with a small step $\Delta\rho_1$ from the edge up to a given radial positon ρ_m, and then with a larger step $\Delta\rho_2$ up to the centre. In the simulations we have chosen $\rho_m = 0.9$. The number of points N on the radial mesh has usually been taken equal to 39. For simulations involving short range variations of the pressure or current profile, we have used higher values of N, up to $N = 72$ for some simulations of the sawtooth period (Section 5.3).

Time evolution and sequence in the solution of the transport equations

As we have pointed out in Section 3.1, the transport equations are coupled. Their numerical solution would therefore involve the inversion of a single large non–tridiagonal matrix. A strong simplification is provided by solving the set of transport equations in sequence. This does not involve large errors as long as little time steps in the time evolution are considered. On the other hand, this allows very fast computation. Transport equations are solved by an implicit scheme in time and by a finite difference scheme in space. Solving the equations in sequence implies that only tridiagonal matrices must be inverted. In particular, the highest error is introduced in the equipartition term, which is not exactly the same in the electron and ion heat transport equations at each time step. Indeed it is evaluated with both the old electron and ion temperatures in the ion heat transport equation, and with the old electron temperature and the updated ion temperature in the electron heat transport equation. PRETOR runs with a non constant time step δt. The value of δt is determined by the following relation

$$\delta t^{(\mathrm{new})} = c_{\mathrm{speed}} \left\{ \max \left[\mathrm{abs} \left(\frac{\Delta W_{e,i}(\rho)}{\delta t^{(\mathrm{old})}} \, \frac{1}{W_{e,i}(\rho = a)} \right) \right] \right\}^{-1/2} .$$

Here c_{speed} is an input parameter and $W_{e,i}$ are the profiles of the electron and ion energy contents respectively. The parameter c_{speed} determines the order of magnitude of the value of δt and therefore the speed of the simulation. As a rule of thumb, one can choose this parameter as given by 1/20 of the confinement time expressed in seconds (in other words, for a plasma with $\tau_E \simeq 2\ 10^{-2}$ s, one takes $c_{\rm speed} \simeq 1\ 10^{-3}$). If the previous formula provides a value of $\delta t < 1$ μs, the minimum value of 1 μs is considered.

Interfaces with codes computing the heating sources

For the simulation of heated discharges we have implemented interfaces with the output of specific codes computing the heat sources. These codes are routinely run as post–processing codes after the experiments and use as input the experimental profiles. This approach can be considered self–consistent only as long as the simulated plasma profiles are close to the experimental ones, since the output of the auxiliary heating codes depends on the plasma and equilibrium profiles used in input. On the other hand, this approach allows to simulate the discharges using the most realistic estimation of the heating sources, and therefore becomes more stringent in assessing the role of the transport model. During this thesis work, specific interfaces have been implemented with different codes: TORAY–GA [26] for electron cyclotron resonance heating in TCV (Sections 4.6 and 5.3), PENCIL [35] and PION [29] for neutral beam injection (Section 5.4) and ion cyclotron resonance heating respectively in JET.

A different approach, which is completely independent of any experimental data, is to couple the auxiliary heating codes to the transport code, using as input the plasma and equilibrium profiles directly computed by the transport simulation. This approach, as already mentioned, has been used coupling PRETOR with PION for predictions of the ITER performance with ICRH [30].

3.6 Transport models

Several different transport models have been developed by the fusion community over the years. They can be divided in two main groups: the semi–empirical models and the theory based models. Semi–empirical models can involve physical ideas like simplified theoretical models, dimensional analysis, critical gradients, but they mainly determine the parameter dependence and magnitude of particle and heat diffusivities by experimental comparisons. On the other hand, theory based models are completely derived from first principle physics, and can eventually include a few fitting parameters which arise from theories which are not entirely developed, like for instance for the turbulence saturation levels. A comprehensive and very recent review of all the main transport models currently used and developed can be found in Ref. [21], together with a complete list of References. Another important, although less recent, review which must be cited is Ref. [36]: it includes the first detailed comparisons of the predictions of several different models with the experimental results. A more specific application and comparison of the simulations and predictions of the most recent theory based models is presented in Ref. [37].

The predictions of these models can strongly disagree. For instance the predicted ITER fusion power can differ by a factor 6 among the most pessimistic and most optimistic models [21]. The validation of a transport model over a wide experimental database, including data from the largest possible number of exisiting tokamaks, is therefore of major importance in order to obtain the most reliable predictions of the performance of the designed future devices. Nevertheless, as already mentioned, in what follows we shall not enter in this research domain, and we shall not compare results given by the application of different transport models in the simulation of TCV discharges. During the present thesis work we have almost completely focused (and limited) our analysis to the application of one specific model, the semi–empirical RLW transport model, regarded as a tool to investigate the nature of the heat electron transport in TCV.

3.6.1 The Rebut–Lallia–Watkins local transport model

The Rebut–Lallia–Watkins transport model has been derived with the assumption that confinement degradation in tokamaks due to the presence of anomalous transport must be ascribed to a single underlying phenomenon. This physical phenomenon has been identified in the model as turbulence in the magnetic topology. In Ref. [38] a theoretical model has been developed in order to evaluate the effect on the heat flux of the interaction of several sets of almost overlapping small magnetic islands and the consequent surrounding ergodisation of the magnetic field lines. These results have been revised on the basis of a dimensional analysis [39], in which a set of normalized structural parameters have been identified, representing the power flow, the plasma pressure, the resistivity and the thermal diamagnetic drift speed, and assuming that a single relationship must exist among them. From experimental observations suggesting a large resilience to changes in the electron temperature profile in JET [40], such relationship has been interpreted as defining a critical value for the electron temperature gradient, above which the anomalous transport starts to be at play. The power balance between the kinetic energy associated to the flow of electrons around the islands, at the diamagnetic velocity, and the resistive dissipation of the induced currents needed to mantain the perturbed magnetic topology of the islands provides an expression for the critical electron temperature gradient [39], Eq. (3.40). When the electron temperature gradient exceeds the critical value, also the overlapping parameter of magnetic islands exceeds a corresponding critical value, and islands overlap radially, involving a chaotic behaviour of the field lines. On the basis of the evaluations of the heat flow generated by this turbulent magnetic topology [38], a global scaling law and a complete model both for electron and ion heat conductivities has been proposed in [15]. This model exhibits a gyro–Bohm nature. In [14] the model has been extended also to particle transport, assuming that the same underlying phenomenon is responsible for both particle and heat anomalous transport. Moreover, the ion heat conductivity has been modified introducing factors which imply a Bohm nature to capture ITER-89P [41] scaling law. This model has been applied also by the ITER 1D Modelling Working Group [21, 25] and identified by the acronym RLWB. This model has been implemented in PRETOR and will be presented in this form in the following paragraph.

3.6.2 Transport coefficients in PRETOR

The transport coefficients are made up of the neoclassical and anomalous contributions. Hence, for the heat conductivities we can write:

$$\chi_e = \chi_{e,neo} + \chi_{e,an} \qquad \chi_i = \chi_{i,neo} + \chi_{i,an} \tag{3.38}$$

The neoclassical contribution can be evaluated using formulae given in Section 2.4. The different terms can be easily identified by means of the general expressions for the thermodynamic fluxes given in Eqs. (2.40). The anomalous contribution $\chi_{e,an}$ is given by

$$\begin{aligned} \chi_{e,an} \; = \; & \frac{\mathrm{C}_{e,an}}{R_0^{1/2}}\, \epsilon^{1/2} \sqrt{1+Z_{eff}} \left| \left(\frac{\nabla T_e}{T_e} + 2\frac{\nabla n_e}{n_e} \right) \frac{q\,\rho}{s} \right| \sqrt{\frac{T_e}{T_i}}\, {B_t}^{-1} \\ & \left(1 - \frac{\nabla T_{RLW}}{\nabla T_e} \right) \mathrm{H}(\nabla T_e - \nabla T_{RLW}) \end{aligned} \tag{3.39}$$

where H(x) is the Heaviside function, and where the notation ∇T_e simply means $\mathrm{d}T_e/\mathrm{d}\rho$. The critical electron temperature gradient is given by the expression

$$\nabla T_{RLW} = \mathrm{C}_{gcrt}\, \frac{1}{q} \left(\frac{\eta\, j\, {B_t}^3}{n_e \sqrt{T_e}} \right)^{1/2}, \tag{3.40}$$

where η is the neoclassical resistivity, as given in Section 2.4. For the anomalous ion heat conductivity, we use the following expression

$$\chi_{i,an} = \chi_{e,an}\, \mathrm{C}_{i,an}\, \frac{2T_e}{(T_e+T_i)^{\frac{3}{2}}}\, \frac{0.3\, R_0\, B_t}{\sqrt{1+Z_{eff}}}\, \frac{n_e}{n_i+n_p}. \tag{3.41}$$

No heat pinch contribution has been introduced in the model, therefore $v_{PTe} = v_{PTi} = 0$.

Particle diffusion coefficients and pinch velocities can be written in the same way

$$D_i = D_{i,neo} + D_{i,an} \qquad D_p = D_{p,neo} + D_{p,an} \tag{3.42}$$

$$v_{Pi} = v_{Pi,neo} + v_{Pi,an} \qquad v_{Pp} = v_{Pp,neo} + v_{Pp,an} \tag{3.43}$$

The neoclassical particle pinch velocity is essentially given by the Ware pinch [42]. For instance, this can be easily related to formulae given in Section 2.4

$$v_{Pi,neo} = -\frac{F}{R_0 B_{po}}\, \frac{\tilde{E}}{B_0}\, F_{13}(f^{31}_{\mathrm{teff}}),$$

where F_{13} is given by Eq. (2.27c) and f^{31}_{teff}, taking into account collisional effects, by Eq. (2.33a). The anomalous particle diffusion coefficients are assumed proportional to $\chi_{e,an}$ while the ratio of the anomalous pinch terms to the particle diffusivities are assumed proportional to the magnetic shear $s = \rho\,\mathrm{d}\mathrm{ln}q/\mathrm{d}\rho$,

$$D_{i,an} = D_{p,an} = \mathrm{C}_{D,an}\,\chi_{e,an} \qquad v_{Pi,an} = v_{Pp,an} = \mathrm{C}_{P,an}\,D_{i,an}\,\frac{s}{\rho}\,\mathrm{H}(s) \tag{3.44}$$

The coefficients C_{gcrt}, $\mathrm{C}_{e,an}$, $\mathrm{C}_{i,an}$ and $\mathrm{C}_{D,an}$, $\mathrm{C}_{P,an}$ have been determined on the basis of a set of simulations of JET discharges and fixed as follows

$$\mathrm{C}_{crt} = 6, \quad \mathrm{C}_{e,an} = 2, \quad \mathrm{C}_{i,an} = 2, \quad \mathrm{C}_{D,an} = 0.5, \quad \mathrm{C}_{P,an} = 0.5. \tag{3.45}$$

Values close to these ones have been found adequate to simulate the temperature profiles of recent JET discharges, in a work dedicated to the simulation of the sawtooth period during neutral beam injection, Section 5.4. On the contrary, this choice has not been found appropriate to simulate the temperature and density profiles in TCV, subsection 4.5.2. Note that since TCV does not yet have accurate T_i measurements, $\mathrm{C}_{i,an}$ has been always kept equal to 2, consistently with Eq. (3.45).

The expressions for the anomalous heat conductivity and the critical electron temperature gradient will be largely discussed in the applications on TCV in the next Chapter. Nevertheless, at this stage, some comments can be useful in order to introduce what will follow. We note first that, even if the RLW local transport model involves a threshold on the temperature gradient, it can not be considered similar to theoretical models based on drift–waves microinstabilities, which involve a critical value of the normalized gradient $R/L_{Te} = R|\nabla T_e|/T_e$. Actually, the expression for ∇T_{RLW} is inversely proportional to the electron temperature, which is a somewhat opposite behaviour than the one predicted by theoretical models. Furthermore, the strong dependence on the magnetic field as well as its independence on the magnetic shear have been largely analyzed in Ref. [43] and found inadequate. In this Reference it was proposed to modify the expression for the critical gradient ∇T_{RLW}, eliminating the B_t dependence as follows

$$\nabla T_{RLW\,H} = \frac{15}{q}\left(\frac{\eta j}{n_e\sqrt{T_e}}\right)^{1/2}.$$

This formula recovers Eq. (3.40) for $B_t = 1.8$ T. In TCV the toroidal magnetic field is not largely flexible and operation is performed usually at a fixed value of B_t, around 1.4 T. As it will be discussed in detail in subsection 4.5.1, this low value of the magnetic field, consistently with the findings of Ref. [43], plays a favourable effect for the satisfactory application of the RLW model to TCV plasmas. We shall show that the RLW formula gives values of the critical gradient which are well below the measured temperature gradients in TCV.

The expression of the heat conductivity involves the term

$$\left|\left(\frac{\nabla T_e}{T_e}+2\frac{\nabla n_e}{n_e}\right)\frac{q\,\rho}{s}\right|$$

which can lead to singularities for $s = 0$. For this reason in the numerical implementation we add 1/100 to the absolute value of the term $s/(q\rho)$. Local minima or maxima of the q profile imply local spikes in the transport coefficients which do not modify essentially the temperature profile, as long as they remain sufficiently localized. In the case of extended plasma regions with flat q profiles, like for instance in the plasma centre, on the contrary, the formula implies an effective increase of transport. Note this is somewhat balanced, since the increase of χ_e due to q flattening reduces the temperature and density gradients, which imply in their turn a reduction of χ_e. Low temperature gradients imply also lower values of the term $(1 - \nabla T_{RLW}/\nabla T_e)$. The two effects ascribed to low temperature gradients are usually dominant as compared with the effect due to low shear. We shall show that temperature profile broadening obtained by off–axis electron heating implies a broader central region with flat q profile, but also a low central heat conductivity from the RLW model (subsection 4.6.5, Figures 4.37 and 4.38). On the contrary, with this model it is almost impossible to obtain strongly peaked temperature profiles when the shear is too flat in the centre. This has been found to have important implications in the simulation of discharges in TCV in which a regime of improved confinement has been obtained by on–axis counter current drive (Section 4.6). We must also stress that, in the case of negative shear, we do not involve any additional reduction of the transport coefficients. The reduction of transport is just the one provided by the corresponding increase of shear, due to the dependence $\chi_e \propto |1/s|$. However, it must be mentioned that in the literature different options have been chosen on this point. In particular in Ref. [44], for the simulation of the JET PEP mode, the ion and electron transport coefficients were reduced to the ion neoclassical levels within the region of negative shear. The term $\sqrt{T_e/T_i}$ plays also an important role, in particular when the critical gradient becomes negligible as compared with the temperature gradient, like in the case of TCV plasmas with auxiliary heating. In this case this term allows an overall dependence of the heat conductivity on the electron temperature of the kind $\chi_e \propto T_e^{\alpha}$. In subsection 4.5.4 we shall show that due to this specific dependence, the model allows one to reproduce in the simulations the experimentally observed stiff behaviour of the electron temperature.

In PRETOR, the simulation of H–mode profiles is produced by a reduction of the transport coefficients from the edge up to a given position on the minor radius. This position can be chosen by the user. The level of this reduction needs also to be given in input. Note that even if the edge pedestal temperature is fixed by the boundary condition, a factor reducing transport close to the edge becomes necessary in order to prevent the simulated profile to assume non–monotonic oscillations close to the edge, when the pedestal is large. The L–H transition is automatically triggered during a simulation when the edge value of the electron heat source, including equipartition, exceeds a threshold whose value must be provided in input. This empirical model has been used in the simulation of H–mode profiles in JET, in the work dedicated to modelling and simulation of the sawtooth period during neutral beam injection (Section 5.4).

For the prediction of ITER burning plasma profiles, the RLW coefficients in PRETOR are multiplied by a factor which allows the simulation to follow the global plasma performance predicted by a prescribed scaling law. Let us assume that at a given time step the confinement time in the simulation is τ_E and that, adopting the plasma parameters of the simulation at the same time step, the scaling law provides a value τ_L. At the next time step, after a time δt, all the transport coefficients are then reduced by the factor

$$1+\left(\frac{\tau_E}{H\,\tau_L}-1\right)\,\delta t,$$

where H is a supplementary factor enhancing the plasma performance as compared with the scaling law.

Bibliography

[1] P.H. Rutherford and E.A. Frieman, Phys. Fluids **11**, 569 (1968).

[2] J.B. Taylor and R.J. Hastie, Plasma Physics **10**, 479 (1968).

[3] B.B. Kadomtsev *Plasma Turbulence* (London: Academic) (1965).

[4] J.W. Connor and O.P. Pogutse, Plasma Phys. Control. Fusion **43**, 155 (2001).

[5] J.D. Callen and M.W. Kissick, Plasma Phys. Control. Fusion **39**, B173 (1997).

[6] P.A. Politzer, Phys. Rev. Lett. **84**, 1192 (2000).

[7] P.H. Diamond, T.S. Hahm, Phys. Plasmas **2**, 3640 (1995).

[8] X. Garbet, R.E. Waltz, Phys. Plasmas **5**, 2836 (1998).

[9] B.A. Carreras, D.E. Newman, V.E. Lynch, P.H. Diamond, Plasma Phys. Rep. **22**, 740 (1996).

[10] J.M. Carlson *et al*, Phys. Rev. Lett. **65**, 2547 (1990).

[11] B.A. Carreras, Bull. Am. Phys. Soc. **43**, 1920 (1998).

[12] J.A. Krommes, Phys. Plasmas **7**, 1752 (2000).

[13] F. Porcelli, E. Rossi, G. Cima, A. Wootton, Phys. Rev. Lett. **82**, 1458 (1999).

[14] D. Boucher, P.H. Rebut, in Proc. IAEA Tech. Committee Meeting on *Advances in Simulation and Modelling of Thermonuclear Plasmas*, Montreal 1992, p. 142 (1993).

[15] P.H. Rebut, P.P. Lallia and M.L. Watkins, Proc. 12th Int. Conf. on *Plasma Physics and Controlled Nuclear Fusion Research*, Nice 1988, IAEA Vienna 1989, Vol. 2, p. 191.

[16] G. Bateman *et al*, Phys. Plasmas **5**, 1793 (1998).

[17] M. Kotschenreuter *et al*, Phys. Plasmas **2**, 2381 (1995).

[18] G.V. Pereverzev, *et al*, Rep. IPP 5/42, Max-Planck-Institut für Plasmaphysik, Garching (1991).

[19] C.E. Singer *et al*, Comp. Phys. Comm. **49**, 275 (1988).

[20] G. Cenacchi, A. Taroni, *"JETTO: A free Boundary Plasma Transport Code"*, Rep. JET-IR(88)03, JET Joint Undertaking, Abingdon (1988).

[21] ITER Physics Expert Groups on Confinement and Transport and Confinement Modelling and Databases, ITER Physics Basis Editors, Nucl. Fusion **39**, 2175 (1999).

[22] A. Airoldi, G. Cenacchi, Nucl. Fusion **37**, 1117 (1997).

[23] J. Wesson, *"Tokamaks"*, Clarendon Press, Oxford 1987.

[24] F. L. Hinton and R. D. Hazeltine, Rev. Mod. Phys. **48**, 239 (1976).

[25] The ITER 1D Modelling Working Group: D. Boucher, J.W. Connor, W.A. Houlberg, M.F. Turner, *et al*, Nucl. Fusion **40**, 1955 (2000).

[26] R.H Cohen, Phys. Fluids **30**, 2442 (1987);
K. Matsuda, IEEE Trans. Plasma Sci. **PS-17**, 6 (1989);
Y.R. Lin-Liu *et al*, in Controlled Fusion and Plasma Physics (Proc. 26th Eur. Conf Maastricht, 1999), Vol. 23J, European Physical Society, Geneva (1999), p. 1245.

[27] T.J.J. Tala, *et al*, Plasma Phys. Control. Fusion **43**, 507 (2001), and References therein.

[28] T.S. Hahm and K.H. Burrell, Phys. Plasmas **2**, 1648 (1995).

[29] L.-G. Eriksson, T. Hellsten and U. Willén, Nucl. Fusion **33**, 1037 (1993).

[30] F. Louche, in *Theory of Fusion Plasmas*, Proc. Joint Varenna-Lausanne International Workshop, Varenna 1998 (J.W. Connor, E. Sindoni, J. Vaclavik, Eds), ISPP-18, Ed. Compositori, Bologna 1999, p. 537.

[31] M. Bornatici, R. Cano, O. De Barbieri, F. Engelmann, Nucl. Fusion **23**, 1153 (1983), and references therein.

[32] S. Tamor, *"Studies of Emission and Transport of Synchrotron Radiation in Tokamaks"*, Science Applications Inc., La Jolla, Report LAPS-72, SAI-023-81-110 LJ (March 1981).

[33] S. Tamor, *"Simple Fast Routine for Computation of Energy transport by Synchrotron Radiation in Tokamaks and Similar Geometries"*, Science Applications Inc., La Jolla, Report LAPS-72, SAI-023-81-189 LJ, (May 1981).

[34] P.E. Post *et al* Atomic Data and Nuclear Data Tables **20**, 397 (1977).

[35] D Bailey, JET-R (1998) 04;
P.M. Stubberfield and M.L. Watkins, JET-DPA(06)/87, 1987;
M Cox, Culham report for JET KR5-33-04, 1984.

[36] J.W. Connor, Plasma Phys. Control. Fusion **37**, A119 (1995).

[37] A.M. Dimits, *et al*, Phys. Plasmas **7**, 969 (2000).

[38] P.H. Rebut, *et al*, in *Plasma Physics and Controlled Nuclear Fusion Research*, Proc. 11th IAEA International Conf., Kyoto 1986, **2**, 187 (1987).

[39] P.H. Rebut, M.L. Watkins, and P.P. Lallia, Proc. of 14th European Conf. on *Controlled Fusion and Plasma Physics*, Madrid 1987, **11D(1)**, 172 (1987).

[40] P.H. Rebut, M. Brusati, Plasma Phys. Control. Fusion, **28**, 113 (1986).

[41] P.N. Yushmanov *et al*, Nucl. Fusion **30**, 1999 (1990).

[42] A.A. Ware, Phys. Rev. Lett. **25**, 916 (1970).

[43] G.T. Hoang, B. Saoutic, L. Guiziou *et al*, Nucl. Fusion **38**, 117 (1998).

[44] M. Hugon, B.Ph. van Milligen, P. Smeulders *et al*, Nucl. Fusion **32**, 33 (1992).

Chapter 4

Modelling transport in TCV

4.1 Introduction

In this chapter we present an analysis of electron transport in TCV, with particular emphasis on heat transport in discharges with dominant electron cyclotron heating (ECH). This study has been performed with the PRETOR code, described in the previous Chapter, developing some specific numerical tools intended for data analysis related to heat transport, in particular for power balance calculations. This work had the preliminary purpose of validating the RLW local transport model in the simulation of TCV plasmas over a set of different heating and plasma conditions. The high shape flexibility and the powerful ECH system of TCV enable interesting and relevant transport studies. Auxiliary–heated TCV plasmas have low density, due to the cut–off for the X2-mode, and large ratios of electron to ion temperature. The model turns out to be remarkably successful in these conditions. We investigate the reasons for this good agreement, in an attempt to infer information on the nature of anomalous electron transport. In particular the model correctly reproduces the record electron temperature gradients obtained during discharges with improved confinement in TCV. The successful application of this transport model has allowed us to supply the tokamak with a set of numerical tools suited for transport analysis, adopting user–friendly interfaces and automatic procedures which allow one to use the code as a complete TCV simulator and predictor. The continuous interaction between experiment and modelling has significantly supported the research and the identification of a quasi–stationary regime of improved confinement in TCV. A large part of this Chapter, Section 4.6, will be dedicated to the presentation of the experimental observations, simulation results and discussion of this regime.

4.2 Brief description of TCV

The Tokamak à Configuration Variable (TCV) at the Centre de Recherches en Physique des Plasmas (CRPP) is a medium size tokamak, designed to investigate the effects of plasma shape on confinement and stability [1]. The principal design parameters of the machine are presented in Table 4.1. In Figure 4.1 is shown a schematic view of TCV. TCV is equipped with an air core transformer and the toroidal magnetic field is produced by 16 toroidal field coils, connected in series. The flexibility of TCV to produce both diverted, single and double null, and limited highly shaped plasmas is due to its unique shaping control system, which consists of active feedback–controlled coils both outside and inside the vacuum vessel. The 16 external coils are mounted in two vertical stacks on both external sides of the vacuum vessel and are driven by slow power supplies. The fast internal coils (time response ~ 0.1 ms) are placed behind the graphite tiles and allow the stabilisation of highly elongated plasmas [1].

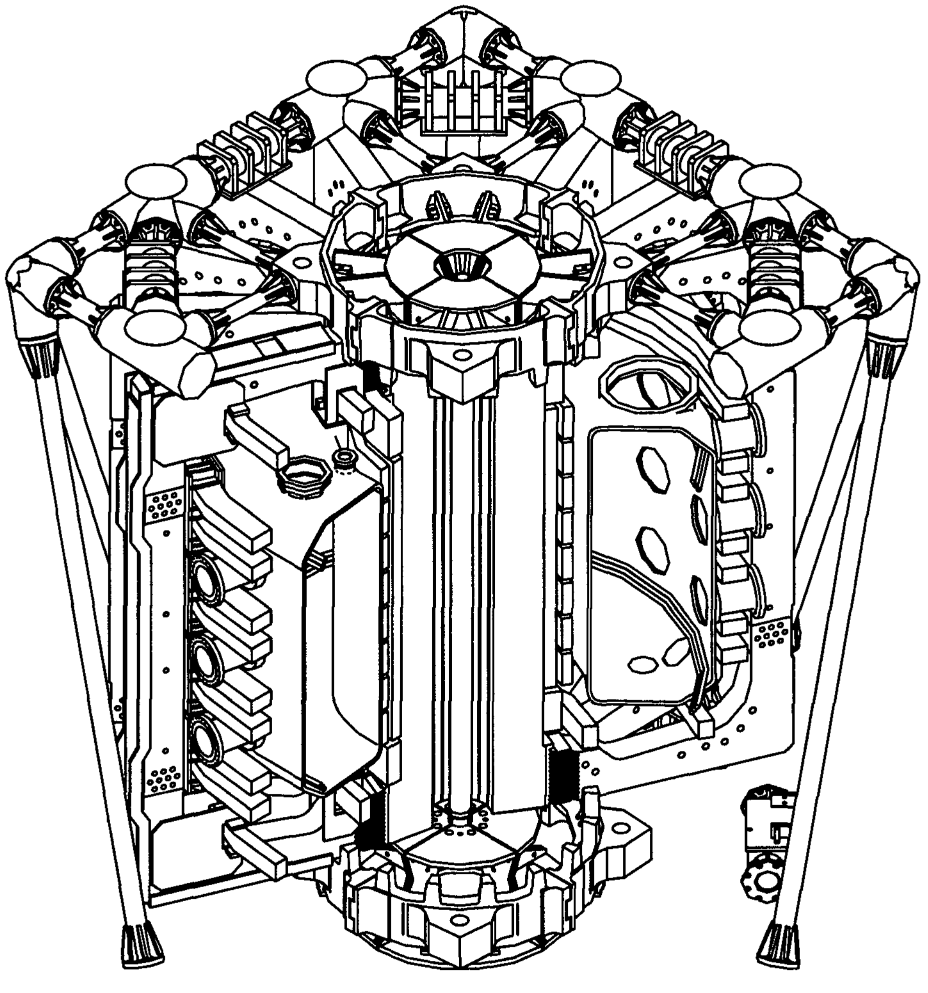

Figure 4.1: *Schematic view of TCV*

Parameters	Symbol	Value
Major radius	R_0	0.88 m
Minor radius	a	0.25 m
Nominal aspect ratio	$A = R_0/a$	3.5
Vacuum vessel elongation	k_{TCV}	2.9
Maximum plasma current	I_p	1.2 MA
Maximum central magnetic field	B_0	1.54 T
Maximum loop voltage	V_{loop}	10 V
Discharge duration		< 4 s
edge plasma elengation	k_a	1 - 2.82
edge plasma traingularity	δ_a	(-0.8) - (+0.9)

Table 4.1: *Main TCV parameters*

Since the beginning of operations, in November 1992, TCV has produced a wide range of different plasma configurations (Figure 4.2), limited (a), single null (b, c), and double null (d) diverted, obtaining low confinement (L–mode) and high confinement (H–mode) modes of operation in both limited and diverted configurations. Plasmas have been substained with currents up to 1 MA (e), and several different plasma shapes have been obtained, from standard D shapes to more exotic shapes, such as pear (g) and rectangular (l) shapes as well as doublets (h). The extreme plasma shapes produced so far are also illustrated by the case of maximum elongation as well as maximum negative and positive triangularity and squareness, Figure 4.2(i), (j), (k) and (l) respectively.

4.3 The TCV Electron Cyclotron heating system

TCV is equipped with a very flexible ECH system [2], which was designed to provide a maximum coverage of the poloidal cross section, because of the wide variety of plasma shapes, and which allows one also to modify the toroidal injection angles, thus permitting the generation of substantial electron cyclotron current drive (ECCD), both in co and counter directions. The system consists of two clusters of three gyrotrons each operating at the second harmonic frequency, f_{2ce} = 82.7 GHz, and one cluster of three gyrotrons at the third harmonic frequency, f_{3ce} = 118 GHz. The nominal power for each 82.7 GHz gyrotron is 465 kW and for each 118 GHz gyrotron is 480 kW, resulting in a total radio frequency power of 4.2 MW for a maximum pulse length of 2 s. Each gyrotron couples the electron cyclotron beam to an evacuated transmission line through which it propagates to a quasi-optical launching antenna installed on the TCV vessel. The polarization of each beam can be varied and is usually set for a propagation in the extraordinary mode (X2 and X3). The cut–off density for the X2-mode is $n_e \simeq 4.25\,10^{19}$ m^{-3}, while the X3-mode

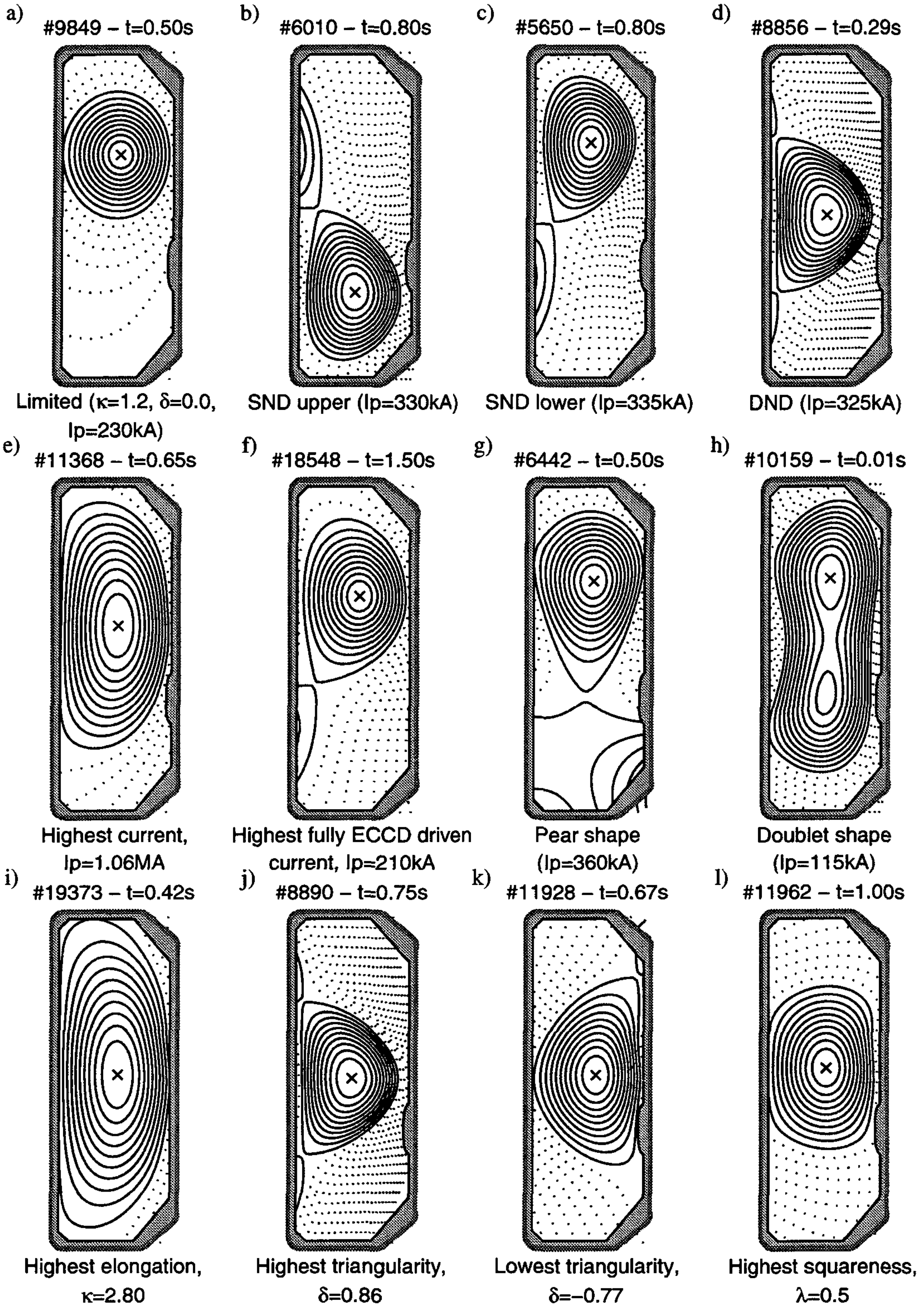

a) #9849 - t=0.50s
Limited (κ=1.2, δ=0.0, Ip=230kA)

b) #6010 - t=0.80s
SND upper (Ip=330kA)

c) #5650 - t=0.80s
SND lower (Ip=335kA)

d) #8856 - t=0.29s
DND (Ip=325kA)

e) #11368 - t=0.65s
Highest current, Ip=1.06MA

f) #18548 - t=1.50s
Highest fully ECCD driven current, Ip=210kA

g) #6442 - t=0.50s
Pear shape (Ip=360kA)

h) #10159 - t=0.01s
Doublet shape (Ip=115kA)

i) #19373 - t=0.42s
Highest elongation, κ=2.80

j) #8890 - t=0.75s
Highest triangularity, δ=0.86

k) #11928 - t=0.67s
Lowest triangularity, δ=-0.77

l) #11962 - t=1.00s
Highest squareness, λ=0.5

Figure 4.2: *Various plasma configurations and shapes produced in TCV*

extends the accessible domain of operation up to $n_e \simeq 11.5\,10^{19}$ m^{-3}, although with less localized power deposition.

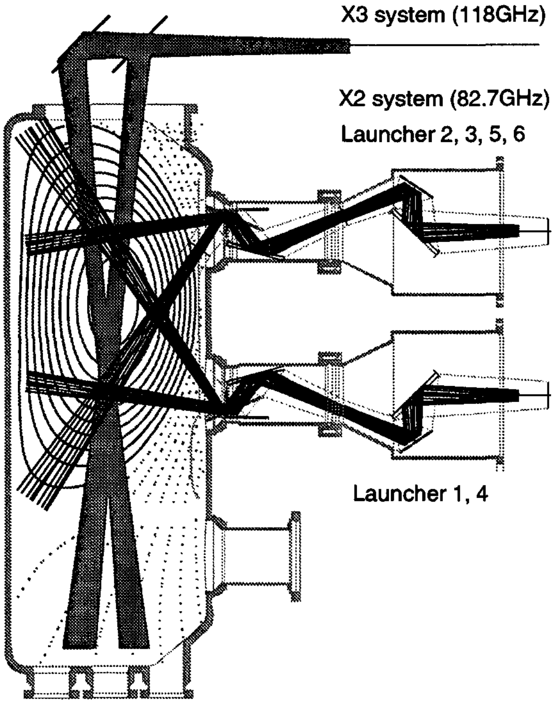

Figure 4.3: *X2 and X3 ECH launching system on TCV*

As shown in Figure 4.3, X2 launchers are placed on two equatorial (L1, L4) and 4 upper lateral ports (L2, L3 and L5, L6). Each launcher has two degrees of freedom. One provides steering of the microwave beam in a fixed plane, changing the poloidal injection angle, even during the discharge, allowing experiments with a sweep of the power deposition location. The other degree of freedom allows the rotation of the sweep plane between discharges, permitting experiments with different amounts of ECCD.

The three beams of the recently added X3 cluster are combined at one launcher at the top of the vessel, Figure 4.3. The mirror can be displaced radially ($\Delta r = \pm a/3$) between discharges to inject the beam either from the low or the high field side of the resonance. In order to maximize the absorption by increasing the path length through the plasma, the beam is injected nearly tangential to the resonant surface. The mirror can also be rotated during the discharge by ±5 degrees for fine adjustment of the beam direction.

In the present work, we have considered only discharges with Ohmic heating or ECH additional heating in X2.

4.4 Electron temperature behaviour with ECH in TCV

Several investigations have been undertaken to analyze both the global and local features of electron transport and electron temperature profiles in Ohmic discharges in TCV, [3] – [8]. For discharges with ECH, a more specific study of the global plasma response to auxiliary heating has been performed, deriving a TCV scaling law for the confinement time [9], but no detailed analysis on the local features of the electron temperature profiles in response to ECH has been carried out. This has motivated a preliminary investigation, in order to obtain a deeper understanding of the experimental behaviour to be simulated by transport modelling. This has also enabled us to supply TCV results to a comparative study of electron transport in different tokamaks [10], recently performed with the aim of identifying normalized plasma parameters related to electron transport whose value turns out to be independent of the machine and of plasma conditions.

In the tokamak plasma cross-section we can identify three regions relevant for transport studies: a central region, inside the mixing radius, in which transport is believed to be mainly determined by sawtooth activity in conventional scenarios; the confinement region, in which the intrinsic transport of both heat and particles plays the crucial role in determining the plasma profiles; and the edge region, close to the limiter or the separatrix, in which convection, radiation losses and atomic physics, as well as transport barriers and ELMs in H–modes should play the most important role, determining the boundary conditions for the profiles in the confinement region. In what follows we are directly concerned with the description of the electron temperature behaviour in the confinement region. We call central heating the auxiliary heating provided to the plasma inside the central region, hence without affecting directly the confinement region, whereas we shall refer to power depositions inside the confinement region as off–axis heating.

4.4.1 Central heating

TCV plasmas show a stiff behaviour in the confinement region in response to strongly increasing heating power in the centre. Indeed when the heating power is varied from Ohmic, to 1.35 MW ECH and then up to 2.7 MW ECH, the electron temperature profiles show a remarkable similarity in the confinement region when plotted in logarithmic scale, Figure 4.4. The power balance analysis of this discharge shows that the electron heat conductivity increases strongly in the confinement region, whereas the normalized dimensionless electron temperature gradient remains almost the same, independently of the power level, and essentially constant along the minor radius, Figure 4.5. Note also that in the central region, the electron heat conductivity does not respect the gyro-Bohm scaling, since $\chi_e/T_e^{3/2}$ in the plasma center becomes lower and lower with increasing heat-

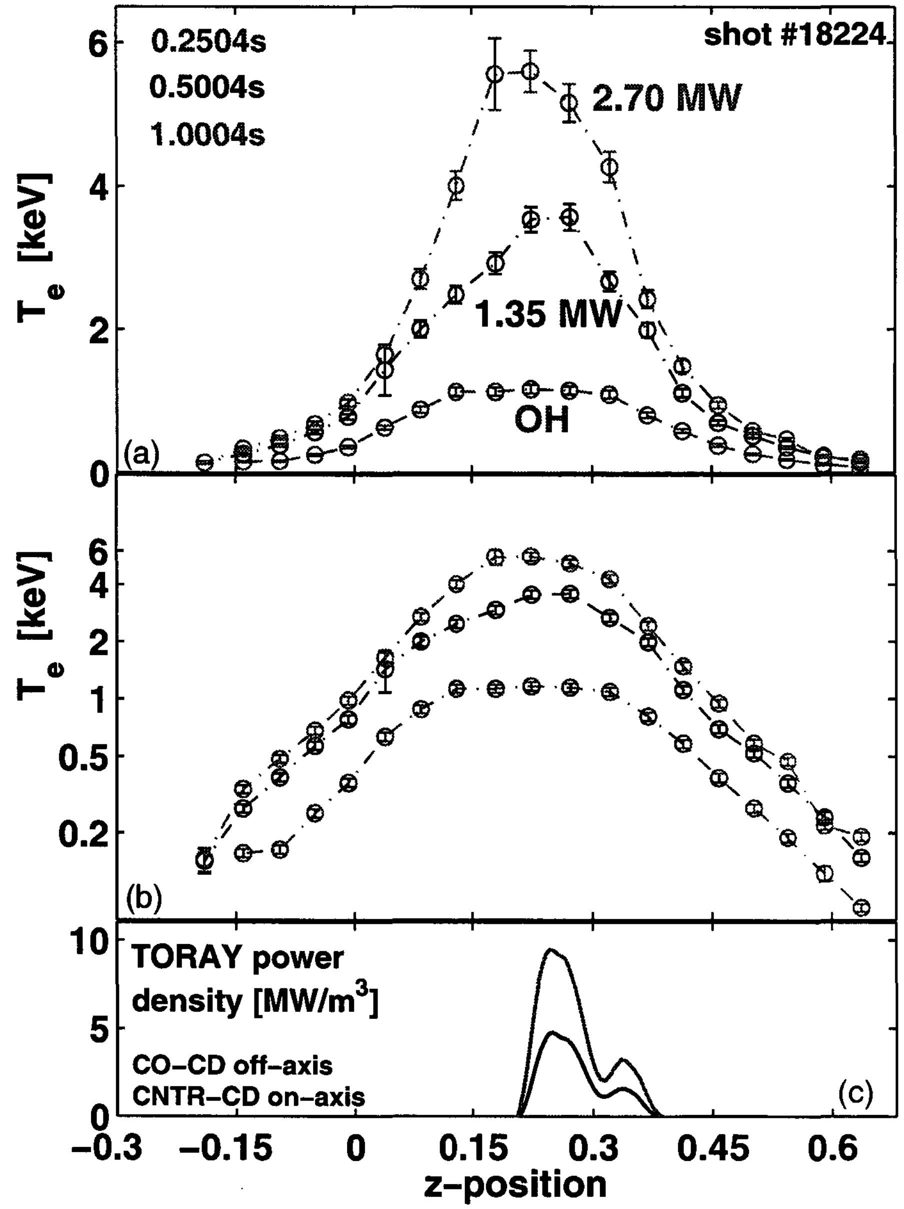

Figure 4.4: *Electron temperature profiles for shot ♯18224, in linear (a) and semi-logarithmic scale (b). In (c) the power deposition profile computed by TORAY-GA is plotted on the z-position of the vertical chord of the experimental measurements by means of the LIUQE equilibrium reconstruction.*

ing power.

In order to show the profile stiffness behaviour, a particularly important test is to plot the value of the electron temperature at the inside boundary of the confinement region, roughly $r/a = 0.4$, versus the value of the electron temperature at the ouside boundary of the same region, roughly $r/a = 0.8$. We have considered 6 time slices among 5 different shots, with increasing power from Ohmic up to 2.25 MW ECH, with on–axis deposition,

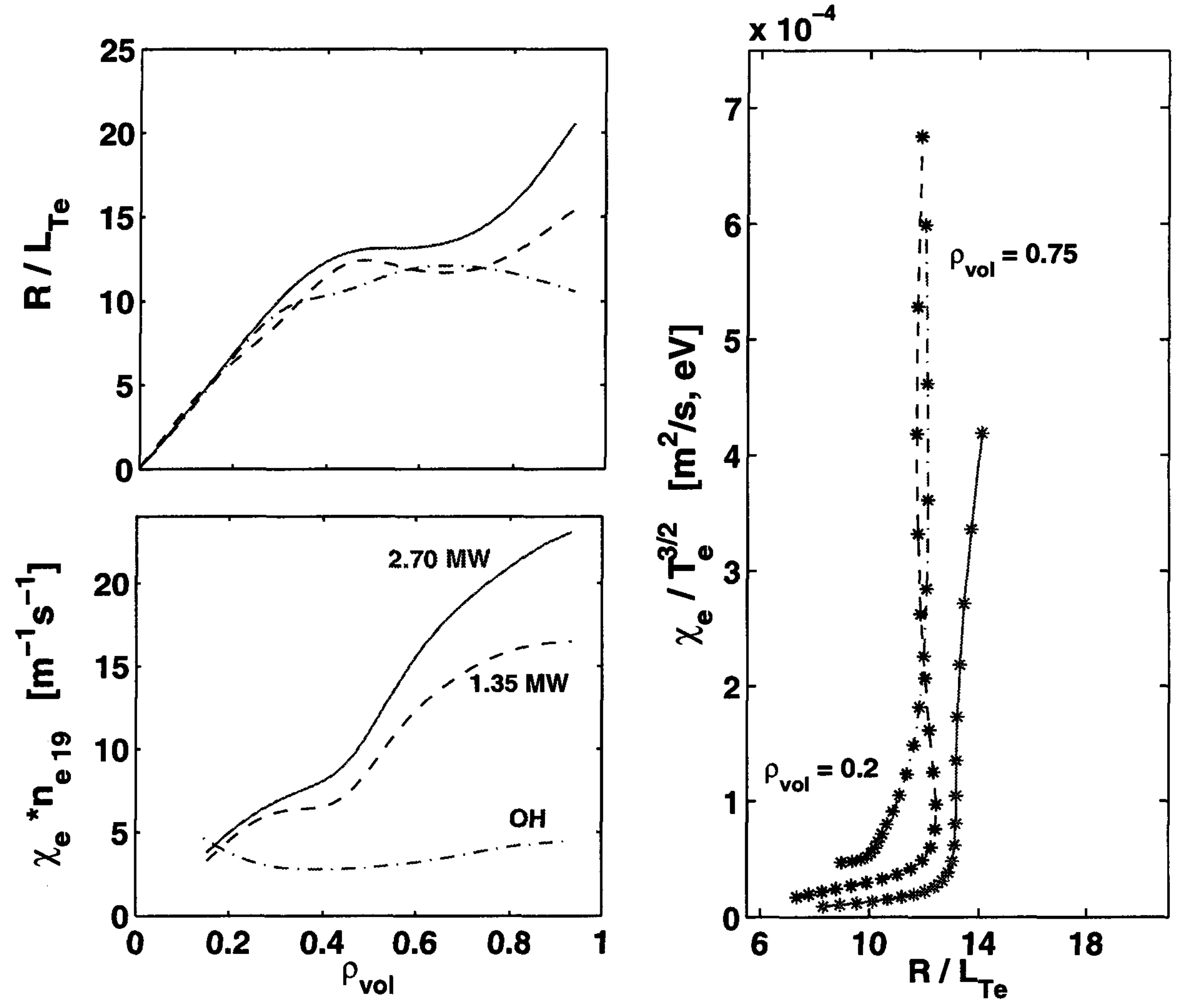

Figure 4.5: *Power balance analysis for shot* $\sharp$*18224, highlighting the stiff behaviour of the electron temperature in response to increasing central heating power (Ohmic heating is plotted with dash-dotted lines, 1.35 MW ECH with dashed lines and 2.70 MW with solid lines).*

hence with the centre of the deposition located at $\rho_{dep} = 0$ and all the power absorbed inside $r/a = 0.4$. The result of this analysis is shown in Figure 4.6. As already shown in the specific case of shot $\sharp$18224, Figure 4.5, the normalized dimensionless electron temperature gradient, R/L_{Te}, remains almost constant as a function of both space and power in the confinement region. Indeed, in Figure 4.7, we have plotted the profiles of R/L_{Te} for 20 time slices among 10 shots, from Ohmic up to 2.70 MW ECH. All these discharges have central heating, $\rho_{dep} < 0.4$, with line average density $n_{e\,lin} = 1 - 2\ 10^{19}\,\mathrm{m}^{-3}$ and different degrees of power localization, enabling the power density to range from 5 up to 150 MW/m^3, with corresponding levels of heat flux at $\rho_{vol} = 0.4$, computed by power balance analysis, from 0.02 to 0.5 MW/m^2. At $\rho_{vol} = 0.6$, roughly in the middle of the

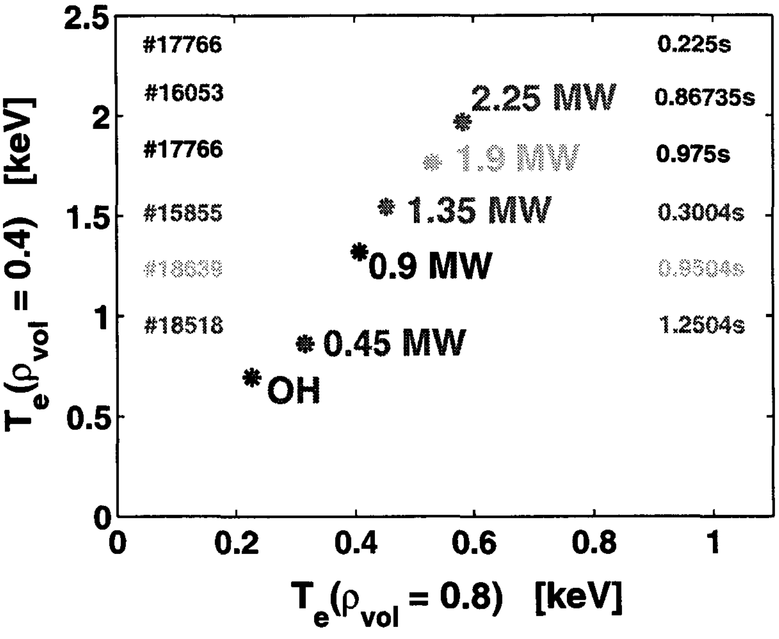

Figure 4.6: *Values of $T_e(\rho_{vol} = 0.4)$ vs values of $T_e(\rho_{vol} = 0.8)$, in shots with on-axis heating, turn out to well aligned, providing a further proof of profile stiffness.*

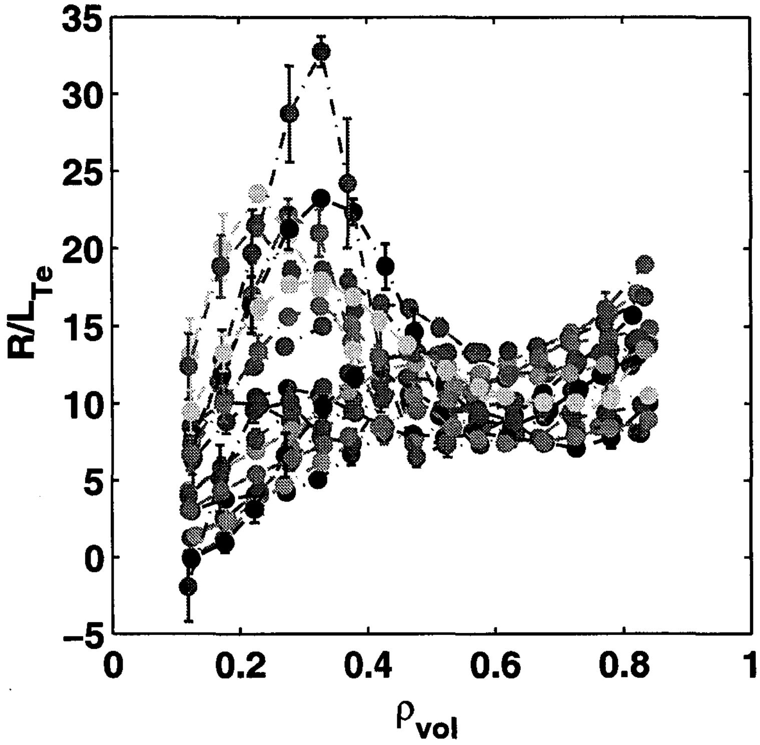

Figure 4.7: *Profiles of R/L_{Te} for 20 time slices among 10 shots, from Ohmic up to 2.70 MW ECH.*

confinement region, $R/L_{Te} \simeq 10 \pm 30\%$. The same behaviour of the electron temperature has also been observed in other tokamaks, with typical values of R/L_{Te} very close to the TCV value [10]. This analysis leads to the conclusion that indeed with central heating, the electron temperature in TCV shows a stiff behaviour in the sense that a dimensionless parameter, R/L_{Te}, can be identified, which is largely independent of the level of radial heat flux. In particular the value of R/L_{Te} turns out to be independent of the ratio T_e/T_i, which can vary by more than a factor of 5 from ohmic to ECH plasmas. This behaviour suggests the existence of a critical value of this parameter, possibly determined by microinstabilities producing the relevant anomalous transport, above which transport increases strongly, preventing the plasma profile from evolving further.

4.4.2 Off–axis heating

The stiff behaviour of the electron temperature in the confinement region with central heating motivates the investigation of the behaviour of the electron temperature when ECH is deposited inside the confinement region. A good example is provided by shot ♯19696, in which a stationary scenario has been obtained in a highly elongated plasma, $k = 2.4$, with 0.9 MW of ECH power deposited at $\rho_{\text{vol}} = 0.5$ and $\rho_{\text{vol}} = 0.8$ [11]. This discharge is characterized by very high values of q_{edge}, larger than 10 during the ECH phase, with q_0 largely above 1 and without sawteeth. The corresponding electron temperature profile, compared to the profile during the Ohmic phase, is shown in Figure 4.8. We see clearly that in this situation the profile can no longer be described as stiff. Indeed the ECH is able to "bend" the profile, changing the profile convexity, which is concave in Ohmic, typical for a highly elongated plasma with low plasma current and high q_{edge}, and becomes convex with additional off–axis heating. The power balance analysis comparing the two situations is shown in Figure 4.9(a). The Ohmic heating in the central region is strongly reduced during the ECH phase, but, in spite of this, the electron temperature profile, as shown in Figure 4.8 remains peaked in the centre. This implies a very strong reduction of the power balance heat conductivity in the centre, to values of 0.3 – 0.5 m^2/s. This is largely below the Ohmic level (2 – 3 m^2/s), and remarkably close to the neoclassical level ($\sim$0.1 m^2/s). Around the region in which the auxiliary heating power is deposited, the values of R/L_{Te} with ECH are below the corresponding values with only Ohmic heating [Figure 4.9(b)]. This can be regarded as consistent with the picture of a critical value of R/L_{Te} below which profile modifications are possible, and above which profile modifications are not permitted. Close to the edge, outside the deposition, R/L_{Te} becomes larger and larger, with edge values of the temperature which are below the corresponding values in Ohmic. This behaviour is somewhat opposite to the one observed with central heating, in which, increasing the auxiliary heating power in the centre, an increase in the value of the edge

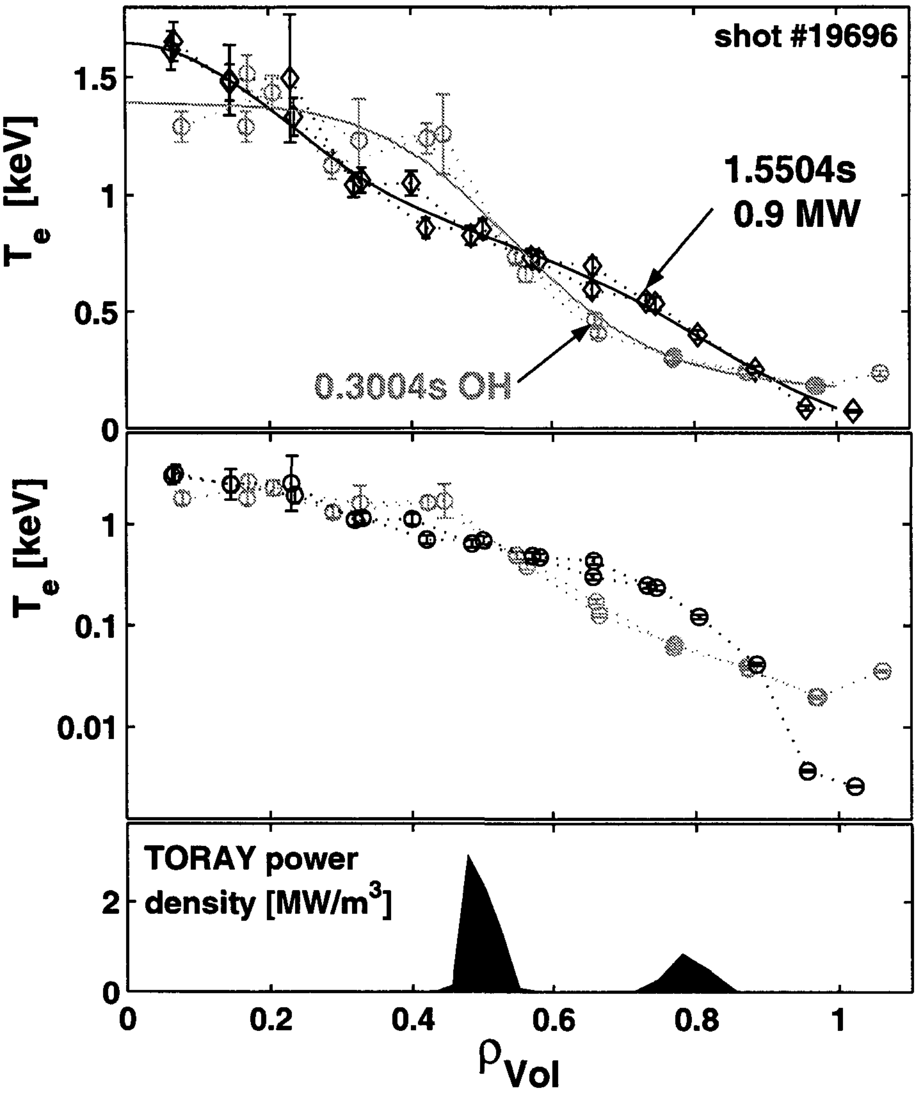

Figure 4.8: *Electron temperature profiles for shot ♯19696 in the Ohmic (circles in light grey) and in the ECH phase (diamonds in black). Solid lines show best fits to the data.*

temperature is observed, Figure 4.4. In any case this point needs further investigation, and a definitive statement about the connection between the edge and the centre of the plasma in response to different heating conditions cannot be formulated yet. The new diagnostic devoted to measuring the electron temperature at the plasma edge, by Thomson scattering with a high spatial resolution, will be very useful in order to assess this issue. Note that the strong reduction of the heat conductivity in the centre as a consequence of localized off–axis heating has not been observed only in the absence of sawtooth activity. Rather, this is a very general phenomenon. An example is given in Figure 4.10, showing the electron heat conductivity for the sawtoothing shot ♯17766.

In TCV the local power balance heat conductivity has always been found to be positive.

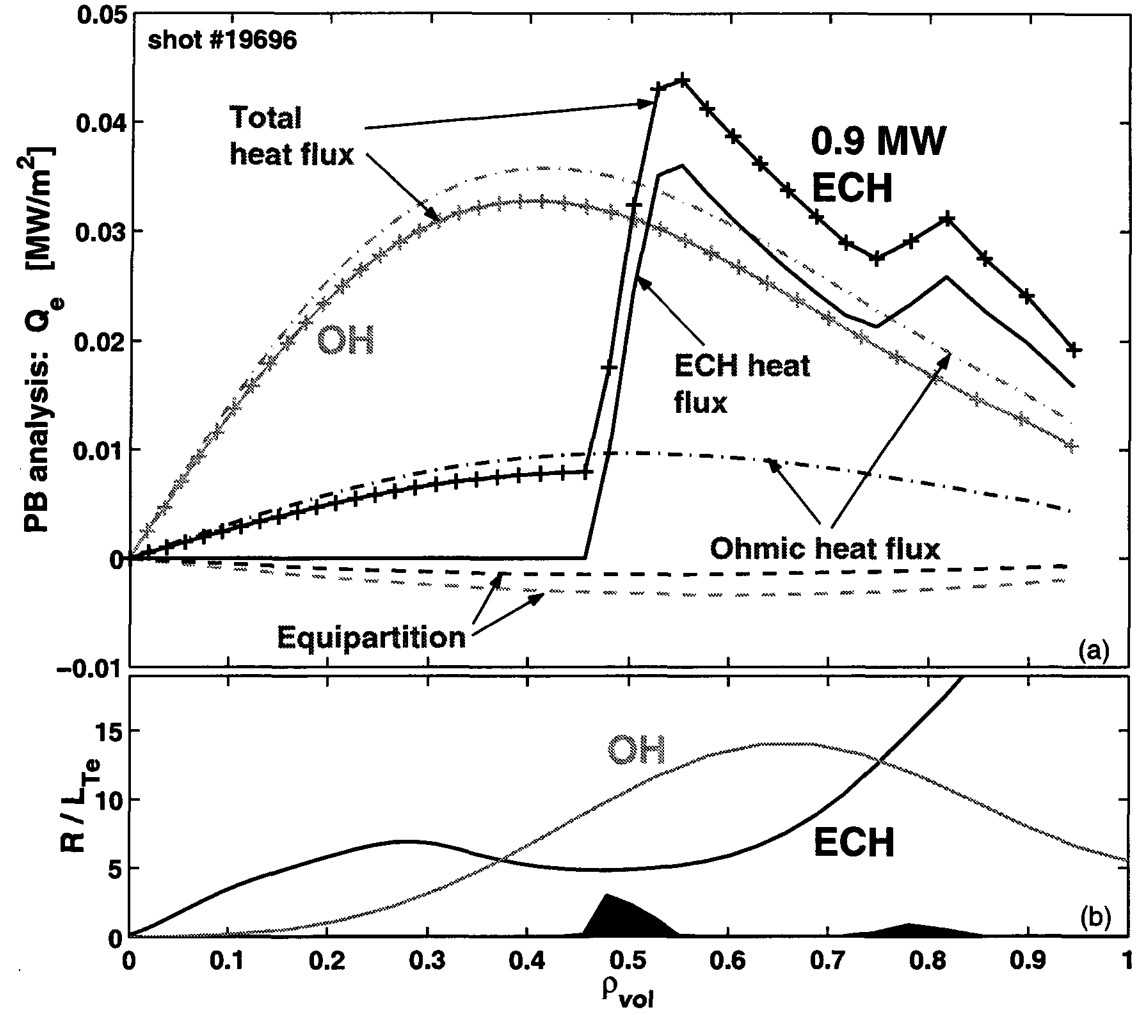

Figure 4.9: *(a) Power Balance analysis for shot ♯19696, comparing the Ohmic (light grey) and the ECH phase (black) of the discharge. (b) Corresponding dimensionless electron temperature gradient lengths R/L_{Te}.*

This is different from previous observations in DIII-D [12], and recent observations in FTU [13], in which the heat conductivity turns out to be locally negative in the centre, owing to the very high densities leading to very high radiation loss even in the plasma centre. This has suggested the presence of an inward heat pinch, which would restore a positive heat conductivity. In TCV, in which ECH operation is performed at very low plasma densities, there is pratically no radiation loss in the centre. Therefore, a power balance analysis cannot distinguish between the reduction of the effective transport arising from a lower electron heat conductivity or from the presence of an inward heat pinch. Only experiments with modulated electron cyclotron heating (MECH) could distinguish between the two cases, and would generate conclusive information about the presence or absence of a heat pinch with off–axis ECH in TCV. At this stage, we can only conclude that, with off–axis heating, in the interior of the deposition region, transport is strongly

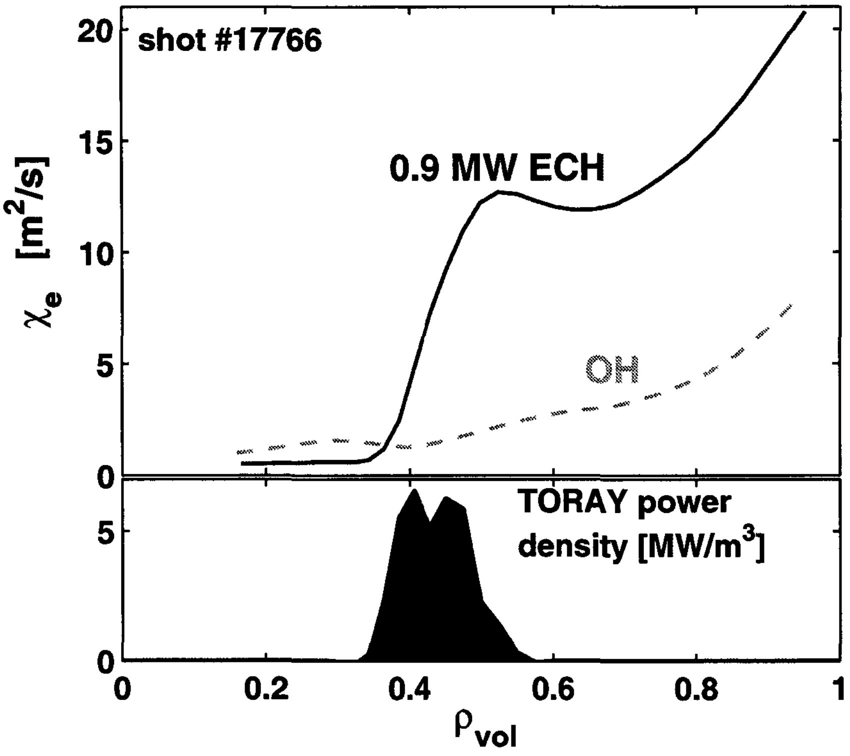

Figure 4.10: *Power Balance electron heat conductivity for shot ♯17766, comparing the Ohmic (dashed line) and the ECH (solid line) phase of the discharge.*

reduced, largely below the Ohmic level. Recent experiments in ASDEX Upgrade have shown an analogous behaviour of the power balance electron heat conductivity, with very low transport in the plasma centre, a step at the location of the off–axis ECH deposition, and high transport outside [14]. The analysis of MECH experiments have confirmed such a difference between transport levels inside and outside the deposition region and have shown that the transport reduction must be completely ascribed to a reduction of the heat conductivity, with no contribution coming from an inward heat pinch [14].

As a concluding remark we would like to emphasize that, as previously shown for the case of shot ♯19696, with sufficiently high levels of ECH power and correspondingly of ECH power densities compared to the Ohmic power density, (note that from this point of view TCV can reach regimes of operation which are not possible in other devices), the electron temperature profile can be strongly modified in the confinement (stiff) region, producing locally lower values of R/L_{Te}.

4.5 The RLW transport model applied to TCV discharges

The experimental observations described in the previous Section suggest that transport models which can be considered as good candidates to correctly simulate the electron temperature are those involving a critical value in R/L_{Te}. This is not the case for the semi-empirical model RLW [16], which involves a critical value of the electron temperature gradient ∇T_e and not of $\nabla T_e/T_e$ (subsection 3.6). On the other hand, the RLW global scaling has been found a valuable predictor of TCV global plasma performance both in Ohmic [4] and in ECH L–mode [9].

Moreover, the expression of the electron heat conductivity provided by this model has already been found to be in good agreement with several experiments, [17, 18, 19, 20], and more recently in [21]. In this last Reference a detailed analysis has allowed the authors to state that in the RLW model the plasma parameter dependence of the anomalous heat conductivity is correctly described, whereas the expression for the electron temperature critical gradient was found inadequate. In particular the model has been found to be in agreement with the experimental observations when the electron temperature gradient is well above the critical value provided by the model. Note also that the expression for the electron heat conductivity in the RLW model has a weak dependence on the ion temperature profile, as it only involves the ratio T_e/T_i to power 0.5, which is nearly independent of T_i at very high values of T_e/T_i. This turns out to be particularly appropriate for the typical TCV regime of operation with ECH, in which low plasma densities, imposed by the density cut–off for X2 absorption, imply that electron and ions are completely decoupled, with ratios of T_e/T_i ranging in general from 10 to 30. Note that this is also fortunate for TCV, in the absence of precise measurements of the ion temperature profile.

On the basis of all these elements, it can be stated that the RLW local transport model remains a good candidate for modelling the electron transport in TCV plasmas, in particular in the presence of ECH. We shall show, in subsection 4.5.4, that this model, even though it does not involve a critical value of the normalized electron temperature gradient $|\nabla T_e|/T_e$, allows one to reproduce the stiffness features observed in EC heated plasmas in TCV, by means of the specific dependence of the transport coefficient expression on plasma parameters in typical TCV plasma conditions. On the grounds of the results of Ref. [21], the first step in order to validate the RLW model for TCV transport modelling is to compare the experimental values of the electron temperature gradient to the corresponding critical values provided by the model.

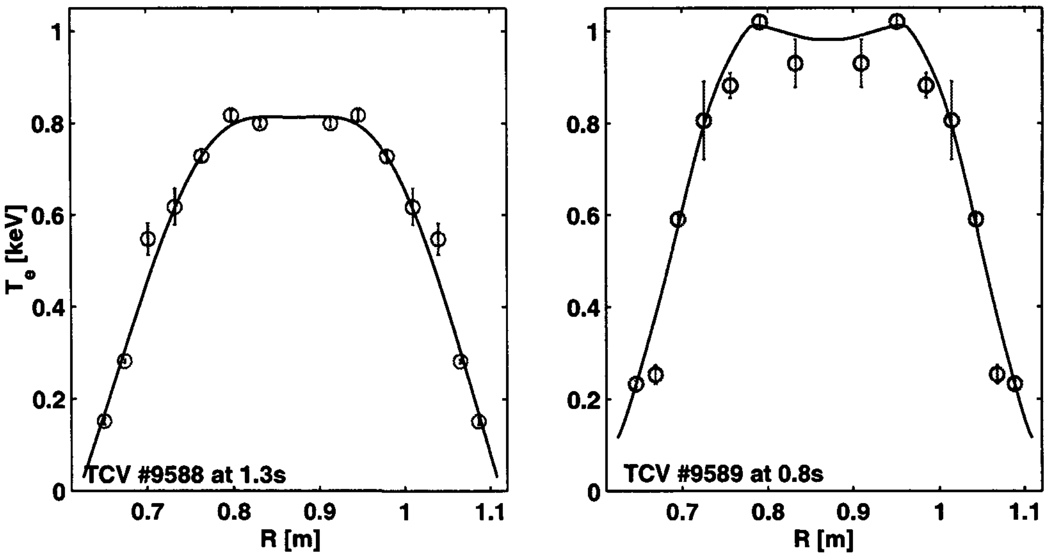

Figure 4.11: *Electron temperature profiles for shots ♯9588 and ♯9589, experimental measurements (symbols) and simulation results (solid lines). The experimental points have been mapped to the major radius on the midplane by means of the equilibrium reconstruction.*

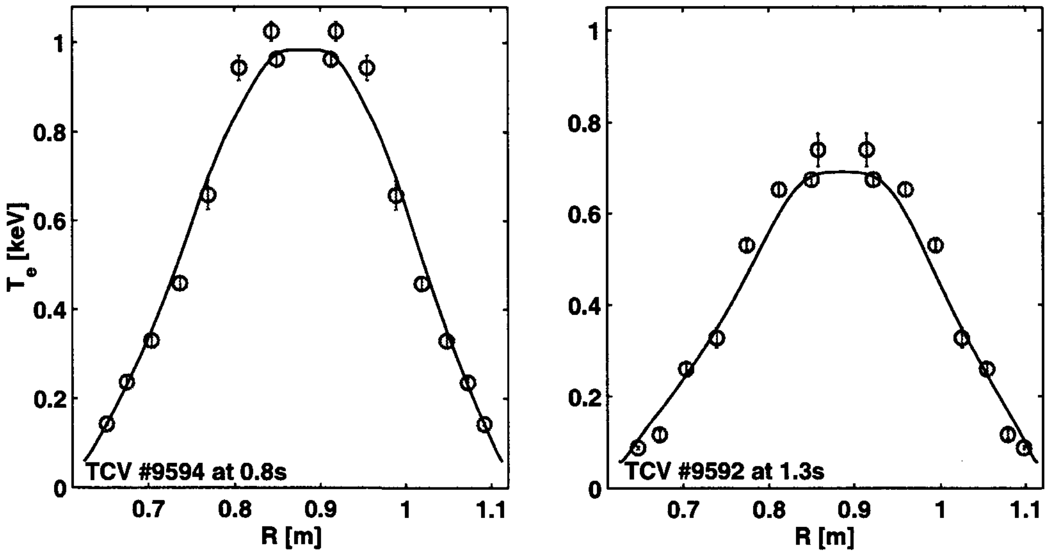

Figure 4.12: *Electron temperature profiles for shots ♯9594 and ♯9592, experimental measurements (symbols) and simulation results (solid lines). The experimental points have been mapped to the major radius on the midplane by means of the equilibrium reconstruction.*

4.5.1 The RLW critical gradient in TCV plasmas

Ohmic plasmas

In Figure 4.11 and Figure 4.12 we have shown the simulated profiles for 4 different Ohmic limited discharges during a phase of stationary operation. The four shots have been chosen in order to cover a sufficiently wide range of variation of two plasma parameters, density and current, keeping the plasma shape almost constant, with edge triangularity around 0.3, and edge elongation 1.55. Shots ♯9588 and ♯9589, Figure 4.11, have the same plasma current, $I_p = 450\,\mathrm{kA}$, with a corresponding $q_{edge} = 2.45$, but differ strongly in the value of the volume average plasma density, $7.4\ 10^{19}\,\mathrm{m}^{-3}$ and $2.4\ 10^{19}\,\mathrm{m}^{-3}$ respectively. By contrast, shots ♯9594 and ♯9592 have a lower value of plasma current, $I_p = 250\,\mathrm{kA}$, $q_{edge} = 4.3$, and volume average densities $2.8\ 10^{19}\,\mathrm{m}^{-3}$ and $6.8\ 10^{19}\,\mathrm{m}^{-3}$ respectively. We have carefully simulated the experimental electron temperature and density profiles, in order to consistently compute also the plasma current density profile, which appears in the RLW critical electron temperature gradient, ∇T_{RLW}. In Figure 4.13 we show the computed RLW critical electron temperature gradient and we compare it with the simulated gradients, which match closely the experimental ones. The region affected by sawtooth oscillations can be identified roughly with the central region characterized by low temperature gradients. The radial extent of this region strongly depends on the value of the plasma current, being large at high current, Figure 4.13(a), and narrow at low current, Figure 4.13(b). The confinement region is located somewhat outside the region affected by sawtooth oscillations, and therefore the plasma current determines its radial extent. The RLW critical gradient is inversely proportional to the square root of the electron

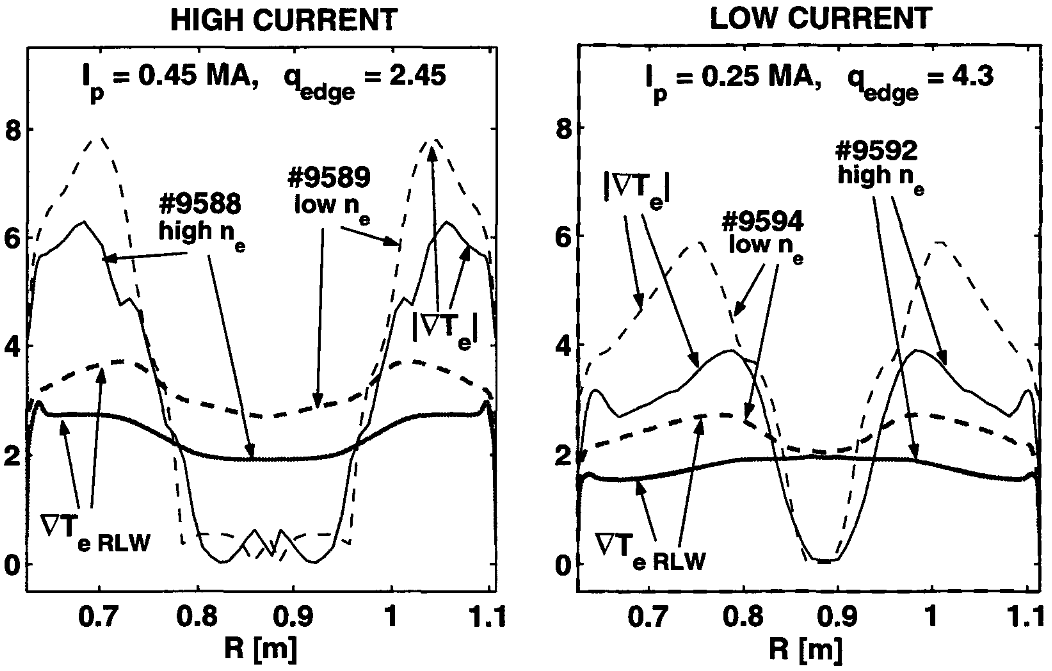

Figure 4.13: *(a) Electron temperature gradient profiles for shots ♯9588 and ♯9589 compared to the corresponding RLW critical gradient. (b)Electron temperature gradient profiles for shots ♯9592 and ♯9594 compared to the corresponding RLW critical gradient.*

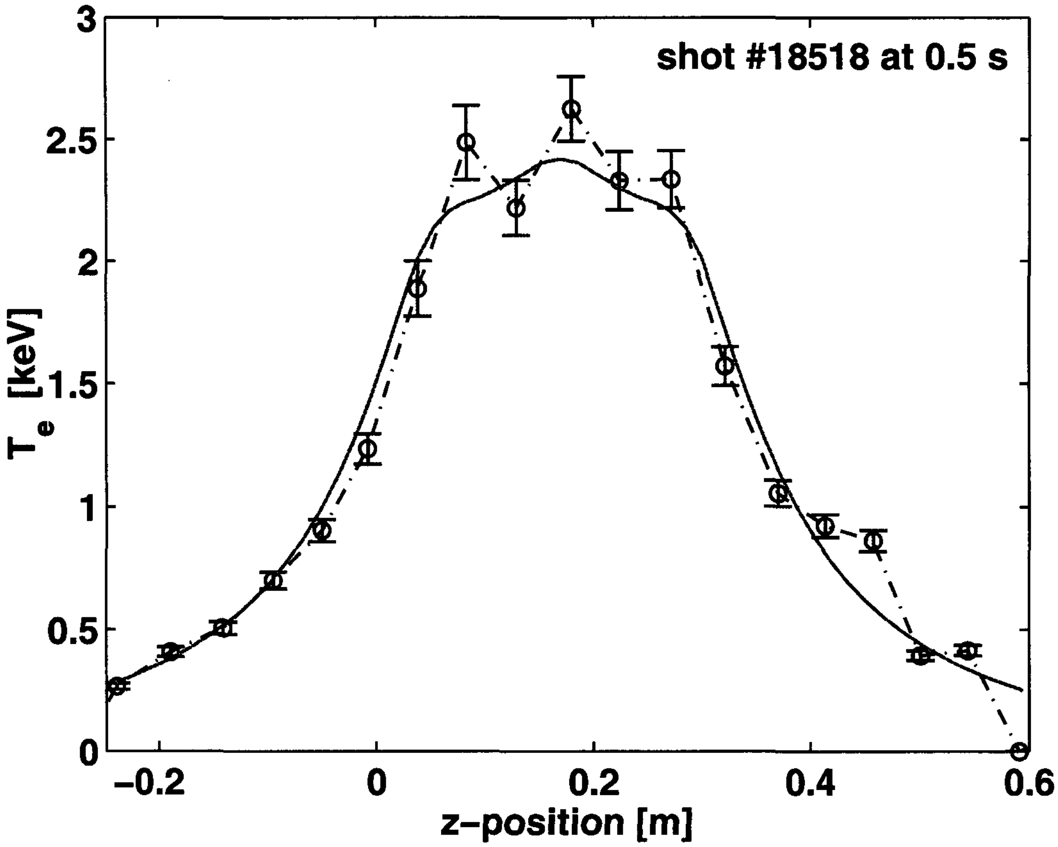

Figure 4.14: *Electron temperature profile for shot ♯18518 simulated, solid line, and experimental measurement, symbols, on the z-position of the vertical chord on which the experimental measurements are performed.*

density: this dependence can be seen in the respective confinement regions in Figure 4.13, comparing the critical gradient ∇T_{RLW} plotted with solid lines for high densities and with dashed lines for low densities. Also the temperature gradient $|\nabla T_e|$ is larger for low densities and lower for high densities. In all the situations presented, in the confinement region the temperature gradient $|\nabla T_e|$ is larger than ∇T_{RLW} at least by a factor of 2 or more. This explains why except for discharges with extreme plasma shapes, the RLW scaling law has been found in good agreement with the experimental thermal electron confinement time for a wide database of TCV discharges in Ohmic operation [4]. This is indeed consistent with what was found on Tore Supra [21], namely the RLW model is in agreement with the experimental observations only when $\nabla T_e > 3\,\nabla T_{RLW}$. The electron thermal conductivity in Tore Supra turns out to be significantly different from the one predicted by the RLW model when the ratio $\nabla T_e/\nabla T_{RLW}$ is below 2. Note that ∇T_{RLW} is proportional to $B_t^{3/2}$. As already mentioned, in a series of shots where B_t ranges from 1.3 to 3.9 T in Tore Supra this dependence has been found in disagreement with the experimental data and a correction to the RLW formula was proposed in which the dependence

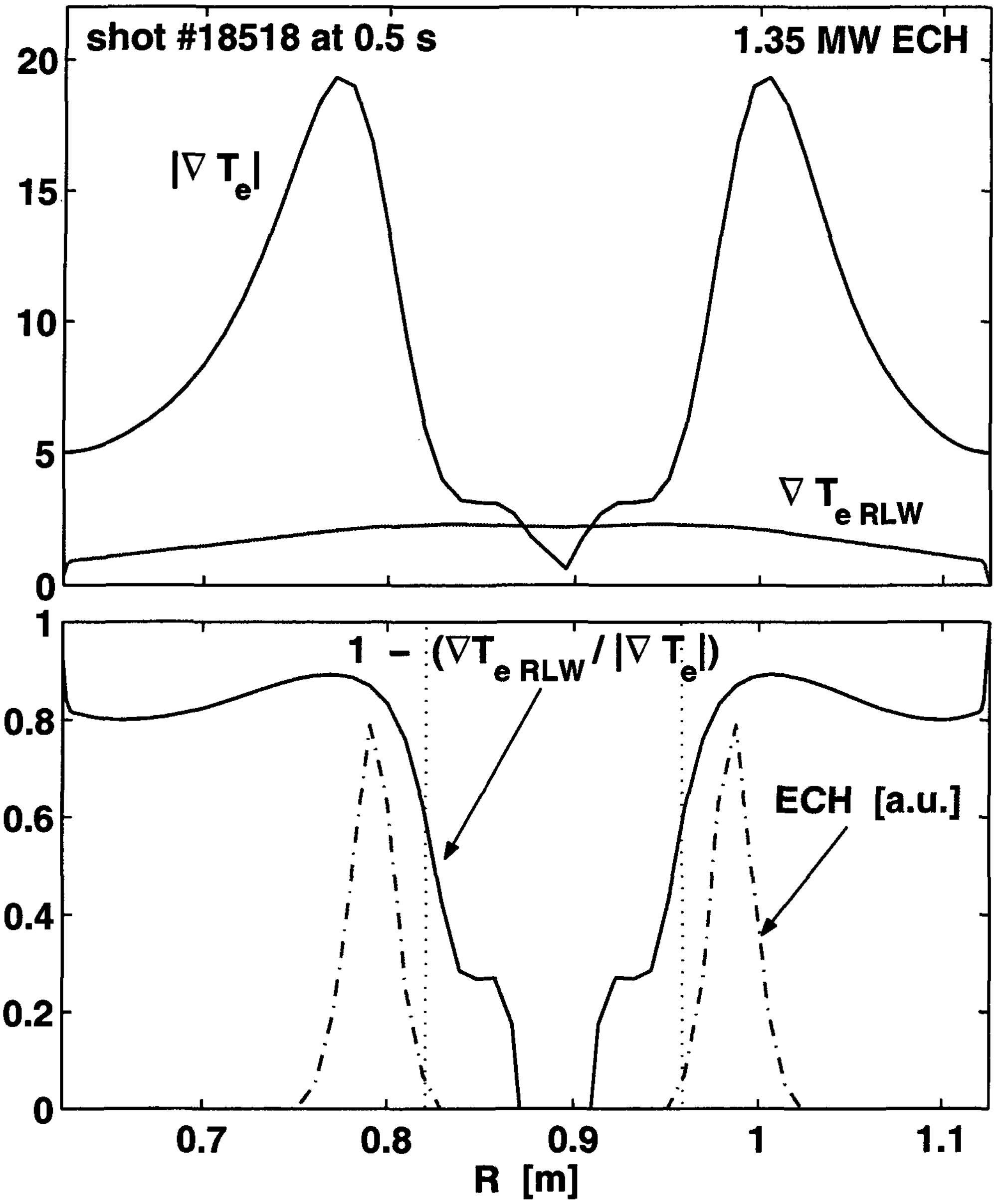

Figure 4.15: *(a) Electron temperature gradient profiles for shot ♯18518 at 0.5s compared to the corresponding RLW critical gradient. (b) Plot of* $(1 - |\nabla T_{RLW}/\nabla T_e|)$*, with, dashed line, the power density profile computed by TORAY-GA in arbitrary units.*

on the toroidal magnetic field was completely eliminated [21]. In the case of TCV, there is limited flexibility in modifying the magnetic field, and the operation is performed always around 1.4 T, which is a low value compared to other tokamaks. For this reason, the strong dependence of the RLW critical gradient on the toroidal magnetic field cannot be tested, and on TCV ∇T_{RLW} is always well below the experimental electron temperature gradients. The anomalous transport contribution is added to the neoclassical transport in the whole confinement region, and a factor $(1 - |\nabla T_{RLW}/\nabla T_e|)$ appearing in the electron thermal conductivity provides a reduction which is usually between 1/2 and 2/3, almost constant along the minor radius ($|\nabla T_{RLW}/\nabla T_e| \simeq 2-3$). In this sense we can conclude that the RLW critical electron temperature gradient for TCV Ohmic discharges does not play a crucial role in determining the heat transport level of the plasmas.

Electron cyclotron heated plasmas

When ECH is added, the situation becomes even more extreme and it can be stated that the RLW critical gradient becomes pratically negligible outside the deposition region. In Figure 4.14 we show the simulated electron temperature profile for shot ♯18518, with 1.35 MW of ECH deposited around $r/a = 0.35$, and we compare it with the experimental profile. By means of the equilibrium reconstruction, the simulated profile has been plotted versus the z-position of the vertical chord on which the experimental profile is measured by Thomson scattering. In Figure 4.15 the corresponding comparison between ∇T_e and ∇T_{RLW} for this shot is presented. In the presence of auxiliary electron heating, with the corresponding increase of the electron temperature, the critical gradient, inversely proportional to the electron temperature, is strongly reduced, whereas the electron temperature gradient increases. For the case presented in Figure 4.14, with a normal level of auxiliary heating for TCV operation, ∇T_e is well above ∇T_{RLW} along the whole profile outside the deposition region, and the factor $(1 - |\nabla T_{RLW}/\nabla T_e|)$ is everywhere constant and between 0.8 and 0.9 ($|\nabla T_{RLW}/\nabla T_e| \simeq 5-15$). Inside the deposition region the temperature gradient goes rapidly below the critical gradient but not as fast as the power balance evaluation of the electron heat conductivity suggests. Indeed, as presented in subsection 4.4.2 and shown in Figure 4.16, dashed line, with off–axis heating the electron heat conductivity computed by power balance analysis drops rapidly very close to zero inside the deposition region, which suggests that the real level of the critical gradient is substantially higher than the value provided by the RLW formula. When comparing the RLW heat conductivity and the PB heat conductivity, Figure 4.16, we see that it is indeed in the region just inside the deposition that the two curves differ the most. Nevertheless, the RLW model provides a formula which gives on average exactly the same level of transport along the minor radius on the one evaluated by power balance from the experimental data. This allows us to obtain simulated profiles which are in very good agreement with the experimental ones, Figure 4.14. Note also that with typical off axis depositions with $\rho_{dep} \simeq 0.35$, the central part of the plasma, inside the deposition region, is also affected by sawtooth activity, which modifies the profiles continuously during the sawtooth ramp both in the experiment and in the simulation, and which renders the comparison of the transport coefficients less accurate in this region and relaxes the need for a precise agreement between the simulated and the experimental profiles. When the ECH power deposition is on–axis the RLW critical gradient becomes completely negligible. Indeed in

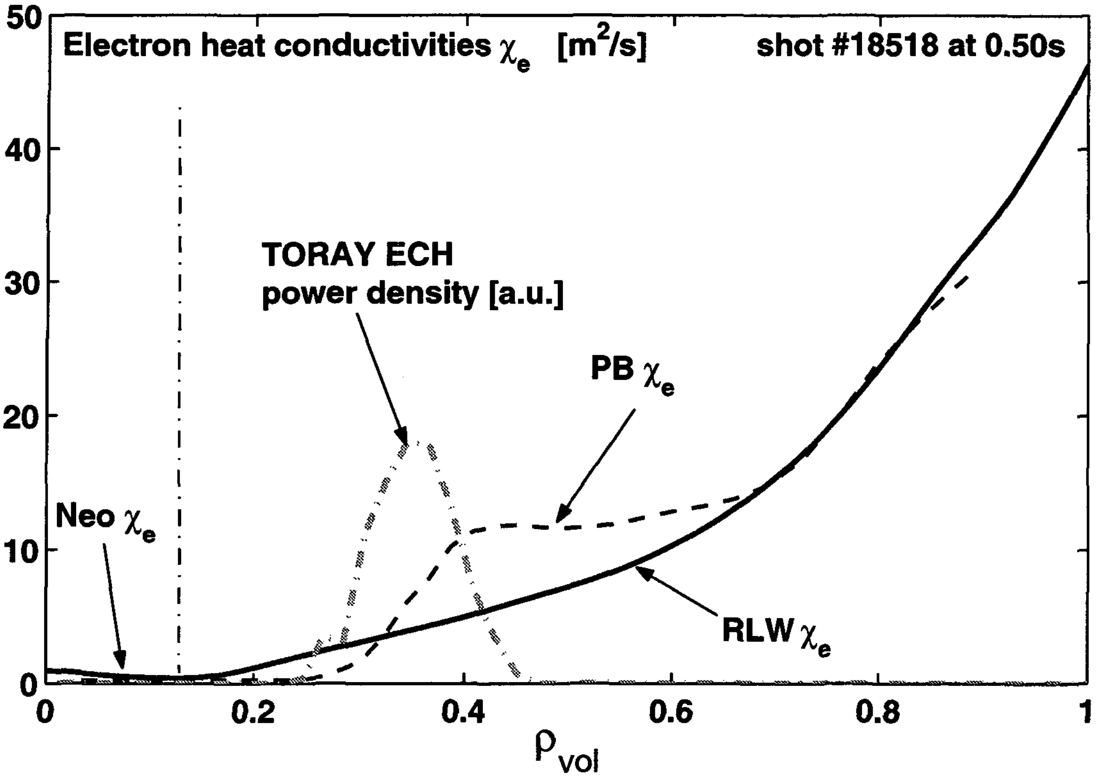

Figure 4.16: *Electron heat conductivity for shot ♯18518 at 0.5s, from the RLW model (solid line), and from PB analysis of the experimental data (dashed line). Inside the vertical dash-dotted line,* $|\nabla T_e| < \nabla T_{RLW}$*, and only the neoclassical contribution remains.*

this case the electron temperature gradient is considerably larger than the critical value along the whole minor radius, and the factor $(1 - |\nabla T_{RLW}/\nabla T_e|)$ in the expression for the electron heat conductivity is higher than 0.9 everywhere. From all these considerations, we can conclude that the RLW local transport model is indeed a very good candidate for modelling the electron transport in TCV, particularly in discharges with strong ECH, since TCV plasmas are in the validity domain of the model, as identified by previous studies comparing the model predictions to experimental data in other tokamaks.

4.5.2 Ohmic plasmas

As we have presented in Section 4.2, the principal specificity of TCV is that it allows very different plasma shapes. In Ref. [4] it was found that the RLW global scaling law is in remarkable agreement with the Ohmic TCV database, including very different plasma shapes and a large range of different plasma conditions. Nevertheless, it was found that the spread of the points obtained when plotting the experimental confinement time versus τ_{RLW} could be significantly reduced by introducing a shape enhancement factor H_S [3] which takes into account the effects of plasma shape on the flux surface configuration.

Indeed it was found that the dependence of confinement time on plasma shape, namely the increase of confinement time with plasma elongation and its decrease with positive plasma triangularity, can be explained by the geometrical effects of flux surface expansion and compression on the temperature gradients together with the effects of power degradation, without the need to invoke a specific shape dependence of the transport coefficients. In this sense one should expect that profiles in discharges with very different plasma shapes can be simulated keeping the same expression for the transport coefficients, and even keeping a fixed choice of the free parameters allowed by the model, introduced in Section 3.6, provided the terms describing the flux surface configuration of the toroidal geometry in the transport equations are properly taken into account, as described in subsection 3.2.

In order to verify this hypothesis, we have simulated 58 shots on 152 available in the TCV database of Ohmic shots [22], in the following range of variation of four parameters which have been chosen as the main independent parameters determining the different discharges:

$$\begin{array}{ccccccccccc} 2\,10^{19} & < & n_{\mathrm{e\,lin}} & < & 12\,10^{19}\mathrm{m}^{-3} & ; & 1.1 & < & \text{elongation} & < & 1.9 \\ 0.0 & < & \text{triangularity} & < & 0.6 & ; & 2 & < & q_{edge} & < & 5 \end{array} \qquad (4.1)$$

where $n_{\mathrm{e\,lin}}$ is the line average density. In this range, the variation of the plasma current is from 0.1 MA to 1 MA. The simulations, performed with the transport code PRETOR, are aimed at correctly reproducing the electron temperature and density profiles, the loop voltage, and the effective charge number, in stationary plasma conditions, using as input the total plasma current, the vacuum central magnetic field, the volume average density,

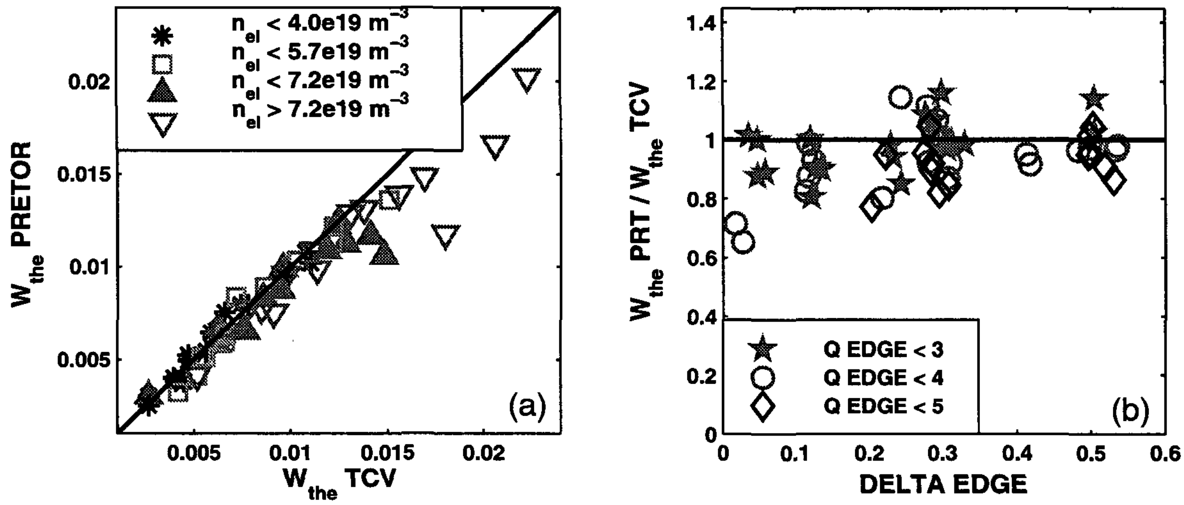

Figure 4.17: *(a) Experimental and simulated electron thermal energy. (b) Ratio between simulated and experimental electron thermal energy as a function of triangularity.*

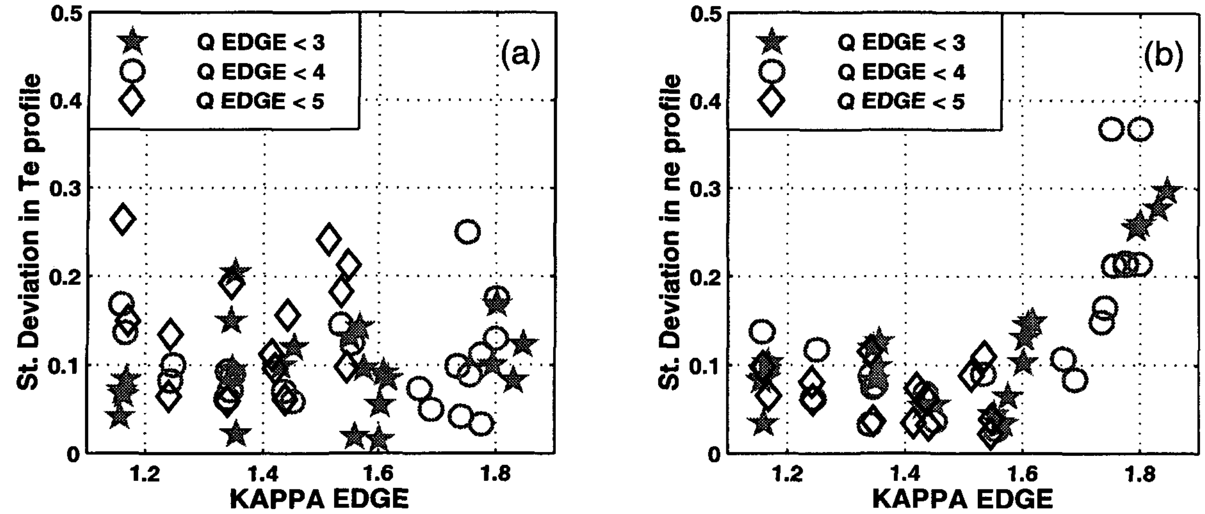

Figure 4.18: *(a) & (b) Standard deviations in the profiles as a function of elongation.*

the edge temperature, and the plasma boundary. The plasma equilibrium is computed self–consistently with the updated density and temperature profiles at almost every time step. In agreement with expectations, we have shown that a single choice of the free parameters allows a satisfactory simulation of almost all the discharges, without invoking a specific dependence of the transport coefficients on the plasma shape parameters. The fixed values assigned to the parameters, defined in Section 3.6, are the following:

$$C_{crt} = 6 \qquad C_{e,an} = 0.4 \qquad C_{D,an} = 3 \qquad C_{P,an} = 0.8 \tag{4.2}$$

These values have been chosen in order to minimize the average error between simulation and the experimental data, as presented below, in the whole domain defined by Eq. (4.1). Obviously a fine tuning of some coefficients, in particular $C_{e,an}$ and $C_{P,an}$, can reduce the discrepancies in any given shot so as to obtain an almost perfect agreement with the experimental profiles, as shown for the cases of Figure 4.11 and Figure 4.12. Note that the choice proposed in Ref. [19], respectively 6, 2, 0.5 and 0.5, Eq. (3.45), which has been validated on JET, results in temperature values which are always too small as compared with the experimental ones in TCV. In the simulations we have also included a model for the sawtooth period and amplitude in order to simulate the sawtooth activity, Section 5.2. Even though a detailed simulation of the sawtooth period in stationary Ohmic plasmas is not necessary in order to correctly model the plasma profiles, the correct simulation of the sawtooth inversion radius turns out to be very important, in particular with Ohmic heating. Indeed, current and pressure profiles in Ohmic plasmas are seen to be strongly correlated with the value of the inversion radius, since both the inversion radius and the peaking factor of the pressure profile ($< p_e > /p_{e0}$) are inversely proportional to the value of q_{95} [6]. As will be presented in subsection 5.3.1, because of the specific dynamics of the $q = 1$ surface during the sawtooth ramp, the sawtooth inversion radius can be more easily reproduced than the sawtooth period itself. For this reason, in the simulations performed in the present analysis, a simplified sawtooth crash trigger condition, $s_1 > 0.2$, has been adopted instead of Eq. (5.20), namely a sawtooth crash is triggered when the shear at $q = 1$ is larger than 0.2. Following [23], we have chosen a number of tests to compare simulation and experiment. We have considered the electron thermal energy, the electron thermal confinement time, and the standard deviation in temperature and density profiles. These four test parameters are defined as follows:

$$W_{the} = \int \frac{3}{2} n_e T_e \, dV \qquad \tau_{the} = W_{the}/P_{ohm} \tag{4.3}$$

$$\begin{aligned} \text{St. Deviation in Te profile} &= \frac{\sqrt{\sum \left(T_{e,PRT} - T_{e,TCV}\right)^2}}{\sqrt{\sum \left(T_{e,TCV}\right)^2}} \\ \text{St. Deviation in ne profile} &= \frac{\sqrt{\sum \left(n_{e,PRT} - n_{e,TCV}\right)^2}}{\sqrt{\sum \left(n_{e,TCV}\right)^2}} \end{aligned} \tag{4.4}$$

We have analyzed the results as functions of the four independent plasma parameters, in the whole domain described by Eq. (4.1), and we have found that almost all the simulations are in agreement with the experimental data, to within 20% in all the test parameters. Nevertheless, some specific features under particular plasma conditions are not completely reproduced by the model, and require further investigation. Firstly, we see in Figure 4.17 that the highest values of the thermal electron energy, obtained at high density and low triangularity, are generally underestimated by the model. Secondly, at high edge safety factor, $q_{edge} \simeq 5$, only shots with low density, low elongation [Figure 4.18] and high triangularity [Figure 4.17(b)] can be satisfactorily simulated. In the other cases, the experimental temperature profiles are in general more peaked than the predicted ones, and the sign of the convexity is opposite in the confinement region. Other geometrical effects can be seen on the density profile at high elongation and low edge safety factor, k $\simeq$ 1.8, as shown in Figure 4.18(b). The experimental density profiles are very steep close to the edge possibly with non-monotonic "shoulders", which are not reproduced by the model. On the other hand, as we can see in Figure 4.18(b), a good agreement in temperature profiles is found at low q_{edge} even at high elongation.

In order to present a clearer investigation of these features, we show the simulation results of two selected configurations, following the choice of Ref. [4], Figure 3. We have considered two shots with exactly the same plasma shape, ♯9933 and ♯11101, but which differ by more than a factor of two in q_{95}. The flux surface configurations of the two shots are shown in Figure 4.19. In Figure 4.20 we have plotted the corresponding profiles, experimental and simulated. The simulation has been performed with the choice of coefficients presented in Eq. (4.2). The simulation results correctly distinguish between the two situations, producing a broader profile for shot $\sharp$9933, $q_{edge} = 2.5$, and a narrow profile for shot $\sharp$11101, $q_{edge} = 5.5$. As will be better clarified later, this must not be interpreted as an indication that the transport model correctly describes the real physics that governs transport. In order to better exhibit the difference between the profiles, in Figure 4.21 the profiles have been rescaled to the corresponding values at the centre. We note in these specific cases a general feature of the density profiles: they are broader than the corresponding temperature profiles. This is also correctly reproduced by the model, even though clearly in the case at low q_{edge}, the simulated profile is not as broad as the experimental one (best fit plotted with a dash–dotted line), and in particular the steep gradient at the edge, typical of high elongations, is not at all reproduced. The simulated density profiles are almost proportional to the corresponding profiles of $1/q$, dashed lines in the figure (actually proportional to $(1/q)^{C_{P,an}}$). This is a direct consequence of the expression chosen for the anomalous particle pinch, Eq. (3.44). Note that this choice is consistent with theories on turbulent equipartition [24] which has been found recently in good agreement with the TCV sawtoothing Ohmic behaviour of the electron density [25]. On the other hand, in Figure 4.21(a), we see clearly that increasing the value of q_{edge} the profile not only changes in width, but also in convexity, being convex at low q_{edge}, and becoming increasingly concave when $q_{edge} > 5$. The best fit of the experimental points plotted with a dash–dotted line shows clearly that this specific feature is missed by

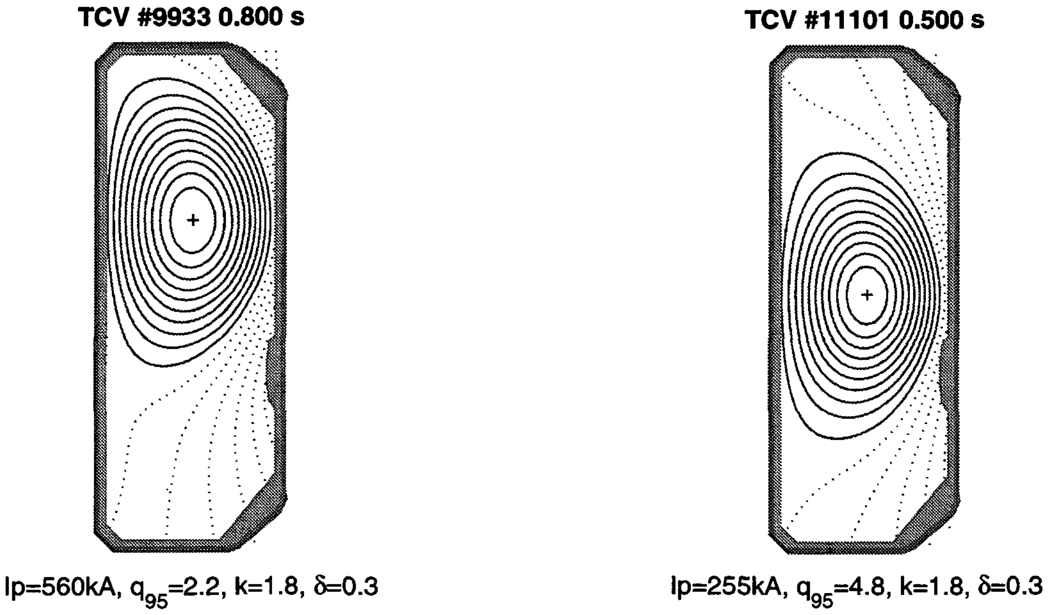
TCV #9933 0.800 s
TCV #11101 0.500 s
Ip=560kA, q_{95}=2.2, k=1.8, δ=0.3
Ip=255kA, q_{95}=4.8, k=1.8, δ=0.3

Figure 4.19: *Flux surface configurations for shots $\sharp$9933 and $\sharp$11101*

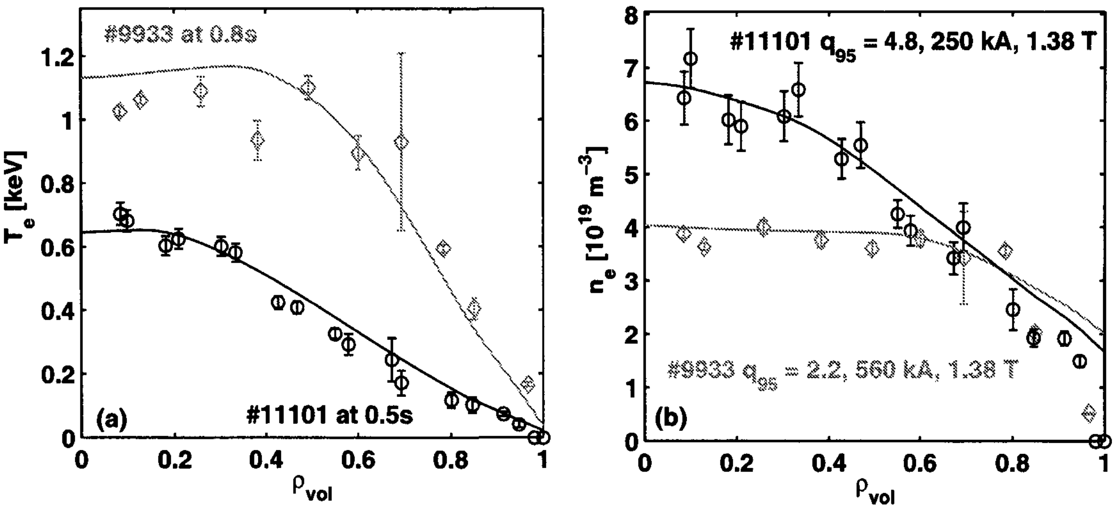

Figure 4.20: *(a) Experimental electron temperature (a) and density (b) profiles (symbols with error bars), and corresponding simulated profiles, (solid lines) for shots ♯9933 (light grey) and ♯11101 (black).*

the model. The discrepancy, which could be considered negligible at this level, becomes increasingly significant at higher values of the edge safety factor. This has motivated us to modify the RLW expression of the heat conductivity for discharges with $q_{edge} > 5$, as presented in the following subsection. It is also interesting to note that, consistently with what was presented in subsection 4.5.1, there is no apparent correlation between the

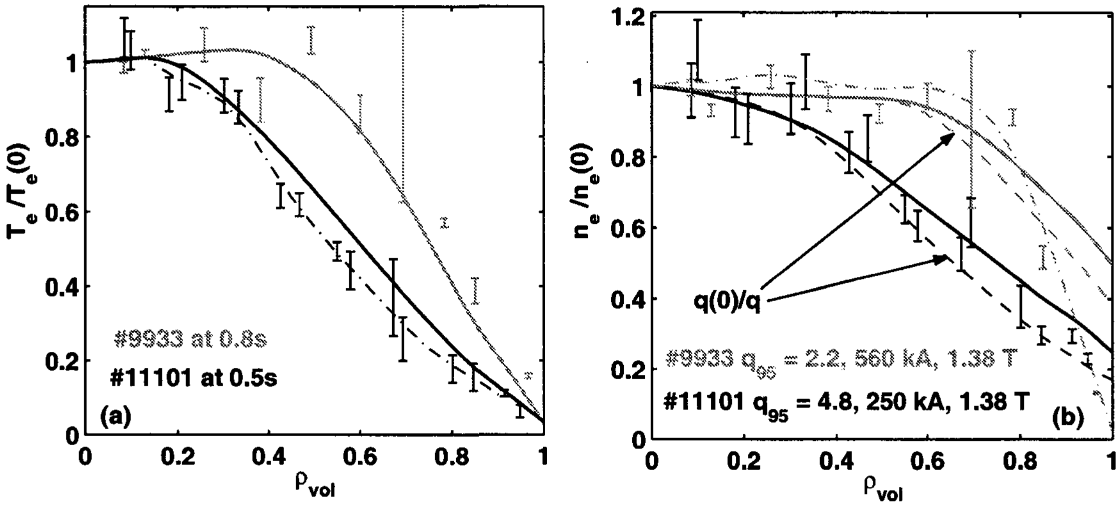

Figure 4.21: *(a) Experimental electron temperature (a) and density (b) profiles (error bars at the position of the measurements), and corresponding simulated profiles, (solid lines) for shots ♯9933 (light grey) and ♯11101 (black), rescaled by the corresponding values at the plasma centre. The dash-dotted lines show the best fits of the experimental points in the case of the temperature profile for shot ♯11101, and the density profile for shot ♯9933. The profiles of the corresponding inverse safety factor are plotted with dashed lines.*

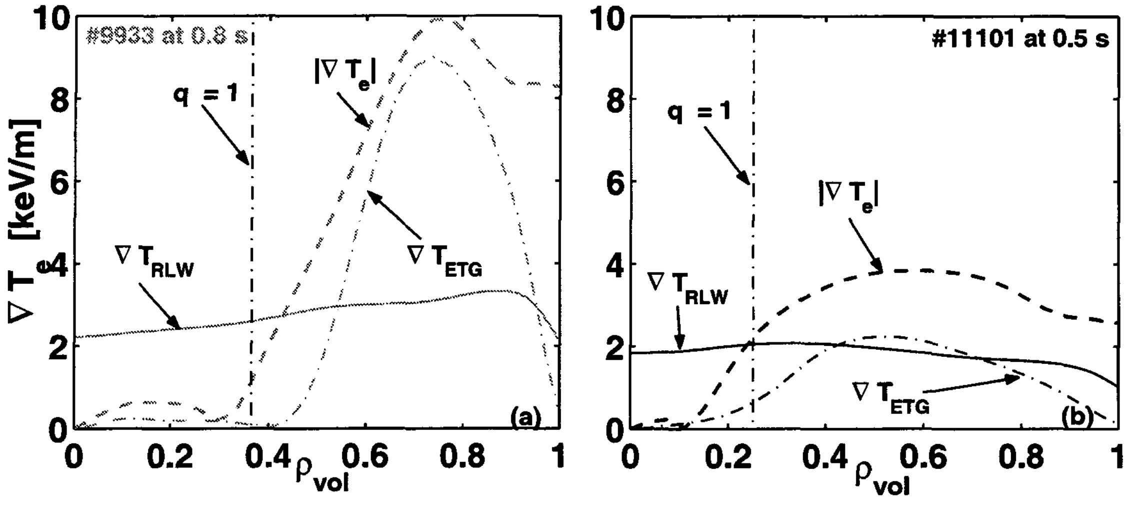

Figure 4.22: *(a) Electron temperature gradient, and critical temperature gradients, RLW and ETG, for shots ♯9933 (a) and ♯11101 (b).*

electron temperature gradient and the RLW critical gradient, Figure 4.22. We have also plotted the term

$$\nabla T_{ETG} = C_L T_e \left(\frac{s}{q}\right) \left(1 + Z_{\text{eff}} \frac{T_e}{T_i}\right),$$

which gives an estimation for the critical threshold gradient for the ETG turbulence [26, 27], with $C_L = 3/2\sqrt{\pi/2}$. The electron temperature gradient behaves very similarly to ∇T_{ETG}, in particular to $T_e\,(s/q)$. This is in any case due to the strong correlation that exists between the electron temperature profile and the current profile in Ohmic plasmas [4], which involves a form of degeneration in such analysis, as the Ohmic heating power profile also follows the current density profile. The agreement between the ETG turbulence formula and the electron temperature gradients hence can not be considered conclusive, as in Ohmic plasmas the two profiles are correlated. Note that in ECH plasmas in TCV, in which the strong auxiliary electron heating breaks the degeneration, the ETG turbulence is not expected to be excited. The ETG critical gradient exceeds by far the experimental values of the temperature gradients, since the ratio $Z_{\text{eff}}\,T_e/T_i$ ranges from 10 to more than 50 in TCV with ECH.

In conclusion, it must be emphasized that, when simulating Ohmic plasmas, the most important tasks are to treat properly the coupling between the transport equations and the field diffusion equation, with a consistent 2D magnetic equilibrium reconstruction, and to describe with a reliable model the sawtooth activity. Once the poloidal magnetic field, and thus the Ohmic heating power density are correctly computed, this determines directly the width of the temperature profiles. The profile remains essentially flat from the centre up to the inversion radius, because of sawtooth relaxations. The effects of sawteeth, in particular a good profile relaxation model, must necessarily be taken into account in order to correctly simulate sawtoothing Ohmic discharges. The profile width is mostly determined by the position of the $q = 1$ surface at the sawtooth crash (or the sawtooth inversion radius), while it is quite insensitive to the detailed physics governing transport in the confinement zone. Once even a single free parameter has been adjusted in order to correctly reproduce an integral parameter, such as the global plasma energy content, as we have done in the case of the coefficient $C_{e,an}$ in Eq. (4.2), the most important profile features and values are determined. The specific transport model then determines the profile behaviour from the inversion radius out to the edge, where usually in simulations the experimental temperature is given as a boundary condition. Therefore, the profile features on which the detailed physics involved in the model can be identified are strongly limited when simulating Ohmic plasmas: only an accurate inspection of specific features of the profiles in the confinement zone, such as the concavity at high edge safety factor shown in Figure 4.21 for shot ♯11101, can allow one to discriminate between the predictions of the different models. However this needs very precise measurements of the plasma profiles, which are not always available.

4.5.3 Adapting the RLW model to plasmas with large q_{edge}

As we have shown in the previous paragraph, for high values of q_{edge}, the concavity of the experimental temperature profile is not well reproduced by the model, even by changing the free parameter $\mathrm{C}_{e,an}$. The predicted profiles, for plasmas with low current, $q_{edge} > 5$, turn out to be too convex, whereas the experimental profiles are clearly concave in the confinement region. This is important for TCV, as the usual target plasmas in ECH operation and in particular in experiments dedicated to improved confinement scenarios, are at relatively low plasma current, with values of q_{edge} between 5 and 8. In order to better simulate the temperature profile in these conditions, a geometrical factor has been introduced in the expression of the electron heat conductivity, Eq. (3.39),

$$\begin{aligned} \chi_{e,an} &= \frac{\mathrm{C}_{e,an}}{R_0^{1/2}}\,\epsilon^{1/2}(1+Z_{eff})^{1/2}\left|\left(\frac{\nabla T_e}{T_e}+2\frac{\nabla n_e}{n_e}\right)\frac{q\,\rho}{s}\right|\left(\frac{T_e}{T_i}\right)^{1/2} {B_t}^{-1} \\ &\quad \left(\frac{1}{2}+\frac{\rho}{a}\right)^{\alpha}\left(1-\frac{\nabla T_{RLW}}{\nabla T_e}\right)\,\mathrm{H}(\nabla T_e-\nabla T_{RLW}) \end{aligned} \tag{4.5}$$

where the exponent α is given by

$$\alpha = 2\ \mathrm{int}\left(\frac{q_{edge}}{5}\right)$$

The function int gives the integer part. The coefficient $\mathrm{C}_{e,an}$ in the simulation of TCV discharges is usually equal to 0.4 for normal density values, but for very low densities ($\mathrm{n}_{el19} < 2$), like in the case of some ECH discharges, it must be increased to higher values up to almost a factor 2. The dependence on density has been analyzed over a large number of discharges, and can be expressed in the form

$$\mathrm{C}_{e,an} = \frac{1}{8} \left[3 + \mathrm{int}\left(\frac{5}{n_{\mathrm{el}\,19}}\right)\right]. \tag{4.6}$$

Note that, since reliable measurements of the ion temperature are not yet available on TCV, such a dependence on density may be an artefact introduced by an incorrect simulation of the ion temperature, which results in a miscalculation of the equipartition term. Hence it can not be assessed whether it is the electron heat conductivity or the ion heat conductivity that must be corrected. The former option has been chosen [Eq. (4.6)] for the practical reason that χ_e more directly affects the electron temperature, whose experimental profiles are available. In this sense this last formula must be considered merely as a rule of thumb for the simulation of the electron temperature profile in TCV discharges, and not as a universally reliable correction to the RLW model. This issue calls for further investigation once measurements of the ion temperature profile will be available on TCV.

This transport model has been applied on a regular basis to the simulation of several TCV experiments, in particular for discharges with ECH and ECCD, and it has been found in agreement with several different experimental observations, obtained with different heating and current drive schemes. A set of examples of these simulations will be presented

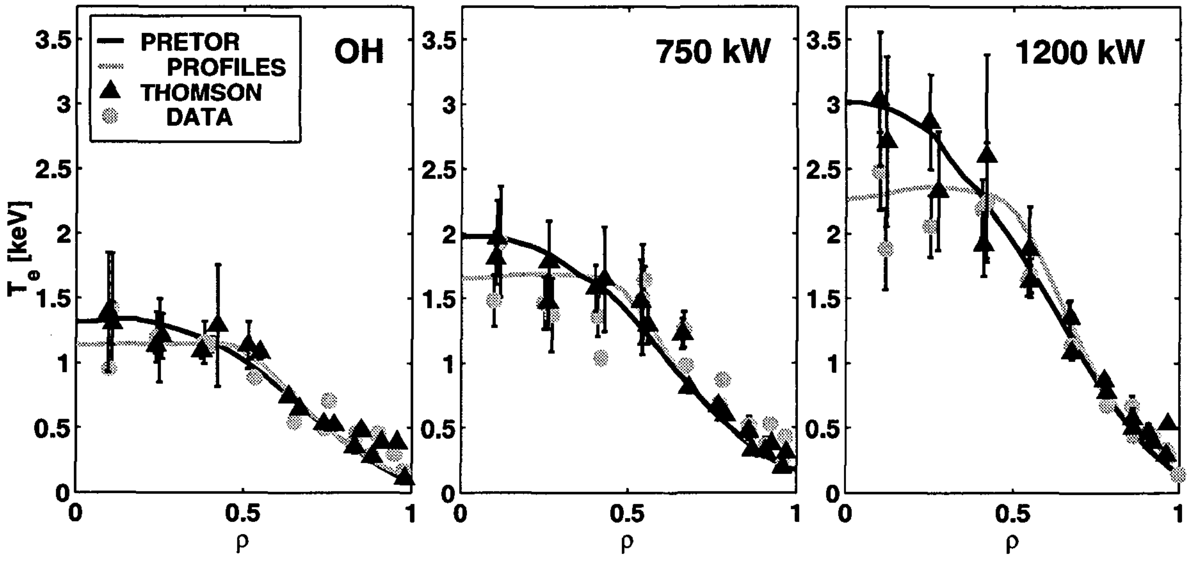

Figure 4.23: *Comparison between simulated electron temperature PRETOR profiles (lines) and TCV experimental measurements, Thomson scattering, (symbols), for shot ♯14337; (a) Ohmic heating, (b) and (c) two different power steps of ECH with absorption location at* $\rho = 0.2$. *Profiles before (solid triangles) and after sawtooth crash (solid circles) are shown.*

in the following section. The model is in fact sufficiently reliable that it has been used in the planning of experiments, that is to predict specific dependences.

4.5.4 Electron cyclotron heated plasmas

Power scan

The first application of the transport model presented in the previous subsection to discharges with ECH has been dedicated to the simulation of power scan experiments [9]. These experiments have been performed with a broad power deposition profile, located slightly off–axis. The goal of the simulations was to check whether the values of the central electron temperature predicted by the model were in agreement with the experimental measurements, keeping fixed the parameters included in the expression of the heat conductivity, Eq. (4.5). In Figure 4.23 we show an example of these simulations [9], for shot ♯14337, comparing the profiles before and after the sawtooth crash for Ohmic heating and two different ECH power levels. The sawtooth relaxed profiles as well as the sawtooth period have been determined following prescriptions provided by the sawtooth model presented in Section 5.2. The agreement between experimental data and simulations is good, confirming the general agreement found between the RLW scaling law and the experimental confinement time [9].

Heat conductivity with off–axis heating

We have already mentioned that when ECH is deposited off–axis, a step in the power balance electron heat conductivity is found, located at the power deposition, subsection 4.4.2. In Figure 4.14 we have shown an example of the application of the transport model presented in subsection 4.5.3, simulating the electron temperature profile at a specific time of a discharge with ECH localized at $\rho_{dep} = 0.35$. The simulated profile compares very well with the experimental points. The corresponding electron heat conductivity has been shown in Figure 4.15, compared to the experimental profile obtained by power balance. As already discussed in subsection 4.5.1, the disagreement between the power balance conductivity and the RLW formula calls for a transport model in which such an abrupt step of χ_e at ρ_{dep} is produced by the temperature gradient being above the critical value outside ρ_{dep}, and below inside [14]. This is not the case for the RLW model. The critical gradient ∇T_{RLW} remains below the temperature gradient $|\nabla T_e|$, even inside ρ_{dep}. Although this does not reproduce the rapid step of χ_e at the location of the power deposition found with power balance, the RLW heat conductivity is strongly reduced in the central region of the plasma, with a behaviour which on average describes correctly the conductivity computed by power balance. For this reason, as already mentioned in subsection 4.5.1, the model still allows satisfactory simulations of the temperature profiles with off–axis heating.

Profile stiffness with central heating

We have shown in Section 4.4 that the electron temperature profiles in TCV remain stiff outside the power deposition region, and we have pointed out that this would suggest the existence of a critical $|\nabla T_e|/T_e$. This is not at all the case for the RLW model, as ∇T_{RLW} is almost negligible as compared with the measured temperature gradients in the confinement region. We call that we have defined stiff behaviour in TCV the fact that, outside the deposition region, the value of $|\nabla T_e|/T_e$ remains constant and independent of the amount of power deposited in the plasma centre and consequently independent of the heat flux propagating radially through the plasma. Therefore a necessary further step in the validation of the model is to check whether this general feature of experimental response of the electron temperature to ECH is adequately reproduced. As already mentioned, the most direct interpretation of such a stiff behaviour is to assume the existence of a critical value in the normalized electron temperature gradient $|\nabla T_e|/T_e$. In this picture, the experimental value of the normalized temperature gradient is expected to remain relatively close to the normalized critical gradient, $(|\nabla T_e|/T_e)_{crit}$. An expression for the heat conductivity consistent with this hypothesis is [14]

$$\chi_e = T_e^{3/2}\,[\xi_0 \,+\, \xi_{TG}\, G(R/L_{Te} - R/L_{T\,crit})]\,, \tag{4.7}$$

where ξ_0 represents transport when the temperature gradient (TG) turbulence is not active, $R/L_{Te} = R\,|\nabla T_e|/T_e$ is the dimensionless temperature gradient length, and $\xi_{TG}\,G$ gives the transport enhancement caused by the temperature gradient turbulence. This simple model reflects the expression for the heat conductivity arising from microinstabilities generated by trapped electron modes (TEMs) or electron temperature gradient modes (ETG), and it has been found in agreement with the observations obtained in some dedicated experiments on profile stiffness recently performed in ASDEX Upgrade [14, 15]. We have shown in subsection 4.5.1 that, on the contrary, these features of the heat conductivity are not at all encompassed by the RLW model. In particular the RLW critical gradient does not play any role in determining the local transport level, and it can be practically neglected for plasmas with central ECH. From the analysis of subsection 4.5.1, one could expect that the stiffness features presented in subsection 4.4.1 are completely missed by such a model. Somewhat surprisingly, this is not the case, because of the overall dependence of the transport coefficient expression on electron temperature. We have simulated a power scan, from Ohmic up to 3 MW of ECH power, in three steps, with on–axis power deposition, in a plasma with volume average density $\langle n_e\rangle_{\mathrm{Vol}} \simeq 1.5\ 10^{19}\,\mathrm{m}^{-3}$, a typical value of TCV operation with ECH, and $I_p = 200kA$. The Ohmic power in the Ohmic phase is 0.28 MW, and becomes negligible as compared with ECH power during the three ECH cases, at most 15% of the total heating power with 1MW ECH, and considerably less in the other cases. The resulting electron temperature profiles, in logarithmic scale, together with the power deposition profile, are shown in Figure 4.24. The edge temperature has been imposed as a boundary condition and has been slightly increased with increasing power, whereas the density profile has been kept fixed during all the power steps. The electron temperature profiles of the three ECH power steps turn out to be strongly parallel. Only the Ohmic profile shows a different slope.

A simple analytical model

In order to explain this stiff behaviour, obtained with a transport model which does not involve a critical $|\nabla T_e|/T_e$, it is useful to consider the simulated plasma conditions in cylindrical geometry, which allows a simple analytical treatment. We consider a stationary plasma, with central auxiliary electron heating strongly dominant compared to Ohmic heating, in such a way that the Ohmic contribution to the radial heat flux is neglected. In this case, outside the deposition region, the heat transport equation in the absence of

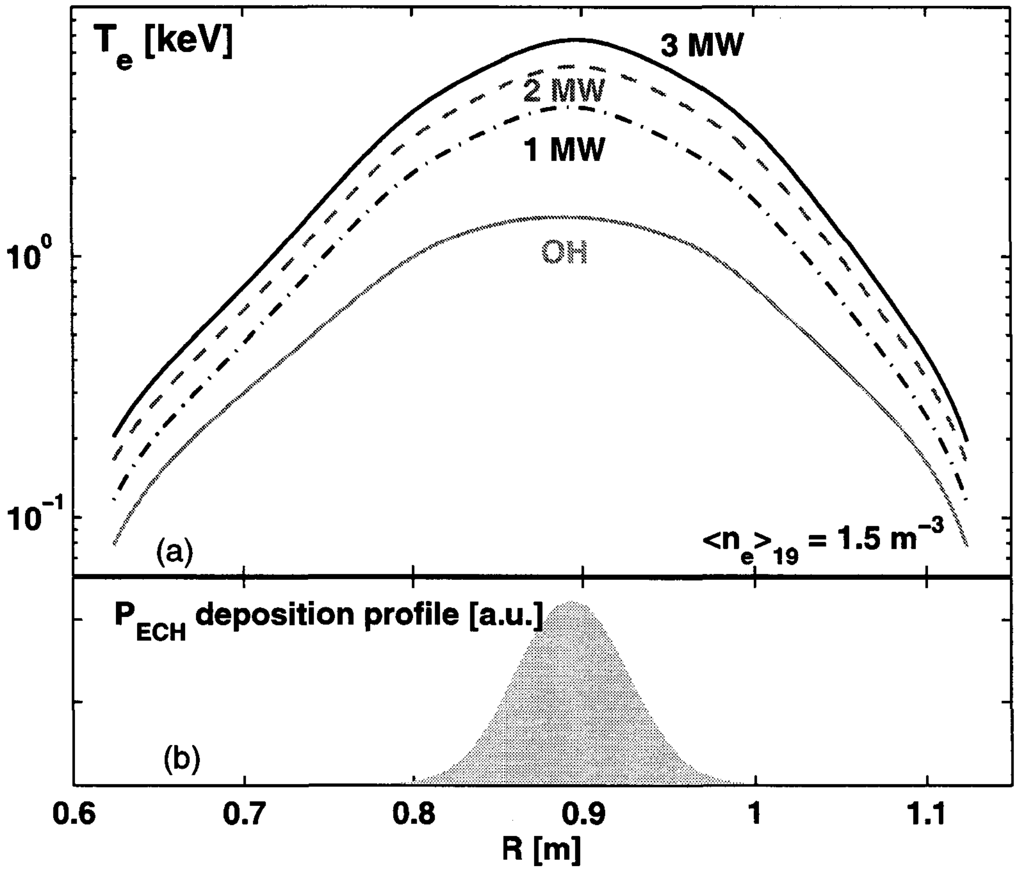

Figure 4.24: *(a) Electron temperature profiles for PRETOR simulations of three central ECH power steps, compared to the corresponding Ohmic profile. The deposition profile is shown in (b).*

source terms reads

$$\frac{1}{r}\frac{d}{dr}\,r\,Q_e = 0, \qquad \text{where} \qquad Q_e = -n_e\,\chi_e\frac{dT_e}{dr}$$

is the heat flux. The solution of the first equation gives simply $Q_e = P/r$, where P is an integration constant proportional to the amount of heating power deposited in the plasma centre. Therefore we can write

$$-n_e\,\chi_e\frac{dT_e}{dr} = \frac{P}{r} \tag{4.8}$$

If we now assume that $\chi_e = K(r)\,T_e^{\alpha}$, where $K(r)$ is some given function of the minor radius, independent both of T_e and of the amount of heating power, Eq. (4.8) can be easily solved by separation of variables with the result

$$T_e^{\alpha+1}(r) = -(\alpha+1)\,P\int_a^r \frac{1}{n_e(r')\,K(r')}\frac{dr'}{r'} + T_e^{\alpha+1}(a), \tag{4.9}$$

where a is the minor radius at the plasma edge. From Eq. (4.9) we see that if the edge temperature is sufficiently close to zero, or/and if it increases with increasing central heating power as $T_e^{\alpha+1}(a) \propto P$, the electron temperature is simply proportional to the power $1/(\alpha+1)$ of the central power. The electron temperature profiles with increasing central heating power show the same normalized gradient $(dT_e/dr)/T_e$, given by

$$\frac{1}{T_e}\frac{dT_e}{dr} = -\left(\frac{P}{T_e^{\alpha+1}}\right)\frac{1}{r\,n_e(r)\,K(r)}, \tag{4.10}$$

which is a function of radius r, independent of the value of the central heating power P. This simple analytical derivation shows that the features of a stiff electron temperature behaviour, in the sense presented in subsection 4.4.1, are adequately reproduced by an electron temperature heat conductivity which is proportional to the electron temperature, provided that the edge temperature varies accordingly, but without involving any critical value of the temperature gradient in the expression of the heat conductivity. Whether this specific edge condition, namely $T_e(a) \propto P^{1/(\alpha+1)}$, is or is not satisfied in experiments is difficult to ascertain, considering the errorbars in the measurements. A visible increase of the edge temperature is certainly recorded, in L–mode, when passing from Ohmic to strong auxiliary central heating, creating a sort of pedestal, see Figure 4.4, whereas further increase of the central ECH power, a factor of 2 in the specific case of shot ♯18224, does not seem to cause a corresponding increase of the edge temperature. Note that recent accurate measurements in ASDEX Upgrade have shown that the edge temperature increases significantly with increasing central heating power at each power step [15]. In any case, regardless of the specific behaviour of the electron temperature at the edge, the proportionality between the heat conductivity and the electron temperature in the confinement region guarantees that electron temperature profiles obtained with increasing central heating power remain essentially parallel when plotted in semi–logarithmic scale, as shown in simulations presented in Figure 4.24. In the simulations the edge temperature has been increased without following the proportionality to the square root of the central power prescribed by Eq. (4.9).

T_e dependence of the RLW χ_e

In Figure 4.25 we have plotted the ratio χ_e/T_e corresponding to these four PRETOR simulations. The overall dependence of the RLW electron heat conductivity on the electron temperature in the three simulated cases with central ECH heating is exactly the one assumed in the simplified analytical model, with $\alpha = 1$, justifying the profile stiffness behaviour obtained in the simulations. Consistently with the experimental profiles, when plotted in semilogarithmic scale, the profiles are essentially straight lines in the confinement region. This feature of the RLW model must be ascribed mainly to the term $\sqrt{T_e/T_i}$ included in the electron heat conductivity, noting that when $T_e/T_i \gg 1$, as in the present case with $\langle n_e \rangle_{\mathrm{Vol}} \simeq 1.5\ 10^{19}\ \mathrm{m}^{-3}$, the model gives also $T_e \propto 1/T_i$. In the case of Ohmic heating the power is no longer localized in the centre, and the heat conductivity shows a different behaviour. Also, contrary to the ECH cases, the RLW critical gradient is not completely negligible compared to the temperature gradient; this introduces an extra

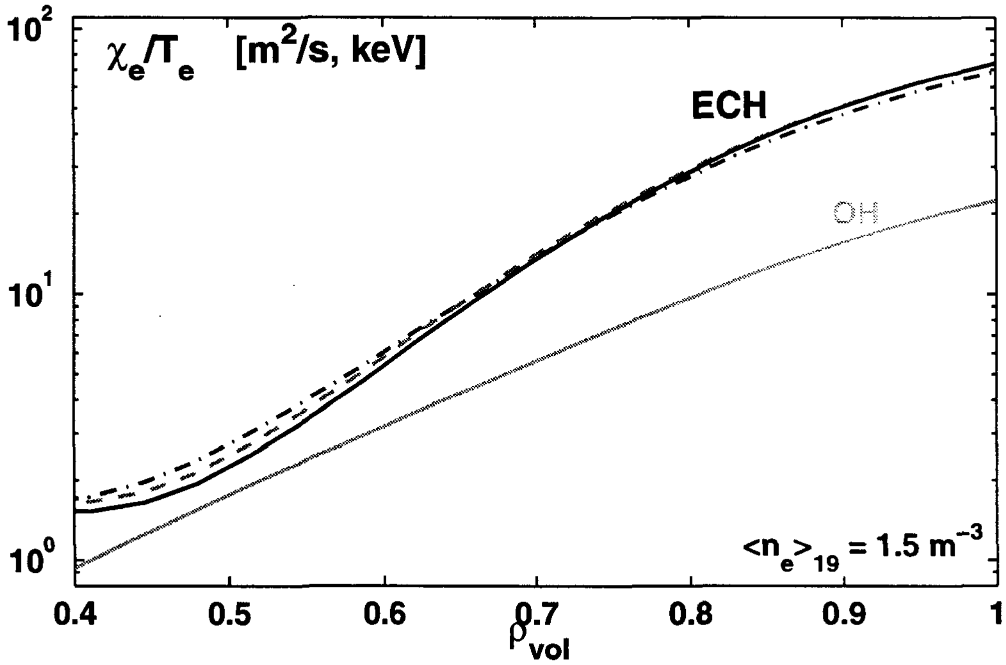

Figure 4.25: *RLW electron heat conductivity profiles, divided by the electron temperature profiles, corresponding to the simulations shown in Figure 4.23, computed with the model presented in subsection 4.5.3. Curves corresponding to simulations with ECH: 1 MW (dash-dotted line), 2 MW (dashed line) and 3 MW (solid line).*

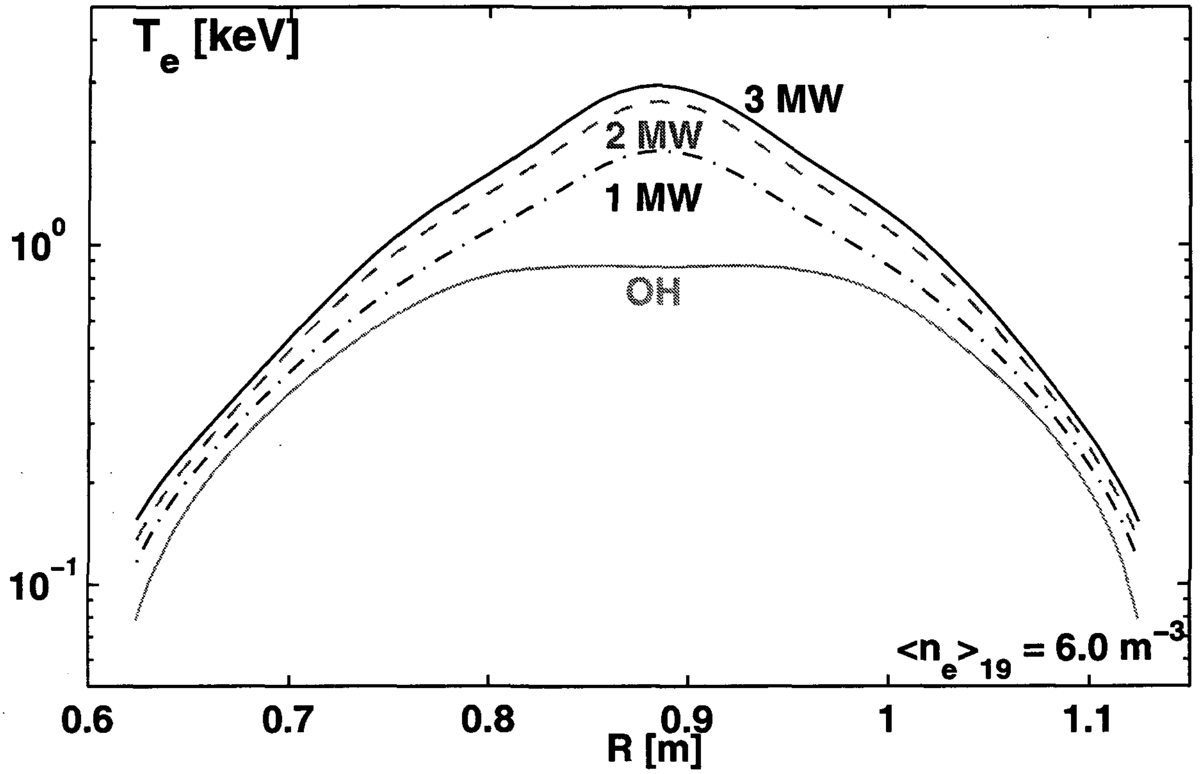

Figure 4.26: *(a) Temperature profiles in semi-logarithmic scale, for 3 ECH power steps and Ohmic heating, at high plasma density. The profiles are still parallel (stiffness), but not straight.*

dependence in the heat conductivity which affects the proportionality to the electron temperature. Nevertheless, the Ohmic profile also turns out to be almost parallel to the ECH profiles, even though not as much as in the experimental case, and the difference would be difficult to distinguish experimentally. Note that this specific feature of the RLW model occurs also at high density, but a different value of the exponent α appears in the relation between χ_e and T_e. We have performed a second set of simulations, always with central heating, increasing the density up to $\langle n_e \rangle_{\mathrm{Vol}} \simeq 6.0\ 10^{19}\ \mathrm{m}^{-3}$, and with a plasma current of 430 kA, with a consequent Ohmic power of 1.1 MW (with Ohmic heating). In this case, provided the auxiliary heating power does not exceed a few MWs, neither ohmic heating nor equipartition is negligible compared to the ECH power. The ratio T_e/T_i, which was equal to 60 in the plasma centre at low density and 3 MW ECH, is now reduced, at the same power level, by a factor of ten, leading to regimes in which electron and ion temperatures are almost of the same order of magnitude. Figure 4.26 shows that in this case the model still gives stiff electron temperature profiles, as in semilogarithmic scale the curves are parallel, but the profiles are not straight lines in the confinement region. In contrast with both the experimental observations and the model predictions at low density, at

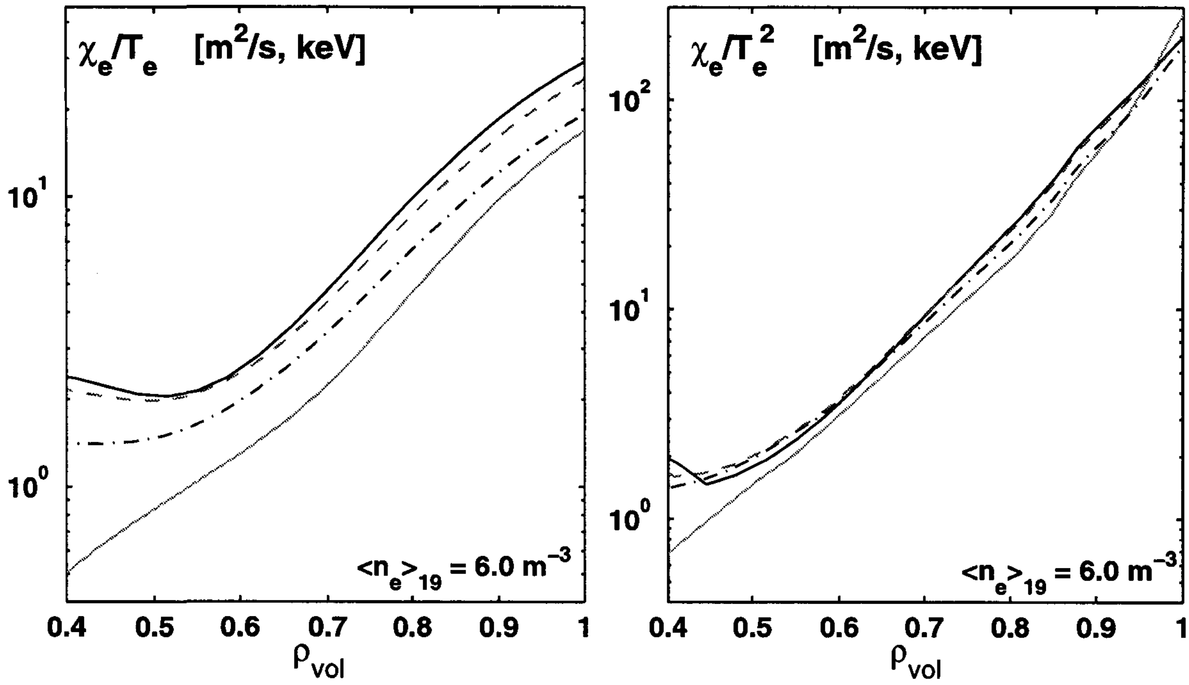

Figure 4.27: *With high density the RLW heat conductivity is not proportional to the electron temperature, as shown in (a), but proportional to the square of the temperature (b).*

high density $|\nabla T_e|/T_e$ is not constant along the minor radius in the confinement region. The stiffness can still be explained by the relation $\chi_e \propto T_e^\alpha$, but, with a volume average density $\langle n_e \rangle = 6.0\ 10^{19}$ m^{-3}, we find $\alpha = 2$, as shown in Figure 4.27. Plasma and heating conditions explored by this second set of simulations are far outside the accessible experimental domain of TCV. Note that in the near future, transport analysis at high density will become possible, thanks to the three gyrotrons of the X3 cluster, with 1.35 MW, Section 4.3. This should allow one to experimentally assess the issue of profile stiffness at high density in TCV, with ratios of $T_e/T_i < 5$. In this plasma regime, which cannot be explored in TCV with the X2 clusters, discrepancies with the predictions of the RLW model could be identified, the key signature being a constant $|\nabla T_e|/T_e$ in the confinement region as in the low density case.

Profile stiffness with off–axis heating

When heating off–axis, as shown in subsection 4.4.2, the electron temperature profile can be strongly modified, while stiffness features can still be identified outside the deposition region. When the heating power is localized close to the edge, the effect of the edge temperature on the profile up to the deposition region becomes important, and general considerations become difficult. We have performed a set of three simulations, showing

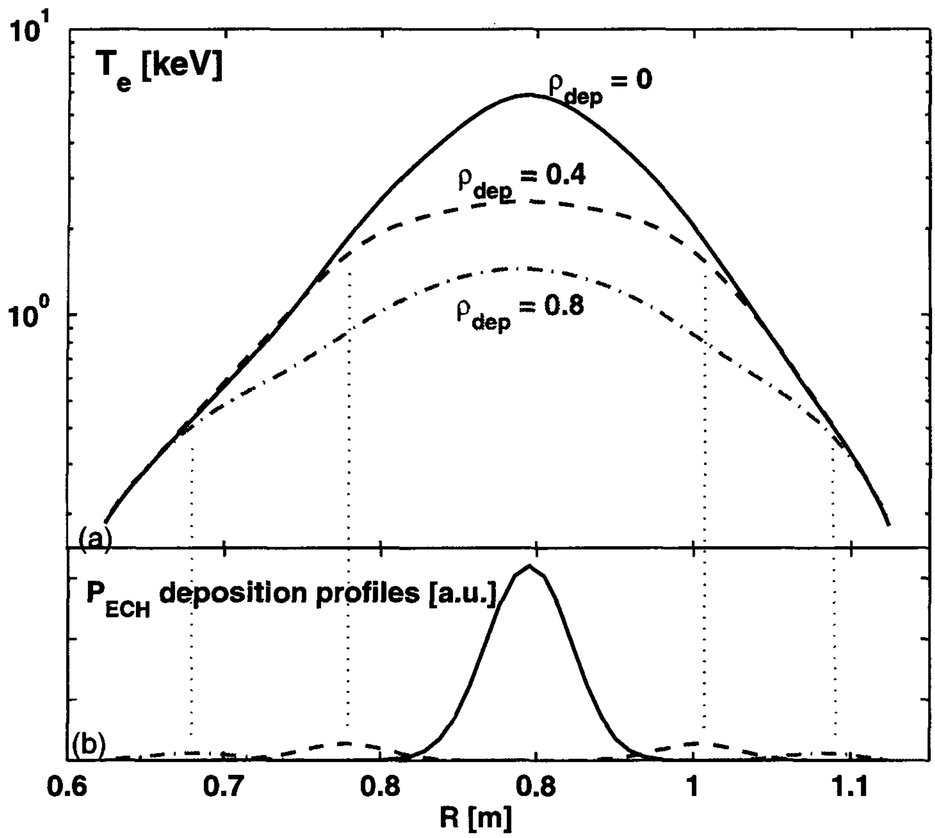

Figure 4.28: *(a) Electron temperature profiles corresponding to power depositions located at three different positions on the minor radius, shown in (b).*

the effect of a deposition scan on the electron temperature, with ECH power dominant compared to Ohmic heating, and again a plasma close to the experimental conditions, hence with very low density $\langle n_e \rangle_{\rm Vol} \simeq 1.5\ 10^{19}\ \rm m^{-3}$. The same amount of ECH power, 1.5 MW, has been deposited in three different positions in the plasma, keeping the value of the temperature at the edge and the density profile fixed. The resulting electron temperature profiles are shown in Figure 4.28. Again, consistently with the result of the simple analytical model presented above, the electron temperature profiles coincide outside the respective depositon regions, with the ratios χ_e/T_e aligned on the same curve.

Concluding remarks

In conclusion, the overall dependence of the RLW heat conductivity on the electron temperature in plasmas with $T_e/T_i \gg 1$, typical of TCV with ECH, allows the model to properly reproduce the most important stiffness features presented by the experimental behaviour of the electron temperature with ECH. We have shown that this is peculiar of the low density regime, used in TCV operation because of density cut–off. The experimentally observed stiff behaviour is reproduced in this case by a model which does not involve any critical value of the temperature gradient, particularly in the domain of the TCV plasma parameters.

Recently in ASDEX Upgrade the application of physics–based models in the simulation of both modulated and steady state ECH experiments [28, 10], has shown that the best agreement with the experimental results is provided by the Weiland model for TEMs [29]. It is found that the critical gradient $(\nabla T_e/T_e)_{crit}$ provided by the theoretical model is lower than the experimentally measured $\nabla T_e/T_e$ by a factor of about 2. An analogous result has been found applying an empirical model like Eq. (4.7) and determining the value of the critical gradient in order to match the experimental behaviour of the electron temperature in modulated experiments [30]. These results indicate that the stiff electron temperature behaviour observed in several tokamaks does not justify equating the experimental temperature gradient with the critical gradient. The plasma reacts to increasing heating power by keeping a constant value of $|\nabla T_e|/T_e$ at a working point which is largely above the threshold. Therefore, the temperature profiles, even though stiff, are not merely determined by the critical gradient, rather by the global parameter dependence of the heat conductivity that describes transport. In this context, a transport model which does not include an adequate expression of the critical temperature gradient, like the RLW, can still provide useful indications on the parameter dependence of the heat conductivity, when found in good agreement with the experimental results.

4.6 Improved Central Electron Confinement

In TCV, significant amounts of current can be driven non–inductively with the ECH system, even sufficient to sustain the whole of the equilibrium current density profile [31, 32, 33]. Therefore, global modifications of the current density profile are possible [34]. In the absence of diagnostics measuring the current profile in TCV, a transport code like PRETOR, consistently coupled with a 2D magnetic equilibrium solver, and directly interfaced with the experimental measurements as well as with the auxiliary heating and current sources computed by a ray-tracing code, like TORAY–GA [35], becomes an indispensable tool. It provides information on the current density and safety factor profiles produced by specific heating and current drive scenarios. In particular, with experiments involving strong amounts of counter–ECCD in the centre in order to obtain reverse shear configurations, this numerical tool allows investigations of the effects of current profile modifications on transport. On the other hand, as the modelling has provided several simulations in very good agreement with the experimental observations, it has been useful also in the opposite direction, namely in planning new experiments, in order to predict the effect of different heating conditions, and choose the best one to obtain specific plasma responses. This is useful and economical to minimize the number of test shots necessary in order to obtain the desired plasma scenario. A good example of such interaction between predictive modelling and experiment is given by the results presented in Ref. [11]. In this work different heating schemes have been modelled in order to investigate the effects on current profile broadening, with the ultimate goal of increasing the plasma shape through ECH. The simulations, involving the coupling between TORAY–GA and PRETOR, led to the selection of the simple scheme of off–axis ECH, $\rho_{dep} \sim 0.7$, over off–axis co–ECCD or on–axis counter–ECCD: these results have later been confirmed experimentally. The main applications of this numerical tool, composed by the 1D transport code PRETOR, the 2D equilibrium solver, and the interfaces with the experimental data and the output of the ray–tracing code TORAY–GA, have been the analysis and simulation of discharges with high plasma performance, namely central electron temperature enhancement with central counter–ECCD [36] and improved central electron confinement (ICEC) [37, 38]. In subsection 4.6.1, the general methodology applied for the simulation of the time evolution of a full EC heated discharge is outlined. In subsection 4.6.2 we present the experimental observations of the central electron temperature enhancement with counter–ECCD, and their interpretation by means of transport simulations as due to sawtooth stabilization. In subsection 4.6.3 the main experimental features of the ICEC regime are described. In subsection 4.6.4 and 4.6.5 the analysis of the experimental observations and the simulation results are presented.

4.6.1 Simulation methodology for the time evolution of an ECH discharge

A direct and user–friendly procedure has been optimized to automatically perform PRETOR transport simulations of TCV discharges, in particular in order to follow the complete time evolution of a full EC heated discharge [38]. The code takes as input the plasma boundary, the experimental traces of the time evolution of the plasma current, the toroidal magnetic field, the volume average electron density, as well as the heating power and external current drive sources. These are obtained by means of an interface with the output of the ray-tracing code TORAY–GA [35]. The outputs of the code are the temperature and density profiles, the safety factor and the equilibrium magnetic field profiles, the loop voltage and the effective charge number. In the case of ECH/ECCD discharges, at very low density with strong central heating, the simulated electron density profiles are too peaked on–axis compared to the experimental ones, which on the contrary remain considerably flat and become even hollow with central heating due to particle pump–out effects [39]. This effect is not included in the PRETOR particle transport model. Therefore, in order to properly focus the analysis on heat transport effects, in the simulation of the time evolution of a full discharge with ICEC regime, we have also used as an input the experimental density profiles, measured every 50 ms by a 35 chord Thomson scattering system [40]. TORAY–GA uses as input the toroidal and poloidal microwave injection angles and the experimental electron temperature and density profiles, and it is interfaced with the TCV equilibrium reconstruction code LIUQE [41]. It provides the power absorption percentage, the CD efficiency, and the power and driven current density profiles. TORAY–GA is run for each time slice at which the electron temperature and density Thomson scattering profiles are measured.

4.6.2 Central electron temperature enhancement with counter–ECCD

In experiments performed with weakly elongated plasmas (k = 1.2, $\delta = 0.2$, $I_p = 170$kA), it was observed that when counter–ECCD was applied at the magnetic axis the central electron temperature was strongly enhanced [36]. In these experiments the plasma was moved vertically during each discharge, across the EC beam, in order to study the influence of the ECCD depostion location on fast electron generation [42]. With other heating schemes, both heating or co–ECCD, the central electron temperature remained a factor of 2 lower, even when the beam power was absorbed at the plasma centre. A strong dependence of the plasma performance on the direction and magnitude of the central driven current was observed in response to a systematic variation of the toroidal injection angle. The resulting electron temperature profiles, Figure 4.29, obtained with 1.35 MW of auxiliary heating, remain very similar independently of the heating conditions in the confinement region. On the contrary, in the centre, with counter–ECCD the profiles are strongly peaked, with peaking factors, $T_{e0}/ < T_e >$, of 6 to 8, which exceed by far the values obtained with ECH and co–ECCD $T_{e0}/ < T_e >\sim 3$. As the profile peaking involves only the most central plasma region, this implies that, even if the central electron temperature is increased by a factor of 2 in the case of counter injection, the electron thermal confinement time is not significantly increased. In the case of counter–ECCD, $\tau_{Ee} \simeq 4\,\mathrm{ms}$, whereas in the case of ECH or co–ECCD τ_{Ee} is about $3\,\mathrm{ms}$: therefore, the global plasma performance is improved by about 30%. However, the enhanced temperature phase cannot be maintained for a long time. It usually lasts for about 150 ms, a time which is comparable to the current redistribution time, and it is then terminated by a "catastrophic" event accompanied by sudden energy loss: during the enhanced temperature phase no sawtooth activity is observed. The situation is different from co–ECCD or ECH, in which the temperature growth remains limited and sawteeth are present. We have performed simulations of the discharges with the three different current drive conditions. Representative temperature and safety factor profiles are shown in Figure 4.30.

The difference between the counter–ECCD, co–ECCD, ECH and Ohmic profiles is well reproduced. The sawtooth crash trigger conditions, presented in Section 5.2, have been taken into account. The simulation shows that in the case of counter–ECCD the safety factor profile remains everywhere above unity, in contrast to the other situations. In order to assess the role of sawteeth in the plasma performance, the co–ECCD and ECH cases were simulated again with an artificially increased sawtooth crash threshold, hence stabilizing sawteeth in the simulation. In this case the same central temperature was obtained as in the counter–ECCD case. This indicates that the temperature enhancement is just produced during this temporary phase by a very long period of sawtooth stabilisation. The poorer global confinement observed with ECH and co–ECCD is due to the periodic core energy loss caused by sawtooth crashes. The "catastrophic" event terminating the enhanced temperature phase can be interpreted as a "monster" sawtooth crash, occurring when the current density and pressure profiles become too peaked for ideal MHD stability. Therefore, the simple heating scheme of counter–ECCD is not sufficient in order to obtain a stable configuration involving an improved plasma performance. Moreover, as we have already mentioned, while the central temperature is strongly increased by saw-

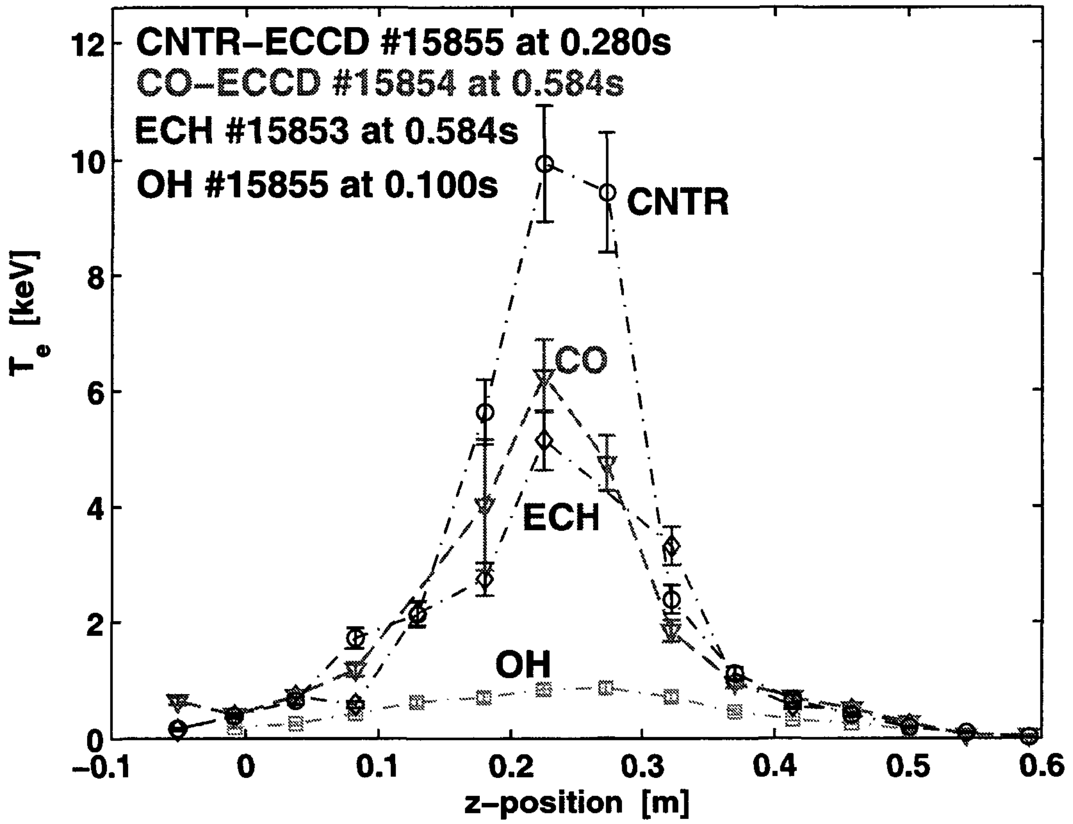

Figure 4.29: *(a) Electron temperature profiles obtained with central deposition of 1.35 MW, with perpendicular injection, ECH only, parallel injection, co–ECCD, and antiparallel injection, counter–ECCD. A corresponding Ohmic profile is also plotted for comparison.*

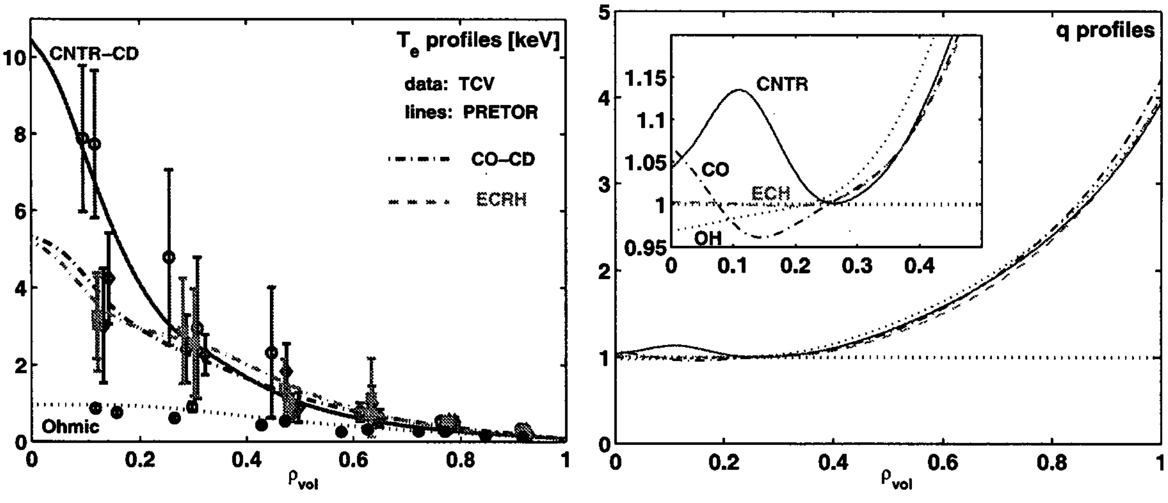

Figure 4.30: *PRETOR simulations for the three different heating schemes, counter–ECCD, co–ECCD and ECH, and for Ohmic heating. (left) Simulated temperature profiles (lines) and experimental measurements, (symbols with errorbars). (right) Corresponding safety factor profiles.*

tooth stabilisation, the global plasma performance is not enhanced as dramatically, as the confinement time increases only from 3 to 4 ms. In order to stabilize this configuration and broaden the temperature profile, off–axis heating has been added, and a particular heating scheme has been identified leading to a stable regime of improved confinement, as will be described in the following subsection.

4.6.3 Experimental observations of ICEC

A quasi–stationary regime of improved central electron confinement (ICEC) has been obtained in TCV, under conditions of dominant ECH and with strong current profile tailoring by counter–ECCD [37]. This regime characterized by central electron temperatures near and above 10 keV and global electron energy confinement times 3 to 4 times higher than those predicted by the RLW scaling law. The heating scenario consists of two different phases, separated by a time delay which is longer than the current redistribution time τ_{crt}. The first is a preheating phase with localized off–axis power deposition (constant plasma current). This phase broadens the temperature profile and consequently the current density and safety factor profiles. In accordance with what has been presented in subsection 4.4.2, off–axis heating also lowers the transport level in the plasma centre. After 300 ms, the high performance phase is generated with additional power injected in the plasma centre in counter–ECCD orientation, with a toroidal component of the beam launching angle of about –30 degrees. Power levels of 0.9 and 1.35 MW are used for the preheating phase, injected at a normalized radius $\rho \simeq 0.3$, whereas 0.9 MW are used for on–axis heating and counter–ECCD. The target plasma for these ex-

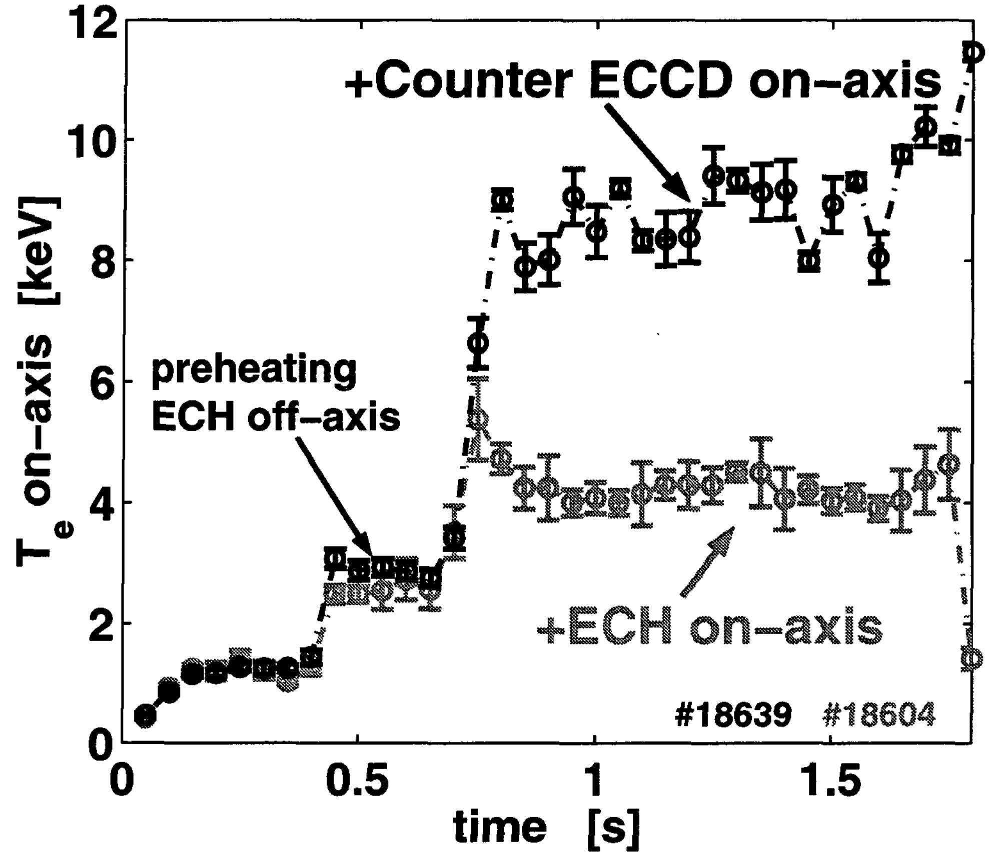

Figure 4.31: *Comparison of the central electron temperature in the case of a shot with ICEC phase, obatined with on-axis counter-ECCD, and a reference shot in which only on-axis heating is applied.*

periments, in limiter configuration, is described by the following parameters: line average density $n_{el} = 1.5\,10^{19}\,m^{-3}$, plasma current $I_p = 200\,\mathrm{kA}$, elongation $k \simeq 1.7$, triangularity $\delta \simeq 0.2 - 0.22$, $q_{edge} \geq 7$. In Figure 4.31 the time evolution of the central electron temperature, measured every 50 ms by a 35 chord Thomson scattering system [40], in the case of a discharge with a ICEC phase (shot ♯18639), is compared with a similar discharge (♯18604) in which the same heating power was applied, but without counter–ECCD during the second power step. The effect of counter–ECCD is remarkable, causing the central temperature to increase by more than a factor of two. As we have already mentioned in subsection 4.5.2, an important and appropriate reference confinement time for TCV is that given by the RLW scaling, which has been found to agree with experiment in Ohmic [4] and in L-mode conditions with ECH auxiliary heating [9]. Hence the confinement enhancement can be characterized by the factor $H_{RLW} = \tau_{Ee} \,/\, \tau_{RLW}$, the ratio of the electron energy confinement time τ_{Ee}, obtained from Thomson scattering data (assuming 100% absorption as computed with TORAY–GA), to the confinement time τ_{RLW} predicted by the scaling law. In Figure 4.32 we show the time evolution of the H_{RLW}

factor in three discharges, shots ♯18639, ♯18604, and ♯18636. Even though substantial confinement improvement is observed with ECH alone, with $H_{RLW} \simeq 2$, it is clear that counter–ECCD is essential to reach the best confinement, with $H_{RLW} > 3$. In Figure 4.32 we have also presented the case of shot ♯18636, in which the time sequence involving a delay between the off–axis and on–axis heating phases was not respected, with counter–ECCD applied on–axis directly from the beginning of the heating phase. In this case the plasma response is particularly unstable, and after a brief phase of improved confinement, the H_{RLW} factor drops to values close to the ones obtained in the case of pure heating. Remarkably, the confinement time undergoes almost no power degradation in the case of shot ♯18604 with heating alone, remaining around 4.5 ms both in the first and second power steps, and even increases in the case of the ICEC regime, from 4.5 up to 5.5 ms when adding central ECCD to off–axis heating. The electron temperature and density profiles during the three phases, Ohmic, off–axis heating, off–axis heating and on–axis counter–ECCD are shown in Figure 4.33. We note that the electron temperature during the ICEC phase turns out to be strongly peaked in the centre, with local gradients up to more than 100 keV/m, consistent with a transport level remaining considerably low in the central region, where intense and localized electron heating is produced, with corresponding power densities up to 50 MW/m^3. The temperature profiles in the confinement zone

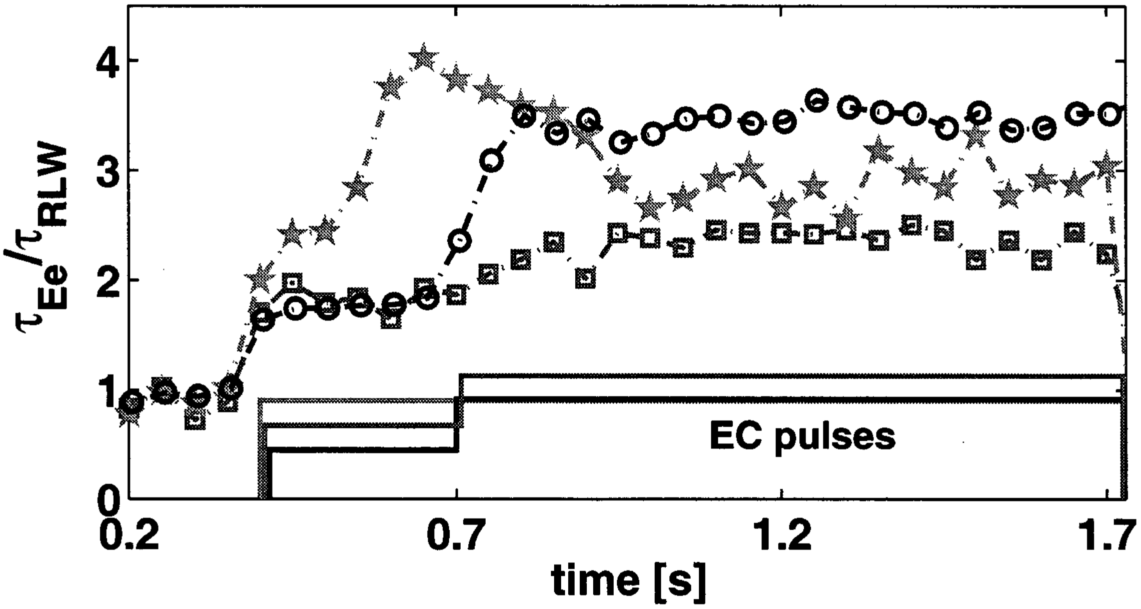

Figure 4.32: *Comparison on the* $H_{RLW} = \tau_{Ee}/\tau_{RLW}$ *for three shots, one presenting the ICEC phase, obtained with on–axis counter–ECCD (open circles), with only on–axis heating without counter–ECCD (open squares), and with on–axis counter–ECCD but without respecting the time sequence (full stars). The corresponding ECH pulses are sketched in the bottom of the figure.*

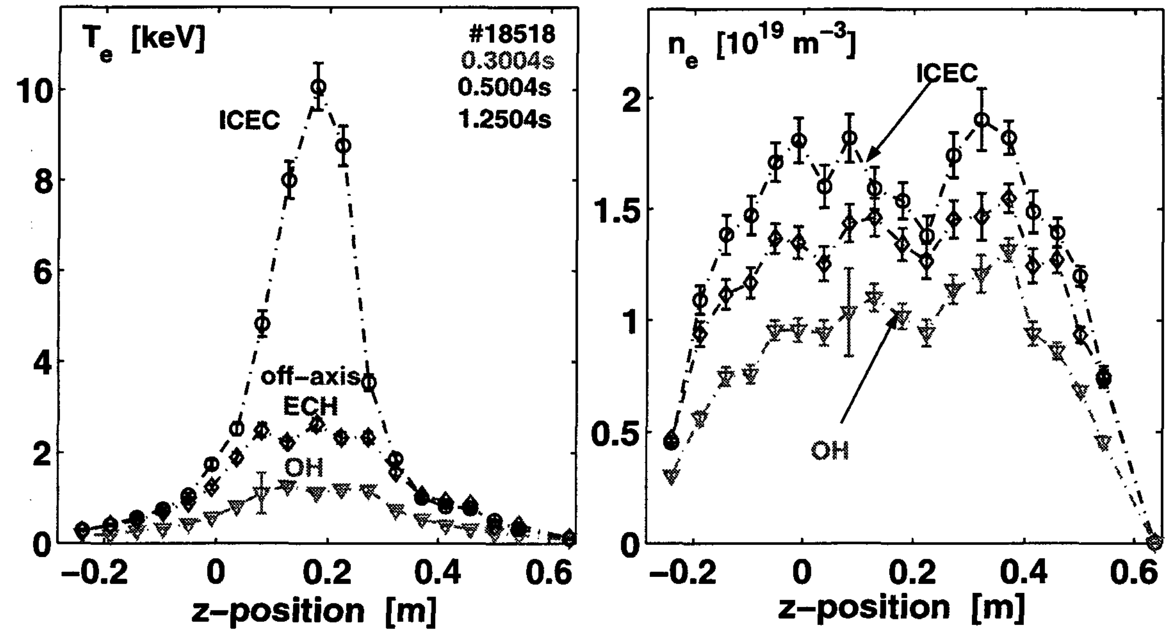

Figure 4.33: *Electron temperature and density profiles from Thomson scattering during the three heating phases (Ohmic, pre-heating with off-axis ECH, and ICEC with on-axis counter-ECCD and off-axis ECH), for shot ♯18518.*

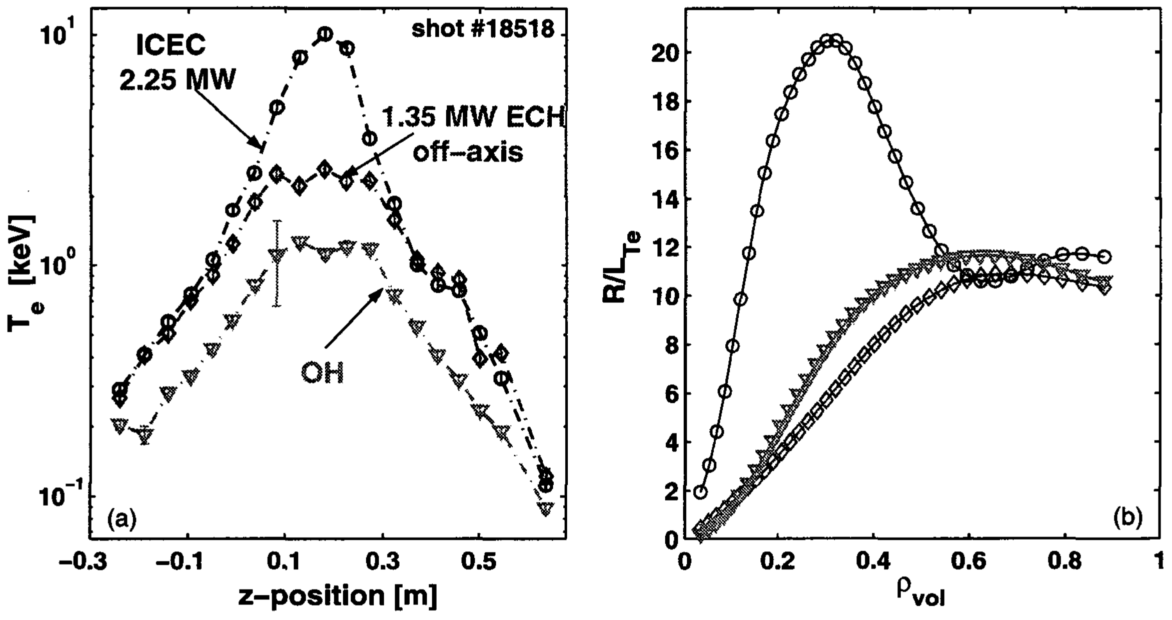

Figure 4.34: *(a) Electron temperature profile from Thomson scattering during the three heating phases (Ohmic, pre-heating with off-axis ECH, and ICEC with on-axis counter-ECCD and off-axis ECH), for shot ♯18518 in semi-logarithmic scale. (b) Corresponding profiles of* $R/L_{Te} = R\,|\nabla T_e/T_e|$*, computed by fitting and smoothing the raw data.*

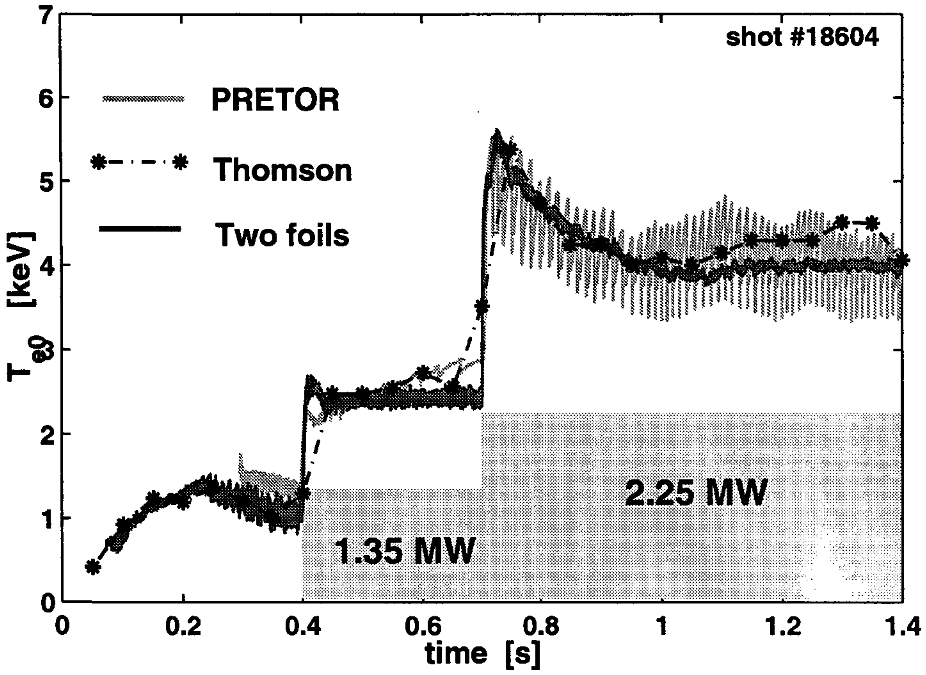

Figure 4.35: *Simulated and measured electron temperature on–axis for shot ♯18604. The PRETOR trace is plotted in light grey solid line, the Thomson scattering measurements are plotted with symbols linked by a dash-dotted line, the temperature measured by the two foil–absorption method is plotted with a dark solid line.*

show a stiff behaviour, in the sense presented in subsection 4.4.1, with a fixed and almost constant value of the normalized temperature gradient length $R/L_{Te} \sim 10$, independently of the heating power, and hence of the radial heat flux, as shown in Figure 4.34. Note that, in contrast to the usual plasma profiles, in the case of the ICEC regime the dimensionless electron temperature scale length R/L_{Te} has a strongly non–monotonic behaviour. The dimensionless electron temperature scale length R/L_{Te} increases up to more than 20 at $r/a \simeq 0.3$, and drops rapidly for larger radii, remaining almost constant around 10 in the confinement region, outside $r/a \simeq 0.5$, Figure 4.34(b). The electron density profiles show rather little change during the different heating phases of the discharge, apart from a tendency towards centrally hollow profiles during the on–axis heating phase, an effect which is known as particle pump-out [39] and which becomes significant at low triangularity ($\delta \leq 0.2$), as in the case of plasmas used for the improved confinement experiments.

4.6.4 Central heating, simulation of shot ♯18604

As we have mentioned in subsection 4.6.3, with on–axis heating alone, without producing counter–ECCD, improved confinement is obtained as compared with the RLW scaling law, with $H_{RLW} \simeq 2$. Therefore, even though the central counter–ECCD has indeed a very strong influence on the plasma response, allowing it to reach $H_{RLW} \geq 3.5$ in the ICEC regime, the investigation of the ICEC must begin with the analysis of the heating only case, whose performance shows that a non negligible component of the ICEC is independent of the specific current profile modifications produced with ECCD. In Figure 4.35 we have shown the time evolution of the central temperature as measured with Thomson scattering (open circle) and as given by the PRETOR simulation for shot ♯18604. In this discharge a first ECH phase has been produced with 1.35 MW deposited off–axis ($\rho_{dep} \simeq 0.35$), then 0.9 MW has been added on–axis after 300 ms, with injection perpendicular to the magnetic field, producing no significant current drive. A good agreement between simulation and measurements is obtained in all the different phases of the discharge. This agreement may seem surprising, as PRETOR uses a χ_e expression based on the local RLW transport model, while the experiment exhibits $H_{RLW} \simeq 2$ during the latter part of the discharge. To better understand the physics mechanism involved, we have performed the following simulations presented in Figure 4.36, using the transport model described in subsection 4.5.3. Three different values of deposition width in a gaussian ECH deposition profile have been considered, Figure 4.36(a), with two power steps at 1.35 and 2.25 MW. In the same figure an illustrative χ_e profile is shown, as typically produced during the off–axis pre–heating phase, which clearly displays a region with good confinement properties in the central part of the plasma cross section. Indeed, as the heat transport coefficient is usually lower in the central plasma region and larger towards the edge, it is reasonable to foresee that the global plasma performance will be directly related to the amount of ECH power deposited inside the good confinement region. With a broad deposition

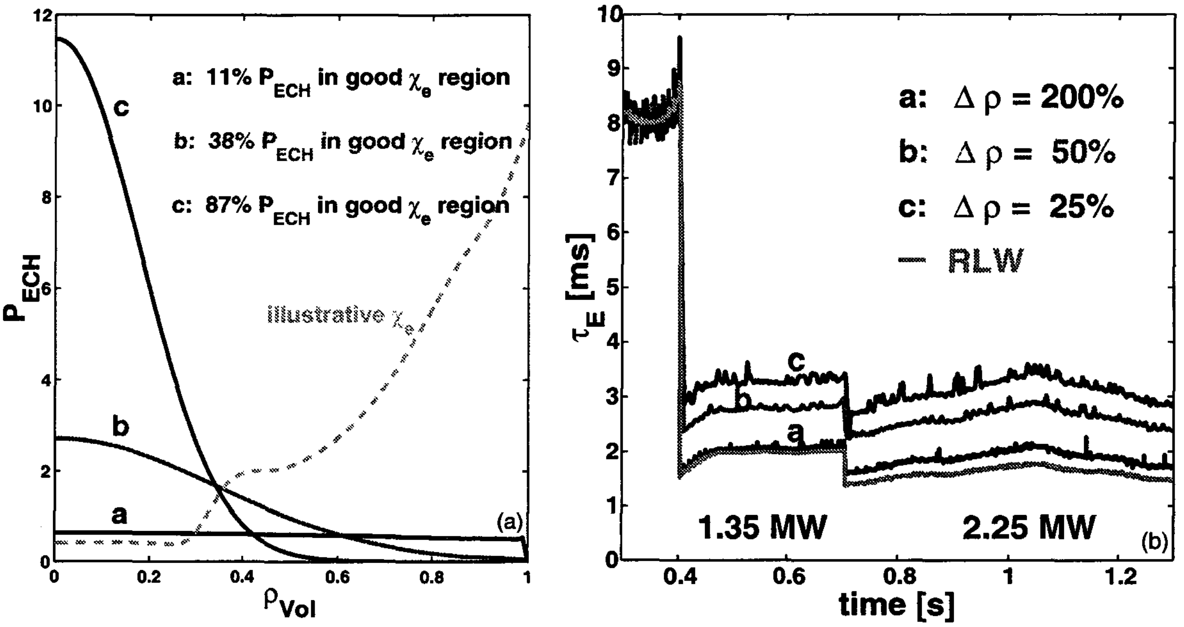

Figure 4.36: *Comparison between the confinement time with three different deposition widths and the RLW global scaling law.*

profile, $\Delta\,\rho = 200\%$, case (a) in Figure 4.36, only the 11% of the total power is deposited in the good confinement region and the RLW global scaling is recovered. When more localized power deposition profiles are considered, the confinement time rapidly exceeds the global RLW scaling. With $\Delta\,\rho = 25\%$, 87% of the power is inside $\rho = 0.3$, case (c), and a much better global confinement time is obtained, with a H_{RLW} factor of 1.75, even though the same RLW expression for the local χ_e is used, Eq. (4.5). The actual power deposition profile for shot ♯18604, as computed with TORAY–GA and used in the simulation presented in Figure 4.35, is similar to case (c). For this reason PRETOR can reproduce the temperature profiles correctly without lowering the χ_e coefficient even with a high H_{RLW} factor. Note that this effect is encouraging for reactor plasmas as α–heating of the electrons is predicted to be rather peaked, concentrated in the plasma region with good confinement properties.

4.6.5 ICEC discharges

As we have already presented in previous subsections, the ICEC regime is obtained with a specific heating scheme, involving a preheating phase with ECH at $\rho_{dep} \simeq 0.3 - 0.4$ and a high performance phase with a large amount of counter–ECCD highly localized on–axis. The amount of driven current is usually $-I_{CD} > 0.5\,I_p$. Therefore, the simulation of the ICEC regime is much more challenging than the case presented in subsection 4.6.4, since not only does the experimental behaviour exhibit very peaked electron temperature profiles with a stronger improvement of the internal confinement, but a strong localized source term must also be taken into account in the field diffusion equation, involving the radial derivative of the driven current density profile (Section 3.3). Owing to the strong current drive, as computed by the ray–tracing code TORAY–GA, the poloidal magnetic field, and consequently the plasma current density and safety factor, turn out to be very sensitive to the ECCD current density profile. Very small differences in the driven current profile can result in very different safety factor profiles in the plasma core. The heat transport coefficient strongly depends on the magnetic shear, therefore the application and validation of the transport model is crucially related to the reliability of the ECCD current density profile reconstruction, which is known only to within a non negligible uncertainty due to the experimental errorbars on the electron temperature and density profiles and, even more importantly, on the magnetic equilibrium reconstruction, in particular involving the determination of the plasma vertical position. Indeed when the standard methodology, as described in subsection 4.6.1, is applied to two discharges presenting an ICEC phase, very different results are obtained. In Figure 4.37(a) the simulated central electron temperature for shot ♯18518 is compared with the experimental data measured by Thomson scattering and by the two foil–absorption method. A very good agreement is found in all the phases of the discharge. As shown by the safety factor profiles, Figure 4.37(b), the central counter-ECCD produces a largely reversed safety factor profile in the centre, which results in a low transport coefficient in the centre, at the same level as in Ohmic even with 2.25 MW, Figure 4.38(a), and in agreement with the experimental estimations obtained by power balance analysis from the Thomson scattering profiles. Note the increasing broadening of the safety factor profile obtained in the simulation, first with off-axis ECH and then adding on-axis counter-ECCD. The simulated temperature profiles are in very good agreement with the experimental measurements in all the phases of the discharge, Figure 4.38(b). This very good agreement has not been found in the simulation of all the ICEC shots. Figure 4.39(a) shows the simulated

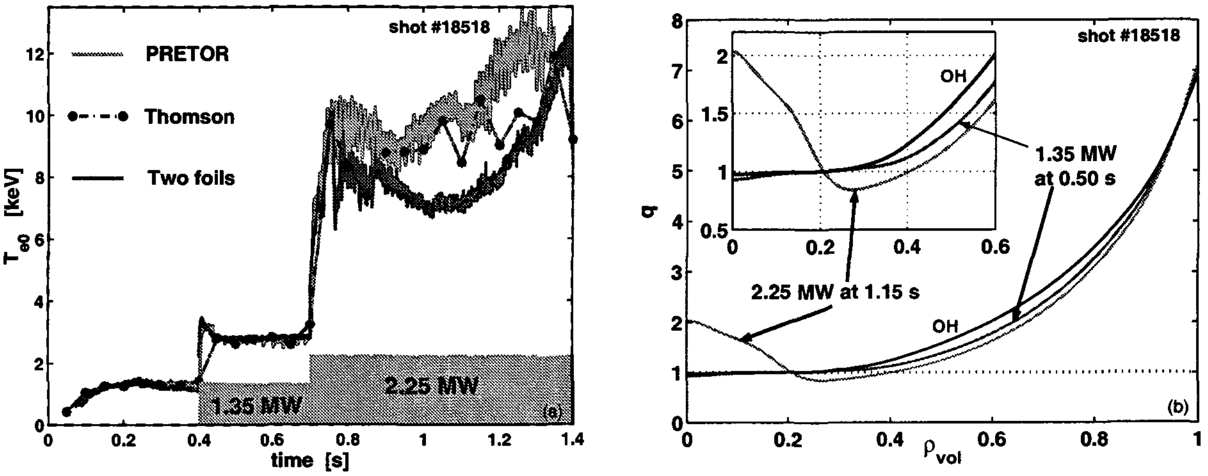

Figure 4.37: *(a) Simulated and measured T_e on-axis for shot ♯18518. (b) Safety factor profiles for ♯18518 at three time slices of the simulation.*

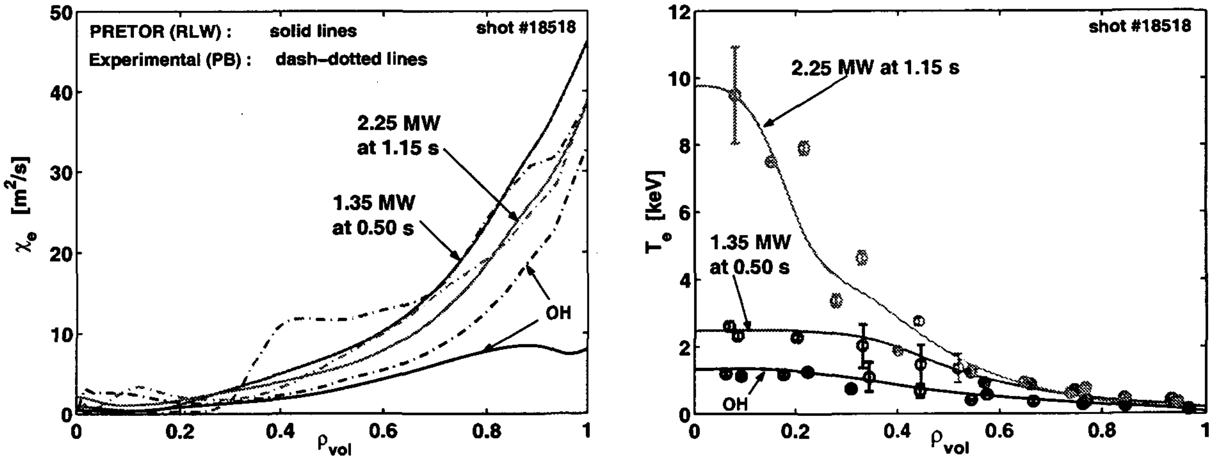

Figure 4.38: *(a) χ_e profiles for ♯18518 compared to the experimental profiles computed by power balance. (b) Electron temperature profiles for ♯18518 compared to the Thomson scattering measurements.*

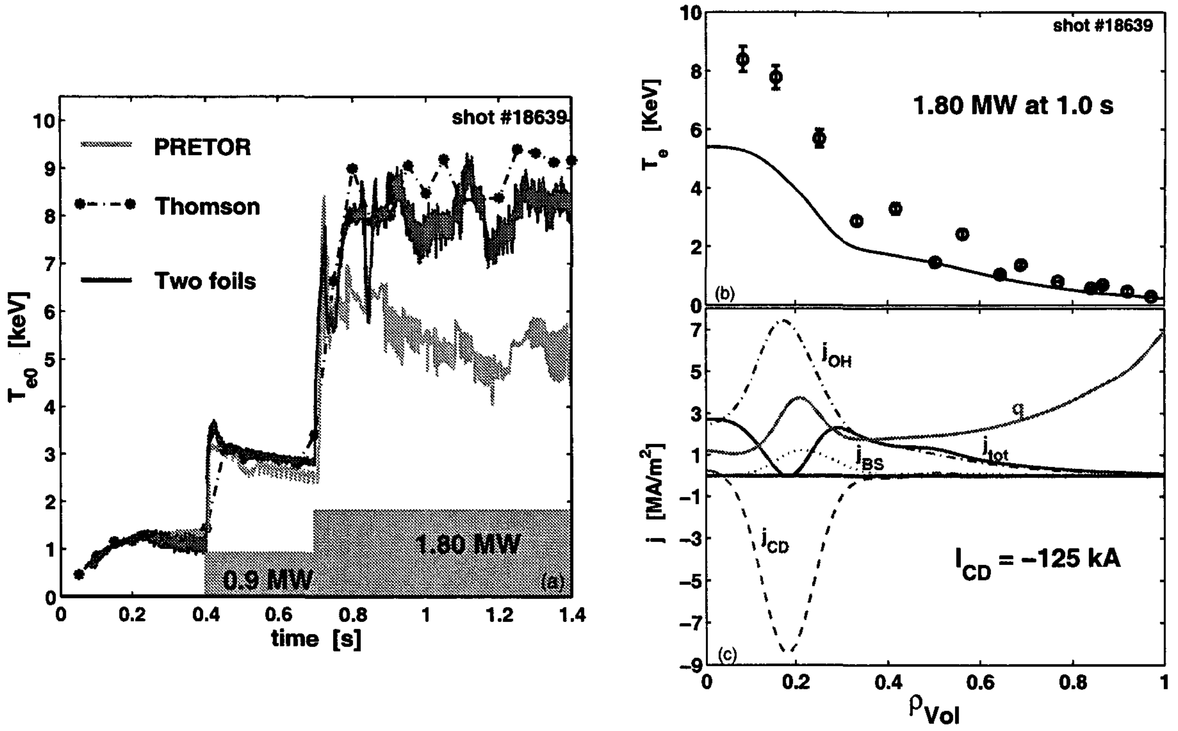

Figure 4.39: *(a) Simulated and measured T_e on–axis for shot ♯18639. Simulated and Thomson measured T_e profile (b) and simulated current densities and safety factor profiles (c) for shot ♯18639 at 1.0 s, with 1.80 MW ECH and -125 kA ECCD.*

and experimental central temperature for shot ♯18639. The result of the transport simulation is largely below the experimental data. The temperature, current density and safety factor profiles are shown in Figure 4.39(b). In the simulation, the on–axis heating and counter–ECCD deposition are too far from the centre to allow a sufficient increase in the temperature. Correspondingly the Ohmic current is not able to increase enough to compensate the strong negative effect of counter–ECCD and this results in a "hole" in the total current profile. The corresponding safety factor profile is not favourable for confinement in the RLW local transport model: this then produces a loop in which the simulated temperature drops indefinitely.

Steady–state current density and safety factor profiles

In order to investigate in more detail the reasons of these apparently contradicting results, we have performed the following analysis on shot ♯18639. We have assumed a quasi steady-state situation during the ICEC phase. Therefore we can assume from Eq. (3.20) that the parallel electric field is constant up to the magnetic axis and its value simply given by $E_0 = V_{\text{loop}}/2\pi R_0$, which can be taken from the experimental measurements. From Eq. (3.21), the relation between the total steady–state current density profile $\tilde{\jmath}_{SS}$

and the ECCD density profile $\tilde{\jmath}_{CD}$ can then be written

$$\tilde{\jmath}_{SS} = \frac{E_0}{\eta_{neo}} + \tilde{\jmath}_{BS} + \tilde{\jmath}_{CD}, \tag{4.11}$$

in which the first two terms of the right hand side, involving the neoclassical resisitivity and the bootstrap current, are computed from the experimental data, using formulae presented in Chapter 2 [see Eq. (3.19) and subsection 3.3 for the definition of $\tilde{\jmath}$]. We have implemented this simple calculation in PRETOR. In this interpretative mode of operation PRETOR takes directly the experimental temperature and pressure profiles, by-passing all the transport package of the code, and it can therefore be considered an equilibrium reconstruction code which consistently takes into account the experimental pressure profiles and the current density sources in order to determine the magnetic equilibrium profiles, assuming steady–state conditions. We have computed the safety factor profiles corresponding to a set of different ECCD current density profiles, within the expected errors. A set of very different safety factor profiles in the plasma core is obtained, varying inside the patched area presented in Figure 4.40(a). The current profiles resulting in the dashed q profile are shown in Figure 4.40(b). This illustrates clearly the difficulties encountered in simulating the ICEC regime. Indeed the high central temperature leads to very good counter–ECCD efficiency, that is to a large negative $\tilde{\jmath}_{CD}$ contribution. To compensate this current, a large centrally peaked Ohmic current is generated, consistently with the peaked temperature profile. Therefore the total current density profile is the result of

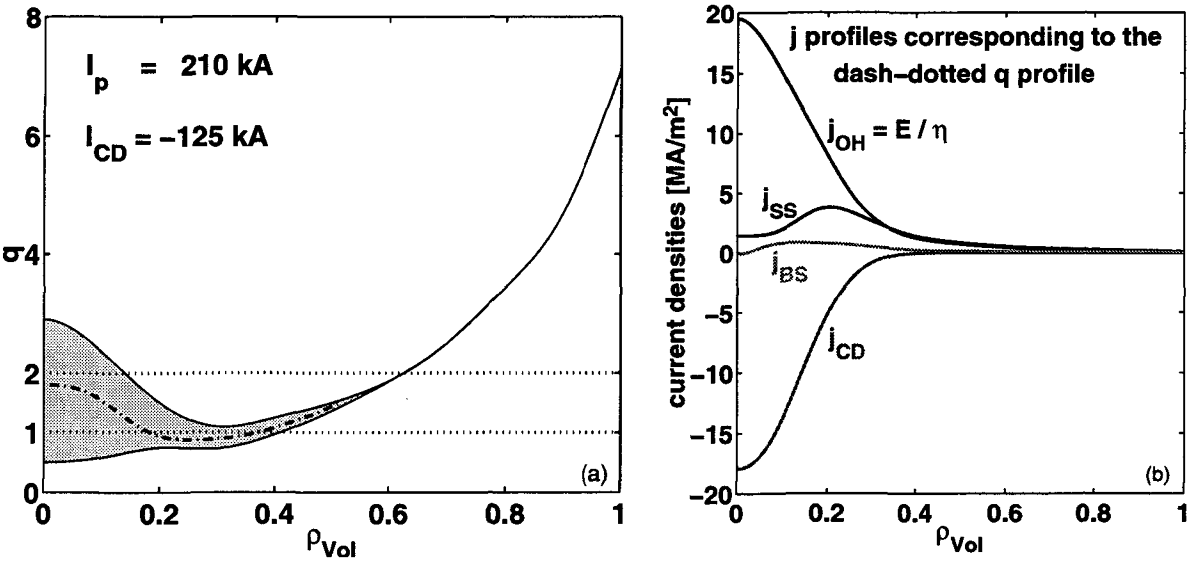

Figure 4.40: *(a) Range of possible steady–state q profiles for shot ♯18639 as obtained in PRETOR using the experimental density and temperature profiles and varying slightly the power deposition location with respect to the TORAY–GA results. (b) Contributions to the current density profile corresponding to the dashed q profile in (a), which is obtained with on–axis counter–ECCD as indicated by the $\tilde{\jmath}_{CD}$ profile.*

the difference of two large contributions in a relatively small central volume. Moreover a slight shift, $\Delta\rho \sim 0.1$, of the peaked $\tilde{\jmath}_{CD}$ towards an off–axis position, or a change in the deposition width changes the current density profile considerably. The fact that PRETOR can simulate the ICEC phase is mainly due to the possibility to obtain a reverse shear and a low q profile in the plasma core. Since χ_e, Eq. (4.5), is proportional to $|\nabla T_e|/T_e$ and to $q/|s|$, a large shear is beneficial, and in particular it becomes necessary precisely in the region in which the temperature gradient is large. But the fulfillment of this precise condition directly depends on the ECCD current density profile, and a small error in its reconstruction can lead to completely different electron temperature behaviours in the simulation. Hence, as we have a wide range of safety factor profiles consistent with the experimental measurements, within the error bars, we cannot conclusively validate or invalidate the transport model. On the other hand, a testable prediction of the model is the high sensitivity of the electron temperature and of the confinement time τ_{Ee} to small changes in the exact location of the on–axis power deposition. Indeed, from the simulations presented above, as shown in Figures 4.37(a) and 4.39(a), a small outward shift of the on–axis deposition, with $\Delta\rho \sim 0.1$, should result in a drop of the central electron temperature roughly from 10 keV to 5 keV.

Further experiments

A series of specific experiments have been performed to test this effect, obtaining results in remarkably good agreement with the modelling predictions. In these experiments the orientation of the 2 beams used for central counter–ECCD has been varied by a small

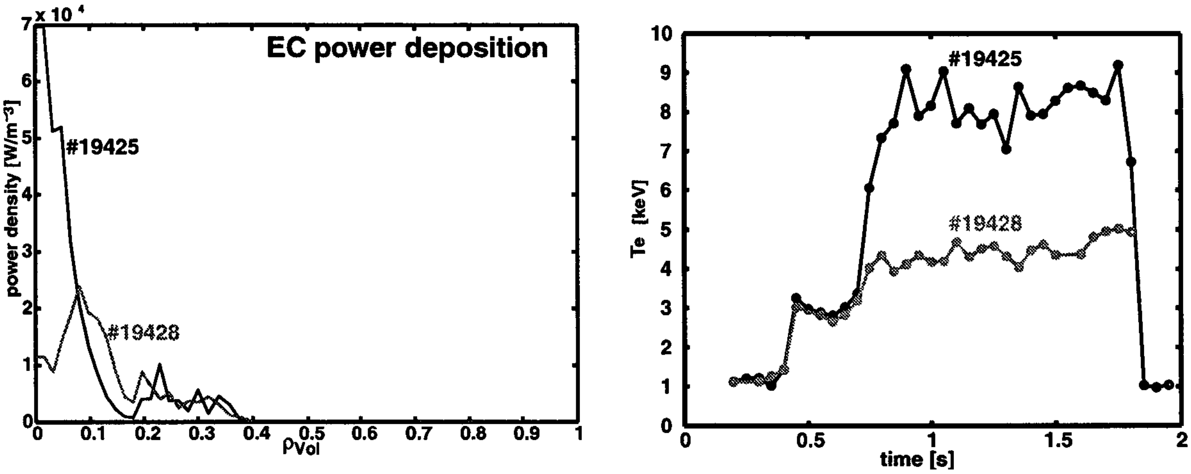

Figure 4.41: *(a) Profiles of the EC power deposition as obtained from TORAY-GA for shots ♯19425, optimized for central power deposition, and ♯19428, shifted off–axis by 3 degrees in the poloidal launching angle. (b) Central electron temperature for shots ♯19425 and ♯19428: the slight shift in the on–axis deposition reduces both the central temperature and the global energy content by almost a factor 2.*

amount, a few degrees in the poloidal launching angle. The equilibrium reconstruction of these shots has been run carefully in order to correctly identify the plasma vertical position. With such reconstruction, accurate TORAY–GA runs have been performed. The effect of a shift of 3 degrees in the poloidal launching angle on the ECH power deposition profile is shown in Figure 4.41(a), as computed by TORAY–GA. The corresponding time evolution of the experimental central electron temperature for the two shots ♯19425 and ♯19428 is shown in Figure 4.41(b), in complete agreement with the PRETOR predictions. Note that not only is the central temperature strongly reduced when the ICEC regime is not achieved, as in shot ♯19428, but so are the total electron energy content W_e and the thermal electron confinement time τ_{Ee} also reduced: for shot ♯19425, $W_e \simeq 9.5kJ$ and $\tau_{Ee} \simeq 5.8$ ms, typical values for the ICEC regime, whereas for shot ♯19428 $W_e \simeq 5kJ$ and $\tau_{Ee} \simeq 3$ ms. In order to investigate the effect of the TORAY–GA ECCD current density profiles on the safety factor profile, we have again used PRETOR in the interpretative mode, as presented above, in order to reconstruct the current density balance and derive the safety factor profile consistently. The results of such a calculation are presented in Figure 4.42. In the case of shot ♯19425, an ECCD current density profile as peaked as that computed by TORAY–GA, similar to the power density profile plotted in Figure 4.41(a), cannot be run by the code, as it would produce negative current densities in the plasma centre, which can not be resolved by the coupled equilibrium solver. For this reason we have used in the calculation a slightly broader deposition profile, driving 80% of the ECCD current predicted by TORAY–GA. In the case of shot ♯19428, the

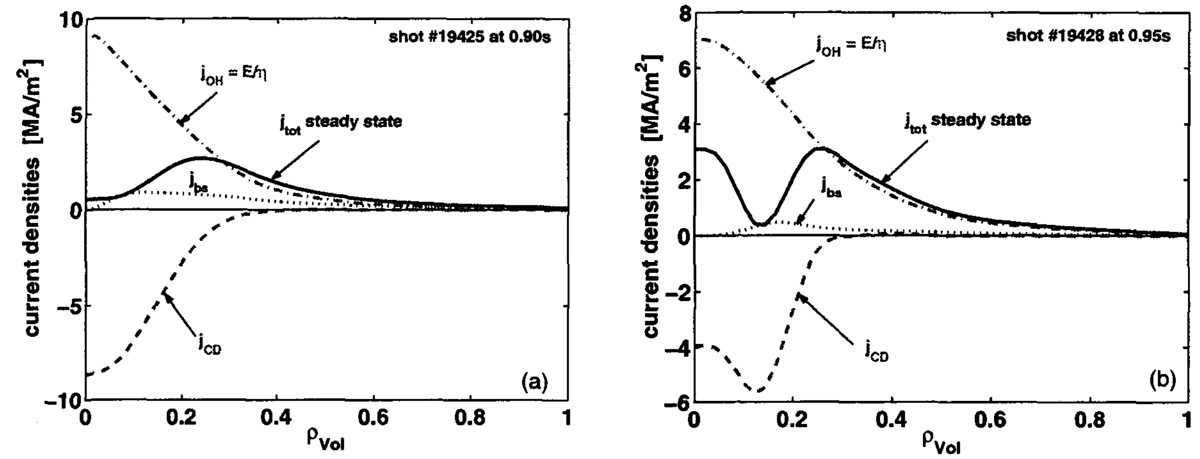

Figure 4.42: *(a) Contributions to the total current density for optimized on–axis counter–ECCD (shot ♯19425) with only 80% of the TORAY–GA total amount of driven current and with a broader deposition profile than predicted by ray-tracing. Values chosen in order to keep the total current density positive everywhere along the minor radius. (b) Contributions to the total current density for the off-centered counter–ECCD (shot ♯19428) with 95% of the total amount of driven current predicted by TORAY–GA, and considering the TORAY–GA deposition profile.*

situation is less extreme, and we were able to run the code using the exact TORAY–GA deposition profile, with 95% of the predicted counter–ECCD. The corresponding safety factor profiles are shown in Figure 4.43. The safety factor for the off–centered depositon (shot ♯19428) is remarkably similar to the one obtained in the time dependent simulation of shot ♯18639, Figure 4.39(b), representative of a current profile modification not conducive to lead to the ICEC regime. The case of shot ♯19425 shows on the contrary a strongly reversed safety factor profile, with a larger negative gradient than that presented in Figure 4.37(b), obtained in the time dependent simulation of shot ♯18518. Note that the value of the safety factor on–axis depends strongly on the value of the current density in the centre. Note also that in the time dependent simulation the electric field profile is never completely flat in the plasma core, rather it peaks on–axis, enhancing $\tilde{\jmath}_{ohm}$ and reducing q_0. From this analysis, and the comparison of the experimental results obtained with shots ♯19425 and ♯19428, respectively with and without an ICEC phase, the shear reversal appears to be a necessary ingredient for ICEC. In order to verify this conclusion, but taking into account the exact current drive density profiles and total amounts of driven current given by TORAY–GA, we have computed the current density balance with a simple numerical procedure which uses all the data provided by the experimental measurements. We use again Eq. (3.21), but at this stage we do not make the assumption of steady–state conditons, thus leaving $\tilde{E}$ as an unknown function of ρ. In Eq. (3.21), the neoclassical conductivity and the bootstrap current are computed with the Thomson scattering temperature and density profiles, averaged on the quasi–stationary time intervals of the discharge. The effective charge number, crucial to the determination of η, is left as a free parameter and determined as explained later. Moreover we consider the experimental loop voltage as an edge boundary condition to the parallel electric field

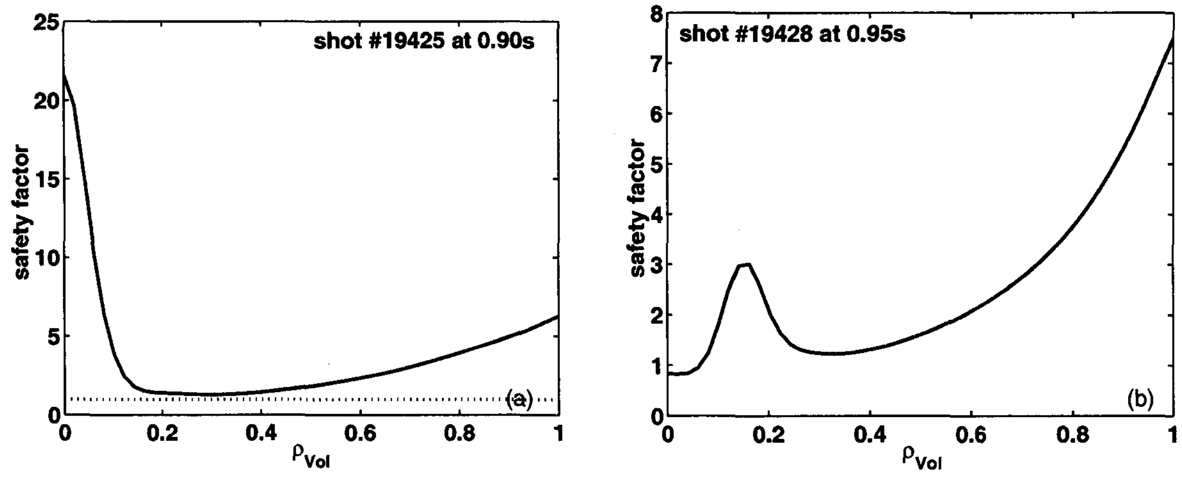

Figure 4.43: *Safety factor profiles corresponding to the plasma current densities shown in Figure 4.41, (a) shot ♯19425, and (b) shot ♯19428.*

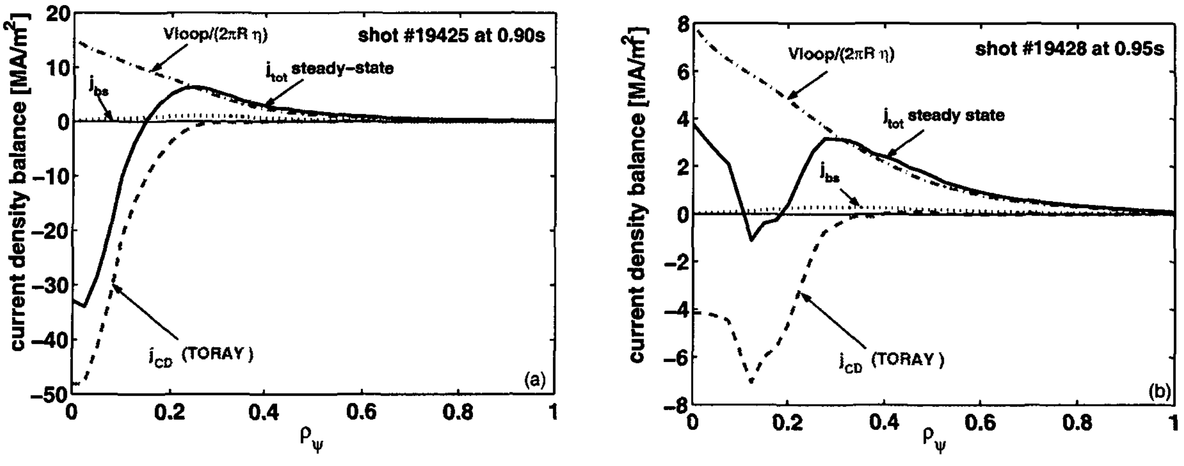

Figure 4.44: *Current density balance, like the one presented in Figure 4.41 assuming steady-state conditions, but this time computed taking into account the exact ECCD current density profiles and amounts of driven current predicted by TORAY-GA, matching the value of the total plasma current by adjusting the effective charge number and consequently the neoclassical conductivity. (a) for shot♯19425, (b) for shot ♯19428.*

profile. All the calculations are performed taking into account the most accurate magnetic equilibrium reconstruction computed by LIUQE. Eq. (3.21) is applied iteratively, using the exact TORAY-GA ECCD profiles and amount of total driven current. Convergence is reached once the value of the effective charge number allows the integral of the total plasma current density to match the experimental value of the plasma current. At this point a hypothesis must be made on the behaviour of the parallel electric field. A possibility, as in Eq. (4.11), is to assume that the duration of these quasi-stationary discharges is sufficient to assume steady-state conditions, and therefore take the parallel electric field as spatially uniform. From the previous PRETOR analysis, Figure 4.42(a), we expect that this assumption, in the case of shot ♯19425 will lead to a total current density profile strongly negative in the center. A second possibility is to assume that small oscillations of the plasma parameters in the core, always present even in stationary non sawtoothing plasmas, prevent the attainment of true steady-state conditions. This implies that, at least in the plasma core, the parallel electric field is not flat, but strongly peaked. The electric field profile can be determined imposing that the current density profile does not drop below zero.

Let us consider the former option first. The current density balance as produced by such a procedure for the two shots ♯19425 and ♯19428 is shown in Figure 4.44. These results are completely consistent with the results obtained with PRETOR. In the case of shot ♯19428 the PRETOR simulation was able to take into account almost the totality of the amount of the driven current computed by TORAY-GA. The profiles presented in Figure 4.41(a) and Figure 4.44(a) are very similar, except for the locally negative current density obtained by allowing the totality of the driven current predicted by TORAY-GA. In the case of optimized on-axis counter-ECCD, which leads to the ICEC regime (shot ♯19425) consistently with the PRETOR reconstruction, the TORAY-GA ECCD density profile and total amount of driven current involve a strongly negative current density profile in the plasma centre, with the assumption of steady-state conditions. Indeed, the Ohmic contribution to the current density, $j_{OH} = E/\eta$, within the experimental errorbars on the electron temperature profile, cannot be so peaked on-axis as to compensate the effect of counter-ECCD. The effective charge numbers resulting from the iterative procedure are 3 and 2.7 for shots ♯19425 and ♯19428 respectively. These values are somewhat below the value usually estimated for TCV during ECH operation, which is around 4. Note, in this context, that the neoclassical theory could underestimate the effective plasma conductivity, which can be modified by the presence of a hot tail in the electron distribution function, due to current drive [43, 44].

On the contrary, the current density balance for shot ♯19425 obtained by imposing that the total current density not drop below zero, namely $\tilde{\jmath}_{tot} \geq 0$, gives the result shown in Figure 4.45(a), with a value of the effective charge number of 3.9. The corresponding parallel electric field profile is plotted in Figure 4.45(b). This implies a value of $|\partial \tilde{E}/\partial \rho|$ of about 4 V/m^2 in the plasma centre: this value provides an estimate of the order of magnitude of the oscillations of the poloidal magnetic field in T/s. In the absence of measurements of the current density profile, it is difficult to state which description is the more realistic between Figure 4.44(a) and Figure 4.45. Nevertheless, the present analysis suggests that in the ICEC regime effects similar to those recently observed in extreme

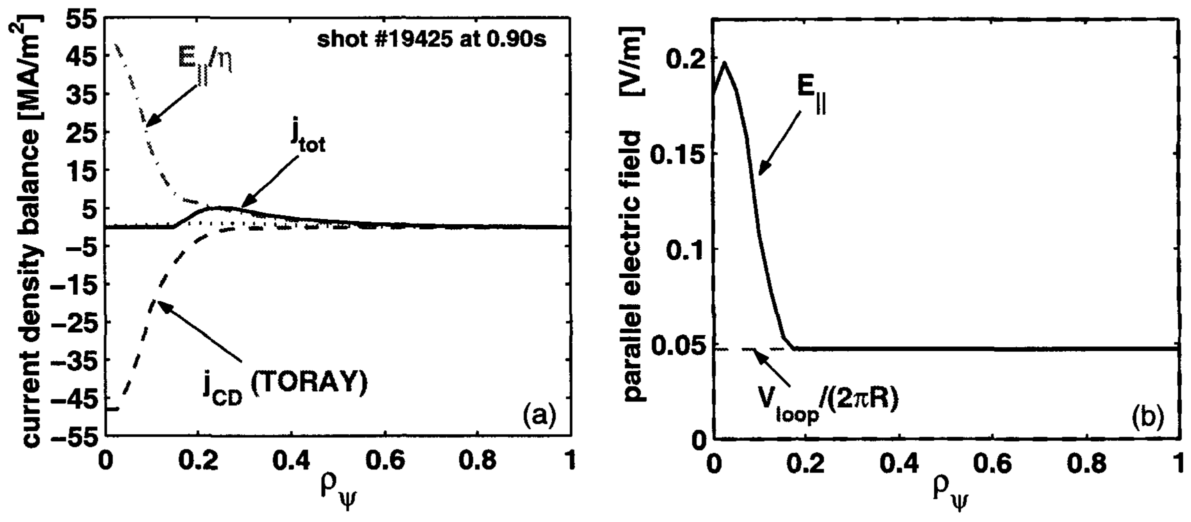

Figure 4.45: *(a) Current density balance for shot ♯19425, computed imposing* $\tilde{\jmath}_{tot} \geq 0$. *(b) Corresponding profile of the parallel electric field.*

shear reversal scenarios in JET are produced [45].

4.7 Summary and Conclusions

In this Chapter we have presented an analysis of the properties of electron transport in the TCV tokamak and a set of simulations performed with the transport code PRETOR, focusing in particular on experiments involving predominant ECH.

Experimental observations show that, with central heating, the electron temperature has a stiff behaviour, in the sense that the temperature gradient length L_{Te} is independent of the amount of power deposited in the centre and almost constant in the confinement region. With off–axis heating, the same behaviour is observed outside the deposition region, whereas in the plasma centre a low transport level is estimated by power balance, with a steep step of the heat conductivity at the location of the power absorption. Localized power deposition allows profile modifications in the confinement region, indicating that stiffness is not a universal property preventing any profile modification. These experimental observations, as well as recent observations and transport analysis performed on other tokamaks, indicate that the physical phenomena responsible for the anomalous electron transport are likely to be forms of drift–wave turbulence (TEMs, ETGs) involving a critical value in the normalized temperature gradient R/L_{Te}. Nevertheless, the success of the global RLW scaling in ohmic and ECH L–mode discharges in TCV and the satisfactory results obtained with the RLW local transport model in modelling the electron transport in other tokamaks have motivated us to apply the semi–empirical RLW local transport model in the simulation of a large set of TCV discharges, with very different heating conditions. The RLW model gives in general very satisfactory results; this can be explained, consistently with previous analysis in the literature, by the fact that the experimental values of the electron temperature gradient are well above the RLW threshold ($|\nabla T_e|/\nabla_{RLW} \simeq 2-3$ in Ohmic and $|\nabla T_e|/\nabla_{RLW} \simeq 5-15$ with ECH). In this situation, the parametric dependence of the RLW heat conductivity is found to be adequate to simulate the TCV electron heat transport.

We have simulated a large database of ohmic discharges, with very different plasma shapes. We have shown that, provided that the geometrical factors are correctly taken into account in the transport equations, there is no need to include an explicit shape dependence in the expression for the transport coefficients. The most important requirements in the simulation of ohmic plasmas are, firstly, to consistently solve the transport equations and the field diffusion equation, coupling them with a 2D magnetic equilibrium reconstruction, and, secondly, to employ a reliable sawtooth period and post–crash relaxation model for sawtoothing discharges. This enables one to determine consistently the width of the ohmic power density profile and consequently the most important features of the temperature profile, which turn out to be almost insensitive to the specific transport model. Good simulations of the density profiles have also been obtained for ohmic plasmas with a model involving an anomalous pinch term whose ratio to the particle diffusivity is proportional to s/ρ, with ρ the minor radius and s the magnetic shear (in Ohmic $n_e/n_e(0) \propto (q(0)/q)^{\alpha}$, with $\alpha \simeq 0.8$, works in general remarkably well). A detailed inspection of the ohmic electron temperature in the confinement region has revealed that a factor must be included in the RLW heat conductivity expression in order to reproduce in the simulations the concave profiles observed at high values of the edge safety factor. This is particularly relevant in the simulation of discharges with ECH, usually produced with low plasma current.

Although the RLW model apparently does not involve any stiffness feature in the expression of the heat conductivity, in particular with central ECH, since the RLW critical temperature gradient turns out to be negligible as compared with the experimental gradient, we have shown that the experimentally observed stiff behaviour is well reproduced by the model. We have pointed out that this is due to the specific temperature dependence of the heat conductivity ($\chi_e \propto T_e$) obtained with plasma parameters in the domain of TCV ECH operation, namely relatively low densities and ratios $T_i/T_e \ll 1$.

The numerical tool consisting of the transport code PRETOR, the coupled 2D equilibrium solver, and the interfaces with the ray–tracing code TORAY–GA as well as with the experimental data, allows one to perform transport simulations of the time evolution of full ECH discharges. The code has provided several simulations in very good agreement with the experimental observations and has been used to predict specific dependences in the design of new experiments. We have shown the application of the code in the simulation and analysis of TCV discharges with phases of improved confinement. Intense counter–ECCD on–axis is beneficial to enhance the central temperature by means of sawtooth free phases, but does not allow stable scenarios. Adding off–axis heating before the high performance phase with counter–ECCD on–axis leads to a stable regime of improved central electron confinement, which can last for the whole duration of the gyrotrons pulse, and which can be either sawtoothing or not. The ratio of the confinement time to the RLW scaling can exceed 3.5 during the ICEC phase with counter–ECCD, whereas in experiments with pure heating only, the H_{RLW} factor is limited to values around 2. The latter is already an improved plasma performance, as compared with the global RLW scaling. Nevertheless, satisfactory simulations have been obtained with the local RLW transport model. We have shown that power localization in the plasma centre, where the heat conductivity is low, allows one to successfully simulate global plasma performances which largely exceed those predicted by the power degradation of the global scaling. The ICEC regime leads to confinement times exceeding the global scaling even further. Nevertheless, satisfactory simulations of some ICEC discharges have been obtained, but not in all the cases. An inspection of the causes of the disagreement has revealed that the safety factor profile, which plays a crucial role in the expression of the heat conductivity, depends dramatically on the ECCD density profile. Very different q profiles and correspondingly very different results in the transport simulations can be obtained within the expected uncertainties on the ECH power deposition and ECCD density profiles. Simulations suggested that magnetic shear reversal in the core is likely to be the crucial ingredient for ICEC. Simulations predicted also that when specific shear conditions are not obtained, owing to very small modifications of the ECCD density profile, the plasma performance could be strongly degraded. Dedicated experiments have confirmed the predicted high sensitivity of the plasma performance on the location of the counterg–ECCD. An accurate analysis of these discharges indicates that during the ICEC phase strongly negative shear profiles are produced in the plasma core, or that the central plasma region may even have zero or negative current density. The ICEC experiments provide further evidence for the crucial role of magnetic shear in determining the level of anomalous electron transport.

Bibliography

[1] F. Hofmann *et al*, Plasma Phys. Control. Fusion **36**, B277 (1994).

[2] T.P. Goodman *et al*, Porc. 19th SOFT, Lisbon 1996, p. 565.

[3] J.-M. Moret, S. Franke, H. Weisen *et al*, Phys. Rev. Lett **79**, 2057 (1997).

[4] H. Weisen, J.-M. Moret *et al*, Nucl. Fusion **37**, 1741 (1997) [corrigendum Nucl. Fusion **38**, 1119 (1998)].

[5] H. Weisen *et al*, Plasma Phys. Control. Fusion **39**, B135 (1997).

[6] H. Weisen *et al*, Plasma Phys. Control. Fusion **40**, 1803 (1998).

[7] H. Weisen *et al*, Phys. Plasmas **6**, 1 (1999).

[8] E. Minardi, H. Weisen, Nucl. Fusion **41**, 113 (2001).

[9] A. Pochelon, T.P. Goodman, M. Henderson *et al*, Nucl. Fusion **39**, Yokohama Special Issue 2, 1807, (1999).

[10] F. Ryter *et al*, *Experimental Studies of Electron Transport*, invited paper of the 28th EPS Conf. on Control. Fusion and Plasma Physics, Madeira 2001; to be published in Plasma Phys. Control. Fusion.

[11] A. Pochelon, F. Hofmann, H. Reimerdes, C. Angioni *et al*, to be published in Nucl. Fusion (2001).

[12] T. Luce *et al*, Phys. Rev. Lett. **68**, 52 (1992).

[13] C. Sozzi *et al*, Paper EXP5/13, Plasma Phys. Contr. Fus. Res., Proc. 18th IAEA Conf., Sorrento 2000.

[14] F. Ryter *et al*, Phys. Rev. Lett. **86**, 2325 (2001).

[15] F. Ryter *et al*, Phys. Rev. Lett. **86**, 5498 (2001).

[16] P.H. Rebut, P.P. Lallia and M.L. Watkins, Proc. 12th Int. Conf. on *Plasma Physics and Controlled Nuclear Fusion Research*, Nice 1988, IAEA Vienna 1989, Vol. 2, p. 191.

[17] D. Boucher, P.H. Rebut, M.L. Watkins, in Proc. 18^{th} Eur. Conf. on *Controlled Fusion and Plasma Physics.* Berlin 1991, ECA Vol. 15C, Part I, European Physical Society, p. 177 (1991).

[18] M. Hugon, B.Ph. van Milligen, P. Smeulders *et al*, Nucl. Fusion **32**, 33 (1992).

[19] D. Boucher, P.H. Rebut, in Proc. IAEA Tech. Committee Meeting on *Advances in Simulation and Modelling of Thermonuclear Plasmas*, Montreal 1992, p. 142 (1993).

[20] C.M. Roach, Plasma Phys. Control. Fusion **38**, 2187 (1996).

[21] G.T. Hoang, B. Saoutic, L. Guiziou *et al*, Nucl. Fusion **38**, 117 (1998).

[22] C. Angioni *et al*, in *Theory of Fusion Plasmas*, Proc. Joint Varenna-Lausanne International Workshop, Varenna 1998 (J.W. Connor, E. Sindoni, J. Vaclavik, Eds), ISPP-18, Ed. Compositori, Bologna 1999, p. 493.

[23] J.W. Connor *et al*, in Proc 16^{th} IAEA Fusion Energy Conf., Montreal 1996, IAEA-CN-64 / FP21.

[24] D.R. Baker and M.N. Rosenbluth, Phys. Plasmas **5** 2936 (1998), and References therein.

[25] H. Weisen, private communication. H. Weisen, I. Furno *et al*, to be published in Nucl. Fusion (LRP 701/01); H. Weisen, E. Minardi, submitted to Europhys. Letters (2001);

[26] W. Horton and P. Zhu, G.T. Hoang *et al*, Phys. Plasmas **7**, 1494 (2000).

[27] T.S. Hahm and W.M. Tang, Phys. Fluids B **1**, 1185 (1989).

[28] G. Tardini *et al*, Proc. of the 28^{th} EPS Conf. on Control. Fusion and Plasma Physics, Madeira 2001, Paper P2.053; submitted to Nucl. Fusion (2001).

[29] H. Nordman, J. Weiland, A. Jarmen, Nucl. Fusion **30**, 983 (1990).

[30] A. Jacchia *et al*, Topical Conference on Radio Frequency Power in Plasmas, Oxnard, USA (2001).

[31] O. Sauter *et al* Phys. Rev. Lett. **84**, 3322 (2000).

[32] S. Coda *et al*, Plasma Phys. Control. Fusion **42**, B311 (2000).

[33] O. Sauter, T.P. Goodman *et al*, Fusion Eng. Des. **53**, 289 (2001).

[34] O. Sauter *et al*, Phys. Plasmas **8**, 2199 (2001).

[35] R.H Cohen, Phys. Fluids **30**, 2442 (1987);
K. Matsuda, IEEE Trans. Plasma Sci. **PS-17**, 6 (1989);
Y.R. Lin-Liu *et al*, in Controlled Fusion and Plasma Physics (Proc. 26th Eur. Conf Maastricht, 1999), Vol. 23J, European Physical Society, Geneva (1999), p. 1245.

[36] Z.A. Pietrzyk, C. Angioni *et al*, Phys. Plasmas **7**, 2909 (2000).

[37] Z.A. Pietrzyk, C. Angioni, R. Behn, S. Coda, T.P. Goodman, M.A. Henderson, F. Hofmann, and O. Sauter, Phys. Rev. Lett. **86**, 1530 (2001).

[38] C. Angioni, T. Goodman, Z.A. Pietrzyk, O. Sauter, in *Theory of Fusion Plasmas*, Proc. Joint Varenna-Lausanne International Workshop, Varenna 2000 (J.W. Connor, O. Sauter, E. Sindoni, Eds), ISPP-18, Ed. Compositori, Bologna 2001, p. 73.

[39] H. Weisen, I. Furno, Nucl. Fusion **41**, 1227 (2001).

[40] R. Behn *et al*, Proc of the 26^{th} EPS Conf. on Control. Fusion and Plasma Physics, Maastricht 1999, ECA Vol. 23J (1999), p. 1065.

[41] F. Hofmann, G. Tonetti, Nucl. Fusion **28**, 1871 (1988).

[42] S. Coda, Y. Peysson, L. Delpech *et al*, in Proc. of the 26^{th} EPS Conf. on Controll. Fusion and Plasma Phys., Maastricht 1999, ECA Vol. 23J (1999), p. 1097.

[43] N.J. Fisch, Phys. Fluids **28** 245 (1985).

[44] P. Nikkola, O. Sauter, *ibidem* [38], p. 345.

[45] N.C. Hawkes, B.C. Stratton, T. Tala *et al*, Phys. Rev. Lett. **87**, 115001 (2001);

Chapter 5

Sawtooth period modelling

5.1 Introduction

Sawtooth oscillations in tokamak discharges are periodic relaxations of the plasma temperature, density and other plasma parameters, which develop when the safety factor on–axis, q_0, drops below unity [1]. In a standard triangular sawtooth, a slow rise of the plasma parameters in the central region of the discharge (the sawtooth ramp) determined by heat deposition and transport, is followed by a rapid drop (the sawtooth crash) resulting in an expulsion of energy and particles from the plasma core. The sawtooth crash is assumed to be triggered by the destabilization of an internal kink mode with toroidal $n = 1$ and dominant poloidal $m = 1$ mode numbers.

Pressure profiles in tokamak plasmas can be strongly influenced by sawtooth activity. The temperature and density profiles are strongly and rapidly modified after each sawtooth crash, up to a certain position on the minor radius which is somewhat larger than the $q = 1$ radius of the pre–crash q profile. The plasma current density also changes during this sequence of events, and consequently also the safety factor profile. Hence, for sawtoothing discharges, realistic simulations and predictions of temperature and density cannot be made purely on the basis of a transport model, but must also incorporate a model for the sawtooth period and amplitude. This is particularly important when predicting plasma profiles in the proposed International Thermonuclear Experimental Reactor (ITER)[2]. It is envisaged that this device will have relatively high values of plasma β and, for inductive operation scenarios, low values of safety factor q at the plasma edge. In these circumstances sawtooth activity is expected to play an important role, and perhaps a favorable one, since such activity may facilitate helium ash removal. On the other hand, long sawtooth periods, as the ones which should be produced by α–particle stabilisation in a burning plasma, can have negative effects, providing seed islands able to trigger pressure limiting neoclassical tearing modes (NTMs) [3], or other MHD instabilities. Prediction of the sawtooth period and theoretical investigation of the experimental tools that could be used for controlling sawtooth activity are thus of particular importance.

A sawtooth period model has been proposed to predict the sawtooth period and amplitude in ITER [4]. This model has been implemented in the PRETOR transport code, including a prescription for the relaxed profiles immediately after the sawtooth crash, and applied directly to a prediction of the sawtooth period and amplitude in projected ITER discharges. Preliminary versions of the model were used to simulate the sawtooth behaviour at the Joint European Torus (JET) under a variety of plasma conditions, going from Ohmic [5] to auxiliary heated discharges [6] and discharges with non–inductive current drive [7]. However, in these previous works, only single instability regimes were separately compared with the experimental data, and the numerical implementation of the model was not included in a transport code which could consistently compute all the plasma and magnetic equilibrium parameters involved in the stability thresholds. Note, indeed, that the conditions for the trigger of a sawtooth crash involve several plasma profiles and local plasma parameters at $q = 1$, whose evolution has to be followed during the sawtooth ramp; in particular, the current density profile and the magnetic shear. In the absence of experimental measurements of such crucial parameters, a consistent application of the sawtooth period model requires reconstructions of the magnetic equilibrium profiles which are at least consistent with the available experimental data. For this reason, in order to describe the time evolution of all the terms involved in the stability thresholds, the numerical implementation of the sawtooth period model must be coupled with a transport code and an equilibrium solver.

In this sense, the first application of the sawtooth period model, as described in the following Section 5.2, simulating an experimentally observed sawtooth period behaviour, has been presented in Ref. [8], in which the crash condition for the resistive internal kink has been shown in good agreement with all the TCV Ohmic L–mode discharges with triangularity $\delta \geq 0.1$, $q_{edge} \leq 4.5$, elongation $1 < k < 2$ and line average density $2 < n_{\mathrm{e\,lin\,19}} < 12$ (subsection 5.3.1). A further step has been to apply the model to ECH discharges in TCV [9, 10]: these results indicate that the magnetic shear and pressure scale length at the $q = 1$ surface play indeed a crucial role in destabilizing the resistive internal kink mode and triggering the sawtooth crash, as prescribed by the model (subsections 5.3.2 - 5.3.5). The application of this model in the detailed simulation of the sawtooth period of several TCV discharges, including ECH and current drive effects, and the successful prediction of the sawtooth behaviour in several different heating conditions has provided, in addition, a theoretical understanding of how ECH can be used to control the sawtooth period (Section 5.3). In this model a sawtooth crash is triggered by the destabilization of one of several magnetohydrodynamic (MHD) modes, which can be either ideal or non–ideal, depending on the values of the plasma parameters involved.

The instability thresholds triggering a sawtooth crash are determined within the framework of the resisitive MHD linear theory. It must be emphasized that the aim of such a model is just to determine the sawtooth period by the identification of the relevant instability thresholds at which a sawtooth crash can be destabilized. The model does not describe the time evolution of the sawtooth crash itself. The theoretical description of the crash event is indeed an incomparably more demanding problem, and it has been subject of many works. In particular multidimensional models have been developed in order to describe the evolution of the magnetic topology during the crash event [11, 12, 13] or to compute the crash time exploring the non–linear growth of the mode [14] - [19]. The description both in space and time of the crash event is relevant for the present sawtooth period model, intended for applications in transport simulations, only if one can derive prescriptions for the relaxed profiles (i.e. the profiles at the end of the crash event). Theoretical evaluations of the crash time or multidimensional descriptions of the magnetic topology during reconnection are of little importance, since the relevant transport time–scales are such that the sawtooth crash can be considered in any case instantaneous. The correct application of the present model is, in principle, to sawtooth periods in which no signature of MHD activity is registered during the sawtooth ramp. The occurrence of saturated modes (already in the non–linear phase of their growth) during the sawtooth ramp, as for instance in the case of the so–called saturated and partially saturated sawteeth [20], could imply that such sawtooth periods do not fall within the validity domain of the model. Nevertheless, it turns out that in general the sawtooth period model gives correct simulations of the sawtooth period in several applications which seem not to belong to its strict domain of application. This suggests that in general the sawtooth period is nevertheless strongly determined by linear theory prescriptions, and that saturated modes occuring during the ramp are not the ones directly responsible for the sawtooth crash. This is confirmed by recent results obtained in TCV, concerning the different effects on the sawtooth period due to increasing ECH power, in plasmas with different shapes [21], with which the model has been found consistent. Indeed, the sawtooth period increases or decreases with increasing additional heating power, depending on the plasma shape. This shape dependence has been found consistent with the prescriptions given by the sawtooth period model, determining the role of ideal or resistive MHD in triggering the sawtooth crash, namely sawteeth are triggered by the ideal internal kink at low triangularity and high elongation, and by the resistive internal kink elsewhere. The threshold between these two different behaviours has been found in agreement with the shape dependence of the critical β_{p1} [23] as calculated by the ideal MHD code KINX [24]. These results can be regarded as a physical basis to the underlying assumption that the relevant thresholds determining the sawtooth crash, and hence the duration of the sawtooth period, are correctly described by linear theory.

Recent JET discharges have provided a new interesting validation for the sawtooth period model. Strong experimental evidence for fast ion stabilisation of sawteeth has been observed during neutral beam injection (NBI) experiments [25, 26]. In order to simulate the sawtooth behaviour in these discharges, we have included a beam ion contribution to the internal kink energy in the sawtooth period model proposed in [4]. This contribution has been validated by specific calculations performed with the hybrid kinetic/MHD code NOVA–K [27] and it has been implemented in the 1–1/2 D transport code PRETOR. Detailed analysis and simulation of a few representative recent JET discharges has been carried out [25] (Section 5.4). The predictions of the sawtooth period model are shown to be in good agreement with the experimental results. This confirms the hypothesis that the observed time evolution of the sawtooth period is determined largely by beam ion stabilisation and validates the theoretical model for quantitative predictions of the sawtooth period, at least for plasma and heating conditions similar to those prevailing in JET experiments. It also confirms the main assumptions made in predicting the sawtooth period in ITER–like plasmas [4].

5.2 Sawtooth period model

In this section we present an overview of the sawtooth period model, involving the instability thresholds, subsection 5.2.1, and the post–crash relaxed profiles prescriptions, subsection 5.2.2, implemented in PRETOR and applied in the simulations presented in Section 5.3 and Section 5.4.

5.2.1 Sawtooth crash triggering conditions

We use the notation and normalisations adopted in Ref. [4]. The dimensionless internal kink mode energy functional $\delta\hat{W}$ is defined such that, in the ideal MHD limit, $\gamma = -\delta\hat{W}\,/\,\tau_A$, where γ is the growth rate and $\tau_A = \sqrt{3}R_0/c_A$, R_0 being the major radius and $c_A = B/(\mu_0 n_i m_i)^{1/2}$ the Alfvén speed. Quantities evaluated at the $q = 1$ surface are indicated by the subscript "1"; for instance the magnetic shear at the $q = 1$ surface is indicated by s_1. Obviously, in the ideal MHD limit, the ideal internal kink is unstable when the ideal growth rate is positive, hence simply when, in the adopted notations,

$$-\delta\hat{W}_{MHD} = \gamma_{ideal}\,\tau_A > 0, \tag{5.1}$$

The ideal internal kink growth rate can be evaluated, using linear ideal MHD, as follows

$$\gamma_{ideal} = -\frac{\delta\hat{W}_{MHD}}{\tau_A} = -\frac{\delta\hat{W}_{Bussac} + \delta\hat{W}_{elong}}{\tau_A}\,C_\delta. \tag{5.2}$$

The term $\delta\hat{W}_{Bussac}$, first calculated in Ref. [23], takes into account the effects of toroidicity, for a circular plasma cross section, whereas the additional elongation term $\delta\hat{W}_{elong}$ and the triangularity factor C_δ give the necessary corrections due to the plasma shape. For the first term we use the well-known analytical expression of Ref. [23]

$$\delta\hat{W}_{Bussac} = -\frac{9\pi}{s_1}\left(l_{i1} - 0.5\right)\epsilon_1^2\left(\beta_{p1}^2 - \beta_{pc}^2\right), \tag{5.3}$$

where l_{i1} is the internal inductance inside the $q = 1$ surface, $\beta_{p1} = (2\mu_0/B_{p1}^2)\left(\langle p\rangle_1 - p_1\right)$, in which $\langle\ \rangle_1$ denotes volume averaging within the $q = 1$ surface, involving the total plasma pressure (background plasma + fast particles), and $\beta_{pc} = 0.3\,(1 - 5\bar{r}_1/3\bar{a})$. Note that for elongated cross sections, this expression remains valid provided that effective radii are introduced in the form $\bar{r}_1 = k_1^{1/2} r_1$ and $\bar{a} = k^{1/2} a$, where k and k_1 are the elongations at the edge and at the $q = 1$ surface respectively. For the term $\delta\hat{W}_{elong}$ several different expressions are available in the literature, which in general neglect the effect of triangularity, hence taking $C_\delta = 1$ [4, 28]. A recent improvement [29] has been obtained by interpolating the numerical results of the MHD code KINX [24], which has been found consistent with the experimental observations on TCV [21], starting from the analytic formula for elongation given in Ref. [4]. Several runs of the code KINX at different plasma shapes, but with a fixed aspect ratio of 10, has given the possibility to obtain an interpolating formula with a large validity domain. Further calculations, in particular at lower aspect ratio, have been undertaken. Therefore, following [29], the elongation additional term and the triangularity factor read

$$\delta\hat{W}_{elong} = -\frac{18\pi}{s_1}\left(l_{i1} - 0.5\right)^3\left(\frac{k_1 - 1}{2}\right)^2, \tag{5.4}$$

$$C_\delta = 16\ \left[(\delta_1 + 0.128)^{0.4}\,(0.105 - \delta_1)^{0.4}\,(0.5 - \delta_1)\right], \tag{5.5}$$

where C_δ will need to be modifed according to the results at low aspect ratio.

In Eq. (5.1) we have neglected all kinetic effects. In particular it can be assumed that the ideal internal kink remains stable as long as its growth rate can be stabilized by plasma rotation, provided by diamagnetic effects. Eq. (5.1) is then modified in the following form [30]

$$-\delta\hat{W}_{MHD} > 0.5\,\omega_{*i}\,\tau_A, \tag{5.6}$$

where $\omega_{*i} = (T_i\,dp_i/\mathrm{d}r)/(eBp_i r_1)$ is the ion diamagnetic frequency. Furthermore, it has been shown that trapped thermal particles in the banana regime involve a non negligible contribution to the internal kink potential energy, due to perpendicular compressibility. This contribution, first pointed out in Refs. [31, 32], turns out to be strongly positive and hence stabilizing [33, 34, 35] for standard tokamak profiles. Note that collisionality plays a different role in the electron and in the ion responses. Indeed assuming a typical mode growth rate of the order of ω_{*i}, the condition for trapped-particles to be considered in the banana regime is $\nu_{*\sigma} \ll \omega_{*i}$, where $\nu_{*\sigma}$ is the ratio of trapped particle bounce time to collision time and the subscript σ refers to ions or electrons. The condition is easily satisfied by ions, which can be considered collisionless in the timescale of the mode growth, but is not satisfied by electrons, even with plasma parameters corresponding to the hot core of a reactor. Therefore thermal electrons must be assumed collisional in the characteristic instability timescale γ^{-1}, and the compressional electron contribution can be neglected. Following the results of [33] and [34], the following expression has been proposed in Ref. [4] to take into account the contribution of thermal trapped ions

$$\delta\hat{W}_{KO} = 0.6\, c_p\, \frac{\epsilon^{1/2}\beta_{i0}}{s_1}, \qquad c_p = \frac{5}{2}\int_0^1 dx\; x^{3/2}\hat{p}_i(x), \tag{5.7}$$

where β_{i0} is the central ion toroidal beta, computed at $r = 0$, $x = r/r_1$, and $\hat{p}_i = p(x)/p(x=0)$. Therefore, the effective internal kink potential energy is modified in the form

$$\delta\hat{W}_{core} = \delta\hat{W}_{MHD} + \delta\hat{W}_{KO}, \tag{5.8}$$

and Eq. (5.6) is modified in the so–called Kruskal–Oberman criterion,

$$-\delta\hat{W}_{core} > 0.5\,\omega_{*i}\,\tau_A, \tag{5.9}$$

in which the stability threshold provided by diamagnetic effects has been included in the right hand side. When this condition is satisfied, an internal kink with a structure similar to the ideal mode is destabilized. Therefore it will be referred to the ideal internal kink, even if in Eq. (5.9) non–ideal effects are included. In the absence of fast particles, Eq. (5.9) will be considered as the relevant trigger condition for a sawtooth crash due to the destabilisation of an ideal internal kink.

In the presence of fast ions, another important kinetic effect can be at play, which involves a strong stabilizing effect. This stabilisation arises from the conservation of the third adiabatic invariant Φ [36], which, in a tokamak equilibrium and to the leading order in a Larmor radius expansion, corresponds to the flux of the poloidal magnetic field through the area defined by the trajectory of the toroidal precession of the trapped particles guiding centres. The conservation of Φ is ensured if the guiding center of the banana orbit performes a toroidal revolution in a time τ_{Dh} which is short compared to the instability growth timescale γ^{-1}. Fast trapped particles, therefore, introduce a new relevant frequency, the bounce–averaged toroidal precessional drift frequency of fast ions $\omega_{Dh} \simeq cE_h\,/\,(4eBR_0r_1)$, which, already for fast ion energies E_h of the order of 50 keV, is usually larger than the diamagnetic frequency ω_{*i}. Therefore, in this situation, Eq. (5.9) changes its stability threshold in the right hand side, and becomes [6]

$$-\delta\hat{W}_{core} > c_h\,\omega_{Dh}\,\tau_A, \tag{5.10}$$

where c_h is a numerical factor of order unity. Following [4], the value of c_h has been set equal to 0.4 in all the simulations performed. On the other hand, if $-\delta\hat{W}_{core} < c_h\,\omega_{Dh}\,\tau_A$, fast particles provide a second non-negligible kinetic contribution $\delta\hat{W}_{fast}$ to the internal kink potential energy, which is usually positive and therefore stabilizing. The detailed expression of $\delta\hat{W}_{fast}$ strongly depends on the nature of the fast ion population, in particular whether the fast particle distribution is isotropic or localized in pitch–angle, and, in this case, whether the fast ion population is localized in the plasma center or localized off–axis [37]. The underlying physics is particularly complexe and, since $\delta\hat{W}_{fast}$ is usually dominant over the other terms $\delta\hat{W}_{MHD}$ and $\delta\hat{W}_{KO}$, particular care is necessary in its evaluation, which can imply the use of specific hybrid kinetic/MHD codes, at least in order to validate the analytical formulae. A well known analytical expression for $\delta\hat{W}_{fast}$, valid in the limit $1-q \to 0$ and magnetic shear $s \to 0$ inside the $q=1$ surface, without including finite Larmor radius effects and assuming isotropic energetic ions, reads [38, 39]

$$\delta\hat{W}_{fast} = -\frac{\beta_{0h}}{\sqrt{2}s_1\epsilon_1^{1/2}}\int_0^{r_1}\left(\frac{r}{r_1}\right)^{3/2}\frac{d\hat{p}_h}{dr}dr. \tag{5.11}$$

Here β_{0h} is the toroidal fast ion beta at the magnetic axis and $\hat{p}_h(r)$ is the normalized fast ion pressure profile. Note that this is the expression used in Section 5.4 in order to take into account the stabilizing contribution of beam ions. It has been tested in this specific application by a comparison with the results of the hybrid kinetic/MHD code NOVA-K [27], as it will be discussed in subsection 5.4.2. The resulting global internal kink potential energy is modified in the form

$$\delta\hat{W} = \delta\hat{W}_{MHD} + \delta\hat{W}_{KO} + \delta\hat{W}_{fast} \tag{5.12}$$

and Eq. (5.9) is replaced by

$$-\delta\hat{W} > 0.5\,\omega_{*i}\,\tau_A. \tag{5.13}$$

When both Eq. (5.10) and Eq. (5.13) are not satisfied, we shall say that the ideal internal kink is stable. However, the internal kink can still be destabilized in this situation. Indeed, when the internal kink potential energy is sufficiently close to zero, the mode dynamics and linear growth rate are determined by microscopic non–ideal effects in a narrow layer around the $q=1$ surface, where reconnection of magnetic field lines can occur. In this sense the relevant stability threshold becomes a threshold against $n = 1/m = 1$ magnetic reconnection. The internal kink changes its structure from that of an ideal mode to that of a reconnecting mode and in these conditions will be referred to the resistive internal kink. Furthermore, when the dimensionless internal kink potential energy $\delta\hat{W}$ is positive and larger than a certain threshold, identified in Ref. [4] as basically given by the normalized ion–sound Larmor radius $\hat{\rho}$, the mode structure is again modified from that of a global resistive internal kink to that of a drift–tearing mode [40, 41], strongly localized near the $q = 1$ surface, and assumed too localized to destabilize a sawtooth crash ($\hat{\rho} = \sqrt{(\rho_i^2 + \rho_s^2)}/\bar{r}_1$, where ρ_i is the thermal ion Larmor radius and ρ_s is the same quantity evaluated using the electron temperature rather than the ion temperature). Hence the domain in which the resistive internal kink can be destabilized is given by

$$-c_\rho\,\hat{\rho} < -\delta\hat{W} < 0.5\,\omega_{*i}\,\tau_A, \tag{5.14}$$

where c_ρ is a dimensionless numerical factor determining at which level the internal kink changes towards a drift–tearing mode character. This parameter has been kept equal to 1, following Ref. [4], in all the present work. Note that this value plays a crucial role in the case of fast particles stabilisation, and it has been found strongly consistent with the experimentally observed periods in JET, in discharges with neutral beam heating and consequent beam ion sawtooth stabilisation, Section 5.4.

In the reconnecting regime defined by Eq. (5.14), the reconnection layer width is determined by either the resistive layer width δ_η or by the ion thermal Larmor radius ρ_i. Depending on the values of these scale lengths, the resistive internal kink has different linear growth rates. If $\delta_\eta > \rho_i$, finite resistivity makes it possible for the resistive internal kink to become unstable, with a growth rate given by [42]

$$\gamma_\eta = s_1^{2/3}\,S^{-1/3}\,\tau_A^{-1}, \tag{5.15}$$

where $S = \tau_\eta/\tau_A$ is the magnetic Reynolds (Lundquist) number, with τ_η the resistive diffusion time. If, on the other hand, $\rho_i > \delta_\eta > c/\omega_{pe}$, where c is the speed of light and ω_{pe} is the electron plasma frequency, the reconnection layer width is determined by the ion Larmor radius ρ_i, and the electron inertia can be neglected in the generalized Ohm's law. This is referred to as the semi-collisional ion–kinetic regime. The internal kink growth rate is then given by [43]

$$\gamma_\rho = \left(\frac{2\,(1+\tau)}{\pi}\right)^{2/7}\,\hat{\rho}_i^{4/7}\,S^{-1/7}\,s_1^{6/7}\,\tau_A^{-1}, \tag{5.16}$$

where $\tau = T_{e1}/T_{i1}$, and $\hat{\rho}_i = \rho_i\,/\,r_1$. Therefore, in the interval $-c_\rho\,\hat{\rho} < -\delta\hat{W} < 0.5\,\omega_{*i}\,\tau_A$, we shall consider the internal kink with an effective growth rate given by

$$\gamma_{\text{eff}} = \max(\gamma_\rho, \gamma_\eta, ...). \tag{5.17}$$

Eq. (5.17) is easily generalized, including the growth rate of resistive internal kink type modes in any new instability regime (γ_{eff} is the maximum among all the resistive type growth rates). The physics of this mode is quite complexe, since a number of different effects can be simultaneously important. However it is believed that stabilization is mainly provided by diamagnetic and drift wave effects [4, 17, 18, 35, 44, 45, 46, 47]. As a general simple expression, one expects the mode to be destabilized if

$$\gamma_{\text{eff}} > c_r \, \left(\omega_{*i}^{\alpha_1} \, \omega_{di}^{\alpha_2} \, \omega_{*e}^{\alpha_3} \, \omega_{de}^{\alpha_4}\right)^{1/(\alpha_1+\alpha_2+\alpha_3+\alpha_4)} , \tag{5.18}$$

where $\omega_{d\sigma} = (T_\sigma \, \mathrm{d}n_\sigma/\mathrm{d}r)/(eBn_\sigma r_1)$ is the drift frequency and c_r is a dimensionless numerical factor, also depending on plasma parameters. In particular, it depends on plasma shape [48] and on the collisionality regime. For circular cross sections, in the collisionless limit $c_r \simeq 1$, while $c_r \simeq (D/9)^{1/3}$ in the collisional limit [49], where D, the ratio of resistive time to perpendicular ion momentum diffusion time, is approximately equal to $0.3\beta_{e1}\sqrt{m_i T_e/m_e T_i}$, with $\beta_{e1} = p_{e1}/(B_1^2/2\mu_0)$. The exact form of Eq. (5.18) can not be determined analytically, as realistic plasma conditions are never in asymptotic limits. For ITER plasmas the condition

$$\gamma_\rho > c_r \, \omega_{*i}$$

was proposed [4], on the basis that plasma parameters are such that always $\rho_i > \delta_\eta$ and only the ion–kinetic regime and ion dynamics are relevant [note that in Ref. [4] $c_* = 1/c_r$]. However, both theoretical works and experimental observations [50] indicate that both density and temperature gradients of both species can in principle play a role. Therefore in Ref. [8] the following more general condition has been proposed

$$\max(\gamma_\rho, \gamma_\eta) > c_r \, \left(\omega_{*i} \, \omega_{*e}\right)^{1/2} . \tag{5.19}$$

This choice turns out to be successful in modelling the sawtooth period in Ohmic and ECRH discharges in TCV, as it will be shown in Section 5.3, as well as in Ohmic in JET, Section 5.4. As first noted in Ref. [5], since both growth rates γ_η and γ_ρ involve s_1, the triggering condition can be rewritten in the form

$$s_1 > s_{1\,\text{crit}}, \tag{5.20}$$

where $s_{1\,\text{crit}}$, the critical shear at $q = 1$, is given by different expressions depending on whether the internal kink becomes unstable in the resistive or ion–kinetic regime. The expressions for $s_{1\,\text{crit}\,\rho,\eta}$, obtained inverting Eq. (5.16) and Eq. (5.15) respectively and implemented in the transport code PRETOR, are the followings

$$s_{1\,\text{crit}\,\rho} = 1.12 \, c_r^{7/6} \, \hat{\rho}_i^{1/2} \left(\frac{R_1}{\bar{r}_1}\right)^{7/6} \left(\frac{T_{i1}}{T_{e1}} \frac{\bar{r}_1^2}{L_{pi\,1} \, L_{pe\,1}}\right)^{7/12} S^{1/6} \, \beta_{i1}^{7/12}, \tag{5.21a}$$

$$s_{1\,\text{crit}\,\eta} = 1.355 \, c_r^{3/2} \, \hat{\rho}_i^{3/2} \left(\frac{R_1}{\bar{r}_1}\right)^{3/2} \left(\frac{T_{i1}}{T_{e1}} \frac{\bar{r}_1^2}{L_{pi\,1} \, L_{pe\,1}}\right)^{3/4} S^{1/2} \, \beta_{i1}^{3/4}, \tag{5.21b}$$

$$s_{1\,\text{crit}} = \min\left(s_{1\,\text{crit}\,\rho}, s_{1\,\text{crit}\,\eta}\right) . \tag{5.21c}$$

Note that in both cases there is a strong dependence on the local plasma parameters at $q = 1$. Eq. (5.20) provides an instability condition involving a critical value of the magnetic shear at $q = 1$ which is similar to the one proposed in Ref. [18]. The theoretical model developed in this Reference was found in agreement with the experimental observation of stabilization and onset of sawteeth in TFTR [51]. Note that the stability threshold against the ideal mode has been seen violated in TFTR experiments [51], leading the authors in Ref. [18] to state that the ideal mode theory is irrelevant to the onset of sawtooth oscillations and the ideal threshold not to be considered. This is not consistent with what was recently observed in TCV [21]. Note also that in Refs. [18, 51], no kinetic effects, like diamagnetic, trapped thermal particles or fast particles effects, which can be strongly stabilizing, have been considered in the stability threshold of the ideal kink. This is in contrast with Eqs. (5.10) and (5.13) considered in the present model.

Since both inequalities Eqs. (5.14) and (5.19) need to be satisfied for the onset of a resistive internal kink, there are two ways to prevent a crash, namely $s_1 < s_{1\,\mathrm{crit}}$ or $\delta\hat{W} > \hat{\rho}$. Therefore the sawtooth crash and the duration of the sawtooth period are determined by the last of these two previous stability conditions to be violated. In one case the inequality given by Eq. (5.14) is satisfied during most of the sawtooth ramp, a crash being triggered when the reconnecting mode drive is strong enough to offset stabilizing diamagnetic effects: this corresponds to s_1 exceeding the critical shear, Eq. (5.20). In the other case $s_1 > s_{1\,crit}$ throughout the relevant phase of the sawtooth ramp, and the mode is destabilized by the condition $-\delta\hat{W} > -\hat{\rho}$. The latter situation was found in Ref. [4] to be the one most likely to be relevant for ITER operation, where the strong stabilizing effect of α-particles makes it possible for $-\delta\hat{W}$ to be less than $-\hat{\rho}$ during the sawtooth ramp. In Section 5.4, we show that this is the situation occurring in JET during the NBI heated discharges, with the role of α-particles in ITER being played by NBI fast ions in JET.

The present sawtooth period model, whose crash trigger conditions are given by Eqs. (5.10, 5.13, 5.14, 5.19), that is

$$\begin{aligned}
-\delta\hat{W}_{core} \quad &> \quad c_h\,\omega_{Dh}\,\tau_A, \\
-\delta\hat{W} \quad &> \quad 0.5\,\omega_{*i}\,\tau_A, \\
-c_\rho\,\hat{\rho} < \quad -\delta\hat{W} \quad &< \quad 0.5\,\omega_{*i}\tau_A \quad \text{and} \quad \gamma_{\text{eff}} \quad > \quad c_r\,\left(\omega_{*i}\omega_{*e}\right)^{1/2},
\end{aligned}$$

can be also summarized in the form of 2D graphs, in which the assumed underlying dispersion relation and the corresponding stability thresholds are represented. In Figure 5.1(a) we have sketched the dispersion relation providing the mode growth rate γ versus the potential energy $\delta\hat{W}$. We have normalized the ordinate by the effective growth rate in the resistive regime, defined by Eq. (5.17), and divided the abscissa by the dimensionless

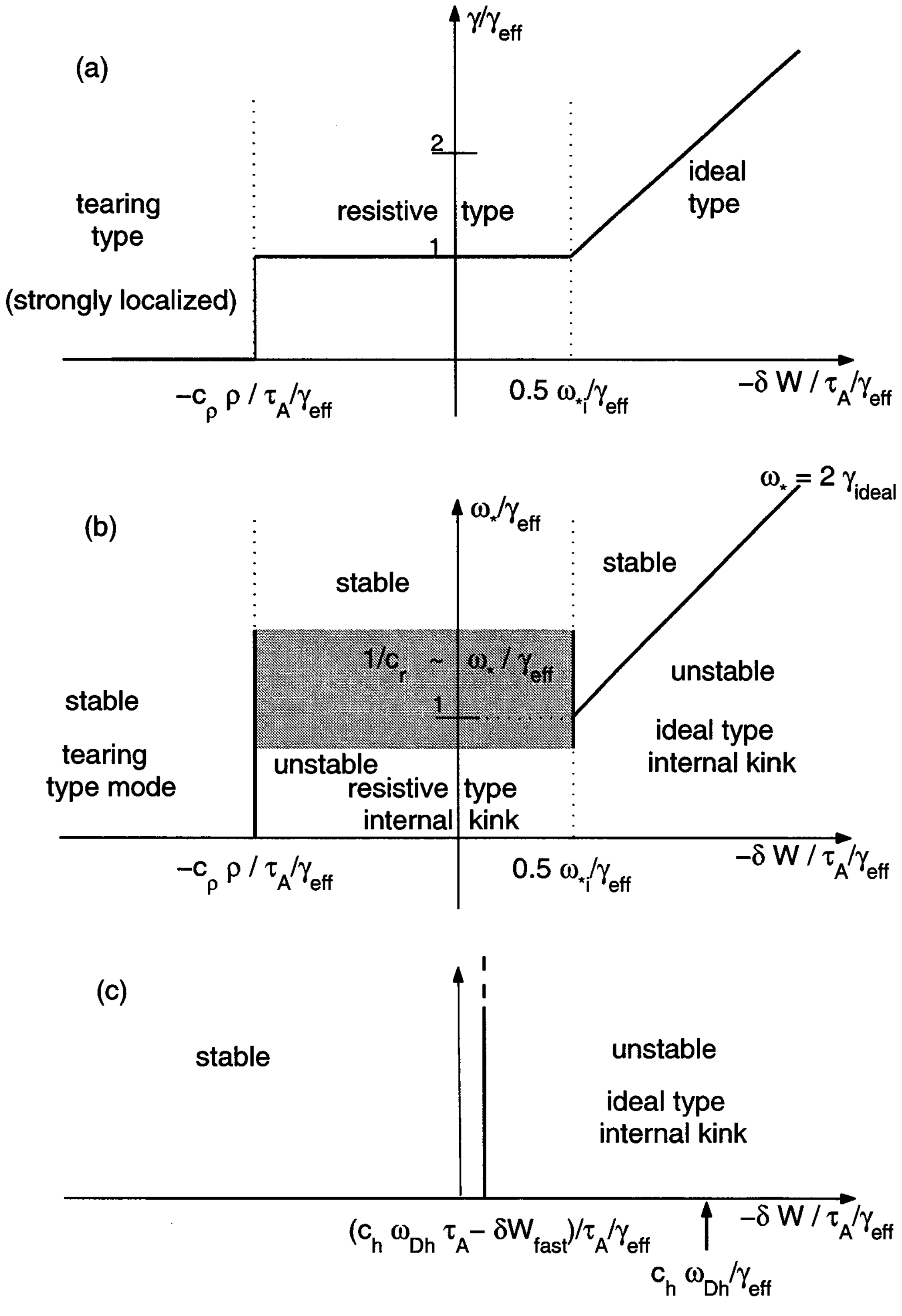
(a)
γ/γ_eff
2
1
tearing type
(strongly localized)
resistive type
ideal type
−c_ρ ρ / τ_A/γ_eff
0.5 ω_*i/γ_eff
−δ W / τ_A/γ_eff
(b)
ω_*/γ_eff
ω_* = 2 γ_ideal
stable
stable
stable
1/c_r ~ ω_* / γ_eff
1
unstable
ideal type internal kink
stable tearing type mode
unstable resistive type internal kink
−c_ρ ρ / τ_A/γ_eff
0.5 ω_*i/γ_eff
−δ W / τ_A/γ_eff
(c)
stable
unstable
ideal type internal kink
(c_h ω_Dh τ_A − δW_fast)/τ_A/γ_eff
−δ W / τ_A/γ_eff
c_h ω_Dh/γ_eff

Figure 5.1: *Diagrams providing an overview of the stability thresholds involved in the sawtooth period model.*

quantity $\tau_A \gamma_{eff}$. If $-\delta\hat{W}/\tau_A$ is large and positive, we are in the ideal limit and we have $\gamma = \gamma_{ideal} = -\delta\hat{W}/\tau_A$. In this situation, when $-\delta\hat{W}/\tau_A > 0.5\,\omega_{*i}$ the ideal internal kink is unstable, as represented in the stability diagram given in Figure 5.1(b). For simplicity in the figure we have assumed $\omega_{*e} = \omega_{*i} = \omega_*$. When $-\delta\hat{W}/\tau_A$ is sufficiently close to zero, namely $-c_\rho\hat{\rho}/\tau_A < -\delta\hat{W}/\tau_A < 0.5\omega_{*i}$, we are in the regime in which the resistive internal kink can be destabilized. In this region $\gamma = \gamma_{eff}$ and the mode is unstable if $\gamma_{eff} > c_r\,\omega_*$ [Eq. (5.19)]. The shaded region reflects the range of variation of the parameter $c_r \in [0.5 \;\; 1.25]$ obtained in our simulations. For values $-\delta\hat{W}/\tau_A$ large and negative the mode takes the structure of a localized tearing mode. These modes are weakly unstable or completely stabilized by other effects which depend on parameters (e.g. collisionality) which are not included in the two variables chosen to describe stability in a 2D plot. These modes can be even destabilized during the sawtooth ramp, but, due to their very localized structure, they do not drive a sawtooth crash. Therefore, beyond the value $-c_\rho\hat{\rho}/\tau_A$, the internal kink is regarded as stable. The parameter c_ρ thus determines the threshold at which the mode structure can be considered too localized for the destabilisation of a sawtooth crash. In the presence of fast particles a supplementary contribution $\delta\hat{W}_{fast}$ is included in $\delta\hat{W}$, which is usually positive and therefore stabilizing. As shown in Figure 5.1(c), when $-\delta\hat{W}_{core}/\tau_A = -(\delta\hat{W} - \delta\hat{W}_{fast})/\tau_A$ is larger than $c_h\omega_{Dh}$, with $\omega_{Dh} \gg \omega_*$, then the ideal internal kink is unstable. Note that high values of $\delta\hat{W}_{fast}$, due for instance to very low values of the shear, can imply that $-\delta\hat{W}/\tau_A < 0.5\omega_{*i}$, even if at the same time very peaked pressure plasma profiles imply that $-\delta\hat{W}_{core}/\tau_A > c_h\omega_{Dh}$. In this case, although $-\delta\hat{W} \in [-c_\rho\hat{\rho}/\tau_A \;\; 0.5\omega_{*i}]$, it is a mode of ideal type which is destabilized.

5.2.2 Prescriptions for the relaxed profiles

Once a sawtooth crash is triggered, the crash event is considered instantaneous compared to the relevant transport time–scale. Hence, in a transport simulation with PRETOR, at the same time step at which a sawtooth crash is triggered, the profiles are relaxed following a set of prescriptions, based on the Kadomtsev complete reconnection model [52]. This model has not always been found consistent with the experimental observations. In particular the model predicts a crash time, due to resistivity and plasma incompressibility, which is much longer than the one experimentally observed [53]. Several theoretical works have been performed later exploring different physical mechanisms than resistivity which could determine the layer width in which the reconnection process takes place. In particular it has been shown that the layer width could be determined by the inertial skin depth when including electron inertia [16], or by the ion–sound Larmor radius in a two–fluid model [17]. This leads to modifications of the Sweet–Parker–Kadomtsev [54, 55, 52] scaling, with reconnection times which are much shorter and closer to the experimental values, even if still longer by a factor of 2–3. Afterwards, non–linear theories have shown that the reconnection rate is strongly increased as the early non–linear phase is entered, namely for magnetic islands widths comparable with the plasma skin depth [18, 56, 19], accounting for the remaining difference with the experimental observations. Unfortunately, a fully consistent non–linear theory describing the island dynamics is not yet available, therefore different ideas exist on the basic collapse mechanism. In particular in several works the underlying hypothesis that the collapse takes place in the form of an accellerated Kadomtsev reconnection is assumed [16, 17, 19, 57]. The same assumption has been made in the present thesis work. While a correct theoretical prediction of the sawtooth crash time would be in any case not relevant for transport timescales, a fully consistent non–linear theory would be able to provide prescriptions for the relaxed state, which is of particular importance for transport studies. From this point of view, a second debated prediction of Kadomtsev model regards the value of the safety factor on–axis, q_0, in the relaxed state. This is set equal to one at the end of the complete reconnection process in Kadomtsev model. The point is controversial, as in certain tokamak experiments q_0 has been observed to remain below unity after the crash [58, 59, 60, 61] whereas in other experiments it does not depart significantly from unity, like for instance in Refs. [62, 63]. The different experimental observations have motivated the development of alternative theoretical models. In particular in Ref. [64] a model for the post–crash state, involving the instability of localized resistive interchange modes and Taylor relaxation [65], has been found in good agreement with TEXTOR experiments, and predicts a safety factor which can remain significantly below unity after the crash. Moreover, in some experiments [61, 66] where q_0 is observed to remain below unity, there is evidence of the formation of a shoulder of low magnetic shear close to the new $q = 1$ surface after crash. This would suggest that relaxed states in which the safety factor remains below unity can be explained by incomplete reconnection processes.

This is consistent with the theoretical model for the sawtooth period presented in subsection 5.2.1, for which the internal kink is stable in the presence of q_0 even strongly below unity, provided that the shear is low at the $q = 1$ surface. In TCV, measurements of the safety factor profile are not available, and this issue remains open. Nevertheless, the analysis of precursors and postcursors of the sawtooth crash in the soft X-ray and magnetic coils traces, for all the different types of sawteeth observed, has suggested that in TCV the reconnection process is always complete, in the sense that a phase of total poloidal symmetry is observed at the end of each sawtooth oscillation [67]. Moreover, although the Kadomtsev model is fairly old, its consequences in the presence of localized auxiliary heating have only recently been fully appreciated. In Ref. [13] it was proposed that the "filament" temperature structures observed in RTP [68] and in TEXT Upgrade [69] may be consistent with the Kadomtsev model. In Ref. [67] we have shown that the same model may also account for the variety of the experimental observations in sawtoothing

TCV discharges. In particular it has been found consistent with specific features of the sawtooth behaviour in the presence of localized ECH, like the formation of a hot ring after crash with peaked pre–crash temperature profiles obtained with localized central heating, or like non-standard sawtooth traces, "humpbacks", obtained with off–axis heating [67]. In this sense, the application of the Kadomtsev complete reconnection model can be considered consistent with the experimental observations in TCV. Incomplete reconnections, yielding a post–crash safety factor profile with q below 1 on the magnetic axis and a low local shear at the $q = 1$ surface, imply that the next crash trigger is reached after a sawtooth period which is shorter than the one obtained after a complete reconnection [4]. Therefore the simulated sawtooth period turns out to be sensitive to the adopted profile relaxation model, particularly when the sawtooth period is comparable with the confinement time. The analysis of the dynamics of the parameters involved in the stability thresholds during the sawtooth ramp shows that the relevant role is played by the value of the shear at the $q = 1$ surface, particularly when the trigger conditions are the ones of Eqs. (5.14) and (5.19). However partial relaxations of the safety factor profile, even though they imply shorter values of $\tau_{\rm saw}$, do not change the global dependence of the sawtooth period on the plasma parameters. Sawtooth period simulations obtained assuming systematic post–crash incomplete reconnections can thus be consistently reproduced with the complete reconnection model, provided that the free parameters of the sawtooth period model, in particular c_ρ in Eq. (5.14) and c_r in Eq. (5.19), are adequately rescaled. In this sense, most of the conclusions obtained in the present work, performed while systematically assuming that a complete reconnection occurs after a sawtooth crash, does not imply a lack of generality.

The Kadomtsev model is based on two major assumptions, and it can be applied only with monotonic safety factor profiles. The first is that magnetic surfaces of equal helical flux Ψ_* reconnect. The helical flux is given by

$$\Psi_*(r) = \int_0^r B_p\,(1-q)\,dr. \tag{5.22}$$

In Figure 5.2 we have shown with a solid line the helical flux corresponding to pre–crash profiles of the safety factor and the poloidal field, as computed by a realistic PRETOR run. Note that if the safety factor goes below 1 in the center, as it must be the case for a pre–crash profile, the helical flux is not monotonic: the helical flux has a maximum where the safety factor is equal to 1 (radius r_1 in Figure 5.2). The second assumption is that the toroidal flux Φ_T is conserved during reconnection. In what follows, we identify how these two assumptions can give prescriptions in order to obtain the relaxed profiles after crash in a 1D transport code. For each radius $r_a < r_1$, see Figure 5.2, it exists a radius r_b, with $r_1 < r_b < r_{mix}$ with the same helical flux. The mixing radius r_{mix}, as shown in

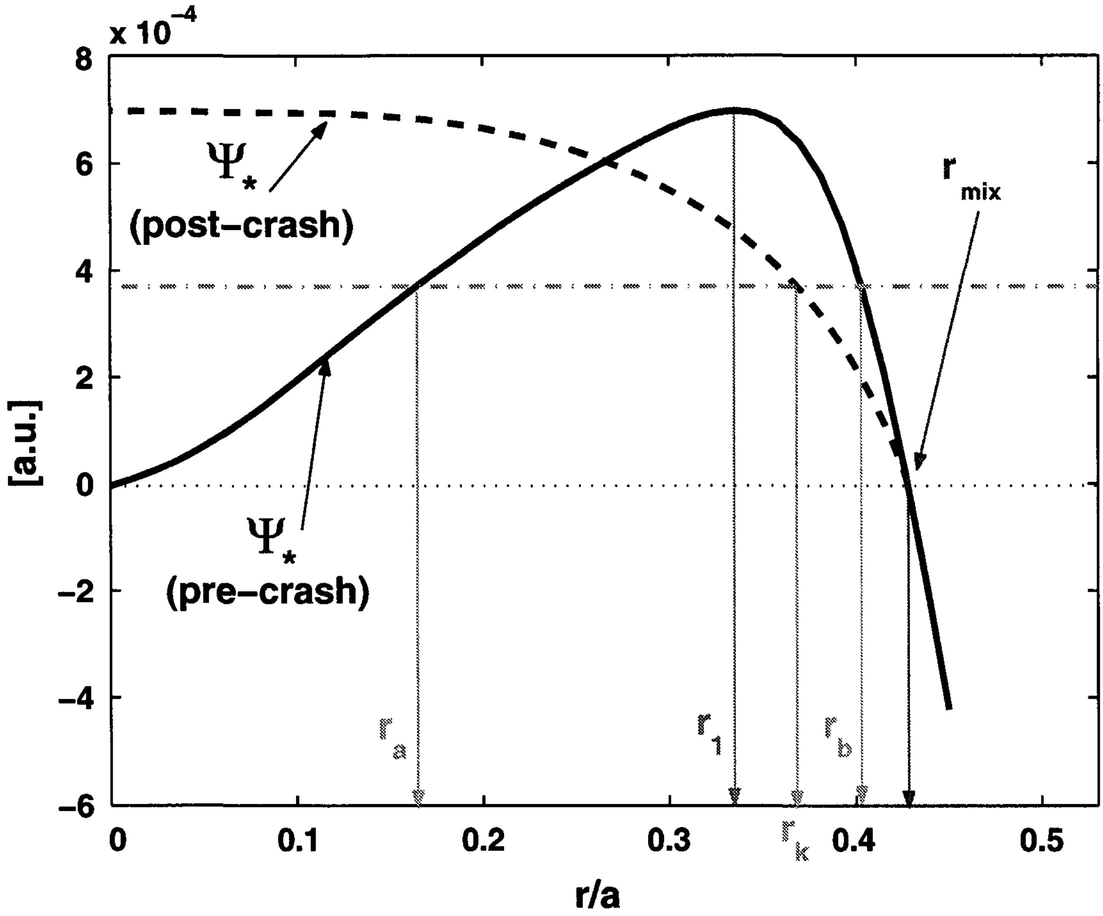

Figure 5.2: *Pre–crash and post–crash helical flux in the Kadomtsev complete reconnection model, as computed by a PRETOR run*

Figure 5.2 is simply defined by the condition

$$\Psi_*(r_{mix}) = \Psi_*(0). \tag{5.23}$$

The conservation of the toroidal flux can be translated in the conservation of areas. The radii r_a and r_b will reconnect in a magnetic surface of radius r_k such that

$$r_k = \sqrt{(r_b^2 - r_a^2)}. \tag{5.24}$$

This equation implies circular concentric flux surfaces, which is usually a reasonable approximation in the central plasma region, up to the mixing radius, for sufficiently large edge values of q and for not extremely high values of edge elongation and triangularity. Once the corresponding radius r_k has been identified for each radius between 0 and r_1, the profile of the post–crash helical flux is determined, as plotted by the dashed line in Figure 5.2. The new helical flux permits the computation of the post–crash profile of the poloidal magnetic field. Indeed, from Eq. (5.22), one can write

$$B_p = \frac{d\Psi_*}{dr} + (q\,B_p).$$

Note now that the product $(q\,B_p)$ involves quantities which in first approximation can be considered not affected by the reconnection process, from Eqs. (3.25) and (3.28),

$$(q\,B_{po}) = \frac{\mu_0\,G_\Phi\,F}{2\,\pi\,R_0},$$

where $G_\Phi = V'\,\langle R^{-2}\rangle\,/\,(2\pi)^2$ [Eq. (3.23)] and $F = 2\pi R B_\Phi/\mu_0$. Hence we can conclude that the poloidal magnetic field profile consistent with the post–crash helical flux is given by

$$B_{po} = \frac{d\Psi_*}{dr} + \frac{\mu_0\,G_\Phi\,F}{2\,\pi\,R_0}. \tag{5.25}$$

Once the new profile of the poloidal magnetic field has been determined, the consistent toroidal integrated current density profile I_t and F are updated with the usual equations, Eqs. (3.25) and (3.26),

$$I_t = \frac{2\pi R_0}{\mu_0}\,G_\theta\,B_{po}, \qquad F^2 = F_0^2 + \int_r ho^a \frac{2V'}{\mu_0 G_\Phi}\frac{\partial P}{\partial \rho}\mathrm{d}\rho + \int \frac{1}{G_\theta G_\Phi}\frac{\partial I_t^2}{\partial \rho}\mathrm{d}\rho. \tag{5.26}$$

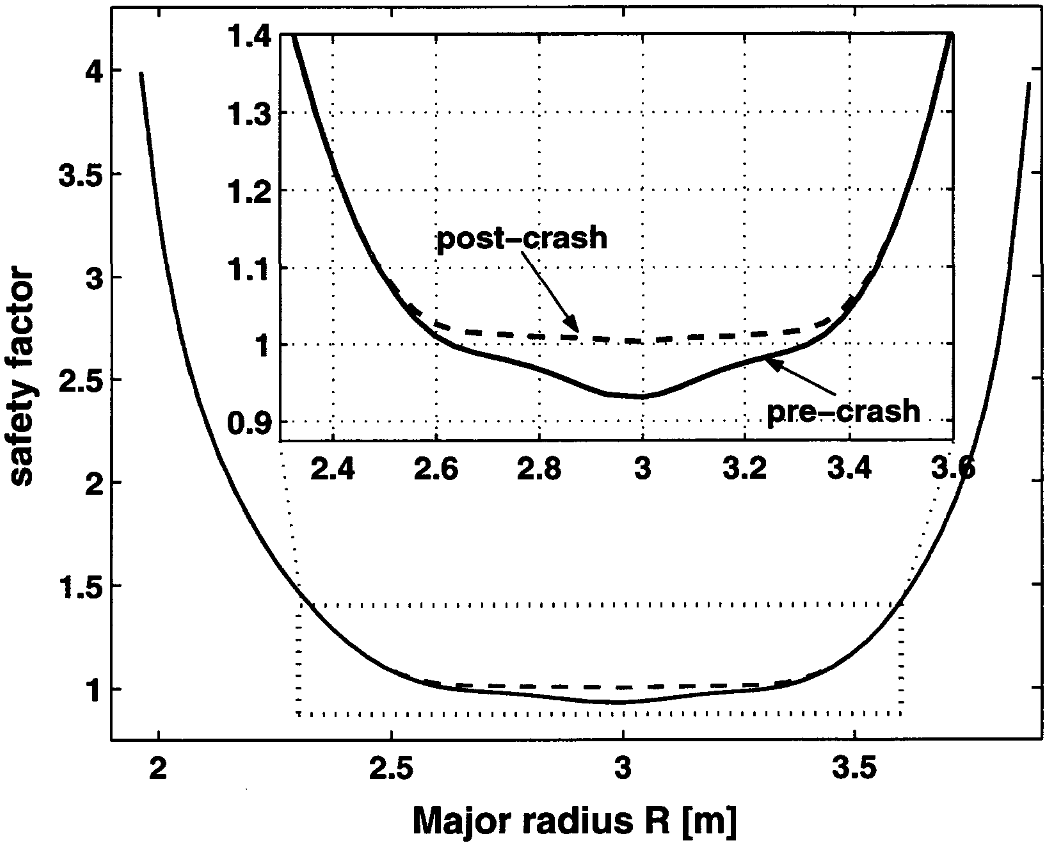

Figure 5.3: *Pre–crash and post–crash safety factor profiles as computed by PRETOR for a JET plasma with additional central electron heating.*

The safety factor and current density profiles are then given by [Eq. (3.28)]

$$q = G_\theta G_\Phi \frac{F}{I_t}, \qquad j = \frac{1}{2\pi R_0} \frac{F}{G_\Phi} \frac{\partial}{\partial \rho} \left(\frac{I_t}{F} \right).$$

In Figure 5.3 we have shown the relaxation of a the safety factor profile as computed with PRETOR by the previous equations in the case of a JET plasma with additional central electron heating. The relaxation of the density and temperature profiles can be simply obtained prescribing a flat profile up to the mixing radius, keeping the total number of particles and the total energy conserved. The resulting electron temperature profiles pre–crash and post–crash for the same PRETOR run of Figure 5.3 are shown in Figure 5.4, respectively with a solid and a dashed line. Note that this is not completely consistent with the Kadomtsev complete reconnection model. Indeed this model implies that density and energy are conserved inside each reconnecting layer during the reconnection process. Always in the limit of circular concentric flux surfaces, this means

$$\int_0^{r_k^2} n_\alpha^f(r^2)\, dr^2 = \int_{r_a^2}^{r_b^2} n_\alpha^i(r^2)\, dr^2, \tag{5.27}$$

$$\int_0^{r_k^2} p_\alpha^f(r^2)\, dr^2 = \int_{r_a^2}^{r_b^2} p_\alpha^i(r^2)\, dr^2, \tag{5.28}$$

where the subscript α refers to each particle species, the radii r_a, r_b and r_k are the ones introduced in Eq. (5.24), and the superscripts "i" and "f" refer to pre–crash and post–crash conditions respectively. This involves precise prescriptions for the relaxed density and temperature profiles, which therefore turn out to be not necessarily flat. Indeed, flat relaxed profiles are obtained only with pre–crash profiles which are exactly parabolic, and in this sense the prescription of flattening the profiles up to the mixing radius can be considered a first order approximation. After differentiation of Eqs. (5.27) and (5.28), one obtains the simple conditions

$$n_\alpha^f(r_k) = 0.5\ \left[n_\alpha^i(r_a) + n_\alpha^i(r_b)\right] \qquad p_\alpha^f(r_k) = 0.5\ \left[p_\alpha^i(r_a) + p_\alpha^i(r_b)\right]. \tag{5.29}$$

For a pre–crash temperature profile more peaked than parabolic, as the one shown in Figure 5.4 obtained with additional central electron heating, these rules imply the formation of a hot ring close to the pre–crash $q = 1$ surface, as shown by the dash–dotted line in Figure 5.4, still computed by PRETOR, and which has been experimentally observed in TCV in 2D tomographic reconstructions of the soft X-ray emissivity [67]. Note that differences in the relaxed density and pressure profiles obtained flattening up to the mixing radius or applying the rules given by Eqs. (5.27) and (5.28), do not imply significative differences in the simulated sawtooth period, also because in the two cases, the same relaxed current density and safety factor profile are considered. For this reason, in PRETOR flat post–crash plasma profiles are usually considered.

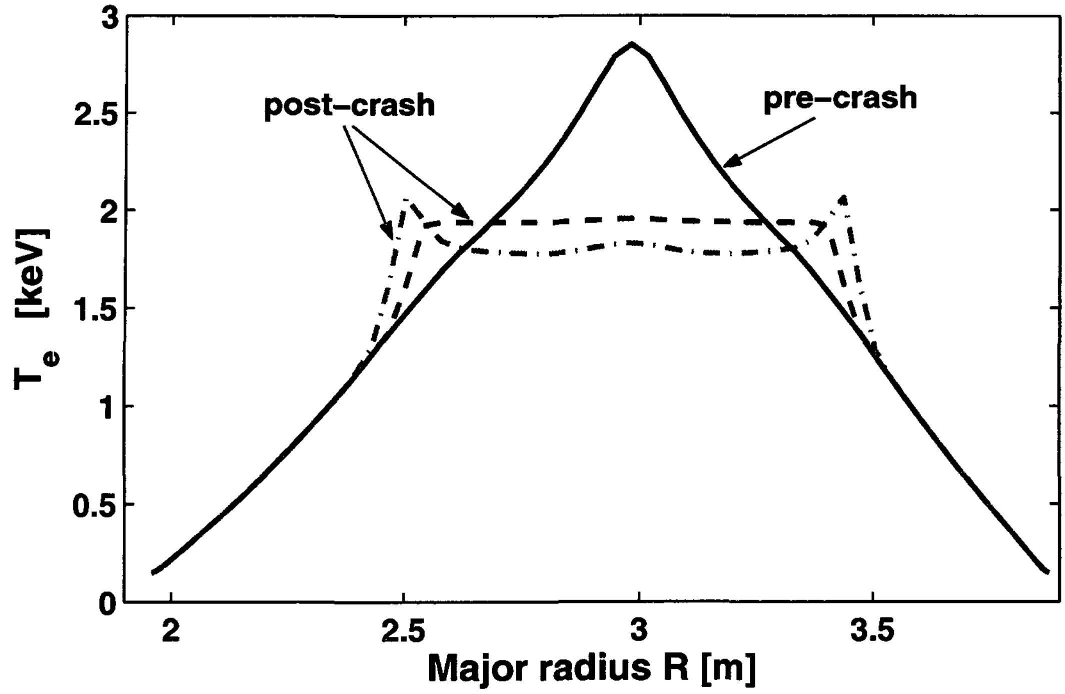

Figure 5.4: *Pre–crash and post–crash electron temperature profiles as computed by PRETOR for a JET plasma with additional central electron heating. The solid line shows the pre–crash profile, the dashed line shows the post–crash profile flattening the profiles up to* r_{mix}*, the dash–dotted line shows the post–crash profiles computed following entirely the Kadomtsev model, Eq. (5.29).*

5.3 Sawtooth period modelling of TCV discharges

The TCV device is a unique facility to explore the influence of plasma shape and ECH on the sawtooth activity. Many types of central relaxation oscillations have been observed in TCV plasmas with ECH [20, 67]. TCV has also allowed a detailed study of the effects of plasma shape on sawtooth period, in Ohmic and electron heated plasmas [21]. Moreover the effects of ECH and current drive on sawteeth can be experimentally analyzed in detail by means of the powerful and highly flexible ECH system available in TCV [50, 70]. All these experiments give the possibility to perform valuable tests for the validation of a sawtooth period model.

5.3.1 Ohmic discharges

The sawtooth period model presented in the previous Section has been applied to 17 Ohmic L-mode shots [8], covering the following range of parameters: $2.3 \leq q_{edge} \leq 4.6$, 0.1 MA $\leq I_p \leq 1$ MA, $2 \leq n_{e19} \leq 12$, $0.1 \leq \delta \leq 0.6$, $1 \leq k \leq 1.9$. The sawtooth period ranges from 2 ms to 8 ms and the inversion radius from 20% to 60% of the minor radius. When performing the simulation of the sawtooth period, as the triggering conditions involve

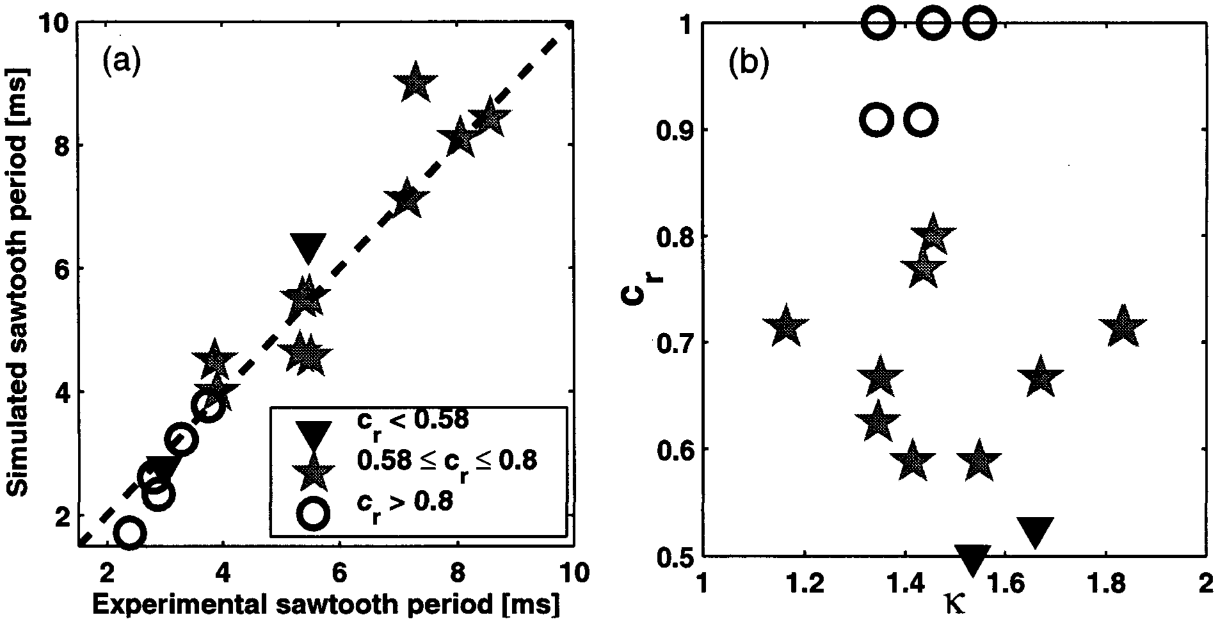

Figure 5.5: *(a) Simulated sawtooth period vs the experimental period for the 17 shots of the database considered. (b) The value of c_r is detailed with respect to elongation.*

several local plasma parameters at $q = 1$ and plasma profiles inside $q = 1$, particular care must be taken in the transport simulation and the consistent calculation of equilibrium profiles during the sawtooth ramp, in particular the current density and the safety factor profiles. In Figure 5.5 we present the results of the simulations of the 17 Ohmic L-mode shots. Figure 5.5(a) shows that in such a wide domain of parameters, the sawtooth period can be simulated with a relatively small variation of the free parameter c_r, between 0.5 and 1. The values of c_r are detailed in Figure 5.5(b) versus elongation. It can be concluded that for most cases we obtain a satisfactory simulation of the sawtooth period with $c_r \simeq 0.75$. Also the inversion radii have been reproduced in good agreement with the experimental observations. As it will be explained later, the correct simulation of the inversion radius is less demanding than that of the sawtooth period. This allows an easier approach when one is only interested on transport effects due to sawtooth activity. For this reason, for transport simulations in subsection 4.5.2, we have adopted the simplified crash condition $s_1 > 0.2$, which does not allow to reproduce exactly the sawtooth period in all cases, but nevertheless permits a correct simulation of the inversion radius. In Figure 5.6 we have shown the sawtooth period simulation of a typical TCV Ohmic plasma, obtained in shot ♯9841. The plasma shape is almost circular, with small elongation, $k = 1.18$, and medium triangularity, $\delta = 0.25$. The average volume density is $3 \cdot 10^{19} m^{-3}$, and the safety factor value at the edge is $q_{edge} = 3$. In Figure 5.6(a) we have plotted the time evolution of the terms involved in Eqs. (5.9) and (5.14). The ideal growth rate is always negative and therefore well below the diamagnetic threshold $0.5\, \omega_{*i}\, \tau_A$, indicating that the

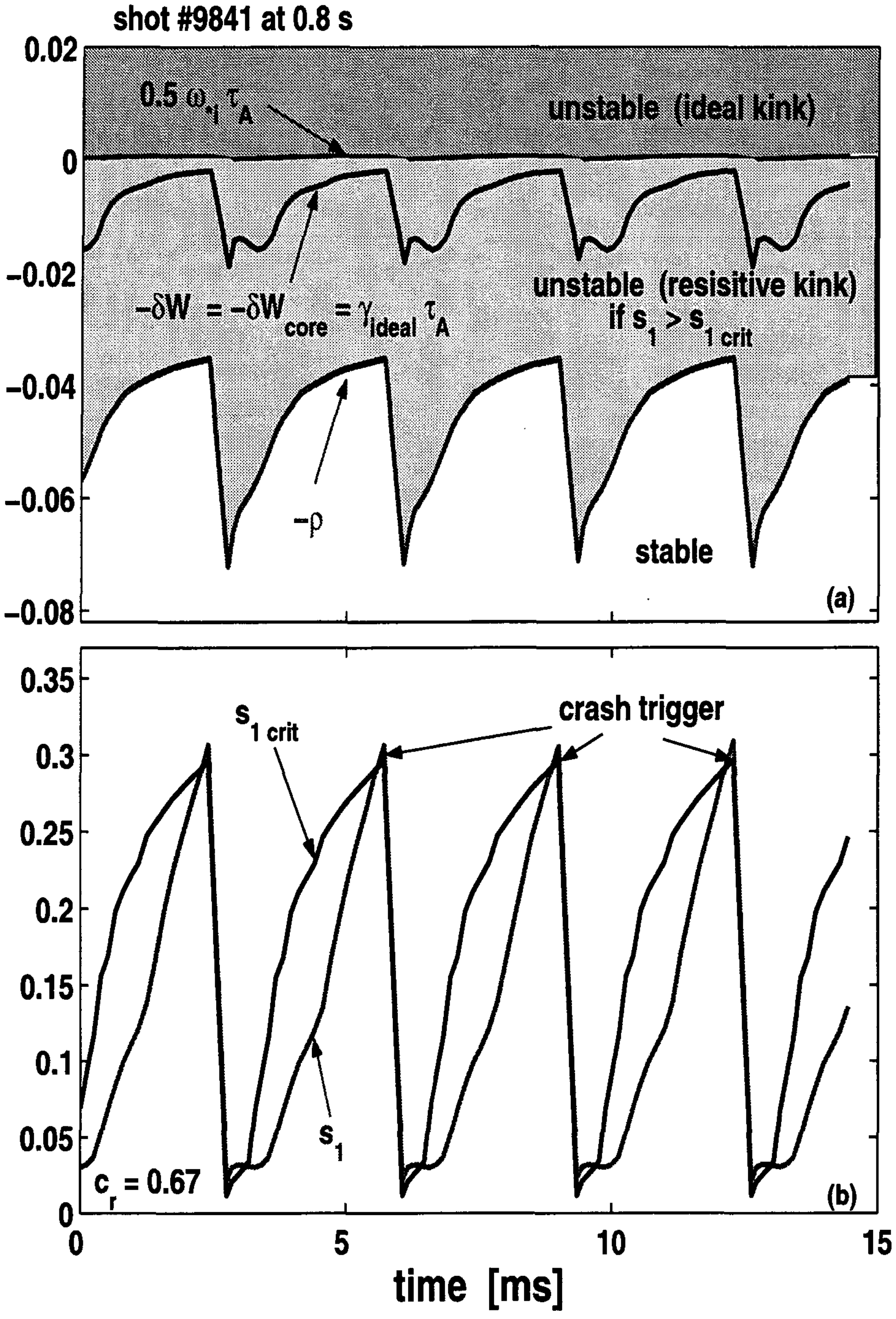

Figure 5.6: *Application of the sawtooth period model to the TCV discharge ♯9841, at 0.8 s, exmaple of a typical plasma with only Ohmic heating. (a) Eqs. (5.9) and (5.14) are plotted. The ideal internal kink remains stable, the potential energy* $\delta\hat{W}$ *always satisfies Eq. (5.14), indicating that the destabilized kink is a resistive mode. (b) The triggering condition for a sawtooth crash is given by Eq. (5.20).*

ideal internal kink remains stable. We identify in this way that the relevant regime for a typical TCV Ohmic discharge is the one given by Eq. (5.14), leading to resistive internal

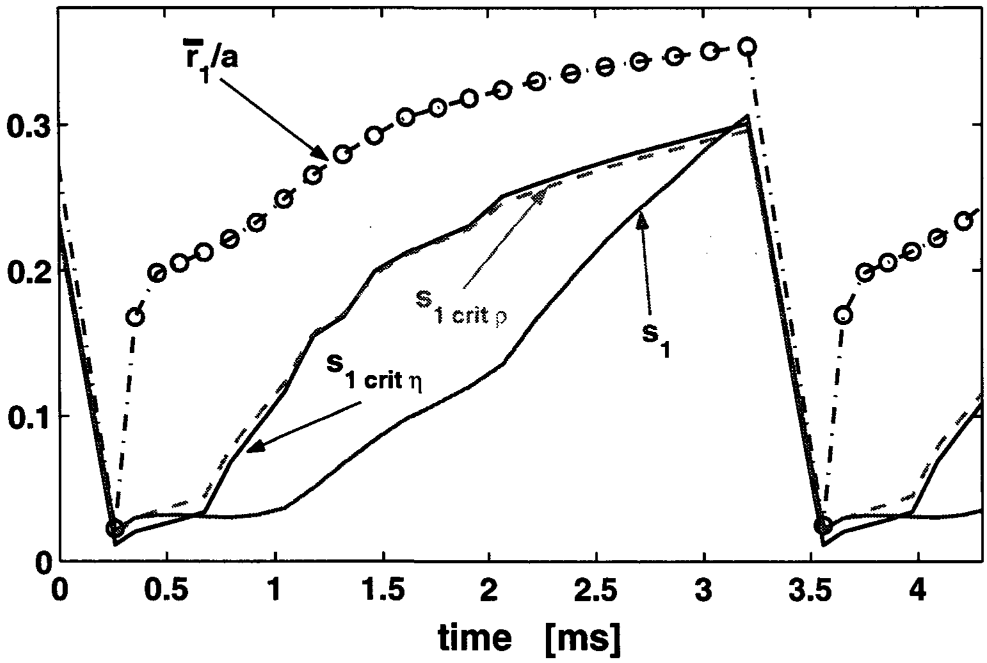

Figure 5.7: *Time evolution of the critical shear for the ion–kinetic internal kink, $s_{1crit\rho}$, Eq. (5.21a), and for the resistive internal kink, $s_{1crit\eta}$, Eq. (5.21b), as computed by PRETOR in the simulation of the TCV discharge ♯9841. Also the time evolution of the shear at $q = 1$, s_1, and of the normalized $q = 1$ radius, $\bar{r}_1/a$ are plotted.*

kink instabilities. In this regime, the instability threshold is given by the comparison between the resistive, Eq. (5.15), or the ion–kinetic, Eq. (5.16), growth rates and the stabilizing term involving the diamagnetic frequencies, Eq. (5.19). The time evolution of the corresponding triggering condition, Eq. (5.20), is shown in Figure 5.6(b). Note that in TCV plasmas both instabilities, resistive and ion–kinetic, have very similar growth rates, and the resulting time evolution of the corresponding critical shear is pratically the same for the two different modes, Figure 5.7, determining the same sawtooth period at the trigger. The free parameter c_r has been fixed in this simulation equal to 0.67, which is, as previously stated, within the range of values on average most consistent with the experimental sawtooth periods in TCV Ohmic discharges. The resulting simulated sawtooth period, $\tau_{saw} \simeq 3.3$ ms is indeed in good agreement (within 10%) with the experimentally observed period of 3 ms. Obviously the parameter c_r can be matched in order to exactly reproduce the experimental sawtooth period. In Figure 5.7 we have also plotted the time evolution of the normalized $q = 1$ radius. Note that during a first phase the $q = 1$ radius moves rapidly outwards, reaching values relatively close to the value at the crash. Therefore the $q = 1$ radius at the crash is not too sensitive to the effective duration of the sawtooth period. This makes it possible to satisfactorily simulate the inversion radius more easily than the sawtooth period. After a sawtooth crash, the critical shear also increases rapidly, with a time scale determined by the confinement time, and then has tendency to saturate. This is because the critical shear is almost proportional to the pressure gradient at $q = 1$. The pressure gradient at $q = 1$ falls to zero as a consequence of the profiles relaxation, but builds up rapidly after the crash by the combination of two effects: the central Ohmic reheating peaks the pressure profile more and more and the $q = 1$ surface moves rapidly outwards, towards plasma regions in which the pressure gradient is larger. On the contrary the shear at $q = 1$, s_1, increases more slowly in this first phase, during which $q = 1$ is moving outwards but always remaining in regions in which the safety factor profile remains flat. Once $q = 1$ is sufficiently off–axis, than the shear begins to build up more rapidly, being able to reach the value of $s_{1\,crit}$. If the time evolution of s_1 and $s_{1\,crit}$ are very close and almost parallel, and this occurs when the confinement time and the resistive time inside the $q = 1$ surface are similar, the sawtooth period is not well determined: small changes in the time evolution of the several terms involved can imply strong non–physical variations of the simulated sawtooth period. In this case, also, the relaxation model becomes more important, which can make the sawtooth period simulation less reliable. Note nevertheless that, at least in Ohmic plasmas, the relaxation model adopted, subsection 5.2.2, allows a correct prediction of both the sawtooth amplitude and the inversion radius in all the discharges analyzed. In this database the experimentally determined inversion radius varies from 0.2 to 0.6 of the minor radius, and there is no experimental correlation between the inversion radius and the sawtooth period.

5.3.2 Adding electron cyclotron heating

From a theoretical point of view, as the sawtooth period depends on local values of the plasma parameters at $q = 1$, one expects that experimentally the sawtooth period would turn out to be very sensitive to the electron cyclotron power deposition location. This is indeed the case, as ECH can be highly localized, directly altering both the electron temperature and thereby the current density and safety factor profiles, all crucially involved in the sawtooth crash triggers. Moreover, the possibility of driving current by the ECH system gives a supplementary possibility of altering the sawtooth period, locally modifying the current density profile and the magnetic shear. Experimentally it has been observed on TCV that small alterations of the EC deposition or seemingly negligible amounts of ECCD close to the $q = 1$ surface can strongly change the sawtooth period and shape [50, 67]. Moreover it has been shown that the sawtooth response to precise heating conditions is highly reproducible: in this sense sawteeth can be used as an ECH deposition detector [50].

In particular, when the power deposition is moved vertically in the poloidal plasma cross

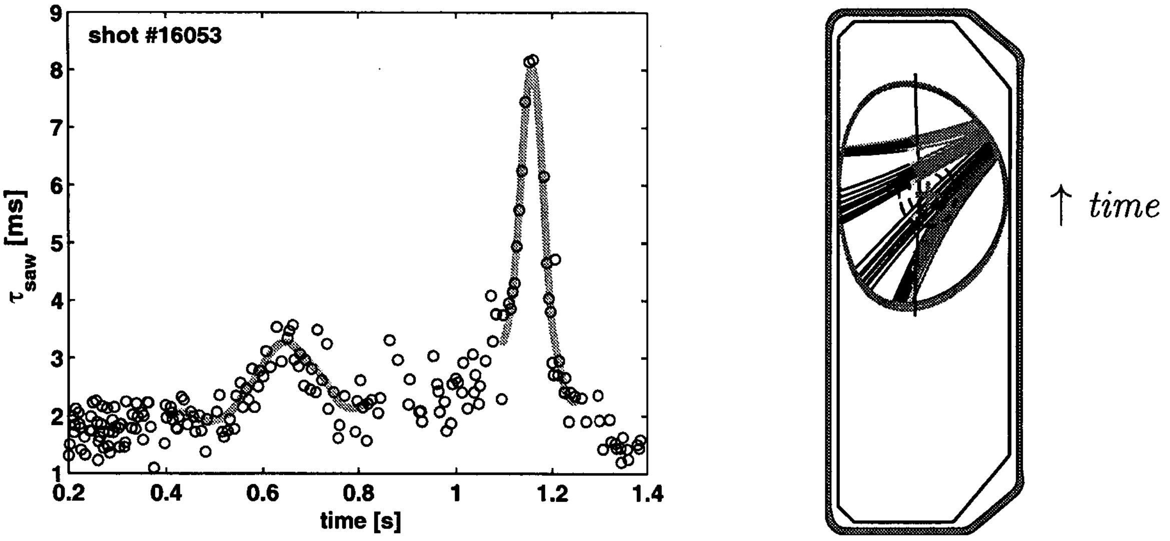

(a) (b)

Figure 5.8: *(a) Experimental sawtooth period in shot ♯16053. (b) Poloidal view of the TORAY-GA results at 4 different time slices during the poloidal sweep of shot ♯16053.*

section from the bottom to the top, it is found experimentally that two specific locations maximize the sawtooth period: this gives a first precise test on the sawtooth period model. In particular, as shown in Figure 5.8(a), the first maximum is of lower amplitude and broader, whereas the second one is of higher amplitude and narrower. This has been explained as due to the geometrical configuration of the ECH launcher, which implies that when heating at the bottom of the plasma the deposition width ($\approx$ beam width) is broader and a small amount of counter–ECCD is produced, whereas when heating at the top the deposition width is narrow and accompanied by a small amount of co–ECCD, Figure 5.8(b). Both the beam deposition width and the amount of current drive can affect the sawtooth period. The first affects the local power density, which can modify the pressure gradients at $q = 1$, the second directly modifies the local magnetic shear. For this reason, a simulation of the sawtooth period performed considering the poloidal sweep of a fixed–width power deposition profile, without taking into account power density and current drive effects, allows one to identify a deposition location maximizing the sawtooth period, but does not reproduce the detailed features of the experimental behaviour as described above, shown in Figure 5.8(a). Therefore, the sawtooth period simulation of the whole shot must carefully take into account not only the sweep of the deposition, but also the combination of both the effects of the deposition width and of current drive, subsection 5.3.5. Dedicated experiments have been designed and performed in order to identify separately the two physical phenomena [70]. First, the dependence of the sawtooth period on the power density is discussed in subsection 5.3.3. Second, as shown in subsection 5.3.4, the effects of very small amounts of current drive close to

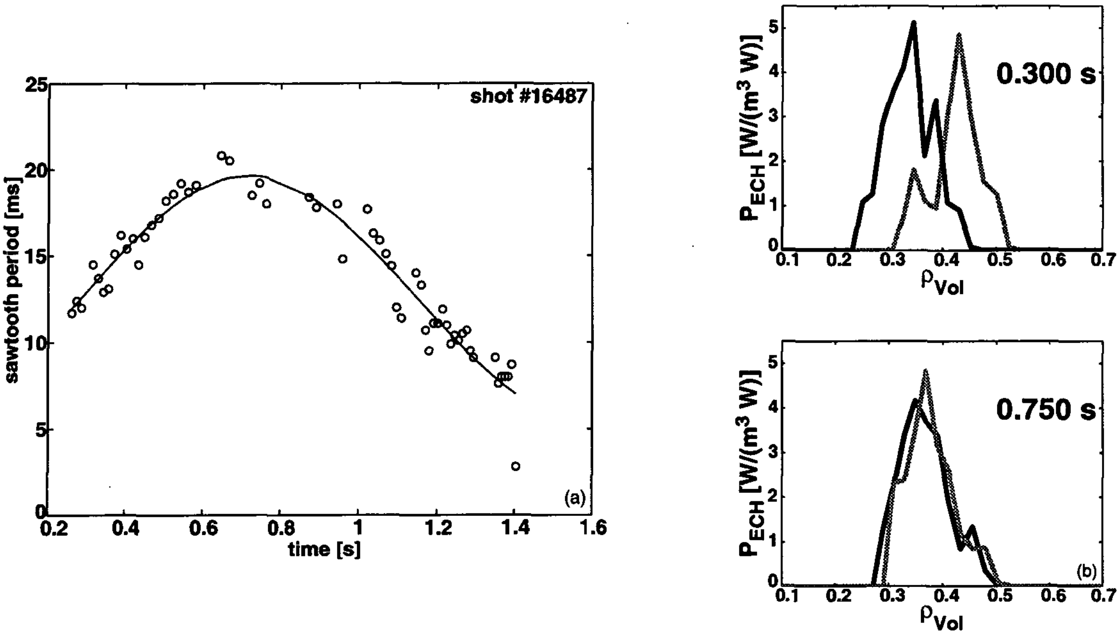

Figure 5.9: *(a) Experimental sawtooth period in shot ♯16487. (b) TORAY-GA ECH deposition profiles at two time slices in shot ♯16487.*

the $q = 1$ surface, less than 1% of the plasma current, can strongly change the sawtooth period. The triggering condition for a sawtooth crash given by Eq. (5.20) for resistive internal kink instabilities allows sawtooth period simulations consistent with the experimental observations for all the heating and current drive conditions described above. The free parameter c_r involved in Eq. (5.20) is determined by matching the sawtooth period during the Ohmic phase of the discharges, and is then kept fixed during the heating phase. Note that in all the experiments considered, the low heating power, less than 0.5 MW, does not change significantly the regime of collisionality of the plasma: this supports the described simulation methodology.

5.3.3 Sawtooth period and ECH power density

A dedicated experiment has been performed in TCV shot ♯16487 which has definitely confirmed the influence of the power density on the sawtooth period. The deposition radius maximizing the sawtooth period was identified in a previous discharge by sweeping two beams in the poloidal plane as described above. Then two launchers were swept in opposite directions across this radius, in such a way as to keep the total power inside the corresponding flux surface constant, while modifying the power density at this location. The experimental result, together with the power deposition densities from TORAY-GA [71] at two instants during the discharge are shown in Figure 5.9, (a) and (b) respectively. The power density at $\rho_{dep} = 0.37$ increases progressively between the two time slices presented, as does the sawtooth period, increasing from 12 ms up to almost 20

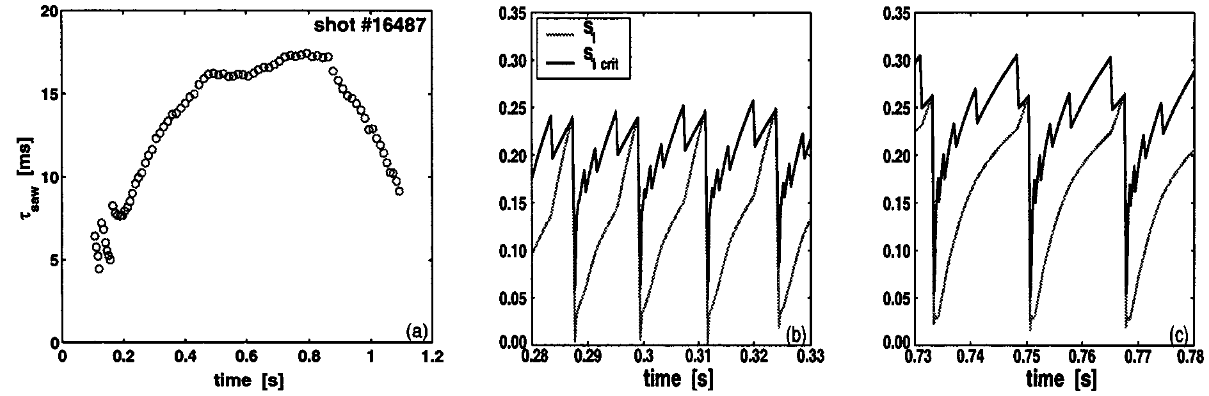

Figure 5.10: *(a) Simulated sawtooth period of ♯16487. (b) and (c) Shear at* $q = 1$ *and critical shear with sawtooth period of 11 ms around 0.3 s (b) and sawtooth period of 18 ms around 0.75 s (c). Steps in the time evolution of the critical shear must be ascribed to numerical discreteness.*

ms. Performing the same crossed sweep with PRETOR, the sawtooth period variation of Figure 5.10(a) has been found consistent with the experimental results. In particular the relative change of $\tau_{\rm saw}$ is well reproduced even if details of the evolution are not fully recovered (e.g. the maximum period, which occurs at 0.75 s in the experiment is found at 0.85 s in the simulation). Note that, similarly to the experiments, we had, first, to identify the position maximizing the sawtooth period in the PRETOR simulation and then have used this position as the reference for the cross–sweep. This position is 0.43 in PRETOR, which is within the experimental uncertainty on the power deposition due to the error bars on the temperature and density measurements, and perhaps most importantly on the equilibrium reconstruction. Analyzing the effect of the power density on the crash trigger, Eq. (5.20), two effects are produced by the larger power density, Figure 5.10(b). First, the shear s_1 after the crash increases more slowly; second, the critical shear also increases because of the enhancement of the pressure gradient at $q = 1$ due to the more localized power deposition outside $q = 1$. Both these effects imply a longer sawtooth period and explain the experimental results.

Hashes in the evolution of the critical shear, clearly visible in Figure 5.10, must be ascribed to the numerical scheme. As already stressed, s_{1crit} depends essentially on the pressure gradient at $q = 1$. As r_1 moves outwards during the sawtooth ramp, it crosses successively the points of the radial mesh. Since the pressure gradient is computed by linear interpolation and finite differences, when r_1 goes over a mesh point, the gradient is computed on the next segment of the pressure profile. This leads to steps in the time evolution of the critical shear, which can be particularly evident when the auxiliary heating power is deposited off–axis, close to the position of the $q = 1$ surface at the sawtooth crash. Indeed in this situation the pressure profile can have short scale variations around

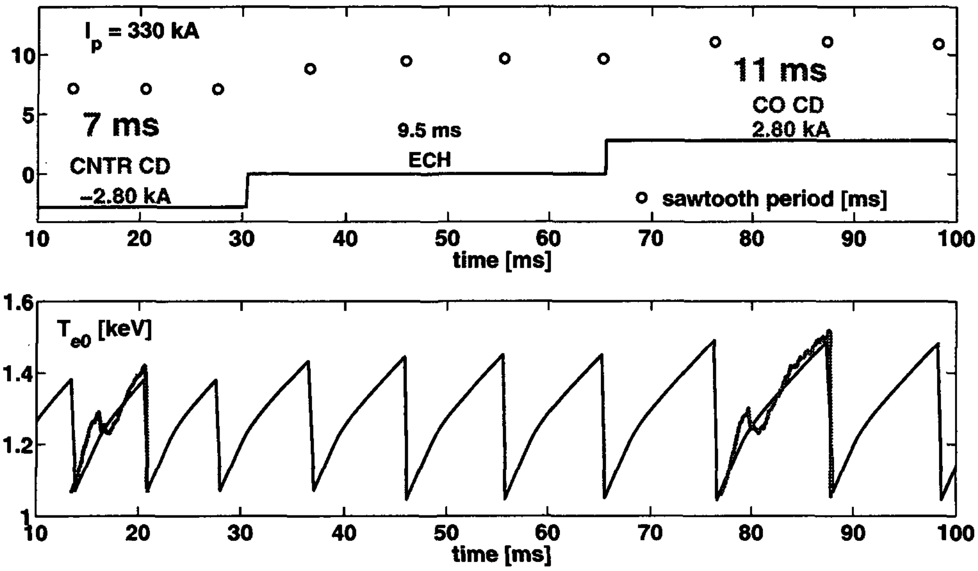

Figure 5.11: *Sawtooth period variation (above) and central* T_e *(below) computed in the simulation of shots ♯15278 and ♯15282. Two experimental sawtooth periods from the soft X-ray traces of the two shots, have been also plotted, rescaled in amplitude.*

the deposition region. The hashes in the time evolution of the critical shear provide an estimate of the numerical error involved in the simulation of the sawtooth period. Note, in this context, that simulations resulting in sawtooth periods shorter than ~2 ms must be considered below the numerical precision.

5.3.4 Sawtooth period and current drive

Two shots have been produced with identical plasma conditions, changing only the amount of CD deposited near $q = 1$. In one case, shot ♯15278, the ECH power deposited close to the $q = 1$ surface is accompanied by a small amount (less than 1% of the total current) of current drive in counter direction. In the other case, shot ♯15282, the same power deposition is accompanied by a similar amount of current drive, but in co direction [70]. The sawtooth period turns out to be strongly sensitive to this seemingly negligible inversion of current drive. This variation is well reproduced by the model. In Figure 5.11 the results of the simulation are shown. The amount of current drive is changed from -2.8 to +2.8 kA, which corresponds to a local modification of the current density profile of less than 3%, with a plasma current of 330 kA. The simulated sawtooth period changes from 7 ms to 11 ms. This is in very good agreement with the experimental results, as shown by the simulated central electron temperature trace, on which two experimental sawtooth periods from the soft X-ray traces of the two shots (rescaled in amplitude but not in time) have been plotted. In this case, as the ECH power deposition is the same in the two shots, the pressure gradient at the $q = 1$ surface is not modified and the critical shear behaviour

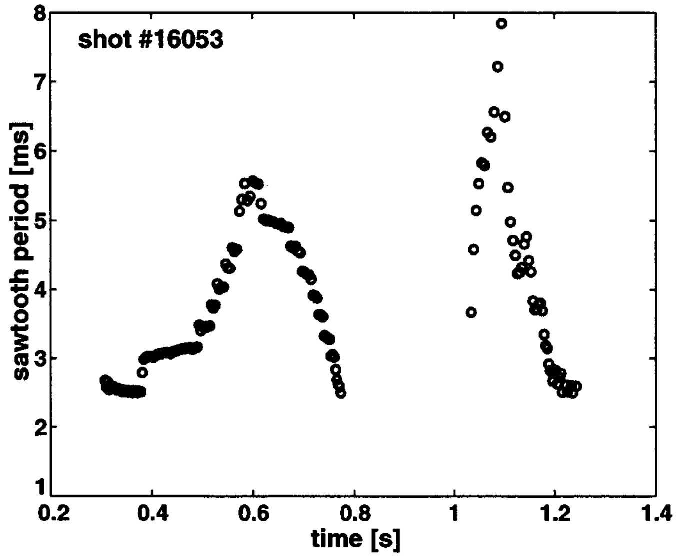

Figure 5.12: *Simulated sawtooth period for ♯16053. Sawtooth periods between 0.8 and 1.05 s turn out to be shorter than 2 ms in the simulation and too affected by numerical uncertainties. Therefore they have not been plotted.*

does not change in the two situations, remaining constant at the trigger. However, the small amount of CD, localized close to the $q = 1$ surface, changes the dynamics of the shear at $q = 1$. It increases more quickly after the crash with the counter–CD contribution and more slowly with co–CD. This is sufficient to alterate the time at which the crash condition is triggered, changing the sawtooth period from 7 ms up to 11 ms.

5.3.5 Simulation of a full poloidal sweep

In the simulation of the sawtooth period for a discharge with a poloidal sweep (TCV shot ♯16053) all the different effects presented above, in particular the variation of the power density and the small amounts of CD involved, must be carefully taken into account. This is possible by interpolating the ray–tracing results, calculated with TORAY–GA every 50 ms. In Figure 5.12 the sawtooth period evolution obtained in the simulation is presented. The main features of the experimental results are well reproduced by the model. In particular the presence of two maxima, the first less localized with shorter sawtooth period, the second more localized with longer sawtooth period. Also the magnitude of the sawtooth period variations is in agreement with the experiment. Between 0.8 and 1.05 s, with power depositions close to the magnetic axis, irregular sawteeth shorter than 2 ms have been obtained in the simulations. As already mentioned, when the simulated periods are as short as this, they are too dependent on the relaxation model and on numerical uncertainties in the evaluation of the local gradients at $q = 1$; therefore, in this situation they can not be considered reliable and have not been plotted in Figure 5.12.

The experimental behaviour also shows irregular sawteeth during the same time interval of the discharge, Figure 5.8; although, the sawtooth periods are on average a factor of 2 longer than those obtained in the simulations. From the simulation it is found that the deposition radius maximizing the sawtooth period is clearly outside the $q = 1$ surface, and even outside the mixing radius for broad deposition profiles; but, closer to the $q = 1$ surface with more localized power. Although some experimental evidence suggests that the deposition radius maximizing the sawtooth period is indeed outside the experimental inversion radius (calculated from soft X–ray tomography), this issue would be finally assessed only with the help of accurate equilibrium reconstructions, involving experimental constraints on the current profile, which are not available on TCV. Hence this prediction amounts to a further validation test for the model. In any case, it must be stressed that the simulations show that local modifications of the plasma parameters at $q = 1$ producing the strongest effect in stabilizing the sawtooth period are not the ones performed by a power deposition localized exactly on the $q = 1$ surface. Power depositions located outside the $q = 1$ surface are those which allow most efficiently the slowing down of the shear build up and the increase of the pressure gradients on $q = 1$ and thereby of the local diamagnetic frequencies, providing stabilisation. How much outside depends on the power localization, the more the deposition profile is narrow the more it needs to be located close to $q = 1$ to produce the maximum effect.

5.4 Sawtooth stabilisation by NBI in JET

Dedicated experiments have been recently performed in the Joint European Torus (JET) in order to assess the effect of fast ions arising from neutral beam injection (NBI) on sawtooth activity. Strong experimental evidence for fast ion stabilisation of sawteeth has been observed during these experiments [26]. Previously, in JET tritium experiments with NBI, the sawtooth period was observed to increase with beam tritium concentration [72]: this phenomenon was attributed to a stabilizing effect of beam ions, whose energy content increased with beam tritium concentration due to the mass dependence of the slowing–down time. Analysis of internal kink stability in these discharges, in terms of thresholds given by a sawtooth period model [4], indicated that in JET hot–ion H–mode deuterium–tritium operation the contribution to the kink energy of the beam ions was greater than that of α–particles, and produced a delay in destabilisation of the ideal internal kink [72].

The stabilizing effect of fast ions, in particular those arising from ion cyclotron resonance heating (ICRH), has already been investigated experimentally [73, 74] and theoretically [6, 75]. When the fast ions are produced either by ICRH or fusion reactions, the highest particle energies are in the MeV range, whereas in the case of NBI the highest energies are of the order of 100 keV. As already mentioned in subsection 5.2.1, fast particle stabilisation arises from conservation of the third adiabatic invariant Φ for trapped fast particles whose bounce orbits precess around the torus in a time which is shorter than the characteristic time scale of the relevant MHD mode [6]. Unstable $m = n = 1$ modes have growth rates of the order of the diamagnetic frequency of thermal ions ω_{*i}, evaluated at the $q = 1$ surface. Thus, a necessary condition for fast particle stabilisation is that $\omega_{Dh} > \omega_{*i}$ [6], where ω_{Dh} is the bounce–averaged toroidal precessional drift frequency of fast ions. In JET this condition is easily satisfied by ICRH ions with energies in the MeV range, even in discharges with very high ion temperature: this gives rise to delays in the sawtooth crash for periods of up to a few seconds [73, 76]. In the case of particles with energies of the order of tens of keV, on the other hand, the condition is generally only marginally satisfied. Sawtooth stabilisation by NBI fast ions was first observed in TEXTOR [77]. In those experiments, the combination of a beam injection energy ~50 keV, low densities $n_e \sim 1.5 \times 10^{19}$ m^{-3} and low ion temperatures $T_i \sim 1$ keV made it possible to stabilize sawteeth for periods of up to 200 ms. In recent discharges in JET, with beam injection at energies 80 keV and 140 keV, powers up to 10 MW, densities in the range $n_e \sim 2 - 4 \times 10^{19}\text{m}^{-3}$ and ion temperatures of a few keV ($T_i \sim 2 - 3$ keV), sawtooth periods of up to 500 ms have been observed. The ratio $\omega_{Dh}/\omega_{*i} \sim 5$ satisfies the condition for stabilisation. An overview of the recent observations in JET experiments is given in subsection 5.4.1.

In order to investigate more deeply the physical processes determining the period of sawtooth oscillations we have applied the model described in Section 5.2, including a beam ion contribution to the internal kink potential energy. The need of including the sawtooth period model in a transport code, in order to consistently compute several time–evolving parameters which are difficult to measure, such as the position of the $q = 1$ surface, the magnetic shear and local gradients at this surface, implies that it is desirable to keep the model in a relatively simple formulation. However, simplifying the model to this extent makes it necessary to neglect additional effects, such as plasma rotation, or to simplify the description of physical effects which are taken into account. For instance one makes the assumption of isotropic distribution function in the expression describing the beam ion contribution to the internal kink potential energy. This limits somewhat the degree to which one can draw firm conclusions regarding the validity of quantitative model predictions. On the other hand, separate calculations can be performed in order to investigate the validity of the assumptions made in the modelling, and to test the simplified expressions used in the transport code, using more rigorous and complete MHD codes. In particular, in order to check the validity of assuming isotropic beam ions, we have computed more realistic fast particle distribution functions, for certain specified time slices, with the post-processing transport analysis code TRANSP [78]. We have used these distribution functions as input for the hybrid MHD/kinetic code NOVA-K [27], in order to calculate accurately the contribution of beam ions to the internal kink energy and compare with estimates based on the approximate formula included in the sawtooth period model. The analytical expression used in the model for the beam ion contribution and the comparison with NOVA-K calculations are described in subsection 5.4.2.

A detailed analysis and simulations of a few representative recent JET discharges have been carried out. The results are presented in subsection 5.4.3. The predictions of the sawtooth period model are shown to be in good agreement with the experimental results. This confirms the hypothesis that the observed time evolution of the sawtooth period is determined largely by beam ion stabilisation and validates the theoretical model for quantitative predictions of the sawtooth period, at least for plasma and heating conditions similar to those prevailing in these experiments.

5.4.1 Experimental observations

Recent experiments in JET with auxiliary heating provided by NBI only have provided several indications of beam ions playing a role in stabilizing sawteeth. In particular, a NBI shot database has been built, showing an inverse correlation between the sawtooth period $\tau_{\rm saw}$ and the electron density n_e [79, 26]. Note that the inverse density scaling of the sawtooth period is opposite to the usual Ohmic behaviour, which shows an increase of $\tau_{\rm saw}$ with density. Since, under steady–state conditions, the beam ion pressure is directly proportional to the slowing–down time, which varies as $T_e^{1.5}/n_e$, it strongly suggests that the stabilisation of the sawtooth period observed during NBI heating is due to fast particle effects. Moreover, the strong T_e dependence suggested by collisionality arguments is confirmed by regression analysis over the sawtooth database, which yields $\tau_{\rm saw} \propto T_e^{1.7}\, n_e^{0.23}$ [80]. Work is in progress in order to identify separate dependeces on temperature, density and NBI power. The dedicated experiments considered in the present analysis have been performed with relatively slow NBI power (P_{NBI}) ramps, in order to obtain sawtooth period data over a wide power range. The NBI power has been rapidly modulated in order to optimize the simulation of a continuous linear variation in time, with a power range up to almost 10 MW. Higher power levels have not been considered, since other instabilities, such as fishbones, would then be expected to occur, thereby complicating the sawtooth analysis.

In Figure 5.13 we have shown an overview of shot ♯53593, with plasma current $I_p = 2$ MA and vacuum magnetic field $B_0 = 2.48$ T. The modulated trapezoidal power waveform is shown in Figure 5.13(a), together with the smoothed total input power, which includes also

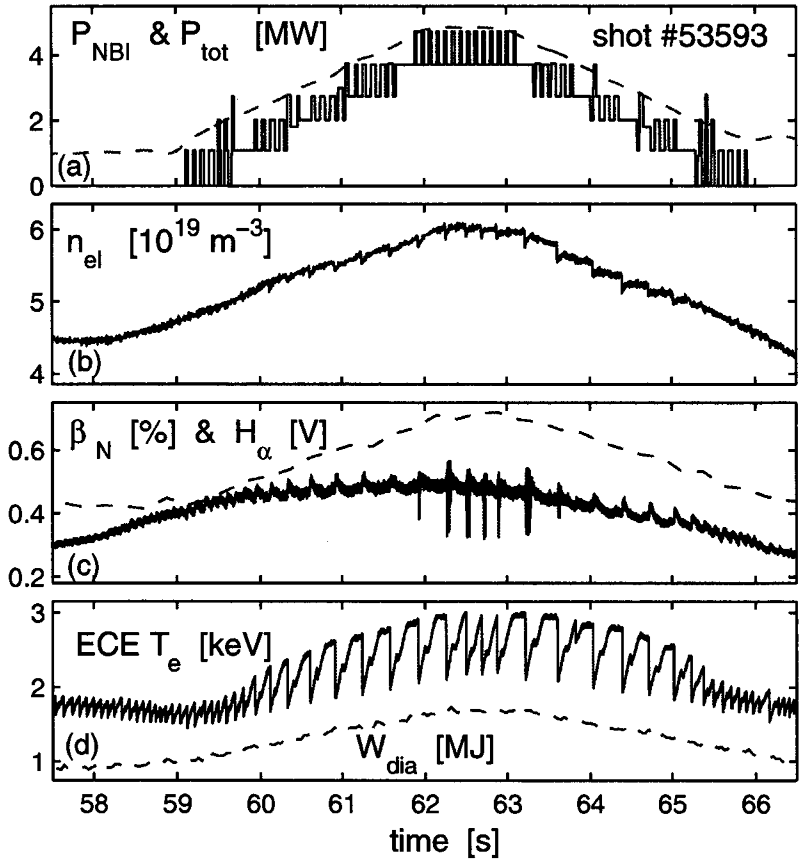

Figure 5.13: *Experimental traces of shot ♯53593, with* $I_p \simeq 2$ *MA,* $B_0 = 2.48$ *T. (a) NBI power (solid curve) and smoothed total input power (dashed curve) in MW. (b) Interferometer central chord line-average density in* 10^{19} m^{-3}. *(c)* H_α *emission signal in V and normalized beta* β_N *(dashed line) (*$\beta_N = \beta[\%]aB_0/I_p$ *where the minor radius* a *is expressed in m, the vacuum magnetic field* B_0 *in tesla, and the plasma current* I_p *in MA). (d) Electron temperature in keV (solid curve) measured by the ECE radiometer and diamagnetic plasma energy in MJ (dashed curve).*

the Ohmic contribution. In this shot the low maximum $P_{NBI} < 5\,\mathrm{MW}$ and the relatively high magnetic field keep the plasma in L–mode throughout the heating phase, with a resulting line average density, plotted in Figure 5.13(b), which evolves symmetrically in time. The H_α emission signal is shown in Figure 5.13(c), together with $\beta_N = \beta[\%]\, aB_0 \,/\, I_p$. In Figure 5.13(d) we have plotted the electron temperature measured by the electron cyclotron emission (ECE) heterodyne radiometer. The present time trace corresponds to a point of the plasma which is located, from magnetic equilibrium reconstruction, approximatively at $r/a \simeq 0.13$, roughly 50% inside the inversion radius. The sawtooth period increases with increasing power already at these low power levels. Figure 5.13(d) shows also the plasma diamagnetic energy.

In all these experiments, the beam power is injected slightly in the co–direction and therefore plasma rotation increases with NBI power. The beam trajectories, in the JET upshifted alignement, allow a strong localization of the power absorption and of the fast particle pressure in the central region of the plasma. This is particularly important in order to obtain a visible effect of fast particles on the sawtooth period, since, from theory, the most important parameter determining sawtooth stabilisation is roughly given by the volume–averaged fast particle energy content inside the $q = 1$ surface with respect to the value of the fast particle energy at that surface. Both simple ramp-up followed by a rapid drop or trapezoidal P_{NBI} waveforms, involving power ramp-up and ramp-down with the same time scales have been analyzed. A linear relation between the sawtooth period and the fast ion energy content $W_{i\,fast}$ has been observed in all the discharges. Moreover, the plot of the evolution of the sawtooth period versus the NBI power exhibits a hysteresis behaviour as P_{NBI} rises and decays, which is slightly reduced when P_{NBI} is plotted versus the energy content $W_{i\,fast}$ [26]. This suggests that the variations in τ_{saw} are better correlated with changes in $W_{i\,fast}$ than with changes in P_{NBI}, supporting the idea that fast ions are responsible for sawtooth stabilisation.

5.4.2 Numerical computation of $\delta\hat{W}_{fast}$ and validation of an analytical expression

In order to compute accurately the contribution $\delta\hat{W}_{fast}$ of beam ions to the internal kink potential energy, we have used [82] the NOVA–K code [27, 81], developed to study low-n kinetic-MHD instabilities, and already used to calculate the nonadiabatic resonant response of fast particles to a given eigenmode structure. The code has been extended in order to evaluate the full fast particle response to the internal kink mode [83]. A perturbative method is used to compute the kinetic effects, while the ideal eigenmode structure is computed by the ideal MHD code NOVA. The perturbative approach is justified, since the fast particle beta on–axis, $\beta_{0\,fast}$, is about 30% of the plasma β_0 in the NBI experiments considered in the present work. The code includes fast ion finite orbit width and finite Larmor radius effects in the kinetic contribution to the MHD quadratic form of the mode energy, provided by the various fast particle groups. The code takes into account the realistic flux surface geometry and the plasma rotation profile. This is particularly important in order to describe properly the fast particle toroidal precession, and estimate correctly the precession drift frequency of the banana orbits. The code is particularly well–suited to this kind of application. Moreover, NOVA–K can be run taking as input realistic numerical calculations of the fast particle distribution function, both in energy and pitch–angle. It is important to use a realistic form of the distribution function in order to estimate correctly the stabilisation effect, since it is primarily due to trapped particles. This also tests the validity of analytical approaches to the problem. The distribution function was taken from the TRANSP Monte–Carlo package and fitted into a factorised form $f_f = f_v f_{P_\varphi} f_\chi$, where v is speed, P_φ is canonical toroidal momentum, and $\chi = (v_\perp^2/v^2)(B_0/B)$, $v_\perp$ denoting the velocity component perpendicular to the local magnetic field B. The factor f_{P_φ} represents essentially the radial dependence of the distribution, and was taken from the TRANSP code [78]. The speed distribution f_v is assumed to be slowing–down, which is also supported by TRANSP modelling. For the NBI ion pitch–angle distribution f_χ, we used the form

$$f_\chi = e^{-(\chi-\chi_0)^2/\Delta_\chi^2}, \tag{5.30}$$

which gives the distribution function in the equatorial plain at the low field side. Comparison with the TRANSP code shows that it can be assumed that $\chi_0 \simeq 0.5$ within the numerical accuracy, and it has been verified that it does not change significantly within the $q = 1$ surface. The pitch–angle width depends strongly on the particle energy, and must be computed from the collisional operator in the Fokker–Planck equation [84], which

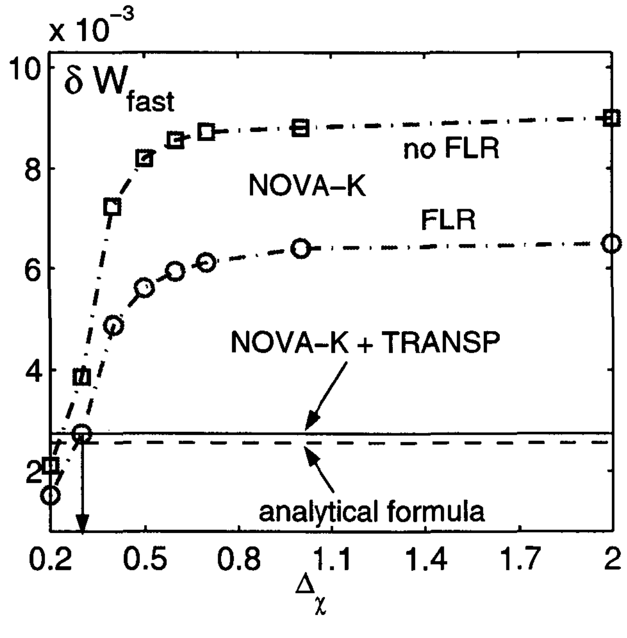

Figure 5.14: *NOVA-K results, showing the fast particle stabilizing contribution* $\delta\hat{W}_{fast}$ *to the* $m = 1$ *internal kink potential energy, for different values of the fast ion pitch–angle distribution width [equation (5.30)]. Circles and square symbols give the NOVA-K results obtained respectively with and without the inclusion of finite Larmor radius effects. The fast ion distributions in energy and space were taken from the results of a TRANSP run corresponding to a specific time slice of a JET discharge (shot ♯53595). The solid horizontal line represents the value of* $\delta\hat{W}_{fast}$ *computed by NOVA-K taking into account also the TRANSP pitch–angle distribution. The dashed line gives the corresponding analytical result [equation (5.11)].*

also determines the speed of a particle as it slows down:

$$v^3 = \left(v_{cr}^3 + v_{b0}^3\right) e^{-3t/\tau_{se}} - v_{cr}^3. \tag{5.31}$$

Here v_{b0} is the beam injection speed and v_{cr} is the speed at which a beam particle slows down on ions and electrons at the same rate. The collisional pitch–angle scattering diffusion coefficient has the form $D_{\chi\chi} = v_{cr}^3/(\tau_{se}v^3)$, and the pitch–angle width at a specific time t is $\Delta_\chi^2 = \Delta_0^2 + \int_0^t D_{\chi\chi}dt$, where particle speed must be treated as a function of time, according to Eq. (5.31). It is straightforward to show that

$$\Delta_\chi^2 = \Delta_0^2 - \frac{1}{3}\ln\left[\frac{v^3\left(1 + v_{cr}^3/v_{b0}^3\right)}{v^3 + v_{cr}^3}\right]. \tag{5.32}$$

Like the parameter χ_0, also Δ_0 can be easily determined from the distribution functions given by TRANSP. Figure 5.4.2 shows the sensitivity of the fast particle contribution $\delta\hat{W}_{fast}$ to the width Δ_χ of the pitch–angle distribution. With open circles we have plotted the code results including FLR effects, whereas open squares indicate the excess of stabilisation obtained when FLR effects are neglected. Two different behaviours can be identified: with a localized distribution function in pitch–angle, roughly $\Delta_\chi < 1$, $\delta\hat{W}_{fast}$ shows a strong dependence on Δ_χ, while for $\Delta_\chi > 1$, $\delta\hat{W}_{fast}$ becomes almost a constant function of $\Delta\chi$, rapidly reaching the isotropic limit. The distribution functions fitted from the TRANSP results have in general pitch–angle widths which turn out to be complicated functions of both the normalized poloidal flux averaged over the particle trajectory $\psi = \psi(\chi,\, P_\varphi, v)$ and of the particle energy $\mathcal{E}$. For example, for a specific time of a JET discharge (shot ♯53595) at which the TRANSP distribution was computed the fitting expression for the pitch–angle width used as input for NOVA–K was

$$\Delta_\chi^2 = 0.13 + 0.45\sqrt{\psi} \;-\; 0.15\ln\left[\frac{(\mathcal{E}/130)^{3/2}\,(1 + 0.729)}{(\mathcal{E}/130)^{3/2} + 0.729}\right],$$

where $\mathcal{E}$ is expressed in keV. The corresponding value of $\delta\hat{W}_{fast}$ computed with this distribution function, fitted from the TRANSP result for this specific time, is shown with an horizontal solid line. This allows us to identify an "effective" value of the pitch angle width $\Delta_\chi \simeq 0.3$, where this horizontal line crosses the curve with open circles. This example shows that the "effective" pitch–angle widths corresponding to the experimental conditions are in general in the region in which $\delta\hat{W}_{fast}$ varies strongly with Δ_χ. This implies that numerical calculations properly taking into account the realistic distribution function are indeed necessary. The dashed horizontal line shows the corresponding value of $\delta\hat{W}_{fast}$ provided by the analytical formula given in Eq. (5.11). The analytical expression clearly underestimates the contribution of fast particles, when compared with NOVA–K results obtained with large Δ_χ values, i.e. in the isotropic limit. This is partly due to the fact that in NOVA–K only co–going particles, in the direction of the plasma current, have been considered, consistently with the experimental set–up. Taking into account both co and counter injected beams, the fast particle contribution in the isotropic limit is reduced from 6.49 10^{-3} to 4.74 10^{-3}, which reduces the discrepancy with the analytical formula to less than a factor of 2. Moreover, NOVA–K uses realistic magnetic geometry and includes rotation effects, which may account for the remaining difference. On the other hand, it turns out that the analytical evaluations are very close to the NOVA–K results obtained using the realistic fast particle distribution function computed by TRANSP. This can be explained considering that, since the pitch–angle distribution is narrower at higher energies, less trapped fast ions contribute to the stabilisation than in the case of an isotropic distribution. We have performed several NOVA–K runs, for specified time slices at different levels of NBI heating power, both considering an isotropic distribution function and the realistic distribution computed by TRANSP. These calculations have shown that Eq. (5.11) in general underestimates the term $\delta\hat{W}_{fast}$ by a factor of about 3 if compared to the results provided by NOVA–K with isotropic distribution functions, but provides a surprisingly good estimate, within 15%, of the fast particle contribution when the realistic distribution functions are taken into account. This makes it possible to use Eq. (5.11) to describe the effect of fast particles on the internal kink in similar JET discharges with NBI heating, when performing simulations of the sawtooth period with a transport code such as PRETOR. The coupling of PRETOR with an MHD code such as NOVA–K at each time–step of the transport simulation would require a prohibitive amount of computation time. The formula given in Eq. (5.11) is straightforward to include in a transport code, as it involves only the global beam ion pressure profile, together with variables such as the shear and inverse aspect ratio at $q = 1$ which are routinely computed using transport codes. This approach can be extended to other heating schemes producing fast ions in the plasma, such as ICRH. In this case the fast ion distributions are generally more complex than those resulting from NBI, in both velocity and coordinate space, and require more complicated analytical descriptions [85, 37]. In principle these analytical distributions can be benchmarked against the results of rigorous numerical modelling, carried out using interfaced Monte–Carlo codes. The simulations presented in the next Section use fast ion pressure profiles computed a steady–state Fokker–Planck code PENCIL [86]. This is a post–processing code for JET discharges, run on a regular basis to determine the NBI heating power absorbed by the plasma, the particle sources, and the beam ion pressure profiles. By computing the fast ion pressure profile from a steady–state solution of the Fokker–Planck equation, time–dependent effects arising from the finite slowing–down time are neglected. The slowing–down time of beam ions in JET is usually between 50 and 100 ms, while in the NBI power ramp–up experiments considered here the characteristic time of the power ramp is of the order of 1 s. The use of a steady–state Fokker–Planck equation to compute the fast ion pressure is thus justified. The slowing–down time is also smaller than the energy confinement time, which is of the order of 200 ms in the discharges considered here.

5.4.3 Comparison between theory and experiment

In order to identify the relevant stability thresholds, we have computed the time evolution of all the quantities involved in the sawtooth period model, taking data directly from the available JET diagnostics and post–processing codes such as PENCIL. We have analyzed in this way five discharges, with NBI power ramps, performed in two different recent JET campaigns, with different NBI power levels, with a L–H mode transition or remaining in L–mode during the NBI heating phase. Figure 5.15 shows the results of this analysis for two shots, ♯50725 during the power ramp–up phase, before the occurrence of fishbones, and ♯53593, with lower maximum power, with a complete trapezoidal power waveform. For all the time slices, we have considered a safety factor profile, and the corresponding current density profile, computed using an equilibrium reconstruction which is consistent with the experimental pressure profiles. The inversion radius has been experimentally determined for all the sawtooth crashes and used as a constraint on the reconstructed safety factor profile. We have assumed a constant "average" value of the safety factor in the center $q_0 = 0.9$. In this way we have computed the instability thresholds taking data the most directly as possible from the experimental measurements, considering the measured profiles as the ones occurring on average at the middle of a sawtooth ramp. Thus we have evaluated the order of magnitude of the different terms occurring in the sawtooth crash trigger conditions [Eqs. (5.10, 5.13, 5.14)] at various phases of the discharges. The safety factor profiles, computed as previously described by the equilibrium code coupled with PRETOR, and which play a crucial role in sawtooth calculations, compare also very well with measurements provided by motional Stark effect diagnostics, when these are available.

In Figure 5.15(a) and (b) we have plotted the time evolution of the heating NBI power, during the power ramp phases, for the two shots. In Figure 5.15(c) and (d) the soft X–ray traces are shown, highlighting the sawtooth period behaviour during the power ramps. The time evolution of the sawtooth period for both discharges is plotted in Figure 5.15(e) and (f). In both cases the sawtooth period increases during the power ramp, and, in the case of shot ♯ 53593, decreases correspondingly during the ramp–down phase. In Figure 5.15(g) and (h) the terms involved in the first sawtooth crash condition, [Eq. (5.10)] are plotted. $\delta\hat{W}_{core}$ remains clearly below $0.4\,\omega_{Dh}\tau_A$, indicating that plasma conditions are such that fast particle stabilisation of the ideal internal kink is indeed possible. In Figure 5.15(i) and (l) we have plotted the quantities in Eqs. (5.13) and (5.14). The

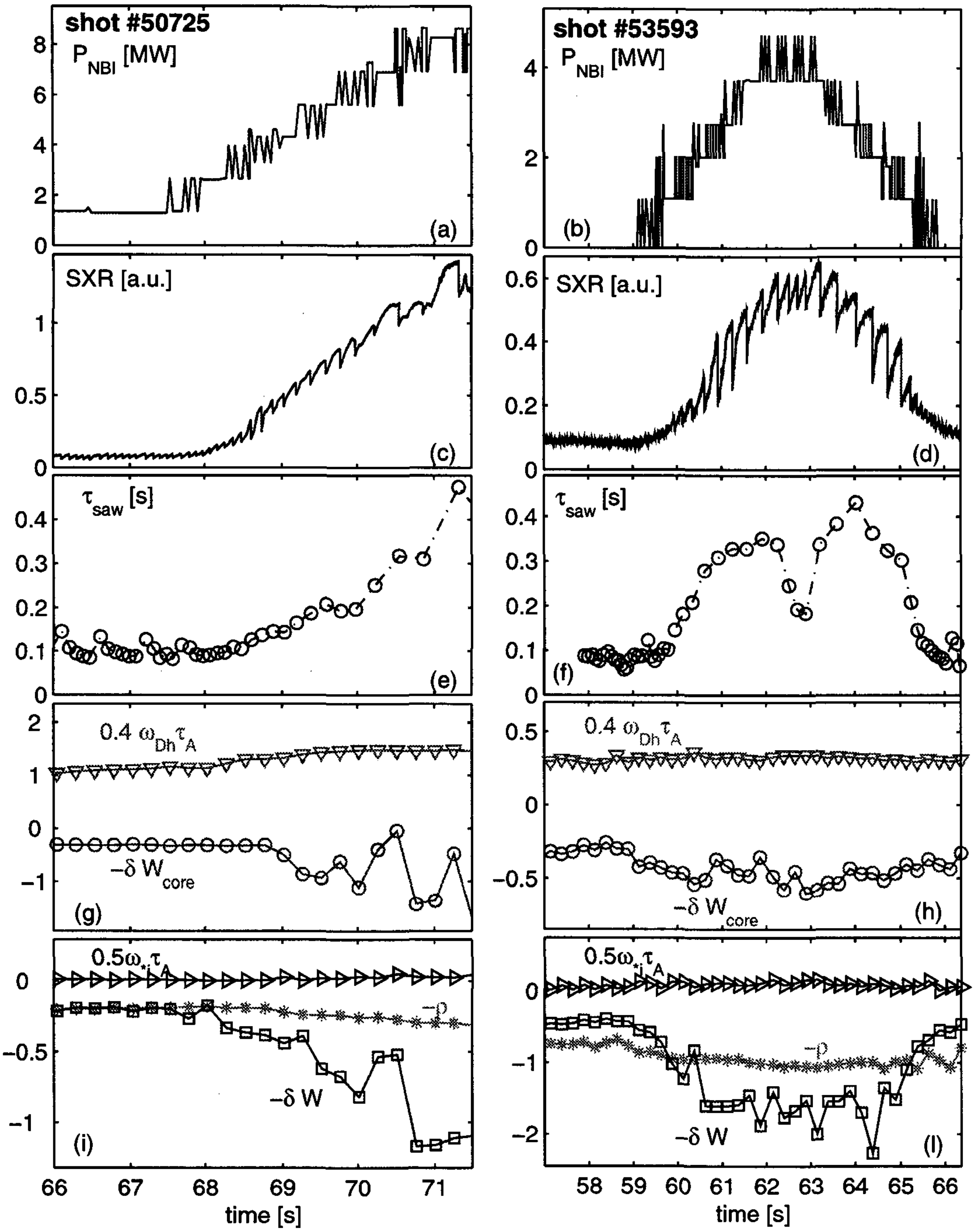

Figure 5.15: *(a) and (b) NBI power for shots 50725 and 53593; (c) and (d) central chord Soft X–ray signals; (e) and (f) corresponding sawtooth periods; (g) and (h) stability threshold described by equation (5.10); (i) and (l) relevant stability threshold terms in equations (5.13) and (5.14), used in the sawtooth period model. All the terms are computed directly from experimental measurements, as described in subsection 5.4.3. In (g) – (l) symbols indicate time slices of the experimental measurements;* $0.4\,\omega_{Dh}\,\tau_A$ *is plotted with triangles pointing down,* $0.5\,\omega_{*i}\,\tau_A$ *with triangles pointing right,* $-\delta\hat{W}_{core}$ *with circles,* $-c_\rho\hat{p}$ *with stars, and* $-\delta\hat{W}$ *with squares.*

fact that $-\delta W$ is always less than $0.5\omega_{*i}\tau_A$ indicates that the ideal kink mode was stable throughout these discharges. In both cases, and in all the other discharges we have analyzed, the instant at which the sawtooth period starts to increase corresponds to the time at which the fast ion stabilizing contribution is such that $-\delta\hat{W}$ becomes smaller than $-\hat{\rho}$, thereby stabilizing the resistive internal kink mode. Corresponding agreement is found during the ramp–down phase in the case of shot ♯53593. Note that in this analysis effects on magnetic shear due to rapid time variations in the current profile are neglected, and the analysis cannot therefore reproduce every detail of the sawtooth period behaviour. Transient current profile modifications could account for the sawtooth period variations observed during the power flat top phase in shot ♯53593. In the first part of the heating phase, before the power ramp, with either purely Ohmic heating [shot ♯53593] or with very low auxiliary heating power [shot ♯50725], the sawtooth period remains almost constant, around 100 ms. In our picture this is the signature of a situation in which equation (5.14) is already satisfied during the sawtooth ramp, and the crash is triggered by the fulfillment of equation (5.19), when the magnetic shear s_1 exceeds the critical shear $s_{1\,crit}$ [equation (5.20)]. In this case the term $\delta\hat{W}_{fast}$ does not play any role in determining the sawtooth period. During the NBI power ramp, with the consequent increase of the fast ion pressure, $-\delta\hat{W}$ drops strongly below $-\hat{\rho}$, due to the growth of the term $\delta\hat{W}_{fast}$. At this point, the condition determining the sawtooth period is switched from equation (5.20), involving the critical shear, to equation (5.14), i.e. $-\delta\hat{W} > -\hat{\rho}$, and it is the $\delta\hat{W}_{fast}$ term, being the dominant contribution to the kink energy, which directly determines the sawtooth period. This accounts for the linear correlation experimentally observed between the sawtooth period and the fast particle energy content inside the $q = 1$ surface.

In order to test this hypothesis we have carried out sawtooth period simulations with PRETOR. These simulations were performed with density profiles taken directly from experimental measurements, and kept constant during the sawtooth evolution. This approximation is consistent with analysis of the interferometer central line–integrated density signals, which in general do not show a strong signature of sawtooth activity, particularly during the H–mode phases. It thus appears that sawtooth relaxations in these discharges did not significantly affect density profiles, which were very flat inside the inversion radius. The experimental temperature profiles were simulated by adapting the values of transport coefficients, in order to reproduce correctly the experimental pressure profiles: this is crucial for a reliable evaluation of all the contributions to the kink energy. Particular care must be taken on this point, since an L–H transition usually occurs during the power ramp. The sawtooth period behaviour was nevertheless unaffected by this event. We have analyzed shots that remained in L–mode, such as shot ♯53593, shots in which the L–H transition occurred after the phase characterized by an increase of the sawtooth period, and shots in which the L–H transition clearly occurred before the beginning of that phase, such as shot ♯50725. In this last example the L–H transition occurred at 67.58 s: from Figure 5.15 it is apparent that the sawtooth period increased only during the H–mode phase. No significant differences in the sawtooth period behaviour were observed in all these different situations. The plasma current density and safety factor profiles in PRETOR are computed by solving a diffusion equation for the poloidal magnetic field, in which the plasma conductivity is assumed to be neoclassical and computed using formulae which take into account collisionality and plasma shape effects at finite aspect ratio, Section 2.4. The 1D transport code is coupled, at each time step, with a self-consistent equilibrium solver. It must be emphasized that application of the sawtooth trigger conditions requires detailed knowledge of several quantities, which must be computed consistently. In particular, the time evolution of the current density and safety factor profiles, involving the radial position of the $q = 1$ surface, as well as the evolution of the pressure profiles, and their related gradients at $q = 1$, play a crucial role in the calculation of all the contributions to the kink potential energy functional. As indicated in the previous section, the fast ion pressure profile, as well as the NBI heating power source, were taken directly from the PENCIL output.

We now concentrate on the power ramp–up phase of shot ♯50725. Figures 5.16, 5.17, 5.18 show the results of the PRETOR simulations for three representative time slices: 67.0 s, in Figure 5.16, during the phase in which the sawtooth period is still constant and sawtooth activity clearly repetitive; 68.6 s, in Figure 5.17, at the middle of the NBI power ramp, during the phase of increase of the sawtooth period; and 70.5 s, in Figure 5.18, at the top of the power ramp, with the longest sawtooth periods. Figures 5.16(a), 5.17(a) and 5.18(a) show the time evolution of the terms involved in Eq. (5.10), while Figures 5.16(b), 5.17(b) and 5.18(b) show the behaviour of the contributions of the kink energy and related stability thresholds for the terms involved in Eq. (5.13) and Eq. (5.14). In Figures 5.16(c), 5.17(c) and 5.18(c) we have shown the time evolution of the magnetic shear s_1 and the critical shear $s_{1\,crit}$, Eq. (5.20).

At 67.0 s [Figures 5.16], the $\delta\hat{W}_{fast}$ term is not yet large enough to be dominant in triggering the sawtooth crash. The condition $-\delta\hat{W} > -\hat{p}$ is reached during the sawtooth ramp before the shear s_1 crosses the critical shear $s_{1\,crit}$. In this situation it is Eq. (5.19), or equivalently Eq. (5.20), which provides the triggering condition, and the destabilized mode is the resistive internal kink in the ion-kinetic regime. During this low NBI power heating phase, not only Eq. (5.10) is largely satisfied [Figure 5.16(a)] but even $-\delta\hat{W}_{core}$ remains negative, showing that in this situation the ideal internal kink remains stable, independently of the stabilizing effect of fast particles.

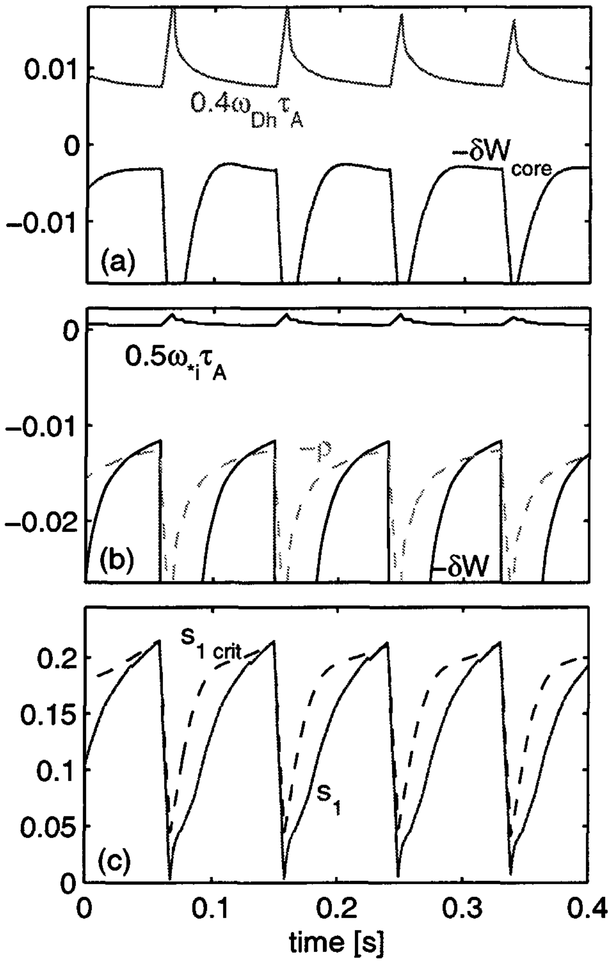

Figure 5.16: *Time evolution of the relevant terms involved in the stability thresholds of the sawtooth period model in a PRETOR simulation of shot 50725 at time 67.0 s.*

At 68.6 s [Figure 5.17], $\delta\hat{W}$ has not yet crossed $\hat{p}$ when s_1 crosses s_{1crit}. The condition given by Eq. (5.20) [Figure 5.17(c)] is before $-\delta\hat{W}$ exceeds $-\hat{p}$, and hence no longer plays the dominant role in triggering the crash. In this case the condition $-\delta\hat{W} > -\hat{p}$ [Eq. (5.14)] triggers the crash. The beam ion stabilizing term $-\delta\hat{W}_{fast}$, being the dominant contribution to the internal kink energy $-\delta\hat{W}$, thus plays the crucial role in determining the sawtooth period in the simulation, yielding a value of τ_{saw} of 150 ms, whereas the experimental value is 125 ms. The destabilized mode is still the resistive internal kink in the ion–kinetic regime. The ideal kink is still largely stable, as shown in Figures 5.17(a) and (b): Eqs. (5.10) and (5.13) are both satisfied. Figure 5.17(a), in contrast to Figure 5.16(a), shows also that the ideal internal kink would be close to instability without the stabilisation provided by energetic ions, as $\delta\hat{W}_{core} \sim 0$ at the sawtooth crash.

At 70.5 s [Figure 5.18] the behaviour is similar. The sawtooth crash is still determined by

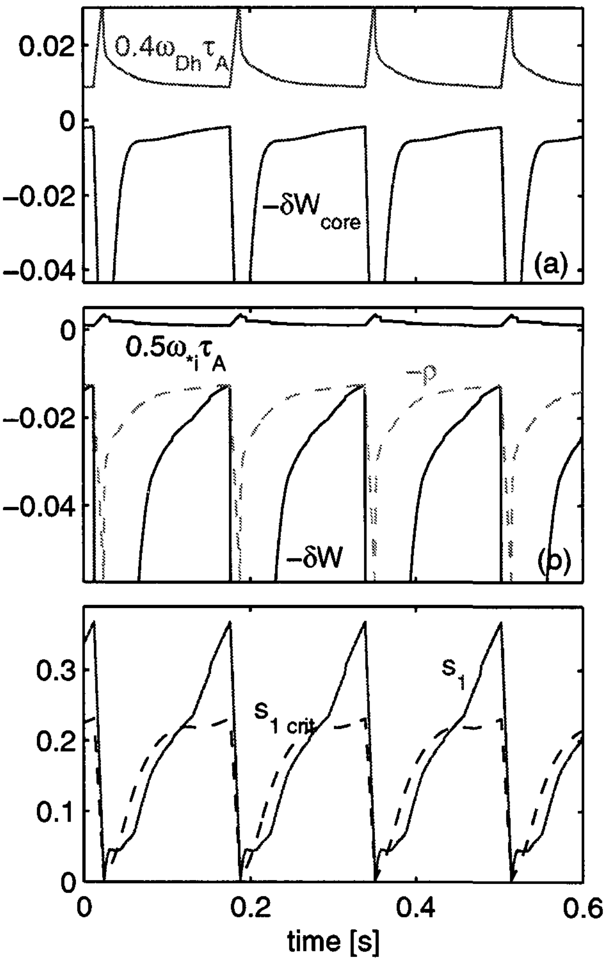

Figure 5.17: *Time evolution of the relevant terms involved in the stability thresholds of the sawtooth period model in a PRETOR simulation of shot 50725 at time 68.6 s.*

the condition $-\delta\hat{W} > -\hat{p}$ since Eq. (5.20) is satisfied earlier. In this case we note from Figure 5.18(a) that the term $-\delta\hat{W}_{core}$ becomes positive during the sawtooth ramp, because of the strong NBI central heating and the consequent strongly peaked profiles. Without the fast ion stabilisation, the ideal internal kink would be destabilized after approximatively 160 ms, well before both the simulated crash, which occurs at $\tau_{\rm saw} = 350$ ms, and the actual crash, which occurs after 325 ms. This strongly indicates the necessity of taking into account fast ion stabilization in order to explain experiments. Figure 5.18(a) shows also that at the time of the sawtooth crash the condition $\gamma_{core} \equiv -\delta\hat{W}_{core} \,/\, \tau_A < \omega_{Dh}$, which is necessary for fast particle stabilisation, is satisfied only marginally. Thus, with strong NBI heating power, the consequent high ion temperature starts to destabilize more efficiently the ideal kink than the fast ions stabilizing effect, even if large fast ions densities are produced. The beam injection energy is then too low for beam ions to stabilize efficiently the internal kink. This indicates that the experiments have been performed in

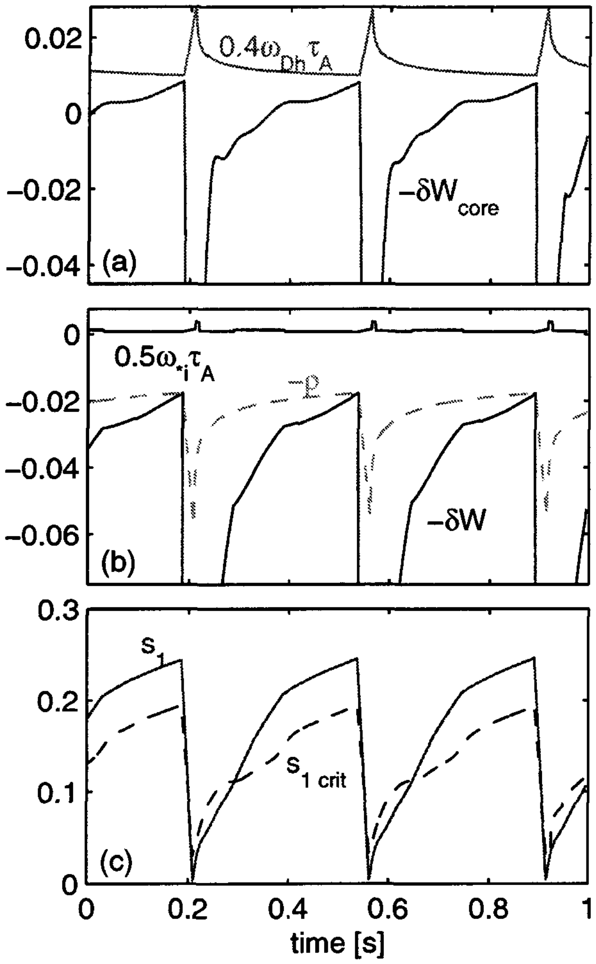

Figure 5.18: *Time evolution of the relevant terms involved in the stability thresholds of the sawtooth period model in a PRETOR simulation of shot 50725 at time 70.5 s.*

a stability window of parameter space, within which beam ion stabilisation can be effective. The value of the shear s_1 at the crash is larger for sawteeth delayed by beam ion stabilisation [Figures 5.17(c) and 5.18(c)] than it is for the case in which s_1 is limited by s_{1crit} at the crash [Figure 5.16(c)]. This may help to account for the excitation of NTMs in JET after long sawtooth periods, resulting from stabilisation by NBI or ICRH [34].

With a completely analogous procedure, we have analyzed two other discharges and performed simulations at time slices with different levels of NBI power [see Ref. [26] for the complete analysis of another shot, ♯53595, not shown in the present thesis]. The simulated sawtooth periods, determined by the triggering condition involving fast ion stabilisation, as in the case of 68.6 s and 70.5 s for shot ♯50725 [Figures 5.17 and 5.18], are found in every case to be in reasonable quantitative agreement, within 20%, with the experimentally observed sawtooth periods.

5.5 Summary and Conclusions

We have presented and discussed in large detail a sawtooth period model and a set of prescriptions to compute the post–crash relaxed profiles [4] suited for implementation in any 1–1/2 transport code. The present results are the first full integration of a sawtooth model in a transport code for detailed comparison with experimental results. Moreover the simulations of very different regimes have enabled us to test almost all the aspects of the model.

This model allows us to include a physical description of the sawtooth activity in transport simulations. This is important for sawtoothing discharges, in particular to predict plasma profiles in designed future devices. On the other hand, the model is correctly applied provided that it is included in a 1–1/2 transport code. Various plasma parameters, such as local gradients of the plasma profiles and the magnetic shear at the $q = 1$ surface, which are difficult to measure, are crucially involved in the stability thresholds and their time evolution must be described consistently.

We have applied this model to the simulation of the sawtooth period in discharges of two tokamaks, TCV and JET. This has enabled us to investigate the effects of different stability thresholds in very different plasma conditions. The simulation of a large set of TCV Ohmic discharges, with very different plasma shapes, allows the identification of the relevant instability regime for the internal kink for TCV operation. The corresponding stability threshold, involving a critical value for the magnetic shear at the $q = 1$ surface ($s_1 > s_{1crit}$), has been found adequate to simulate the sawtooth period with a limited variation of one free parameter included in the crash condition. The sawtooth period simulations have also allowed us to have an insight into the dynamics of the different relevant plasma and equilibrium parameters, in particular the time evolution during the sawtooth ramp of the location of the $q = 1$ magnetic surface and of the magnetic shear at that position. These parameters are important in order to determine in the simulations the position of the mixing radius at the sawtooth crash, and thus of the inversion radius. This plays a crucial role in the simulation of plasma profiles for sawtoothing Ohmic discharges. The model results have been found in good agreement with the experimental profiles in this large set of Ohmic discharges.

The critical shear criterion is also the relevant stability threshold at play in TCV discharges with ECH. We have analyzed and simulated a set of experiments performed in order to assess the role of ECH on sawtooth activity. As a first experimental observation it has been seen that moving the power deposition vertically in the poloidal cross–section from the bottom to the top, two specific locations on both sides of the magnetic axis and close to the sawtooth inversion radius are experimentally observed to maximize the sawtooth period. Two main effects are at play during these experiments: the variation of the heating power density and the current drive. These two effects must be regarded as powerful tools provided by ECH to modify and control the sawtooth period. The experimental and theoretical investigation of this issue is therefore of large interest.

It has been observed that increasing the value of the power density close to the sawtooth inversion radius, at the position maximizing the period in the vertical sweep, the sawtooth period is further stabilized. This effect has been quantitatively reproduced by the model, highlighting that the parameter dependence of the expression for the critical shear is consistent with the experimental observations. In particular the critical shear is almost proportional to the local pressure gradient at the $q = 1$ surface, due to the theoretical expressions of both the resistive and ion–kinetic growth rates. The pressure gradient is the relevant parameter mostly modified by localized ECH. Simulations show clearly that higher values of the power density imply larger pressure gradients, and thus increase the value of the critical shear, stabilizing sawteeth.

Another plasma parameter which plays a crucial role in the stability threshold and which can be locally strongly modified with ECH is directly the magnetic shear. Changing very small amounts of current drive from counter– to co–direction, close to the inversion radius, increases the sawtooth period. The stabilizing effect of co–ECCD and the destabilizing effect of counter–ECCD has been simulated successfully by the model. The magnetic shear dynamics is strongly affected by local amounts of current drive. The shear at $q = 1$ builds up more quickly in the presence of counter–ECCD, whereas it increases more slowly with co–ECCD. Therefore with counter–ECCD the critical shear value is reached earlier, leading to shorter sawtooth periods, whereas the opposite occurs with co–ECCD, leading to longer periods.

These two major effects, due to power density and to current drive, are both at play during the vertical sweeps of the ECH beams in the poloidal cross section. The sawtooth period model is able to reproduce with satisfactory agreement the rather complex experimental behaviour, provided that the heating and current drive sources are accurately taken into account in the simulation. In particular, the two maxima of the sawtooth period at two heating locations on opposite sides of the magnetic axis are also obtained in the simulations. The presence of these two maxima must be ascribed to the increase and decrease of the level of the heating power density close to the $q = 1$ surface during the sweep. The simulations allow us to exactly determine the maximizing locations relative to the position of the $q = 1$ surface. It turns out that the location maximizing the sawtooth period is outside the $q = 1$ surface at the sawtooth crash, contrary to what is usually assumed from the crash conditions, in particular from $s_1 > s_{1crit}$. Narrow power deposition profiles imply that the maximum of the sawtooth period is obtained close to $q = 1$, while broad power depositions imply that the maximum occurs farther outside the $q = 1$ surface, sometimes even outside the mixing radius. Due to the uncertainties in the magnetic equilibrium reconstructions, which are not constrained by any measurement of the current density profile in TCV, these locations are difficult to determine experimentally with the accuracy which would be necessary for a reliable comparison. Therefore this prediction of the model calls for further validation with experiments performed in tokamaks in which accurate measurements of the current profile are available.

Heating systems like ECH which are able to control the sawtooth activity are of crucial importance for future fusion devices. It has been recently discovered that long sawtooth periods provide large seed islands which can efficiently destabilize undesirable pressure limiting neoclassical tearing modes [3], which would reduce the fusion yield. α–particles arising from fusion reactions have been predicted by the present sawtooth period model to strongly stabilize the sawtooth period up to about 100 s [4]. Therefore, if on the one hand it is important to investigate theoretically how the heating systems can modify and control the sawtooth period, on the other hand it is also of specific interest for fusion research to validate the model predictions on sawtooth stabilization due to fast ions. For this reason we have applied the model to the simulation of the sawtooth period in JET discharges in which experimental evidence of sawtooth stabilization due to NBI has been observed.

We have included in the model a simplified expression assuming isotropic ions taking into account the beam ion contribution $\delta\hat{W}_{\text{fast}}$ to the internal kink potential energy $\delta\hat{W}$. This expression has been validated with detailed calculations performed with the hybrid kinetic/MHD code NOVA–K, using realistic distribution functions calculated by the plasma analysis code TRANSP. Sawtooth period simulations have provided results which reproduce the experimental observations with remarkably good agreement. This allows a clear physical explanation of the observed phenomena and indicates that the main physical effects are well described by the theoretical model. The relevant unstable mode is still the resistive internal kink, in the ion–kinetic regime. But the fast ion contribution $\delta\hat{W}_{\text{fast}}$ implies that the relevant stability threshold, with fast ion stabilization, is not the critical shear criterion any more (note however that the value of s_1 is still of importance as $\delta\hat{W}_{fast} \propto 1/s_1$). Large negative values of $\delta\hat{W}$ imply that the mode becomes strongly localized at the $q = 1$ surface, taking the structure of a tearing mode which is assumed to be insufficiently global to destabilize a sawtooth crash. Therefore the relevant threshold with fast ion stabilization is related to the value of the internal kink potential energy $(-\delta\hat{W} > -\hat{\rho})$. Since the fast particle contribution is dominant in $-\delta\hat{W}$, this criterion is able to explain the experimentally observed linear relation between the sawtooth period and the fast particle energy content. It allows simulations in good quantitative agreement, within 20%, with the experimentally observed sawtooth periods and confirms the role of NBI fast ions in sawtooth stabilization. The same criterion was found in Ref. [4] to be the sawtooth trigger most likely to be relevant to burning plasmas with α–particle stabilization. It should be applicable and should provide satisfactory results also in the simulation of sawtooth stabilization observed with fast ions arising from ICRH. But in this case more complicated analytical descriptions of the fast particle contribution $\delta\hat{W}_{\mathrm{fast}}$ are needed, since the fast ion distributions are generally more complex than those resulting from NBI, in both velocity and coordinate space. This calls for further research.

Bibliography

[1] S. von Goeler, W. Stodiek and N. Sauthoff, Phys. Rev. Lett. **33**, 1201 (1974).

[2] R. Aymar, Plasma Phys. Control. Fusion **42**, B385 (2001).

[3] O. Sauter *et al Neoclassical tearing mode seed island control with ICRH in JET*, presented at 28th EPS Conference on Control. Fusion and Plasma Physics, Madeira 2001; submitted to Phys. Rev. Lett. (2001).

[4] F. Porcelli, D. Boucher, and M.N. Rosenbluth, Plasma Phys. Control. Fusion **38**, 2163 (1996).

[5] F. Porcelli *et al*, Report JET-IR(88)16, JET Laboratory (1988).

[6] F. Porcelli, Plasma Phys. Control. Fusion **33**, 1601 (1991).

[7] F. Porcelli *et al*, Int. Conf. Fusion Plasmas (Proc. Conf. Innsbruck, 1992) Vol. **16c**, part II, p. 901, (European Physical Society, Geneva 1993).

[8] O. Sauter *et al*, in *Theory of Fusion Plasmas*, Proc. Joint Varenna-Lausanne International Workshop, Varenna 1998, (J.W. Connor, E. Sindoni, J. Vaclavik, Eds), ISPP-18, Editrice Compositori, Bologna (1999), p. 403.

[9] C. Angioni *et al*, in *Theory of Fusion Plasmas*, Proc. Joint Varenna-Lausanne International Workshop, Varenna 2000, (J.W. Connor, O. Sauter, J. Vaclavik, Eds), ISPP-19, Editrice Compositori, Bologna (2001), p. 73.

[10] O. Sauter *et al*, Phys. Plasmas **8**, 2199 (2001).

[11] A. Sykes and J. A. Wesson, Phys. Rev. Letters **37**, 140 (1976).

[12] G. Vlad, A. Bondeson, Nucl. Fusion **29**, 1139 (1989).

[13] F. Porcelli, E. Rossi, G. Cima, A. Wootton, Phys. Rev. Lett. **82**, 1458 (1999).

[14] B.V. Waddell, M.N. Rosenbluth, D.A. Monticello, R.B. White, Nucl. Fusion **16**, 528 (1976).

[15] R.B. White, D.A. Monticello, M.N. Rosenbluth, B.V. Waddell, Proc. 6th Conf. on Plasma Physics and Controlled Nuclear Fusion Research, Berchtesgaden 1976, IAEA, Vol. 1, 569 (1977).

[16] J.A. Wesson, Nucl. Fusion **30**, 2545 (1990).

[17] L. Zakharov and B. Rogers, Phys. Fluids B **4**, 3285 (1992).

[18] L. Zakharov, B. Rogers and S. Migliuolo, Phys. Fluids B **5**, 2498 (1993).

[19] M. Ottaviani and F. Porcelli, Phys. Rev. Lett. **71**, 3802 (1993).

[20] Z. A. Pietrzyk *et al*, Nucl. Fusion **39**, 587 (1999).

[21] H. Reimerdes *et al*, Plasma Phys. Control. Fusion **42**, 629 (2000).

[22] H. Lütjens, A. Bondeson and G. Vlad, Nucl. Fusion **32**, 1625 (1992).

[23] M.N. Bussac, R. Pellat, D. Edery and J.L. Soule, Phys. Rev. Lett. **35**, 1638 (1975).

[24] L. Degtyarev *et al*, Comput. Phys. Commun. **103**, 10 (1997).

[25] C. Angioni, A. Pochelon, N.N. Gorelenkov, K.G. McClements, O. Sauter *et al*, *Neutral beam stabilisation of sawtooth oscillations in JET*, submitted to Plasma Phys. Control. Fusion.

[26] A. Pochelon *et al*, *Sawtooth stabilisation by neutral beam-injected fast ions in JET*, presented at 28th EPS Conference on Control. Fusion and Plasma Physics, Madeira 2001, P5.009.

[27] N.N. Gorelenkov, C.Z. Cheng, and G.Y. Fu, Phys. Plasmas **6**, 2802 (1999).

[28] C. Wahlberg, Phys. Plasmas **5**, 1387 (1998).

[29] An. Martynov, O. Sauter, in *Theory of Fusion Plasmas*, Proc. Joint Varenna-Lausanne International Workshop, Varenna 2000, (J.W. Connor, O. Sauter, J. Vaclavik, Eds), ISPP-19, Editrice Compositori, Bologna (2001), p. 387.

[30] M.N. Bussac. R. Pellat, D. Edery and J.L. Soule, Proc. 6th Conf. on Plasma Physics and Controlled Nuclear Fusion Research, Berchtesgaden 1976, IAEA, Vol. 1, 607 (1977).

[31] M.D. Kruskal and C.R. Oberman, Phys. Fluids **1**, 275 (1958).

[32] M.N. Rosenbluth and N. Rostoker, Phys. Fluids, **2**, 23 (1959).

[33] B.N. Kuvshinov and A.B. Mikhailovski, Sov. Journal Plasma Phys. **13**, 527 (1987).

[34] T.M. Antonsen Jr., A. Bondeson, Phys. Fluids B **5**, 4090 (1993).

[35] G. Fogaccia and F. Romanelli, Phys. Plasmas **2**, 227 (1995).

[36] T.G. Northrop, *The Adiabatic Motion of Charged Particles*, Interscience, New York, (1963).

[37] K.G. McClements, R.O. Dendy, R.J. Hastie, T.J. Martin, Phys. Plasmas **3**, 2994 (1996).

[38] B. Coppi, S. Migliuolo, F. Pegoraro and F. Porcelli, Phys. Fluids B **2**, 927 (1990).

[39] K.G. McClements *et al.*, Nucl. Fusion **35**, 1761 (1995).

[40] S.C. Cowley, R.M. Kulsrud, T.S. Hahm, Phys. Fluids **29**, 3230 (1986).

[41] S. Migliuolo, F. Pegoraro, and F. Porcelli, Phys. Fluids B **3**, 1338 (1991).

[42] B. Coppi, R. Galvão, R. Pellat, M. Rosenbluth and P. Rutherford, Sov. Journal Plasma Phys. **2**, 533 (1976).

[43] F. Pegoraro, F. Porcelli and T.J. Schep, Phys. Fluids B **1**, 364 (1989).

[44] G. Ara, B. Basu, B. Coppi, G. Laval, M.N. Rosenbluth, and B.V. Waddell, Ann. Phys. (NY) **112**, 443 (1978).

[45] A.B. Mikhailovskii and V.P. Lakhin, Report IAE-5754/6 Kurchatov Institute (1986).

[46] F. Porcelli, Phys. Fluids **30**, 1734 (1987).

[47] F. Porcelli, Phys. Rev. Lett. **66**, 425 (1991).

[48] A. Bondeson, G. Vlad, H. Lutjens, Phys. Fluids b **4**, 1889 (1992).

[49] F. Porcelli and S. Migliuolo, Phys. Fluids **29**, 1741 (1986).

[50] T. P. Goodman *et al*, Proc. of 26th EPS Conf. on Contr. Fusion and Plasma Physics, Maastricht, 1999, ECA Vol. 23J (1999) p. 1101.

[51] F.M. Levinton, L. Zakharov, S.H. batha, J. Manickam, M.C. Zarnstorff, Phys. Rev. Lett. **72**, 2895 (1994).

[52] B.B. Kadomtsev, Fiz. Plasmy **1**, 710 1975 [English translation: Sov. Journal Plasma Phys. **1**, 389 (1976)].

[53] D.J. Campbell, R.D. GIll, C.W. Govers, J.A. Wesson *et al*, Nucl. Fusion **26**, 1085 (1986).

[54] P.A. Sweet, in *Electromagnetic Phenomena in Cosmic Physics*, edited by B. Lehnert (Cambridge Univ. Press, Cambridge 1958), p. 123.

[55] E.N. Parker, J. Geophys. Res. **62**, 509 (1957).

[56] A.Y. Aydemir, Phys. Fluids B **4**, 3469 (1992).

[57] F. Porcelli, C. Angioni, *et al*, Nucl. Fusion **40**, 1691 (2000).

[58] H. Soltwisch, Rev. Sci. Instrum. **59**, 1599 (1988).

[59] J. O' Rourke, Plasma Phys. Control. Fusion **33**, 289 (1991).

[60] W.P. West, D.M. Thomas, J.S. de Grassie, S.B. Zheng, Phys. Rev. Lett. **58**, 2758 (1987).

[61] R.D. Gill, A.W. Edwards, D. Pasini and A. Weller, Nucl. Fusion **32**, 723 (1992).

[62] D. Wroblewski, L.K. Huang and H.W. Moos, Phys. Rev. Lett. **61**, 1724 (1988).

[63] H. Weisen, G. Borg, B. Joye, A.J. Knight, and J.B. Lister, Phys. Rev. Lett. **62** 434 1989.

[64] C.G. Gimblett and R.J. Hastie, Plasma Phys. Control. Fusion **36**, 1439 (1994).

[65] J.B. Taylor, Rev. Mod. Phys. **58**, 741 (1986).

[66] H. Soltwisch, W. Stodiek, J. Manickam and J. Schluter, Plasma Phys. Control. Nucl. Fusion Res., (IAEA, Vienna) Vol. **1**, p. 433 (1986).

[67] I. Furno, C. Angioni, F. Porcelli, H. Weisen, *et al*, Nucl. Fusion. **40**, 1691 (2001).

[68] N.J. Lopez-Cardozo *et al*, Phys. Rev. Lett. **73**, 256 (1994).

[69] G. Cima *et al*, Plasma Phys. Control. Fusion **40**, 1149 (1998).

[70] M.A. Henderson, T.P. Goodman *et al*, in Proc. of Int. Workshop on *Strong Microvaves in Plasmas*, Nizhny Nogvorod 1999, edited by A.G. Litvak (2000), p. 114; M.A. Henderson *et al*, Fusion Eng. Des. **53**, 241 (2001).

[71] R.H Cohen, Phys. Fluids **30**, 2442 (1987);
K. Matsuda, IEEE Trans. Plasma Sci. **PS-17**, 6 (1989);
Y.R. Lin-Liu *et al*, in Controlled Fusion and Plasma Physics (Proc. 26th Eur. Conf Maastricht, 1999), Vol. 23J, European Physical Society, Geneva (1999), p. 1245.

[72] M.F.F. Nave *et al*, in Proc. 25th European Conf. on Control. Fusion and Plasma Physics, (EPS, Prague 1998), ECA Vol. **22C**, p. 365; submitted to Nucl. Fusion.

[73] D.J. Campbell *et al.*, Phys. Rev. Lett. **60** (1988) 2148.

[74] L.G. Eriksson, M. Mantsinen *et al*, Phys. Rev. Lett. **81**, 1231 (1998).

[75] J.P. Graves *et al*, Phys. Rev. Lett. **84**, 1204 (2000).

[76] P.A. Duperrex, A. Pochelon *et al*, Nucl. Fusion **32**, 1161 (1992).

[77] J. Ongena *et al.*, in Proc. 17th European Conf. on Control. Fusion and Plasma Heating, (EPS, Amsterdam 1990), ECA Vol **14B**, Part 1, p. 383.

[78] R.V. Budny, M.G. Bell, H. Biglari *et al*, Nucl. Fusion **32**, 429 (1992).

[79] D. Howell, R. Buttery, and T. Hender, private communication.

[80] P. de Vries *et al*, *"Analysis of shaping effects on sawteeth in JET"*, ibidem [26].

[81] C.Z. Cheng, Phys. Reports, **211**, 1 (1992).

[82] N.N. Gorelenkov, private communication (2001).

[83] N.N. Gorelenkov, M.F.F. Nave *et al Effect of plasma rotation on sawtooth stabilisation by beam ions*, presented at 27th EPS Conference on Control. Fusion and Plasma Physics, Budapest 2000.

[84] S.V. Putvinskij, in *Reviews of Plasma Physics*, Vol.**18** (Kadomtsev, B. B., Ed.), Consultants Bureau, New York (1986) p. 239.

[85] R.O. Dendy, R.J. Hastie , K.G. McClements , and T.J. Martin, Phys. Plasmas **2**, 1623 (1995).

[86] D. Bailey JET-R (1998) 04;
P.M. Stubberfield and M.L. Watkins JET-DPA(06)/87 (1987);
M. Cox Culham report for JET KR5-33-04 (1984).

Chapter 6

Conclusions and outlook

Physical systems relevant for thermonuclear fusion are of high complexity. Pure theoretical models usually require numerical tools suited to provide the connection with the experimental observations. These tools enable one to perform simulations whose results can be directly compared with the experimental measurements. The reliability of the simulations, and therefore of the physical models adopted, is of major relevance. The increasing cost of experiments in nuclear fusion calls more and more for accurate simulations in order to verify the feasibility of future projects and predict their performances. In this way, simulations can guide the research activities, reduce costs, and increase the level of public confidence and support.

During this thesis we have been mainly involved in the development and application of numerical tools which are intended for tokamak plasma simulations, with particular interest to transport phenomena. Two main topics have been tackled in this framework: the analysis and simulation of electron transport in TCV, mainly focusing on the electron temperature response to ECH, and the simulation of the sawtooth period in Ohmic and ECH discharges in TCV as well as in NBI discharges in JET. For this purpose, an existing transport code, PRETOR, has been further developed and now it can routinely supply the TCV device with transport analysis and predictions in a user–friendly numerical environment. Simulations have been performed by describing diffusive and convective transport with the semi–empirical Rebut-Lallia-Watkins transport model and by taking into account with a specific model the rapid transport phenomenon due to sawtooth activity. In order to correctly describe parallel transport, which is usually assumed neoclassical, we have also included in the plasma transport code the results of neoclassical calculations that we have undertaken in order to provide formulae for all the neoclassical transport coefficients valid for arbitrary aspect ratio and collisionality in realistic axisymmetric geometries. These results on neoclassical transport have been obtained in the framework of a third topic related to plasma transport, which adopts a kinetic description, and have been presented in the first part of the thesis.

Neoclassical Transport

The work on neoclassical transport first identified analytically a set of equations suited for implementation in exisisting Fokker–Planck codes (Section 2.2), performed numerical computations of the transport coefficients taking into account effects arising from both the realistic magnetic flux surface configuration and different collisionality regimes (Section 2.3). The analysis of the numerical results and the comparison with an analytical limit has allowed us to identify the adequate geometrical parameters, namely two definitions of the trapped particle fraction, which allow us to encapsulate the geometrical effects (subsection 2.3.2). In this way the numerical results obtained with different magnetic equilibria for each coefficient turn out to overlap on a single simple function of the appropriate trapped fraction parameter. This has enabled us to obtain very simple formulae for all the transport coefficients, by fitting the numerical results (Section 2.4). Parallel transport coefficients, namely the plasma conductivity and the bootstrap current coefficients, have been computed also at different values of collisionality (subsection 2.3.3). Since physically the effect of collisionality is to destroy the trapped particle orbits, the fit of the numerical results at arbitrary collisionality has been efficiently performed including directly the collisional parameter ν_* in the expression of the trapped particle fraction, leading to expressions for the effective trapped particle fractions in the presence of collisionality (subsection 2.4.2). The normal extension of this work is to perform the same kind of calculations at arbitrary collisionality also for all the perpendicular transport coefficients. This is a somewhat straightforward task at this stage, but demands very long computational times. For this reason, comparing the collisionality dependences obtained for the parallel transport coefficients with those of previous semi–analytical formulae available in the literature, we have proposed a set of combined formulae, including collisionality, for all the perpendicular transport coefficients (subsection 2.4.3). In this way we have provided simple numerical routines which compute all the transport coefficients by means of the present formulae, to be directly coupled with the experimental data in tokamaks or with existing transport codes. In the first case, this allows a direct and precise evaluation of neoclassical effects by means of a fast post–processing code after each discharge. This has been done on TCV to obtain the most accurate evaluation of the amount of ECCD in discharges with full non–inductive plasma current, obtaining in this way a reliable estimate of the current drive efficiency. In the second case, this allows a more precise computation of neoclassical coefficients in transport codes, in which neoclassical transport is usually poorly described, adopting relatively old and approximated formulae.

An interesting extension of the formulae is that of calibrating the dependence on the effective charge number Z_{eff} of the present formulae with the results obtained by the multi–species code NCLASS [1]. An interesting and more ambitious development could be to include in these formulas also effects due to the presence of potato orbits, which provide a non–negligible contribution close to the magnetic axis [2, 3], and effects due to the presence of steep gradients, whose characteristic length is comparable to the banana orbit width, which in general imply a reduction of the neoclassical transport [4, 5, 6]. A development of neoclassical theory has been done also to take into account the effect of non–Maxwellian distribution functions due to ECH on the bootstrap current [7], whose inclusion in our formulae would be particularly interesting for TCV operation. Note that neoclassical transport is acquiring now a new relevance in fusion community, in both data analysis and predictions, due to the new proposed devices with very low aspect ratio producing very large amounts of bootstrap current favourable to steady–state operation, and because of the discovery of improved confinement regimes, with internal transport barriers and high values of the plasma gradients. In this improved confinement scenarios neoclassical transport can play a non–negligible role, not only because high pressure gradients are able to drive large amounts of bootstrap current, but also because transport, particularly in the ion channel, is observed to be reduced inside the transport barrier to levels comparable to those given by neoclassical theory.

Electron transport

Thanks to the shape flexibility of the TCV device and its powerful ECH system, specific issues relevant to transport studies can be experimentally adressed in this tokamak. This provides a large amount of experimental results to be analyzed and simulated in order to validate transport models. The analyses of Ohmic discharges in TCV in a wide range of plasma shapes, densities and plasma currents, have pointed out that the crucial role in the simulation of Ohmic sawtoothing discharges is mostly played by the description of the current profile, and therefore of the plasma conductivity and of the field diffusion, as well as by the modelling of the sawtooth activity, more than by the specific transport model adopted (subsection 4.5.2). In the presence of ECH, an investigation of the experimental observations has allowed us to identify the most important characteristics of the electron temperature behaviour with ECH in TCV (Section 4.4). Due to the low density cut–off for X2 absorption, ECH operation in TCV is characterized by low densities and low values of T_i/T_e. The electron temperature response to central auxiliary heating shows a stiff behaviour in the confinement region, in the sense that the gradient scale length turns out to be independent of the heating power and essentially constant along the minor radius. With off–axis heating, the same behaviour is observed outside the deposition region, whereas in the plasma centre power balance analysis reveals a strongly reduced conductivity, since the temperature profiles remain peaked in the core despite the low level of ohmic power. These characteristics have recently been found to be common to several tokamaks

[8]. We have also shown that due to very high levels of power density available in TCV, evident modifications of the temperature profile can be produced even when the power is deposited in the confinement (stiff) region. We have shown that all these characteristics are correctly reproduced by the RLW transport model (subsection 4.5.4), which has allowed us to simulate heat electron transport in TCV with remarkable good agreement, even in some extreme plasma conditions. This has confirmed the very high reliability of this model in predicting electron transport, in particular within the plasma parameter domain which is relevant for TCV operation. This domain has been identified (namely $|\nabla T_e| \ll \nabla_{RLW}$ due to the low toroidal magnetic field in TCV) and discussed, and it has been found consistent with previous analysis on the validity of the model performed on the TORE SUPRA tokamak [9], which allows complementary experiments as compared with TCV (subsection 4.5.1). The new three gyrotrons at the third harmonic, with a much higher density cut–off, will allow transport analysis of discharges with densities up to $10^{20}\,\mathrm{m}^{-3}$. This should also allow us to assess whether the temperature profiles exhibit a constant temperature gradient scale length along the minor radius even at high density, and thus when plotted in semilogarithmic scale look like straight lines, or appear more parabolic, at least with low auxiliary heating powers, consistently with the RLW model predictions.

From a theoretical point of view, experimental observations strongly indicate that the physical process most likely to be at play in the electron anomalous transport involves a threshold in the critical electron temperature gradient scale length [10], like drift wave turbulence of TEMs and ETGs. We have pointed out that, due to the very high values of T_e/T_i and relatively high values of Z_{eff}, the threshold for the ETG turbulence is far above the experimentally observed gradients. Recently the Weiland model for TEMs has been found in agreement with the experimental observations in the ASDEX Upgrade tokamak [11, 8]. This model has already been implemented in PRETOR and it is foreseen to be applied to TCV discharges in the near future, in particular once also the ion temperature measurements will be available.

It is also envisaged to start the comparison of the results of gyrokinetic codes developed at the CRPP with TCV experiments. Work has already been undertaken in the comparison of the code results including the effects of the $\omega_{E\times B}$ shearing rate with discharges of ASDEX Upgrade presenting internal transport barriers and phases of improved confinement [12]. In this context, the new diagnostics very recently installed on TCV will allow new experimental investigations on electron transport and even on ion transport with electron heating at high density. In particular the electron cyclotron emission heterodyne radiometer should allow transport investigations extended to modulated ECH experiments [13], while the charge exchange spectroscopy using the carbon impurity [14] will reveal the behaviour of ions and allow measurements of the plasma toroidal rotation, which are essential for the evaluation of the radial electric field profile and thus of the $\omega_{E\times B}$ shearing rate.

Several experimental observations in TCV indicate that ECH allows important global and local current profile modifications, by both localized heating and current drive. Global current profile modification have been observed to modify the global plasma performance. Local current profile modifications have evident effects on sawtooth activity.

Dedicated experiments in TCV have identified a quasi–stationary regime of improved central electron confinement (Section 4.6). This regime has been widely investigated and simulated: very good agreement has been obtained even for regimes for which $\tau_{Ee}/\tau_{RLW} \simeq 3.5$. The continuous interaction between the code simulations and predictions and the experiments has been particularly fruitful in this context and has provided a valuable example of the role of simulations in support of the experimental activity. We can state that, out of the unavoidable uncertainties on the current density profile reconstruction, the reverse magnetic shear is the key for TCV improved central electron confinement (subsection 4.6.5). Further experimental investigations on the ICEC regime should be envisaged. Indeed some questions remain. In particular, power ramps and systematic scans on the toroidal injection angle in a set of similar discharges should point out if there is any threshold for obtaining this regime, that is a minimum amount of ECH power or of counter–ECCD. Power ramps could also explore the possibility of a hysteresis behaviour in the achievement and loss of the improved confinement. Moreover, the preheating phase could be assisted, or perhaps even replaced, by plasma current ramp–up, favouring the shear reversal formation. We have already performed some simulations for this scenario, pointing out that the effect of frozening the current penetration by increasing the electron temperature profile should produce strong beneficial effects in shaping the safety factor profile for improved plasma performances. These proposed experiments are intended to answer the very basic question: can the TCV plasma performance be further improved as compared with ICEC at the same power level and in quasi–stationary operation?

Experimental investigations on improved confinement regimes are of great relevance for future developments in nuclear fusion research. They allow experimentally to identify plasma parameters which are the keys in suppressing or increasing anomalous transport and therefore are suited to provide non–ambiguous tests for the validation of transport models. Moreover, in future fusion reactors, they allow the fusion yield to be increased, at the same cost of the fusion device and at the same level of input power.

Sawteeth

Several experiments in TCV have clearly assessed the potentialities of the ECH system in controlling the sawtooth period. A sawtooth model first introduced to predict the sawtooth period in ITER [15] has been generalized and used on a regular basis in the transport simulations performed with PRETOR (Section 5.2). Sawtooth activity implies a non–negligible and fast radial transport effect, which can not be ignored in transport simulations of sawtoothing plasmas. We have applied the sawtooth model in the simulation of the sawtooth period of TCV discharges in order to investigate theoretically the physical mechanisms by which the ECH can control the sawtooth activity (Section 5.3). This analysis has provided results in very good agreement with the experimental observations. This allows us to state that the parametric dependence of a stability threshold which compares the linear resistive growth rate of the internal kink with the stabilization provided by the ion and electron diamagnetic frequencies is consistent with the experimental observations in TCV. Low values of the magnetic shear due to ECCD in the co–direction, or large values of the local pressure gradient at the $q = 1$ surface, due to localized ECH, lead to sawtooth stabilization. In particular ECCD in the co–direction induces a slower build up of the magnetic shear s_1 at the $q = 1$ surface after the crash, while localized ECH not only implies a slower build up of s_1 but also implies larger pressure gradients, which increase the stabilization provided by diamagnetic rotation. These effects have been found to be most effective when ECH and ECCD are localized outside the pre–crash $q = 1$ surface, or even outside the mixing radius for broader deposition profiles.

Several experimental observations indicate that in TCV at high elongation and low triangularity the sawtooth crash is triggered by the destabilization of the ideal internal kink [16]. This plasma shape domain should be investigated by PRETOR simulations once a dependence of the ideal growth rate in terms of elongation and triangularity computed for plasmas with the same aspect ratio of TCV will be available.

Another stabilizing effect of particular importance for burning plasmas must be ascribed to the presence of fast particles. This has been investigated in JET with experiments and simulations in discharges with NBI. This work has allowed us to demontrate the role of beam ions in sawtooth stabilization and validate a sawtooth crash stability threshold which was predicted as the one most likely to be relevant for burning plasmas [15] (Section 5.4).

The detailed modelling results presented here are the first comparison of a sawtooth model fully integrated in a transport code with experimental data. The simulation of Ohmic, ECH and ECCD experiments in TCV, of NBI effects in JET and the effect of shape on sawtooth period [16] have allowed an accurate test of all the main characteristics of the sawtooth model described in Section 5.2. Sawtooth activity can not be ignored when predicting the plasma performance in future devices. Not only sawteeth produce a strong effect on the plasma profiles, but also, as recently demonstrated, can provide seed islands able to destabilize pressure limiting NTMs [17], which reduce the plasma performance and the fusion yield. Therefore, the reliability of a sawtooth model in predicting effects due to fast particle stabilization and to auxiliary heating systems available to control the sawtooth activity must be considered of major importance in future research in nuclear fusion. A direct development of the work done so far is to extend and apply the model to the simulation of discharges with ICRH and with both ICRH and NBI. This is a much more demanding task, since fast ions arising from ICRH have much more complex distribution functions, which call for a very accurate description of the $\delta\hat{W}_{fast}$ term [18]. Moreover, with ICRH, current drive and power localization are also significant, and therefore several effects can be at play at the same time, whose consequences on the sawtooth period are difficult to be distinguished. In this sense the work undertaken so far, namely the simulations of ECH and NBI discharges, must be considered as a first step analyzing two simple and independent heating schemes which allow the model to be validated in view of next applications in the simulation of more complex and combined effects, as those due to ICRH. Preliminary work in this direction has been already undertaken [19].

During this thesis we have been involved in several research topics in the field of tokamak plasmas, from kinetic calculations up to the design and analysis of new experiments. The results, fruit of both individual work and collaborations with other theoretical and experimental researchers, can be considered of relevance and utility for the design and operation of next devices towards a fusion reactor, and are of interest for the fusion physicists community.

Bibliography

[1] W. A. Houlberg, K. C. Shaing, S. P. Hirshman, and M. C. Zarnstorff, Phys. Plasmas **4**, 3230 (1997).

[2] K.C. Shaing, R.D. Hazeltine, Phys. Plasmas **5**, 953 (1998).

[3] P. Helander, Phys. Plasmas **7**, 2878 (2000).

[4] P. Helander, Phys. Plasmas **5**, 3999 (1998).

[5] T. Fulop, P. Helander, Phys. Plasmas **6**, 3066 (1999).

[6] H.A. Claassen, H. Gerhauser, A. Rogister *et al*, Phys. Plasmas **7**, 3699 (2000).

[7] P. Helander *et al*, Phys. Plasmas **4**, 3211 (1997).

[8] F. Ryter *et al*, *Experimental Studies of Electron Transport*, invited paper of the 28th EPS Conf. on Control. Fusion and Plasma Physics, Madeira 2001; to be published in Plasma Phys. Control. Fusion.

[9] G.T. Hoang, B. Saoutic, L. Guiziou *et al*, Nucl. Fusion **38**, 117 (1998).

[10] F. Ryter *et al*, Phys. Rev. Lett. **86**, 2325 (2001).

[11] G. Tardini *et al*, Proc. of the 28th EPS Conf. on Control. Fusion and Plasma Physics, Madeira 2001, Paper P2.053; submitted to Nucl. Fusion (2001).

[12] A. Bottino, private communication (2001).

[13] P. Blanchard, H. Weisen *et al*, Proc. of 28th EPS Conf. on Control. Fusion and Plasma Physics, Madeira 2001, P1.077.

[14] P. Bosshard, B.P. Duval, J. Mlynar, H. Weisen, Proc. of 28th EPS Conf. on Control. Fusion and Plasma Physics, Madeira 2001, P1.094.

[15] F. Porcelli, D. Boucher, and M.N. Rosenbluth, Plasma Phys. Control. Fusion **38**, 2163 (1996).

[16] H. Reimerdes *et al*, Plasma Phys. Control. Fusion **42**, 629 (2000).

[17] O. Sauter *et al*, *Neoclassical tearing mode seed island control with ICRH in JET*, presented at 28th EPS Conference on Control. Fusion and Plasma Physics, Madeira 2001; submitted to Phys. Rev. Lett. (2001).

[18] K.G. McClements, R.O. Dendy, R.J. Hastie, T.J. Martin, Phys. Plasmas **3**, 2994 (1996).

[19] M. Mantsinen *et al*, *Analysis of ion cyclotron heating and current drive at* $\omega \approx 2\omega_{cH}$ *for sawtooth control in JET plasmas*, Proc. of 28th EPS Conference on Control. Fusion and Plasma Physics, Madeira 2001; to be submitted to Plasma Phys. Control. Fusion (2001).

Acknowledgments

I would like to thank everyone who has directly contributed to the work undertaken in the present thesis.

I am particularly thankful to my thesis advisor Dr. Olivier Sauter. He has patiently led me through this work, with competence and enthusiasm, motivating me to get in contact with several aspects of tokamak plasma physics, from theory to experiments. During all these years, his door has always been open for any question, at any hour, and regardless the load of his own work. He has been for me a daily example and support, a reference and an encouragement. The human relationship that he has been able to create between us has not only permitted a more efficient scientific collaboration, but also the establishment of a sincere friendship which is everyday more precious for me.
Merci, merci vraiment!

I am indebted with many researchers at CRPP, and in particular with several experimentalists of the TCV team, who guided me in the jungle of plasma diagnostics, leading me towards the valuable quality of observing the experimental data with an objective "experimentalist's eye".

I am very grateful to Drs. Tim P. Goodman, Z. Adam Pietrzyk and Antoine Pochelon, with whom I had the real pleasure of fruitful and assiduous collaborations. I have also benefited from many helpful discussions with Drs. Roland Behn, Stefano Coda, Mark Henderson, Jean-Marc Moret, Jan Vaclavik, Laurent Villard and Henri Weisen, as well as with Ivo Furno and Holger Reimerdes, with whom I have shared these years as Ph.D. student at CRPP. A particular thank-you goes to Drs. Stefano Coda and Tim Goodman for reading carefully several parts of the present thesis.

I would like also to acknowledge the collaboration with Drs. Nikolai Gorelenkov (PPPL, Princeton) and Ken G. McClements (UKAEA, Culham), who have provided an essential theoretical support in the work on sawtooth stabilisation with NBI at JET.

I want to warmly thank Prof. Franco Porcelli. Since my first steps in plasma physics, almost eight years ago at the Politecnico di Torino, he has always supported me and kept his interest on my scientific progresses. I have benefited, in particular, from many explanations and discussions about the complexe domain of "sawtooth theory", on which his competence is invaluable.

I am grateful to Prof. Rakesh Chawla, Dr. G. Tuong Hoang (CEA, Cadarache), Dr. Jean-Marc Moret, Dr. Arthur G. Peeters (IPP, Graching), Dr. Olivier Sauter, Prof. M. Quang Tran, and MER Laurent Villard for accepting to be members of the thesis committee.

And finally, I would like to thank Prof. Francis Troyon, Prof. M. Quang Tran and Dr. Kurt Appert who gave me their confidence allowing me to start a Ph.D. in their laboratory in Lausanne. It has been a wonderful experience. I hope I have been able to not disappoint their confidence.

This work was supported in part by the Swiss National Science Foundation.

Clemente Angioni

Italian, married, date of birth: December 10th 1969

CRPP-EPFL, Bâtiment PPB,
1015 Lausanne, Switzerland.
Telephone : +41 21 6932263
E-mail : clemente.angioni@epfl.ch

Education

April 1997 - present : **Ecole Polytechnique Fédérale de Lausanne (EPFL), Switzerland.** **Ph.D.** Thesis - *"Modelling of electron transport and of sawtooth activity in tokamaks"*, Thesis Advisor Dr. O. Sauter.

June 1989 - Dec. 1994 : **Politecnico di Torino, Department of Energetics, Italy**
Degree: **Laurea** in Nuclear Engineering *cum laude*
"Collisional Transport in magnetically confined plasmas",
Advisor Prof. F. Porcelli.

Postgraduate courses
March 1999 - July 1999 : *"Physique et diagnostic des plasmas"*,
Oct. 1999 - Febr.2000 : *"Physique des plasmas confinés magnétiquement"*,
organized by Prof. M. Q. Tran, CRPP, EPFL, Lausanne.

Work Experience

April 1997 - present : **Centre de Recherches en Physiques des Plasmas, EPFL.**

- Assistant / Doctoral Student

- Implementation and usage of exisisting drift-kinetic Fokker-Planck codes (CQL3D and CQLP) for neoclassical transport calculations.
- Implementation of an existing transport code (PRETOR) for modelling of tokamak discharges, adopting automatic interfaces with experimental data and other numerical codes for the computation of additional heating sources, as well as coupling with different transport coefficient packages. Applied on TCV and JET.
- 1D simulations of the sawtooth period, and 2D simulations of the sawtooth ramp and crash behavior, involving numerical implementation of theoretical models.

- Supervision of general physics courses for Engineers of the EPFL, in support to the didactic activity of the CRPP.

November 2000 : **JET**. Collaboration in Task Force M as EFDA secondee, involved in modelling sawtooth period in discharges with fast ions arising from neutral beam and ion cyclotron heating, and with ion cyclotron current drive.

Sept. 1996 - March 1997 : Collaboration with Prof. F. Porcelli at the Politecnico di Torino in research on magnetic reconnection.

Others

March 1995 - Aug. 1996 : Scuola Militare Alpina (Alpine Military School), Aosta.
Compulsory military service, as an officer.

Language Skills

Italian : Mother tongue
French : fluent
English : fluent

Computer Skills

Operating Systems : UNIX, LINUX and Windows, basic knowledge of VMS.
Languages : C, C++, FORTRAN, Matlab, Maple, HTML.
Word-processing : LaTeX, FrameMaker, Microsoft Word.

Publications and Conference Contributions

[1] **C. Angioni**, D. Boucher, J.-M. Moret, and O. Sauter, *1D Transport modelling of TCV discharges*, in *Theory of Fusion Plasmas*, Proceedings Joint Varenna-Lausanne Int. Workshop 1998, J.W. Connor, E. Sindoni and J. Vaclavik Eds, Ed. Compositori, Bologna 1999, p. 493.

[2] O. Sauter, **C. Angioni**, D. Boucher, I Furno, A. Pochelon, and F. Porcelli, *Sawtooth period simulations of TCV discharges*, in *Theory of Fusion Plasmas*, Proceedings Joint Varenna-Lausanne Int. Workshop 1998, J.W. Connor, E. Sindoni and J. Vaclavik Eds, Ed. Compositori, Bologna 1999, p. 403.

[3] A. Pochelon, et al. (including **C. Angioni**), *Energy confinement and MHD activity in shaped TCV plasmas with localized electron cyclotron heating*, Nucl. Fusion, Yokohama Special Issue II, **39** (11Y) 1807 (1999).

[4] O. Sauter, **C. Angioni** and Y. R. Lin-Liu, *Neoclassical conductivity and bootstrap current formulas for general axisymmetric equilibria and arbitrary collisionality regime*, Phys. Plasmas **6** 2834 (1999);

[7] **C. Angioni**, O. Sauter, *Neoclassical transport coefficients for general axisymmetric equilibria in the banana regime*, Phys. Plasmas **7** 1224 (2000);

[5] O. Sauter et al. (including **C. Angioni**), *Steady-state fully non-inductive current driven by electron cyclotron waves in a magnetically confined plasma*, Phys. Rev. Letters, **84**, 3322, (2000).

[6] F. Porcelli, **C. Angioni**, et al. *Nonstandard relaxations oscillations of magnetically confined plasmas*, Nucl. Fusion **40** 1691, (2000).

[8] Z.A. Pietrzyk, **C. Angioni**, et al., *Central electron temperature enhancements due to sawtooth stabilization during counter electron cyclotron current drive in Tokamak à Configuration Variable*, Phys. Plasmas **7**, 2909 (2000).

[9] I. Furno, **C. Angioni**, F. Porcelli, H. Weisen, et al., *Understanding sawtooth activity during intense Electron Cyclotron Heating Experiments on TCV*, Nucl. Fusion **41** 403 (2001).

[10] **C. Angioni**, T.P. Goodman, A. Pietrzyk, and O. Sauter, *Simulations of Improved Confinement discharges and sawtooth period with ECH and Current Drive in TCV*, in *Theory of Fusion Plasmas*, Proceedings Joint Varenna-Lausanne Int. Workshop. Varenna 2000, J.W. Connor, O. Sauter and E. Sindoni Eds, Ed. Compositori, Bologna 2001, p. 73.

[11] Z.A. Pietrzyk, **C. Angioni**, R. Behn, S. Coda, T.P. Goodman, M. A. Henderson, F. Hofmann, O. Sauter, *Long-pulse Improved Central Electron Confinement in the TCV Tokamak with Electron Cyclotron Heating and Current Drive*, Phys. Rev. Letters **86**, 1530 (2001).

[12] O. Sauter, **C. Angioni** et al, *Steady-state fully non-inductive Operation with ECCD ad Current Profile Control in Tokamak à Configuration Variable*, Phys. Plasmas, **8**, 2199 (2001).

[13] A. Pochelon *et al*, (including **C. Angioni**), *Plasma shape effects on sawtooth/internal kink stability and plasma shaping using EC wave current profile tailoring in TCV*, 18th IAEA Fusion Energy Conference, Sorrento 2000; to be published in Nucl. Fusion.

[14] F. Porcelli *et al*, (including **C. Angioni**), *Macroscopic coherent magnetic islands*, 18th IAEA Fusion Energy Conference, Sorrento 2000; to be published in Nucl. Fusion.

[15] F. Ryter *et al*, (including **C. Angioni**), *Experimental Studies of Electron Transport*, invited paper of the 28th EPS Conf. on Control. Fusion and Plasma Physics, Madeira 2001; to be published in Plasma Phys. Control. Fusion.

[16] A. Pochelon, **C. Angioni** *et al*, *Sawtooth stabilisation by neutral beam-injected fast ions in JET*, presented at 28th EPS Conference on Control. Fusion and Plasma Physics, Madeira 2001, P5.009.

[17] **C. Angioni**, A. Pochelon, N.N. Gorelenkov, K.G. McClements, O. Sauter *et al*, *Neutral beam stabilisation of sawtooth oscillations in JET*, submitted to Plasma Phys. Control. Fusion (2001).